

University of Denver

Digital Commons @ DU

Electronic Theses and Dissertations

Graduate Studies

1-1-2019

Rapid-Scan EPR and Imaging

Yilin Shi

University of Denver

Follow this and additional works at: <https://digitalcommons.du.edu/etd>



Part of the [Chemistry Commons](#)

Recommended Citation

Shi, Yilin, "Rapid-Scan EPR and Imaging" (2019). *Electronic Theses and Dissertations*. 1690.
<https://digitalcommons.du.edu/etd/1690>

This Dissertation is brought to you for free and open access by the Graduate Studies at Digital Commons @ DU. It has been accepted for inclusion in Electronic Theses and Dissertations by an authorized administrator of Digital Commons @ DU. For more information, please contact jennifer.cox@du.edu, dig-commons@du.edu.

RAPID-SCAN EPR AND IMAGING

A Dissertation

Presented to

the Faculty of Natural Sciences and Mathematics

University of Denver

In Partial Fulfillment

of the Requirements for the Degree

Doctor of Philosophy

by

Yilin Shi

August 2019

Advisor: Dr. Sandra S. Eaton

©Copyright by Yilin Shi 2019

All Rights Reserved

Author: Yilin Shi
Title: RAPID-SCAN EPR AND IMAGING
Advisor: Dr. Sandra S. Eaton
Degree Date: August 2019

ABSTRACT

EPR imaging at low frequency is a powerful tool to obtain important biological information *in vivo* in a non-invasive way. Properties of nitroxide and trityl radical imaging reagents have been studied. Developments in rapid scan imaging techniques are reported that improve efficiency of experiments and user-friendliness of software.

Relaxation and signal-to-noise ratio (S/N) in pulse experiments on trityl radicals were measured at frequencies between 400 MHz and 1.5 GHz. Relaxation time increases as the frequency increases and the radical concentration decreases. Since relaxation time is a sensitive and accurate measure of oxygen pressure, this study provides criteria for the selection of the frequencies for *in vivo* applications.

Rapid-scan EPR of irradiated solids at L-band was studied. The results show that for the same data acquisition time, S/N for rapid-scans was significantly higher than for conventional continuous wave spectra.

Rapid scan EPR imaging of nitroxide was performed at 250 MHz. Experimental parameters for the sinusoidal single-sweep method were varied to get better image quality. The results show that larger gradient strength provides higher spatial resolution while smaller gradient step size provides finer texture. Another method based on field-stepped linear-scans was developed; field step size, rapid-scan segment width, rapid-scan frequencies and some other parameters were varied. The field-stepped linear-scan method

was compared with the sinusoidal single-sweep method using criteria including linewidth and S/N, and the former turned out to be a less effective alternative to the latter.

New developments have been made to expand what can be achieved with EPR imaging, such as reduced data acquisition time, quantification of image features, efficient use of instrument time, and simplified experimental procedures from data acquisition to spectral analysis. The Python programming language was used successfully as a new and comprehensive approach to run EPR imaging experiments compared to the prior method that used multiple software packages. These developments will make EPR imaging more accessible for a much wider user group.

ACKNOWLEDGEMENTS

My sincere thanks to Prof. Sandra Eaton, and Prof. Gareth Eaton, who helped and guided me throughout this research.

I want to thank the Department of Chemistry and Biochemistry for providing the facilities for this work.

My thanks to my committee: Dr. Martin Margittai, Dr. Bryan Cowen, Dr. Brian Majestic, Dr. Todd Blankenship.

Many thanks to Dr. George Rinard and Richard Quine for designing, building and repairing the instruments. I want to acknowledge Dr. Mark Tseitlin for providing MATLAB code for spectral deconvolution and image reconstruction. Also, thanks to Dr. Joshua Biller, Dr. Zhelin Yu, Dr. Laura Buchanan, Joseph McPeak and Lukas Woodcock for experimental assistance.

The work in this dissertation was supported by grants from the National Institute of Health grant P41 EB002034 and AIP CA 177744, hard won by Dr. Gareth and Dr. Sandra Eaton.

Finally, my deep appreciation to my parents and friends.

TABLE OF CONTENTS

Chapter 1 : INTRODUCTION.....	1
1.1 Electron Paramagnetic Resonance (EPR) Principle	1
1.1.1 Basic Theory	1
1.1.2 Hyperfine Interactions	3
1.1.3 Relaxation	5
1.2 EPR Techniques.....	6
1.2.1 CW EPR.....	6
1.2.2 Pulse EPR.....	7
1.2.3 Rapid-scan EPR	9
1.2.4 EPR Imaging.....	10
Chapter 2 : LITERATURE REVIEW: <i>IN VIVO</i> EPR IMAGING OF NITROXIDE	14
2.1 Introduction.....	14
2.2 Progress in EPR Imaging	15
2.2.1 Oximetry and Redox Status	15
2.2.2 Metabolism	22
2.2.3 Spatial Distribution	25
2.2.4 Nitroxide Properties.....	28
2.2.5 Method Development.....	30
2.2.6 Instrumentation	37
2.2.7 Other Subjects.....	40
2.3 Summary and Current Work.....	43
Chapter 3 : RELAXATION AND S/N MEASUREMENTS OF TRITYL RADICAL AT VARIOUS FREQUENCIES.....	47
3.1 Introduction.....	47
3.2 Materials	48
3.2.1 Sample.....	48
3.2.2 Instrument	49
3.3 Method	49
3.4 Results for Relaxation Times.....	51
3.4.1 Measurement of Sample Resonator Q	51
3.4.2 Spin-lattice Relaxation Time (T_1)	52
3.4.3 Spin-spin Relaxation Time (T_2)	54
3.5 Results for Relaxation Rates.....	57
3.5.1 Frequency Dependence of $1/T_1$, $1/T_2$ and $1/T_2 - 1/T_1$	57
3.5.2 Dependence of Relaxation Rates on the Concentration of OX063..	58
3.5.3 Dependence of Relaxation Rates on Salt Concentration	60
3.5.4 Dependence of S/N on Resonance Frequency	60
3.5.5 Dependence of S/N on Salt Concentration and Temperature at 700 MHz	61
3.6 Conclusion	62

Chapter 4 : L-BAND RAPID-SCAN EPR OF IRRADIATED SOLIDS	63
4.1 Introduction.....	63
4.2 Materials	64
4.2.1 Sample.....	64
4.2.2 Instrument	65
4.3 Methods.....	65
4.3.1 Resonator Q, Signal and Resonator Bandwidth.....	65
4.3.2 CW EPR.....	66
4.3.3 Rapid-scan EPR	67
4.4 Results.....	68
4.4.1 Power Saturation Curves.....	68
4.4.2 EPR Spectra	71
4.4.3 Line shapes.....	73
4.4.4 Signal-to-Noise Ratio (S/N).....	73
4.5 Conclusion	74
 Chapter 5 : VHF RAPID-SCAN EPR SPECTRA AND IMAGING	 75
5.1 Introduction.....	75
5.2 Materials	76
5.2.1 Sample.....	76
5.2.2 Instrument	78
5.3 Method	80
5.3.1 Rapid-scan EPRI.....	80
5.3.2 Field-reversal Background Subtraction	80
5.3.3 MATLAB Program.....	81
5.3.4 Use of Real and Imaginary Channels.....	83
5.3.5 Impact of 7 W Amplifier.....	84
5.3.6 Measurement of Gradient Coil Constant	85
5.3.7 Xepr and Python API.....	88
5.4 Rapid-Scan Spectra.....	90
5.4.1 Resonator Q Measurement.....	90
5.4.2 Power Saturation Curves.....	90
5.4.3 Background Study of Empty 16 mm CLR.....	95
5.4.4 Rapid-scan Spectra acquired with Various Rapid-scan Frequencies.....	98
5.4.5 Iron Signal Observed in Pyrex Tubes	100
5.5 Sinogram for Images.....	100
5.5.1 Texture of the Sinogram	101
5.5.2 Resolution of Signals from Compartments or Hyperfine Lines	101
5.5.3 Resonator in Effective Space.....	101
5.5.4 Resonator Outside of Effective Space	104
5.6 Rapid-Scan 2D Spectral-spatial Imaging.....	106
5.6.1 Criteria for Image Quality.....	106
5.6.2 Rapid-scan Imaging with Various Parameters.....	106
5.6.3 Trade off Among Different Parameters	112
5.6.4 Image with Other Samples.....	119
5.7 Field-Reversal Background Subtraction	122

5.8 Conclusion	125
Chapter 6 : VHF FIELD-STEPPED EPR SPECTRA AND IMAGING	127
6.1 Field-Stepped EPR Introduction	128
6.2 Materials	129
6.2.1 Sample.....	129
6.2.2 Instrument	129
6.3 Method	129
6.4 Field-Stepped Spectra	131
6.4.1 Comparison of Field-stepped Rapid-scan Spectrum with CW	131
6.4.2 Optimization of Experimental Parameters for a Spectrum	132
6.5 Field-Stepped Linear Scan Imaging.....	135
6.6 Comparison of Field-Step Method with Single Sweep Method	138
6.6.1 EPR Spectra	138
6.6.2 Spectra with Gradients.....	140
6.6.3 EPR Imaging.....	143
6.6.4 Sinogram	145
6.7 Conclusion	146
Chapter 7 : NEW DEVELOPMENTS IN VHF RAPID-SCAN EPR IMAGING.....	148
7.1 EPR Imaging with Various Averages	148
7.2 EPR Image Quantification	153
7.2.1 Dimension of the Subject.....	153
7.2.2 Radical Quantification	155
7.3 Time Distribution in an Imaging Experiment.....	163
7.4 Limitations	165
7.4.1 Software Limitations.....	165
7.4.2 CAEN Power Supply Limitations.....	166
7.4.3 SpecJet-II Digitizer	167
7.5 3D-Printed Sample Holder.....	172
7.5.1 How to Create 3D-prints	173
7.5.2 3D-print Material	173
7.5.3 Waterproof	174
7.6 Imaging with Multiple Samples.....	176
7.7 2D Spatial Imaging	187
7.7.1 Principle	188
7.7.2 2D Spatial Image with One Sample.....	190
7.7.3 Image with More Samples Simultaneously	191
7.8 Python as a New Way of Performing EPRI.....	193
7.8.1 New Spectra Data Format	193
7.8.2 Spectral Analysis	195
7.8.3 Python Language as an All-in-one Solution for EPRI.....	197
Chapter 8 : CONCLUSIONS AND FUTURE WORK	201
Conclusions.....	201
Future work.....	204

BIBLIOGRAPHY.....	205
APPENDICES	220
Appendix A: MATLAB Code for Field-Stepped Linear Scan EPR.....	220
Appendix B: MATLAB Code for Rapid-Scan EPR Analysis	224
Appendix C: Python Code for VHF Experiments	231
Appendix D: Drawings of Hardware	262
Appendix E: 3D Printed Sample Holders for Imaging	273
Appendix F: Equations and Experimental Parameters	274
Appendix G: List of Publications	276

LIST OF FIGURES

Chapter One	1
Figure 1.1 Basic concept of electron paramagnetic resonance, from [1].....	2
Figure 1.2 Examples of hyperfine splitting.....	4
Figure 1.3 Electron spins in a magnetic field, from [1]	5
Figure 1.4 Schematic diagram of CW EPR, from [1].....	7
Figure 1.5 Pulse sequence for echo decay experiment to measure T_2	8
Figure 1.6 Pulse sequence for inversion recovery to measure T_1	9
Figure 1.7 Schematic diagram of rapid-scan EPR	10
Figure 1.8 Cross section of a phantom	11
Figure 1.9 Illustration of EPR imaging using magnetic field gradients	11
 Chapter Three	 47
Figure 3.1 Microwave frequency dependence of T_1 for OX063 in HEPES buffer	54
Figure 3.2 Microwave frequency dependence of T_2 for OX063 in HEPES buffer	56
Figure 3.3 Microwave frequency dependence of relaxation rates for OX063 in pH = 7.4 solution at ambient temperature (19 ° C).....	58
Figure 3.4 Frequency dependence of S/N (normalized by \sqrt{Q}) for OX063 in 10 mM HEPES buffer at 19 °C.....	61
 Chapter Four	 63
Figure 4.1 L-band Power Saturation Curves for 3 of the samples.....	69
Figure 4.2 L-band spectra for 3 of the samples	72
 Chapter Five	 75
Figure 5.1 Block diagram of Rapid-scan imaging system, from [6]	79
Figure 5.2 A functional EPRI system actively collecting data	79
Figure 5.3 Illustration of field reversal background correction method.	81
Figure 5.4 LiPc point sample	85
Figure 5.5 Signal splitting under various gradients for two LiPc samples	86
Figure 5.6 Test image with estimated coil constant, using LiPc	87
Figure 5.7 Verify coil constant with adjusted coil constant, using LiPc	87
Figure 5.8 Power saturation curve of 0.1 mM CTPO at 5 kHz rapid-scan frequency.....	91
Figure 5.9 Power saturation curve of 0.1 mM CTPO, under various rapid-scan frequencies	92
Figure 5.10 Power saturation curve of 0.1 mM OX063 at 5 kHz rapid-scan frequency.....	93
Figure 5.11 Power saturation curve of 0.1 mM OX063, for various rapid-scan frequencies	94
Figure 5.12 Background as a function of gradient for sinusoidal scans	95
Figure 5.13 Background as a function of gradient for linear scan.....	96

Figure 5.14 Background as a function of main magnetic field for sinusoidal scan	97
Figure 5.15 Background as a function of main magnetic field for linear scan	97
Figure 5.16 Sinusoidal EPR spectrum with wider sweep width	100
Figure 5.17 (a) Image (b) sinogram when resonator is not centered	102
Figure 5.18 (a) Image (b) sinogram when resonator is centered	103
Figure 5.19 (a) Image and (b) sinogram when resonator and sample are off-center	104
Figure 5.20 (a) Image and (b) sinogram when resonator and sample are centered	105
Figure 5.21 EPR images and spectral slices with different gradient steps	108
Figure 5.22 EPR image and spectral slice with (a) 1024, (b) 2048, (c) 4096 averages for each projection	111
Figure 5.23 Imaging with more averages, same data acquisition time	114
Figure 5.24 Imaging with more projections, same data acquisition time	115
Figure 5.25 Imaging with more averages for individual projections, same total averages	116
Figure 5.26 Imaging with more projections, same total averages	117
Figure 5.27 EPR image and spatial slice of CTPO and Ni ²⁺ salt	119
Figure 5.28 EPRI of a 3-compartment phantom and its spatial slice	120
Figure 5.29 Sinusoidal single sweep EPR spectra of 0.1 mM OX063	121
Figure 5.30 Sinusoidal single sweep EPR imaging of 0.1 mM OX063	121
Figure 5.31 Rapid-scan image without field-reversal background subtraction method, 8192 averages per projection	122
Figure 5.32 Rapid-scan image with field-reversal background subtraction method, 4096 averages per projection	123
Chapter Six	127
Figure 6.1 Illustration of the field-stepped method, sample is CTPO	128
Figure 6.2 Field-stepped rapid-scan spectrum of 0.5mM CTPO	132
Figure 6.3 S/N for spectra under gradients, 0.1 mM CTPO	141
Figure 6.4 S/N for spectra under gradients, 0.2 mM CTPO	142
Chapter Seven	148
Figure 7.1 Sectioned EPR image	149
Figure 7.2 EPR image (a) and sinogram (b) using variable averages	151
Figure 7.3 EPR image (a) and sinogram (b) using uniform averages	152
Figure 7.4 Spatial analysis of image	154
Figure 7.5 Steps for image quantification	157
Figure 7.6 Rapid-scan EPR absorption spectrum of the system	158
Figure 7.7 Quantify EPR features by ImageJ	161
Figure 7.8 Error message shown on CAEN	166
Figure 7.9 SpecJet-II data acquisition time	167
Figure 7.10 Data acquisition time with different points (same averages)	168
Figure 7.11 SpecJet-II Digitizer efficiency using different time base	170

Figure 7.12 Acetone over-treated ABS tubes have shiny finish but may develop cracks after one year.	175
Figure 7.13 Sample holder for 25 mm CLR.	177
Figure 7.14 Spectral-spatial image with 6 samples all be seen.....	181
Figure 7.15 Spectral-spatial image of 6 samples with overlaps.....	184
Figure 7.16 EPR spectrum of 5 G wide	185
Figure 7.17 EPR image of 5 G wide	186
Figure 7.18 Illustration of the principle	189
Figure 7.19 Illustration of the rotation operation.....	189
Figure 7.20 2D Spatial image using one-dimension gradient.....	191
Figure 7.21 Tube arrangement and dimensions	192
Figure 7.22 Spatial-spectral image taken at the starting position during rotation	192
Figure 7.23 2D spatial image of two tubes with different shape and sample	193
Figure 7.24 EPR spectrum deconvolved by (a) MATLAB code and (b) Python script.....	195
Figure 7.25 EPR image reconstructed by (a) MATLAB and (b) Python language	196
Figure 7.26 EPR Imaging UI design.....	198
Appendices	226
Figure D1 Drawing of L-band dielectric resonator assembly with wire-wound shield and rapid scan coils	262
Figure D2 Drawings of the magnet, dielectric resonator, and capacitor box of the L-band rapid-scan system	263
Figure D3 16mm variable frequency pulse cross-loop resonator for UHF	264
Figure D4 L-band (a) reflection resonator and (b) pulse spectrometer	265
Figure D5 The UHF accessory box	266
Figure D6 Ultra high frequency (UHF) pulse EPR system	267
Figure D7 16mm cross-loop resonator (CLR) and sample tube for imaging	268
Figure D8 Rapid-scan coil driver.....	269
Figure D9 VHF imaging system with 16mm resonator in place	271
Figure D10 25mm VHF rapid-scan imaging cross-loop resonator.....	272

LIST OF TABLES

Chapter One	1
Table 1.1 Number of hyperfine lines for atoms in commonly used radicals	4
Chapter Three	47
Table 3.1 Sample solutions of OX063	48
Table 3.2 Q of resonator#2 at different frequencies for 0.2 mM and 0.4 mM OX063	51
Table 3.3 Electron spin relaxation times (T_1 , μs) for OX063 solutions at room temperature	53
Table 3.4 Spin-spin relaxation times (T_2 , μs) for OX063 at room temperature ...	55
Table 3.5 Dependence of Relaxation Rates for OX063 on Radical Concentration and Salt Concentration ^a	59
Table 3.6 Dependence of S/N (normalized by \sqrt{Q}) on salt concentration for OX063 solutions at 700 MHz	62
Chapter Four	63
Table 4.1 Radiation Doses and Spin Concentrations	64
Table 4.2 Resonator Q values, available resonator bandwidths and signal bandwidths for each sample	66
Table 4.3 Summary of power saturation curves	70
Table 4.4 Parameters for CW and rapid scans	71
Table 4.5 Signal-to-Noise Ratios of Rapid Scan and CW Spectra	73
Chapter Five	75
Table 5.1 Comparison of spectra by using both I and Q channels versus only the I channel	84
Table 5.2 Impact of 7W Amplifier	85
Table 5.3 Summary of resonator Q, resonator and signal bandwidth	90
Table 5.4 EPR spectra of 0.1 mM CTPO with different rapid-scan frequencies for 16mm CLR	99
Table 5.5 EPR spectra of 0.1 mM OX063 with different rapid-scan frequencies for 25mm CLR	99
Table 5.6 Comparison of different gradient step size for CTPO	107
Table 5.7 Comparison of different maximum gradient strength G_{max} and same gradient step size	108
Table 5.8 Comparison of different maximum gradient strength G_{max} and same number of projections	109
Table 5.9 Comparison of different averages	109
Table 5.10 Comparison of different sample concentrations	111
Table 5.11 Comparison of using field-reversal background reversal subtraction method or not	124

Chapter Six	127
Table 6.1 Comparison of field step size.....	132
Table 6.2 Comparison of different rapid scan sweep widths.....	133
Table 6.3 Comparison of different rapid scan frequencies	134
Table 6.4 Summary of field stepped imaging results	135
Table 6.5 Summary of results for various Gmax, gradient step and field step size	136
Table 6.6 Comparison for Rapid-scan spectra.....	138
Table 6.7 Summary of S/N for EPR spectra under different magnetic gradients	140
Table 6.8 Comparison of field step with single sweep	143
Table 6.9 Summary of reconstructed images of CTPO with spatial slice cut at the middle peak.....	144
Table 6.10 Comparison of sinogram by both methods	145
 Chapter Seven	 148
Table 7.1 Projection distribution.....	148
Table 7.2 Comparison of EPR imaging of 0.1 mM CTPO with various averages	150
Table 7.3 Comparison of EPR imaging of 0.2 mM CTPO with various averages	152
Table 7.4 Comparison of using variable averages or not.....	153
Table 7.5 Time distribution in an imaging experiment of 4096 averages using the field reversal background correction method	163
Table 7.6 Time (s) needed for each procedure (same time window).....	164
Table 7.7 Summary of the step boundaries for different points	169
Table 7.8 Maximum digitizer efficiency and the time base to get there.....	171
Table 7.9 On-board averages and data acquisition time (s).....	172
Table 7.10 Summary of EPRI results of samples in the Eaton lab	178
Table 7.11 Linewidth of each sample by itself at 2.2 kHz, no gradient	179
Table 7.12 Linewidth Summary	182
Table 7.13 Sweep width and full linewidth at half height of absorption spectra	183
Table 7.14 Linewidth of spectral slice of image with different numbers of projections.....	187
Table 7.15 Comparison of spectra saving method of Xepr and Python	194
Table 7.16 Procedures and software needed in an EPRI experiment	197
Table 7.17 Python language used as central control in EPRI.....	197
 Appendices.....	 220
Table E1 Examples of 3D prints.....	273

LIST OF ABBREVIATIONS AND COMMON NAMES*

A	Ampere
AWG	Arbitrary wave generator
B₀	Static magnetic field
B₁	RF or microwave magnetic field
CLR	Cross loop resonator
CTPO	3-carbamoyl-2,2,5,5-tetramethyl-3-pyrrolinyl-1-oxyl
CW	Continuous wave
EPR	Electron Paramagnetic Resonance
EPRI	Electron Paramagnetic Resonance Imaging
FBP	Filtered Backprojection Algorithm
G	Unit of magnetic field, 1G = 10 ⁻⁴ T
i.d.	Inner diameter
k	Boltzmann constant, 1.3806 × 10 ⁻²³
L-band	1~2 GHz
LiPc	lithium phthalocyanine
o.d.	Outer diameter
OX063	tris{8-carboxyl-2,2,6,6-benzo(1,2-d:4,5-d)-bis(1,3) dithiole-4-yl}methyl sodium salt
RS	Rapid scan
RF	Radio frequency
S/N	Signal-to-noise ratio

STD	Standard deviation
T₁	Spin-lattice relaxation time
T₂	Spin-spin relaxation time
T_m	Phase memory time
Trityl	Triarylmethyl
VHF	Very high frequency = 250 MHz for EPR
X-band	9~10 GHz

* A separate list of abbreviations is given in Chapter 2, including acronyms for nitroxides

CHAPTER 1 : INTRODUCTION

1.1 Electron Paramagnetic Resonance (EPR) Principle

1.1.1 Basic Theory

This chapter is an introduction to the basic theory of EPR spectroscopy and techniques. EPR was first observed in Kazan State University by Soviet physicist Yevgeny Zavoisky in 1944. Today EPR has become a powerful tool to study the structure of molecules that contain unpaired electrons, including various organic radicals and transition metal complexes, and their applications to *in vivo* biological research.

The basic concepts of EPR are analogous to those of NMR, the splitting of energy levels of electron spins in the presence of magnetic field. When an unpaired electron in the sample is placed in field B_0 produced by a magnet in the laboratory, its energy levels split, which is called the Zeeman effect. Because the electron has a magnetic moment, it acts like a bar magnet. Since energies are quantized, a single unpaired electron has only two allowed energy states: a lower energy state when the moment of the electron, μ , is parallel with the magnetic field B_0 , and a higher energy state when μ is antiparallel with B_0 (Figure 1.1). The two states are designated by the projection of the electron spin, m_s , on the direction of B_0 .

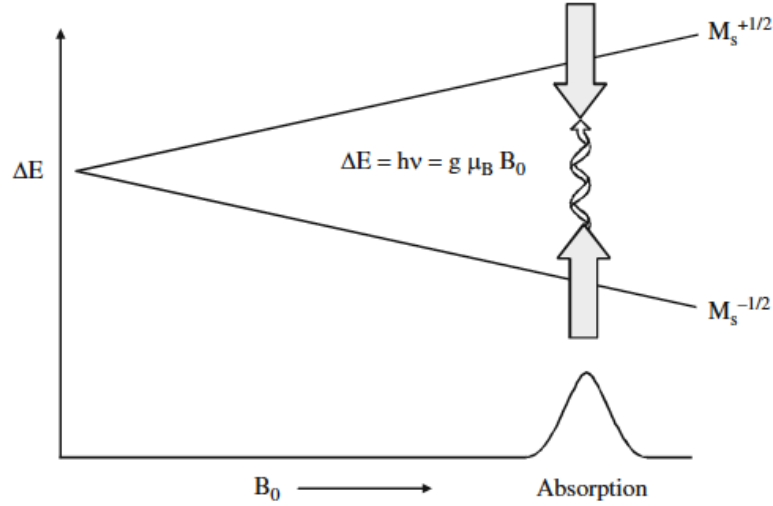


Figure 1.1 Basic concept of electron paramagnetic resonance, from [1]

Since the electron is a spin $\frac{1}{2}$ particle, the parallel state has $m_s = -1/2$ and the antiparallel state has $m_s = +1/2$. The difference between the energies of these two states, caused by the interaction between the electron spin and the magnetic field is shown in Equation (1.1):

$$\Delta E = g \mu_B B_0 \Delta m_s = g \mu_B B_0 \quad (1.1)$$

where g is the g -factor, and μ_B is the Bohr magneton, which is the natural unit of the electron's magnetic moment. The change in spin state for an EPR transition must satisfy the condition of

$$\Delta m_s = \pm 1 \quad (1.2)$$

For electromagnetic radiation, we have Plank's equation which states that the energy of a photon, E , is proportional to its frequency, ν :

$$E = h\nu \quad (1.3)$$

Thus, the energy that is required to cause a transition between the two spin states is given by

$$\Delta E = h\nu = g\mu_B B_0 \quad (1.4)$$

Two conclusions can be drawn from Equation (1.1) and (1.4):

(1) in the absence of a magnetic field, the two spin states have the same energy, so there is no energy difference to measure;

(2) the splitting energy ΔE increases linearly as the B_0 increases.

From Equation (1.4), the search for a signal can be performed in two ways:

varying the RF frequency ν or varying the magnetic field B_0 . Absorption occurs when the input RF energy matches the splitting energy, which is called “resonance”. Because of the difficulties both in scanning microwave frequencies and the use of a resonant cavity for signal detection, most EPR spectrometers operate at constant RF frequency and scan the magnetic field until resonance occurs.

1.1.2 Hyperfine Interactions

Additional information about the paramagnetic system can be obtained from nuclear hyperfine interactions. The nuclei in the system often have magnetic moments, which produce a local magnetic field B_I at the electrons. The interaction between the electron and the nuclei is called the hyperfine interaction, which gives abundant information about the system. The field B_I can add to or subtract from the laboratory magnetic field B_0 , which depends on the alignment of the moment of the nucleus. When B_I adds to B_0 , smaller B_0 is needed for resonance; when B_I opposes B_0 , larger B_0 is needed to achieve resonance (Figure 1.2). The hyperfine splitting constant a_H is equal to the

spacing between the two lines, which is $2B_I$. If there is a second nucleus with $I = 1/2$, each of the signals is further split into a pair.

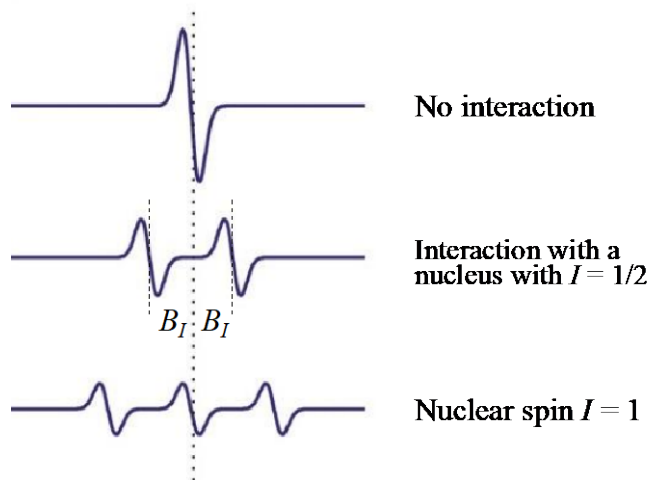


Figure 1.2 Examples of hyperfine splitting

Note that the total intensity of the signal is unchanged by hyperfine splitting and therefore the signal amplitude becomes smaller as more lines are present [2].

A general rule states that, the number of hyperfine lines is equal to $2nI + 1$, where n is the number of symmetry equivalent nuclei and I is the nuclear spin (see Table 1.1).

Table 1.1 Number of hyperfine lines for atoms in commonly used radicals

Atom	Nuclear spin I	Number of lines	Note
^{12}C	0	1	*
^{13}C	1/2	2	†
^1H	1/2	2	†
D (or ^2H)	1	3	**
^{14}N	1	3	**
^{15}N	1/2	2	†

* Nuclei containing even numbers of both protons and neutrons have $I = 0$.

** Nuclei containing odd numbers of both protons and neutrons have $I =$ positive integer.

† Others: $I =$ half integer.

Hyperfine splitting can be very useful in identifying radical species. The magnitude of B_I , and hence the splitting, depends on the type of nucleus as well as spin

density. As the number of nuclei gets larger, the number of lines increases rapidly. Sometimes there are so many lines that they overlap with each other, and a smaller number of broad signals is observed.

1.1.3 Relaxation

In the absence of a magnetic field, the moments are randomly distributed between the $m_s = \pm 1/2$ states. In the presence of a magnetic field, the distribution obeys Boltzmann statistics when it is in thermal equilibrium and can be described by equation (1.5):

$$\frac{n_{\text{anti-parallel}}}{n_{\text{parallel}}} = e^{-\frac{\Delta E}{kT}} \quad (1.5)$$

where n represents the population of the two states, ΔE is the energy difference between the two states and $= g \mu_B B_0$, k is Boltzmann's constant and T is temperature.

Usually we have a system with a large number of spins, and the magnetization is the vector sum of all the magnetic moments in the sample. Since the random orientation of individual precession moments cancel their contribution to the transverse magnetization (Figure 1.3), net magnetization is parallel to B_0 .

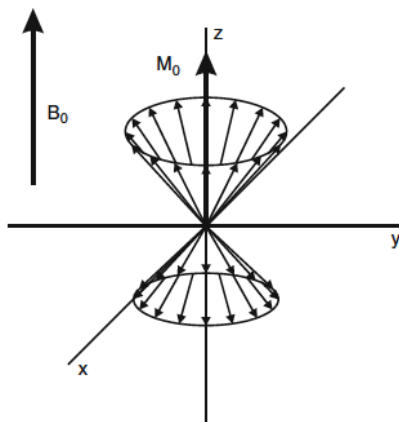


Figure 1.3 Electron spins in a magnetic field, from [1]

Since the moments can only be either parallel or anti-parallel to B_0 , the magnetization is proportional to the difference between these two states, which is usually very small. However, for the same magnetic field strength the population difference for protons is about 600 times smaller than for electrons, which is why EPR spectra can be obtained at lower spin concentrations than NMR spectra. When an RF field is applied, the population balance of the sample is perturbed and is temporarily not at thermal equilibrium. The absorption of RF energy heats up the spin system and eventually returns to thermal equilibrium through the spin system's interaction with the surroundings. This process is named spin-lattice relaxation and is characterized by the spin-lattice relaxation time T_1 , also called longitudinal relaxation time.

M_z is the longitudinal magnetization, M_x and M_y are the transverse magnetization. At equilibrium the longitudinal magnetization is constant, and precesses about B_0 . If there is little interaction between the individual spins of the system, the phase of the precession is random and the sum of the individual magnet moments contributing to the transverse magnetization at equilibrium is zero. However, if this balance is disturbed (for example by a RF field), the system will relax back to zero transverse magnetization in time T_2 , which is known as spin-spin or transverse relaxation time.

1.2 EPR Techniques

1.2.1 CW EPR

The continuous wave (CW) EPR method is the most commonly used method of EPR. The principle is shown in Figure 1.4, as the main magnetic field is scanned slowly

through the EPR line, a small modulation field B_m is applied in the same direction as the main field B_0 .

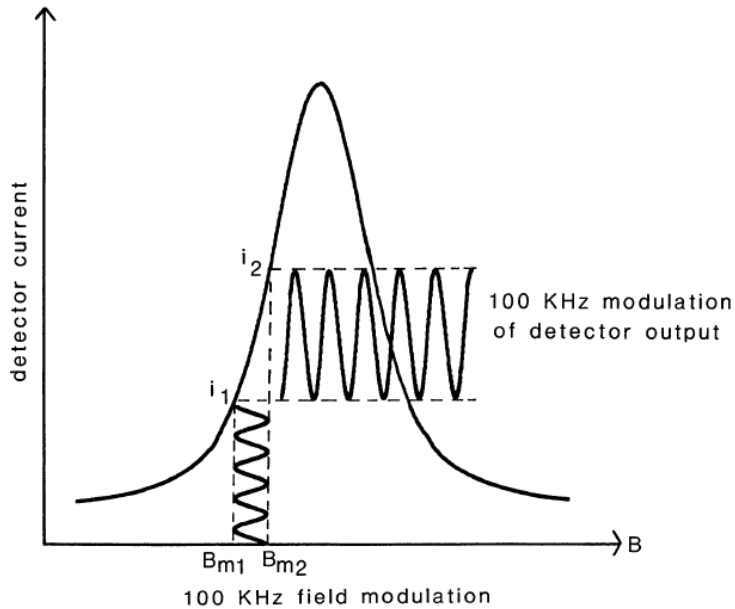


Figure 1.4 Schematic diagram of CW EPR, from [1]

The commonly used modulation frequency is 100 kHz. As B_m increases from the value B_{m1} to B_{m2} , the detector output increase from i_1 to i_2 . If B_m is sufficiently smaller than the signal line width, the detector current has a peak-to-peak value that approximates the slope of the absorption curve. As a result, the EPR spectrum is recorded as a first derivative.

1.2.2 Pulse EPR

The pulsed EPR method is used to measure relaxation times T_1 and T_2 . T_2 can be measured by spin echo decay while T_1 is measured by inversion recovery.

In a spin echo decay experiment, the echo is formed by a two-pulse sequence $90^\circ - \tau - 180^\circ - \tau - \text{echo}$, where τ is the time interval between pulses (Figure 1.5). The first

pulse flips the spin vector from the Z direction to the X - Y plane, after which the spins start to dephase. Next a 180° pulse is applied to flip the spins 180° in the X - Y plane after which they refocus to form the echo. This happens at a time that is twice the time τ between the pulses. Increasing the time between the pulses allows more time for dephasing, which decreases the amplitude of the echo. By fitting this decay curve, we can get the corresponding time constant, which is called T_2 or T_m , depending on the types of processes that contribute to the decay.

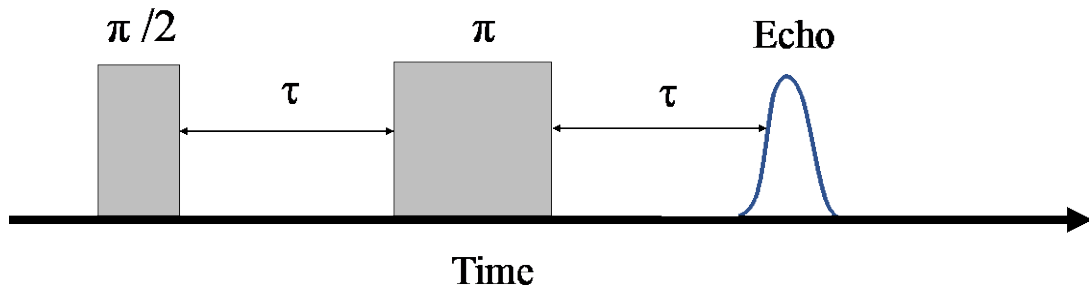


Figure 1.5 Pulse sequence for echo decay experiment to measure T_2

In an inversion recovery experiment a three-pulse sequence is used: $180^\circ - T - 90^\circ - \tau - 180^\circ - \tau - \text{echo}$, where T is the time that is varied and τ is the constant time interval between the two pulses of the spin-echo detection sequence (Figure 1.6). The first 180° pulse is called the inverting pulse, which inverts the net spin vector to the $-Z$ direction. The net magnetization along the Z axis recovers during delay time T . Then the 90° excitation pulse is applied to the spin vector that puts the spins in the X - Y plane. The spins start to dephase in the X - Y plane. The 180° pulse that is applied after a constant time τ flips the spins in the opposite direction. The spins start refocusing in the time period τ to give the desired recovered echo.

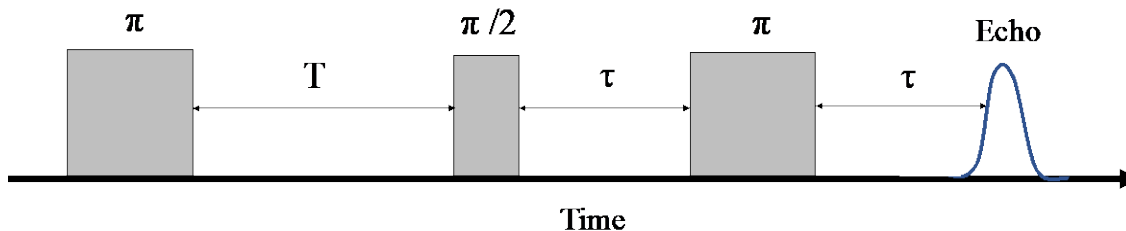


Figure 1.6 Pulse sequence for inversion recovery to measure T_1

1.2.3 Rapid-scan EPR

The Rapid-scan (RS) EPR techniques have been developed in the Eaton lab for more than a decade. RS EPR has been reported at frequencies of VHF (250 MHz), UHF (300 MHz ~ 1 GHz), L-band (1~1.5 GHz) and X-band (9 GHz) [3]. It is based on the phenomena of passage effects that were observed in NMR [4], that is, when the magnetic field scan rate is faster than the electron spin relaxation rates, wiggles are observed after the signal line. The same phenomenon was observed in the early days of EPR [5].

In a rapid-scan experiment the center field is held constant and an additional field is rapidly varied across the full spectrum. Signals are obtained by sweeping the magnetic field or microwave frequency through resonance in times that are short relative to electron spin relaxation times. The full amplitude of the spectrum is detected in each sweep [6]. Deconvolution is performed to recover the EPR absorption signal [7] [8]. The example in Figure 1.7 shows two full cycles of the rapid scan after deconvolution, which is comprised of two up-scans and two down-scans through the signal.

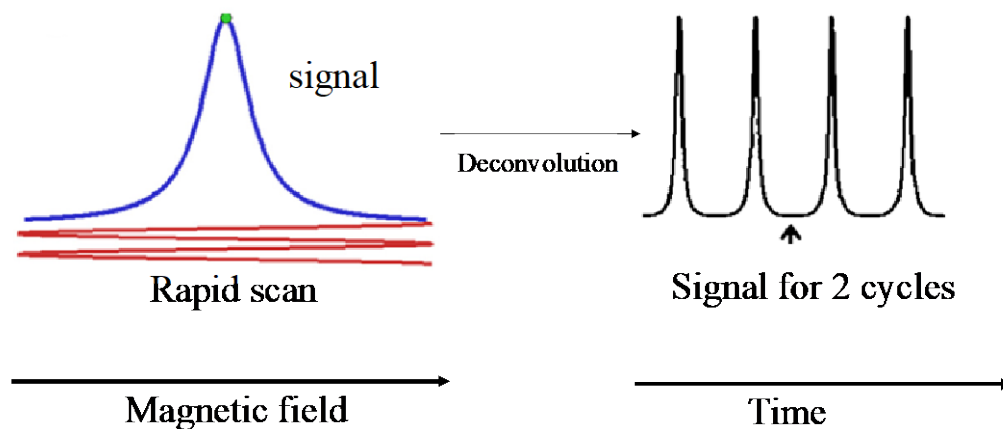


Figure 1.7 Schematic diagram of rapid-scan EPR

The time spent on resonance is very short, which allows the use of high power or high B_1 without saturating the signal [9]. This provides much high S/N and is significantly faster compared to the traditional CW EPR. Rapid-scan EPR is especially advantageous for samples with long spin-lattice relaxation times [9].

Rapid scan EPR is advantageous for imaging because the amplitude of the RS signal (absorption) decreases approximately linearly with magnetic field gradient, while the amplitude of the CW signal (first derivative) decreases approximately quadratically [6]. Besides, fast data acquisition of rapid-scan EPR greatly reduces the time required to take multiple projections for an image.

1.2.4 EPR Imaging

EPR imaging is able to map the spatial distribution of EPR signals by decoding spatial information of the samples that is introduced by spatial variations in magnetic field. A simple phantom (a phantom is a sample with known properties that is used to test an imaging procedure), shown in Figure 1.8, is a 16 mm o.d. quartz tube with 2 mm wall

thickness, and has a divider in the center that is 40 mm high, and 2 mm thick. The two compartments are filled with radical samples such as nitroxide solution.

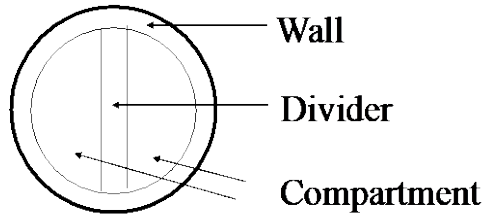


Figure 1.8 Cross section of a phantom

The principle of EPR imaging can be illustrated in *Figure 1.9* using the phantom in *Figure 1.8*.

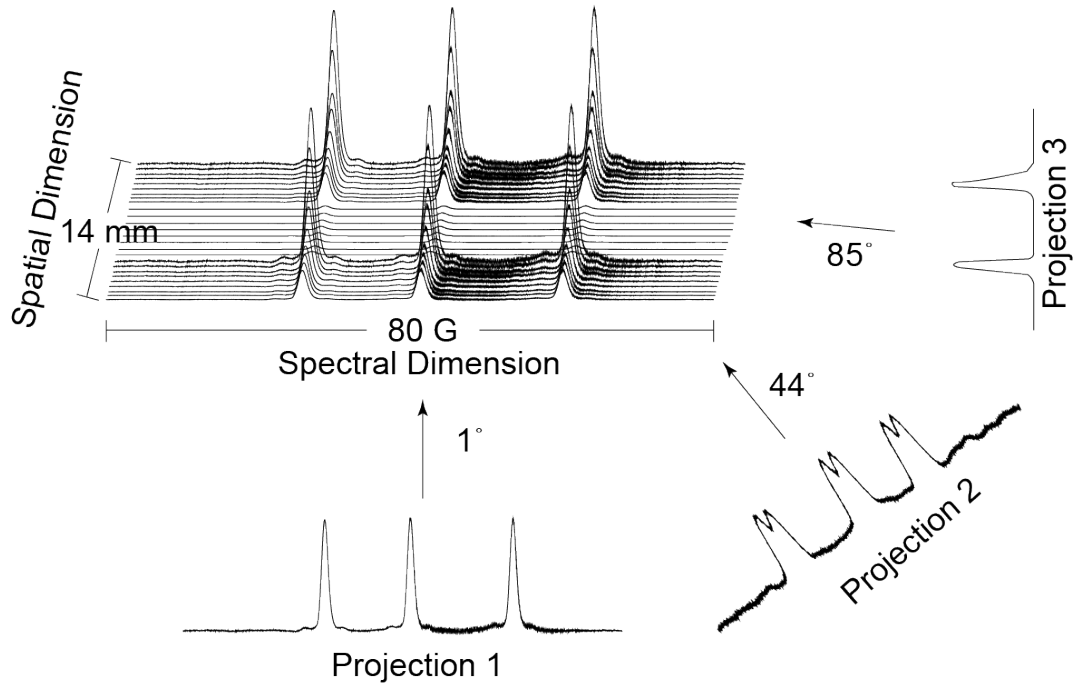


Figure 1.9 Illustration of EPR imaging using magnetic field gradients
(Adapted from Fig.7 of [10])

The image in *Figure 1.9* of the phantom has two dimensions, a spectral dimension that gives the characteristic three-line CTPO spectrum, and a spatial dimension corresponding to the physical dimension of the phantom, in the direction parallel to the magnetic field, which often is defined as the Z-axis. Each compartment generates EPR

signal due to the presence of radical solution, but there is no signal in the region corresponding to the divider. When a magnetic field gradient is applied to the phantom, it is like viewing the image from different angles, also called projections. At an angle almost equals to zero, it is like viewing the image from the front, the two signals overlap like projection 1 in *Figure 1.9*, and the projection contains only spectral information. When the eyes turn around a bit, such as at the angle of 44° , the 'back' part begin to reveal itself, so the peak starts to split, like projection 2. When viewed from the side, like 85° angle, only two lines are visible, and the projection contains mostly spatial information, like projection 3. The spectra as a function of gradient correspond to views of the object from different angles. An algorithm was developed in our lab to reconstruct the image based on a series of projections [11].

Criteria for image quality include resolution of a spatial slice, linewidth of the signal from the radical and S/N of spectral slice, which will be discussed extensively in Chapters 5 to 7.

In summary, EPR is the method of choice for non-destructive measurement of molecules with unpaired electrons. Applications range from general radiation dosimetry, studying the nature of products of radiation chemistry, and the fast growth of imaging techniques in the biological and medical field.

In this dissertation, the work is divided into six chapters. Chapter two is a literature review of EPR imaging on nitroxides. Chapter three includes relaxation and S/N measurements of trityl radical at various frequencies. Chapter four reports measurement of rapid-scan EPR spectrum at L-band for irradiated solids. Chapter five is about rapid-scan EPR imaging. Chapter six is about field-stepped EPR and imaging and

its comparison to the sinusoidal single sweep imaging. Chapter seven is about new developments in EPR imaging.

CHAPTER 2 : LITERATURE REVIEW: *IN VIVO* EPR IMAGING OF NITROXIDE

2.1 Introduction

EPR imaging is a powerful tool for assessing changes noninvasively *in vivo* under various physiological conditions and offering accurate measurements of multiple functional information. Nitroxide radicals have been used as spin probes of changes in properties such as redox status, polarity, viscosity, pH gradients. This chapter reviews the literature concerning EPR imaging of nitroxides for the past thirty years. Information including the object imaged, the nitroxide probe, the experimental parameters, the reconstruction methods, and image modality are summarized.

Prior reviews on the applications of EPR imaging (EPRI) utilizing various nitroxides as metabolic indicators, such as electrical potential, pH, temperature as well as oxygen gradients, are found in the papers of Iannone [12], Sotgiu [13], Yasukawa [14], Krishna [15], among others. The use of spin traps, detection of nitric oxide and some transition metal ions in biological system are in Davies's paper [16]. EPR image reconstruction techniques are reviewed in Sotgiu's paper [13]. The principles and applications of EPR as well as other magnetic resonance methods to measure oxygen concentrations and pH in biology were reviewed in Grucker [17] and Longo's [18] papers and book chapters edited by Eaton [19] [20] and Berliner [21]. Application of EPR imaging to polymer degradation is summarized in Schlick's paper [22]. Zweier's review

summarizes the development and application of EPRI on cardiovascular studies [23]. The application of EPR to study the effect of ultraviolet radiation on human skin is discussed in Linscheid [24], Plonka [25] and He [26]'s papers.

The problems that people tried to solve over the years can be roughly divided into ones that focus on the information revealed by nitroxides or the EPR imaging technique itself. The knowledge acquired based on nitroxide probes can be further categorized as oximetry and redox status, metabolism, spatial distribution, and their chemical and biochemical properties; while the development in EPR imaging techniques papers focus mainly on aspects of method development and instrumentation. In addition to the widely studied *in vivo* systems, researchers have attempted other subjects with EPRI, and these studies are grouped together at the end. The details of each subcategory are discussed further in the following sections.

2.2 Progress in EPR Imaging

2.2.1 Oximetry and Redox Status

Tissue redox status and pO_2 are two important factors that are different in normal and malignant tissues. Since the first report by Berliner et al. [21] [27] on the biological application of EPRI, many works were published on the study of living biological systems. Nitroxides are fairly stable free radicals, and their EPR spectra are sensitive to oxygen levels, which makes them used as oxygen probes of local oxygen concentration. The broadening of the principal hyperfine lines in nitroxide EPR spectra is caused by Heisenberg exchange between nitroxide and molecular oxygen dissolved in solution, thus the measurement of the EPR linewidth can be directly related to the oxygen in the

vicinity of the nitroxide. Also, nitroxide molecules lose their unpaired electron and become EPR silent during redox-reaction processes, which can be monitored with EPR. As a direct analytical technique to quantify free radicals, EPR has been employed widely in research on *in vitro* and *in vivo* redox reactions. EPR can non-invasively discriminate redox status differences between normal tissues and tumors *in vivo*, which brings vast potential for biomedical applications.

For biological samples, because the large water content of living systems reduces the penetration depth of microwaves, low field EPR was developed. Frequencies that have been used include VHF (250 MHz, 280 MHz, 300 MHz), UHF (700 MHz, 750 MHz), L-band (1~1.3 GHz), and S-band (2.2 GHz). The studies are described in the following paragraphs.

B. Epel, H. J. Halpern and their group performed EPR oxygen imaging of mice on a home-built image system. Pulsed EPR imaging of trityl was carried out at 250 MHz; gradient strength was in the range from 7.5 ~ 10 G/cm [28], and an image was acquired in 20 min. Rapid-scan EPR images of ^2H , ^{15}N substituted diradical were acquired, gradient strength was 9 G/cm (0.9 T/cm)¹ and 96 projections were taken in 31s. The central line of an ^{14}N nitroxide was used to reconstruct 3D spatial images [29]. CW EPR of nitroxides were carried out at L-band, gradient strength was 10 G/cm, and 216 projections were taken in 18 min. The first line of an ^{15}N nitroxide was used to reconstruct a 2D spectral-spatial image [30]. The resolution was around 1mm. The group

¹ The unit for magnetic field gradient in the original paper is T/cm and is converted to a uniform unit of G/cm in this review. This comment applies to all cases in this review.

was able to image larger rat and rabbit tumors in about 20 min and used 3D spatial imaging to estimate intracellular thiol concentration.

The A. Sotgiu group performed low frequency (280 MHz) CW EPRI on whole rats to map the *in vivo* spatial distribution of a pyrrolidine nitroxyl (PCA), whose reduction rate was affected by oxygen concentration. Field gradients were 10 G/cm (100 mT/m) in two directions and 2.8 G/cm (28 mT/m) in the third direction to permit the 3D reconstruction. Field and gradient direction can be rotated under computer control, making image reconstruction very similar to that used in computer assisted tomography. 1D transversal and longitudinal mapping of the PCA distribution in rat whole body was obtained. To obtain 2D images PDT was used as the source of the EPR signal. For each image 64 projections were collected with a magnetic field gradient of 90 G/cm [31]. The author stated that spatial resolution (3-10 mm) and collection time (3-5 min) could be improved by using narrow linewidth paramagnetic probes and pulsed techniques. This study gave some examples of the use of EPRI methodology in whole rats in the framework of its possible use in experimental oncology.

The H. Fuji group performed many brain imaging studies of mouse disease models to map the redox status on a 750MHz CW EPR imager [32]. The nitroxides used included BBB (blood–brain barrier) - permeable HMP [33] [34], MCP [32], 3-CP, TEEPONE [35]. The studies used ^{14}N nitroxide as well as ^{15}N substituted nitroxides. All lines of the nitroxide were used. A Hamming filter was used to suppress noise in the process of deconvolution of the non-gradient spectrum [36]. The 3D spatial image was reconstructed by single stage filtered back-projection method, and 2D images were acquired by slicing the 3D images. Data acquisition was controlled by a LabVIEW-based

program on MacOS 10.3 [37]. The FBP reconstruction program was written in MATLAB and run on an Apple iMac computer (Mid 2010, Intel Core i3, 3 GHz, memory 4 GB) [38]. The time needed to take an image has decreased from 53 min [39] to 5 min [40]. The gradient used ranged from 2 G/cm (0.2 mT/cm) [41] to 6 G/cm (0.6 mT/cm) [42]. For a 3D spatial image, the number of projections used is 64 [39] [43], 81 [37] or 181 [44]. For a 4D spatial-spectral image, 181 projections were taken in 7.5 min [38]. The resolution was about 1mm. These studies suggested that 3D *in vivo* EPR imaging combined with BBB (blood brain barrier) permeable nitroxides was a useful noninvasive tool for assessing changes in the redox status in rodent models of brain disease under oxidative stress.

The J. Zweier group performed imaging experiments on home-built CW image systems at various frequencies including 300 MHz [45], 750 MHz [26] [46], L-band (1.2 GHz) [23] [47] [48], and S-band (2.2 GHz) [49]. Radicals used included ¹⁵N PDT and its saline solution, TEMPO, TEMPONE, TEMPOL, and 3-CP. Objects studied included a phantom, perfused rat heart, and mice. At 300 MHz, both 2D and 3D images were acquired. Gradient strength was 3 G/cm (0.3 mT/cm). 64 projections were taken in 11 min and resolution was 5 mm [45]. At 750 MHz, a 2D spectral-spatial image was obtained. Gradient strength was 15 or 80 G/cm. 1024 projections were taken in 5 min and the resolution was 1mm [46]. At L-band, 1D, 2D, 3D and 4D spectral-spatial images were taken, gradient strength was 2~20 G/cm. For the 2D spatial image, 144 projections were taken in 64 min; for the 3D image, 784 projections were taken in 7 min. Resolution was 0.2 mm [50]. At S-band, the gradient strength was 50 G/cm for imaging phantoms, and 75 G/cm for imaging human skin. The resolution was above 100 μ m [49]. Image

reconstruction was done with the FBP method with in-house software in MATLAB or C. The Zweier group's study was the first described work on lossy biological samples at L-band, allowing mapping spectral information over the entire 3D spatial structure of the object.

The M. Krishna group performed imaging experiments on a CW system at various frequencies, including 300 MHz, 700 MHz and L-band. The objects studied included phantom, mouse, and beating heart. Radicals used included Tempol, 3-CP, NMP-TCNQ, ^{15}N -PDT, Tempone, CMP. At 300 MHz, various gradient strength was used, including 1 G/cm [51], 2.5 G/cm [52], 4.7 G/cm [53] [54] and 20 G/cm [55]. 2D images were acquired. 12~18 projections were taken for each image in about 1 min. Only one of the three nitroxide lines was used in the image reconstruction, by the filtered back-projection method with a Shepp-Logan filter. Resolution was 1~3 mm. At 700 MHz, gradient strength was 1.7 G/cm. The central line was used for 2D spatial image reconstruction with a resolution of 1 mm [56]. At L-band, 2D images of mice were reconstructed by the single-stage FBP method. 3D image of the beating heart was also acquired. Gradient strength was 20 G/cm, 144 projections were taken in 64 min. FBP method was used and image resolution was 1 mm [57]. Comparative studies with EPR and MRI on *in vivo* tissue redox status were also performed [56]. Spatially resolved pharmacokinetics of nitroxides were determined by non-invasive imaging methods, which might report on differences that exist in various tissues and display different redox status.

J. Kao, G. Rosen et al. performed imaging experiments at L-band (1.07 GHz). Four types of nitroxides were used and both ^{14}N and ^{15}N isotopes were studied. Gradient

strength was 10 G/cm. For the phantom, 216 projections were taken in 18 min; for the mouse head, 322 projections were taken in 26.5 min. 2D spectral-spatial CW images were reconstructed by the FBP method. Only the central nitroxide line was used for image reconstruction and the resolution was 1 mm [30]. O₂ concentrations were estimated in aqueous media and the study found that full isotopic substitution (¹⁵N and deuterium) of the nitroxides increased peak amplitude by 2.5-fold.

J. Mitchell et al. performed low-frequency (1.3 GHz) *in vivo* CW EPR spectroscopy and imaging with the nitroxide redox probe 3-CP. Projection data were acquired using angular sampling method. The deconvoluted projections were then convoluted with a Shepp-Logan filter. A single-stage, filtered back projection reconstruction algorithm was used to recover the 2D spatial image [57]. The study found significant heterogeneity of tumor redox status and the manipulation of tumor redox status might be important in tumor growth and therapy.

N. Ikota et al. studied heterogeneity of redox status in a mouse tumor model at L-band using nitroxides Carbamoyl-PROXYL, or TEMPO. A stable 10 G/cm (1.0 mT/cm) field gradient was rotated with a 2° angle step, and 90 projections were obtained in 3.5 min. FBP method was used for image reconstruction. The central nitroxide line was used. Resolution was 1 mm [58]. The results indicated the necessity of measurements of both redox status and oxygenation in tumor in order to characterize tumor physiology.

The P. Kuppusamy group performed CW imaging experiments at L-band (1.2 GHz). Objects studied included whole body mouse, phantom and rat heart. Nitroxide used were ¹⁵N-TEMPOL, TEMPOL, 3-CP, ¹⁵N-PDT. Gradient strength was up to 150 G/cm. 1D, 2D and 3D images were reconstructed. Projections were acquired using an

angular sampling method. The measured projections were corrected for removal of hyperfine-based artifacts and deconvoluted with the corresponding zero-gradient projection. The deconvoluted projections were then convoluted with a Shepp-Logan filter. A single-stage, filtered back projection reconstruction algorithm was used to recover the image [59]. For 2D experiments, 13 projections were taken in 130 min [60]. For 3D experiments, 144 projections were needed. Resolution was about 3~5 mm [61]. The studies provided examples of whole-body imaging to investigate the toxicity of biological reactions and organ specific oxidative changes associated with the development of acute asbestosis.

A. Hirayama et al. performed CW EPR imaging at L-band on mice with Carbamoyl-PROXYL. Gradient strength was 10 G/cm (1 mT/cm). The tissue-reducing activity of Nrf2-deficient mice was evaluated using a combination of real-time EPR imaging and spin probe kinetic analysis. For each projection, 6 spectra were taken at 30° steps and required 2 min. Only the central line was used for image reconstruction [62]. The study found EPR imaging to be a powerful tool in the real-time analysis of the tissue-reducing activity.

T. Otsubo et al. performed CW EPR imaging at L-band with a JEOL spectrometer. Spin probes used were Carbamoyl-PROXYL (CP) and CYPMPO. Field gradient strength was 20 G/cm (2.0 mT/cm), changing direction in 20° steps to provide six spectra for each projection. Scanning time was 2 min. 3D images were constructed with the lower field line [63]. EPRI determined that the nitroxide half-life in CV159-treated mice was significantly shorter than that in untreated mice. The study found that

the use of nitroxyl radicals as spin probes is effective for the noninvasive observation of free radicals in living animals.

2.2.2 Metabolism

In addition to tissue oxygen pressure, the EPR imaging technique offers other functional information of the metabolism process, such as pH, viscosity, degradation process, drug release mechanisms and kinetics. Nitroxide molecules are converted to non-paramagnetic species during the metabolism process, thus monitoring the nitroxide signals and calculating its elimination rate is a direct measure of the metabolism rate. Excretion also needs to be taken into account. Since the nitroxide EPR signal decays more quickly in diseased regions, *in vivo* EPR imaging of tissues is a useful tool in tumor diagnosis. Important metabolism parameters have been studied at UHF (700 MHz, 750 MHz), L-band and X-band by EPR imaging.

The H. Hirata group studied extracellular pH maps of tumors on a home-built CW-EPR spectrometer/imager operating at 750 MHz, using a pH-sensitive nitroxyl radical as an exogenous paramagnetic probe. Gradient strength was 7 G/cm (70 mT/m). Fast projection scanning with a constant magnetic field sweep enabled the acquisition of four-dimensional (3D spatial +1D spectral) EPR images within 7.5 min. Four-dimensional spectral-spatial EPR images were reconstructed by an iterative algebraic reconstruction technique (ART, refer to Section 2.2.5 Method Development), with spectral data fitting at each iteration. Computations were performed on an Apple iMac computer (Mid 2010, Intel Core i3, 3 GHz, memory 4 GB) [38]. The proposed EPR-

based pH mapping method enabled quantitative visualization of regional changes in extracellular pH associated with altered tumor metabolism.

The R. Gurny group used CW EPRI to monitor the microenvironmental pH (pH_M) and the rotational correlation time (τ_R) related to the microviscosity spatially and non-invasively at L-band (1.5 GHz). Maximum gradient was 330 G/cm (3.3 T/m), scan time per projection was 20 s; 51 projections were taken, and the resolution was 1 mm [64]. The study successfully used EPRI for the optimization of a pH-controlled formulation in the matrix of tablets.

The H. Yokoyama and H. Kamada group studied the nitroxide decay rate *in vivo*. 700 MHz CW EPR imaging experiments were performed on a home-built system. Objects studied included phantoms, mice and rats. Nitroxides used included Carbamoyl-PROXYL [65], Carbamoyl-PROXYL in saline solution [66], TEMPOL [67], PCAM [68], ACP [69], and hydroxymethyl-PROXYL [70]. The field gradient strength was 10 G/cm (1 mT/cm) or 40 G/cm (4 mT/cm) in a 20-mm range from the center [71] [72] [73]. The field gradient angle was 0~160° with 20° interval, providing nine two-dimensional projections thus one set of 3D data, from which arbitrary 2D slice planes can be cut out [70] [74]. EPR spectral data obtained under the field gradients were deconvoluted, using the line-shape of the zero-gradient spectrum, by the fast Fourier transform method with low pass filtering [67]. Images were reconstructed from the deconvoluted data and reproduced in 256 colors; signals lower than 25% of the maximal signal intensity in all slices were regarded as noise [68]. Image reconstruction used either the low field line [65], or all three lines [75]. Resolution was 1~3 mm [76] [77] [74]. For the whole mice, 81 projections were taken in 44 min [69]; for the rat brain image, 81 projections were

taken in 1.5 min [66]. *In vivo* ESR-CT imaging in the head of a rat was also performed at 300 MHz; the gradient was 10 G/cm (1 mT/cm) and resolution was 1 mm [78]. The decay rate of nitroxide radical *in vivo* can be estimated and the half-life and initial level of nitroxides can be calculated from temporal changes in EPR intensity.

A. Sotgiu group's study demonstrated the capability of EPRI to track the uptake, distribution and reduction of the nitroxide label in the rat. Radicals used were 3-carbamoyl 2,2,5,5 tetramethyl-3-pyrrolidin-I-yloxy, PCA and PDT. At L-band, 2D spectral-spatial and 3D spatial images were reconstructed. Gradient was 1.2 G/cm (0.12 mT/cm). Eight 2D projection at 11.25° step were taken in 16 min. Either full spectra, or the low field line was used in the image reconstruction. Resolution was 1 mm [79]. EPR imaging at 280 MHz was also performed. Gradient strength was 15 G/cm (0.15 T/m) in two directions and 2.5 G/cm (0.025 T/m) in the third direction. Eight projections at 22.5° step were taken in 6 min. Each spectrum was deconvoluted with the zero-gradient line to obtain the real projections. Two of the three lines were used in the image reconstruction of 1D or 2D images. Resolution was 3~10 mm [80]. Distribution of nitroxide PCA in rat body was obtained and the study found that moderate hypoxia (10% O₂-90% N₂) did not significantly affect the spin label reduction rate.

K. Mäder et al. studied drug delivery and drug release mechanisms and kinetics with ¹⁴N Tempol and ¹⁵N PCM nitroxides. EPR permits the direct measurement of microviscosity and micropolarity inside the drug delivery system. Two main techniques were used, (1) a rotating constant gradient which gave 1D spatial-spectral images by the FBP (filter back projection) method; (2) a variable gradient with a fixed orientation, which gives 2D- or 3D-spatial images by the Radon transformation. EPR frequencies

used were 10 GHz (X-band) or 1 GHz (L-band). The spatial resolution was typically lower at L-band (100 μm to mm) and higher at X-band (10 μm). The spatial-spectral image contained all the lines, and a deconvolution algorithm was used [81]. At L-band, 31 projections were taken, and the reconstructed image gives a resolution of 200 μm [82]. Using these approaches, EPR provided unique information on drug release mechanisms and kinetics.

The B. Gallez group performed CW EPR imaging experiments to assess the phagocytic activity of the liver at X-band. 2D EPRI on the livers of rodents was performed using India ink as the probe. The field of view was 20 mm; gradient strength was 40 G/cm (4 mT/cm); pixel size was 0.5 mm; 31 projections were taken. Resolution is 1 mm [83]. The results showed a good correlation between the depletion of Kupffer cells and the EPR signal intensity.

2.2.3 Spatial Distribution

The spatial distribution of nitroxides in biological samples provides vital information about the physical or chemical environment in biological tissues. The studies discussed in this section provided examples of how the distribution of nitroxides can be mapped through EPR imaging in a non-invasive manner. These studies increased the number of biophysical problems that could be investigated by EPRI.

H. Yokoyama et al. studied the spatial distribution of nitroxide radical in rats. Rapid-scan EPR imaging of Carbamoyl-PROXYL nitroxide was performed on a home-built 700 MHz image system. Gradient strength was 10 G/cm (1 mT/cm). Data at 81 gradients were collected in 2.5 min. EPR spectra were deconvoluted by the fast Fourier

transform method and images were reconstructed from the deconvoluted data by filtered back projection. The low field line of the Carbamoyl-PROXYL spectra was used for evaluation and the image resolution was 2.3 mm [65]. A more time-resolved EPR image of the nitroxide distribution in the rat head was demonstrated.

The H. Kamada group studied the distribution of nitroxide radical in rat brain. EPR images of carbamoyl PROXYL radical were measured using a custom-built 700 MHz CW EPR image system. Gradient strength was 40 G/cm. The full EPR spectra were deconvoluted with zero gradient line shape of the spectrum by the fast-Fourier transform method, and then reconstructed into EPR images by filtered back projection. 2D and 3D spatial image were constructed, and the resolution was 2.6 mm [84]. The study presented a method to introduce stable free radicals into a specific area of the brain.

The H. Fuji group studied the dynamic changes in the distribution of BBB permeable nitroxides HMP and MCP in the mouse head. A custom-made 750MHz CW EPR imager was used to obtain 3D EPR images of mouse heads. The data consisted of 181 projections acquired in 5 min. The image was constructed by single stage filtered back-projection method, which does not go via 2D slice-selective images in the process of 3D reconstruction. All 3 lines of the nitroxide spectrum were used. The resolution was 1mm. The results showed that MCP and HMP have different distributions and different reduction reaction kinetics in living mouse brains [40].

B. Epel, H. Halpern and their group studied spin label distribution in a living mouse, to visualize protein expression in tumor cells [85]. EPR image experiments were performed with a home-built 250 MHz system. At this frequency, the skin depth (37% sensitivity) was approximately 7 cm. CW, rapid-scan and pulse imaging were performed.

Radical used included four types of different nitroxides, ^2H , ^{15}N substituted diradical, CTPO [86]. For a 2D spatial-spectral CW image, 16 projections were taken uniformly over 180° in 17 min [86] [87]. For a 2D spatial CW image, 66 projections were taken at 10° step in polar angles in 12 min [88]. For a 2D spatial pulse image, the data were acquired in 20 min [28]. For a 3D spatial image, rapid-scan technique was used, and 96 projections were taken in 1h [29]. For a 4D imaging, it would be 10-fold slower. Gradients used were 9 G/cm (0.9 mT/cm), 2.4 G/cm, 10 G/cm, 5 G/cm (50 mT/m). Only the central line was used for image reconstruction, and the FBP method was used to reconstruct images. Image resolution was 1.2~2.6 mm [89]. The research showed that nitroxides are selectively localized in tumors relative to normal tissue, which made EPR imaging of tumors possible and provides the basis for investigating tumor microenvironment and its response to therapy.

The J. Zweier group studied the distribution of nitroxide label in mouse heart with EPRI. CW EPR imaging was performed at L-band with nitroxide 3-CP. Gradient strength was 20 G/cm (2 mT/cm), and image was acquired in 18 min. The low field line was used in the reconstruction of 3D spatial images [90]. The information obtained can be used to identify risk regions in ischemic hearts noninvasively and nondestructively.

The A. Sotgiu group studied the spatial distribution of free radical PCA in selected regions of the rat at different times. Experiments were performed on a 280 MHz CW EPR spectroscopy and imaging apparatus. For a 1D spatial image, gradient strength was 0.8 G/cm (8 mT/m), and acquisition time was about 50 s. For 2D spatial image, gradient strength was 1.2 G/cm (12 mT/m). Eight spectra at angular increments of 22.5° were collected for 5 min. The 2-D images were calculated by a Fourier reconstruction

technique [91]. The study demonstrated a method to localize nitroxide in the rat abdomen and thorax and was able to image the whole rat up to 150 g.

The J. Freed group studied the macroscopic and the microscopic diffusion coefficients of nitroxide 16-PC in a model membrane utilizing spectral-spatial EPRI at X-band. The microscopic diffusion of the spin probes is obtained from the variation of the spectral line broadening with spin label concentration, which is due to spin-spin interactions. The maximum field gradient was 395 G/cm, providing a spatial resolution of 100 μm . A total of 91 projections was measured for angles between 7.2° and 172.8° in 7 min, of which one minute was used for remote control, computer tasks, field recovery, and field pre-scan. Final image was 128×128 data points. All three lines were used for image reconstruction. Resolution was 0.1 mm [92]. This work is useful in the development of better models for molecular dynamics in membranes. The first two-dimensional Fourier-transform (2D-FT) ESR studies of nitroxide-labeled lipids in membrane vesicles were also reported [93].

2.2.4 Nitroxide Properties

Nitroxides have limited stability *in vivo* due to reduction with low-molecular antioxidants (ascorbate, thiols, etc.) and enzymatic systems, which will affect how they function as an *in vivo* EPR probe. Biological tolerance and cytotoxicity were also important aspects to be evaluated. The chemical and biological properties of several nitroxides were carefully studied, to provide important reference when it comes to the decision of choosing proper probes for *in vivo* EPR imaging.

I. Grigor'ev et al. studied the suitability of ^{14}N and ^{15}N nitroxide 3-Carboxy-2,2,5,5-tetramethyl-3-pyrroline-1-oxyl in mice at L-band. The gradient strength was 4.047 G/cm (0.4047 mT/cm) and the number of projections was 38. Deconvolution and back projection were used to obtain 2D spatial images, and resolution was 1 mm [94]. According to EPR data, both nitroxides had relatively high retention time in mice *in vivo*, allowing EPR imaging experiment for more than 1 h.

X. Wang and the Fuji group developed a scalable synthetic route for ^{15}N -TEEPONE. Test results showed that it was suitable for EPR imaging of brain, and had higher sensitivity compared with its ^{14}N -counterpart [35].

H. Yokoyama et al. made the first attempt to image with the nitroxide radical PFR-2, which was more persistent in a biological system compared to commonly used nitroxides. Experiments were performed at 700 MHz, gradient strength was 10 G/cm, with its direction changed in 20° steps to provide 9 projections. Images were reconstructed from the deconvoluted data by filtered back projection and resolution was estimated to be 3 mm [95]. The results suggested that it was possible to use PFR-2 as an imaging agent which persists in a biological system.

The Kamada group designed and synthesized three acyl-protected hydroxylamines in a search for novel EPR brain imaging agents. The biological relevance of these new compounds in mice has been assessed, and their biodistribution patterns have been compared. The study found out that the five-membered ring derivative AMCPy was a potent EPR brain imaging agent while the other two derivatives, AMCPE and DACPy, were quite ineffective [69].

The Bagryanskaya group studied reduction (by ascorbic acid) of new water- and blood-soluble nitronyl nitroxides NN1 and NN2 in model conditions and *in vitro*. EPR imaging experiments were performed on an L-band CW Bruker Elexsys E-540 spectrometer. Gradient strength was 10 G/cm (1.0 mT/cm), 31 projections were taken in 21 min. Resolution was around 2~3 mm [96]. The results of EPR tomography were compared with MRI data. The study suggested that the fast reduction of the reaction product of NN with NO—imino nitroxides, was the main obstacle to using NN as a spin probe *in vivo*.

2.2.5 Method Development

New methods for performing EPR imaging have been proposed over the years along with the advancement of science and technology, including experiment procedures, image reconstruction algorithms, and combinations with other magnetic techniques. These developments can be categorized into three EPRI modalities: CW, pulse and rapid-scan. Compared to early works emerging in the eighties and nineties, EPRI today has higher resolution, better quality and requires less acquisition time.

1. CW EPRI

As a pioneer in the EPR field, as early as 1984, the Eaton group reported an experimental arrangement that provides routine imaging capability for samples of the dimensions commonly used in EPR and demonstrated its capability. The maximum gradient was 1 G/cm, stepping at 0.1 G/cm. One image took 1 ~ 10 min and resolution was 1mm [97]. M. Maltempo et al. demonstrated a reconstruction method for spectral-

spatial 2D imaging from an incomplete set of projections using an iterative convoluted back-projection image reconstruction algorithm [98].

H. Fujii and L. J. Berliner performed one of the very early EPRI experiments. They applied image reconstruction for nitroxides by the convolution difference method. Several examples were compared with and without this treatment. A phantom using tempol was imaged at L-band. Gradient strength was 0.28 G/cm (2.8 G/mm). 2D spatial image was reconstructed by FBP method. Resolution was 1 mm [99].

H. Yokoyama and H. Kamada developed the Selected-region intensity determination (SRID) method for obtaining the temporal changes in EPR signal intensity from a selected region. In contrast to previous imaging methods, the SRID method does not require complicated procedures, such as integration, reconstruction. Reading the intensity from the select region makes it possible to determine the signal decay rate in experimental animals. Nitroxide carbamoyl-PROXYL was imaged on a 700 MHz home-built CW EPR imager. The linear magnetic field gradient was 10 G/cm (1 mT/cm) and was changed in 20° increment. The EPR spectrum was taken at selected regions (e.g. lung area) and its spectrum was deconvoluted using the line shape of the spectrum without the gradient. The amplitude of the deconvoluted spectrum at the center represented the signal intensity of the selected region. The EPR image was obtained via FBP reconstruction from the deconvoluted data. The EPR signal intensity at the selected region was obtained at a spatial resolution of 2.7 mm [74]. Using this model and the results from EPR measurements, the degrees of nitroxide reduction in different organs were measured. It was also found that the reaction rate in lung mainly reflected the reduction of local nitroxide radical.

The Drescher group proposed a simultaneous iterative reconstruction algorithm (SIRT) method for reconstruction of CW EPRI experimental data as an alternative to the widely applied FBP. X-band CW imaging experiments were performed on a two-capillary phantom. The radical studied was spin label IPSL. The magnetic field gradient strength was varied in 130 steps between +171 G/cm and 171 G/cm, which corresponded to equidistant angles of -48° to $+48^\circ$. The data acquisition time was 130 min. Image reconstruction using SIRT took 12 min for 90 iteration steps in a single CPU thread, while FBP took 7 s. A 2D spectral spatial image was reconstructed with a resolution of 1 mm. They found that for low signal to noise ratio and spectral–spatial images that are limited by the maximum magnetic field gradient strength SIRT is more suitable than FBP, in terms of sharper edges and less noise [100].

High dimensional EPRI was implemented in several groups. M. Alecci et al. in the Sotgiu group described the first 3D examples of *in vivo* CW EPR imaging at 1.2 GHz. Fourier reconstruction zeugmatography was used to obtain the 3D images [101]. The role of different experimental and instrumental parameters on the resolution of EPR images in different organs were investigated in the paper of M. Ferrari et al. [102].

H. Hirata and his colleagues developed a fast back projection-based reconstruction method for the 4D spectral-spatial EPR image, called the algebraic reconstruction technique (ART). The spectral-spatial EPR images were reconstructed using projections acquired with the constant sweep of a magnetic field. A phantom of ^2H , ^{15}N -DCP was imaged at 750 MHz on a locally built CW EPR spectrometer. Gradient strength was 2 G/cm (0.2 mT/cm), 3375 projections were taken in 7.5 min. Only the low field line was used in the image reconstruction and resolution was 1 mm [41].

The J. Zweier group made multiple developments in imaging methodology. P. Kuppusamy's paper presented the development and application of 4D spectral-spatial EPRI technique for determination of spectral shape and spin distribution of paramagnetic samples. Strategies for optimizing acquisition and computation times, image resolution, and data presentation were described [48]. Another paper of P. Kuppusamy described the development and optimization procedures for obtaining high-quality 3D spatial EPRI of large lossy samples at L-band. Strategies for selecting optimized parameters for projection acquisition, instrumentation, and algorithms for correcting drifts in microwave frequency and inaccuracies in the static and gradient magnetic fields were described [47]. G. He et al. described an approach for whole-body, EPRI-based, free-radical imaging along with proton MRI in mice. This technique was particularly valuable for *in vivo* assessment of the role of free radicals and altered free-radical metabolism in organ-specific disease pathophysiology [46]. The low-field line rather than the high-field line is used in image reconstruction to apply their hyperfine correction algorithm [26]. Z. Chen et al. developed a fast gated EPRI acquisition technique for biomedical applications for the study of cardiovascular disease. This technique enabled the measurement and mapping of myocardial free-radical concentrations and metabolism as a function of the cardiac contractile cycle [103].

P. Kuppusamy et al. presented a spatial-spectral imaging technique that provided an order of magnitude reduction in acquisition time, compared to iterative tomographic reprojection. A model was developed for the spectra measured with magnetic field modulation. The processing technique was experimentally demonstrated on a one-dimensional phantom containing nitroxide PDT on an L-band spectrometer. The image

was reconstructed using FBP, which was based on the direct inversion of the Radon transform. The approach provided reliable reconstruction of spin density and spectral linewidth with less data acquisition time [60].

T. Czechowski et al. described a home-built image system to perform two-dimensional study of free radical distributions by CW EPR at X-band. The sample was diphenyl-picrylhydrazyl. Gradient strength was 50 G/cm. Reconstruction was based on the iterative simultaneous algebraic reconstruction technique (SART). The EPR signals were recorded for 45 projections with the angle varied from 0 to 180° which was changed in steps of 4° over a period of 1.5h [104]. A method was proposed to calculate the projections for radical distribution, based on iterative procedures [105]. A new method for fast 2D EPRI was also presented [106]. Recently, they proposed to use overmodulation of projections as a method to enhance signal-to-noise ratio in EPR imaging [107]. A study concerning the image quality in EPR in 2D spectral-spatial imaging experiments was also presented [108].

K. Matsumoto et al. compared EPR imaging and T₁-weighted MRI to detect nitroxyl contrast agents [109]. A combination of the constant-time spectral-spatial imaging (CTSSI) modality and projection-reconstruction modality was tested to simplify data acquisition for multi-dimensional CW EPR spectral-spatial imaging. The data acquisition process for multi-dimensional spectral-spatial imaging was consequently simplified [110].

T. Ogata et al described a method of determining the absolute concentration of carbamoyl-PROXY by EPR imaging. The experiment was carried out on a 720 MHz CW EPR image system. For 2-D spatial EPR imaging, the field gradient was applied at 10

G/cm (1 mT/cm), changing direction in 10° steps to provide data for 18 projections. The spectral data obtained with the field gradients were deconvoluted with the lineshape of the zero-gradient spectrum, by the fast Fourier transform method with low pass filtering. 2D EPR images were reconstructed by a simultaneous iterative reconstruction technique. The absolute concentration of the sample was calculated by using the gray-scale value (i.e., the signal intensity) of the marker [75].

2. Pulse EPRI

A. Blank et al. present a new method, based on pulsed EPR microimaging to obtain a 3D mapping of the oxygen concentration in millimeter-scale biological samples. A new crystallographic packing form (denoted tg-LiNc-BuO) was used, which interacted with paramagnetic oxygen molecules causing a spectral line broadening which is linearly proportional to the oxygen concentration. The four-dimensional images were acquired by employing the FID (free induction decay) imaging pulse sequence. A typical measurement takes 20 ~ 40 min and the currently available resolution is 80 μm [111]. The first spatially-resolved electrically-detected magnetic resonance images (EDMRI) of paramagnetic states was demonstrated on an amorphous silicon (a-Si:H) solar cell with 20 μm -scale pixel resolution [112]. A statistical reconstruction algorithm for CW electron spin resonance imaging was later developed in the Blank lab [113].

The Krishna group also made significant contributions in pulse imaging technique. F. Hyodo et al. showed the first pulsed EPR imaging of a cell-permeable nitroxide in mice, which opens the possibility of using time-domain EPR to determine pO_2 in specific intracellular locations [51]. N. Devasahayam et al. developed a method to

generate shaped radiofrequency pulses for uniform excitation of electron spins in time-domain radio frequency (RF) EPR imaging. The study showed that shaped sinc pulses had advantages to improve uniform excitation over a relatively wide bandwidth in time-domain RF-EPR imaging (RF-FT-EPRI) [114]. S. Subramanian presented a new strategy for fast RF CW EPR imaging by direct detection of signals without low-frequency field modulation. These projections were suitably filtered and back-projected to produce the 2D or 3D image of the object [55]. C. Dharmaraj et al. presented a windows-based, object-oriented, feature identification system for EPRI. The standard principal component transform (PCT) and a color quantization method were combined to identify regions of interest (ROI). The system is useful in quantifying the probe distribution faster which made it suitable for pharmacokinetics studies [115].

3. Rapid-scan EPRI

The rapid-scan EPR method was developed in the Eaton group. The principles, instrumentation and sample results of rapid-scan imaging method were described in S. Eaton's paper [7]. In rapid-scan EPR the magnetic field or frequency is scanned through the spectrum at rates that are much faster than in conventional CW EPR and the signal is directly-detected as the absorption spectra. Rapid-scan EPR showed improved S/N relative to conventional CW EPR, which is very desirable at low frequencies [6]. A new algorithm using regularized optimization (RO) for EPR imaging oximetry was described and tested with experimental data for the case of one spatial and one spectral dimension [116]. The background removal procedure for rapid-scan EPR were developed [117].

M. Tseitlin et al. developed a new spectral–spatial imaging algorithm for full EPR spectra of multiline nitroxides and pH sensitive trityl radicals. The algorithm was tested with a phantom containing ^{14}N -PDT, ^{15}N -PDT and triarylmethyl radical at 251 MHz. Gradient strength used was 10 G/cm with 1G/cm step, and each projection took 60 s. An image was successfully reconstructed, and achieved a resolution of 1 mm. Compared to the widely used FBP method, the new algorithm lifts the limitations imposed on data collection to allow full-spectrum imaging of multiline EPR spin probes [11].

J. Biller et al. compared CW and RS imaging at 250 MHz using ^{14}N -PDT and ^{15}N -PDT phantoms. The maximum Z-gradient was 8 G/cm and eighteen equally-spaced projections were recorded from $\pm 5^\circ$ to $\pm 85^\circ$ in the spectral-spatial pseudo-plane. Images were reconstructed from 18 equally-spaced filtered back projection on a 512×512 grid. The comparison results showed that, for the same data acquisition time, RS EPR provides projections with significantly improved S/N than CW EPR, particularly at higher magnetic field gradients. The improved S/N in the projections results in improved accuracy in linewidths calculated from slices through spectral-spatial images. The ability to acquire data more quickly and with improved S/N will facilitate *in vivo* applications of nitroxide imaging [118].

2.2.6 Instrumentation

Research on EPR imaging instruments is an indispensable part in the development of EPR to provide faster, more precise and more reliable equipment, pushing the limit of what can be achieved by EPRI. Many research groups built their own imaging systems, at frequencies from 250 MHz to 700 MHz.

The Fujii group designed and tested a 750 MHz CW-EPR digital console for small animal imaging. *In vivo* 3D EPR images of COP in a mouse's head were successfully obtained. Data acquisition was controlled by a LabVIEW-based program through a USB port on MacOS 10.9.5. Based on the filtered back projection method, image reconstruction from the EPR spectra was carried out. The acquisition time for a single image was 10 s for 181 projections. The 20 projection data sets were averaged and used to construct a 3D image with a one-step filtered back projection method without deconvolution. All three lines were used and resolution was 1 mm [119].

The Kamada group built a 700 MHz *in vivo* EPR-CT system. 3D-pictures of the distribution of C-PROXYL injected in brains and livers of rats and mice were obtained. Gradient strength was 10 G/cm (1 mT/cm) with field gradient angle between 0 to 160° with 20° intervals. 81 projections were taken in 1.5 min for one 3D image. Spatial-time images of the animals were also obtained with resolution of 1 mm [66]. The group later reported the first *in vivo* CT (i.e. three-dimensional imaging) study with 300 MHz ESR [120].

Y. Lin, T. Ogata et al. built a 700 MHz CW ESR system with a flexible surface-coil resonator as an endoscope- or a stethoscope-like device to measure nitroxide radicals at a specific area in rats. The sample was carbamoyl-PROXYL solution. Magnetic field gradient strength was 10 G/cm (1 mT/cm). EPR data were deconvoluted by the fast Fourier transform method. One image took more than 2.5 min to acquire and was reconstructed by filtered back projection. The low field line of the Carbamoyl-PROXYL three-line spectra was used for evaluation. Resolution was 2 mm [67].

The Eaton group constructed various home-built EPR instruments for different purposes over the years. The lab currently has a home-built 250 MHz rapid-scan EPR image system [121], a pulse and CW 250 MHz EPR spectrometer [122] [123] and a 700 MHz rapid-scan and pulse system [124]. A linear magnetic field scan driver [125] and rapid-scan coil driver [126] were designed and constructed later. Cross-loop resonators for rapid-scan EPR and imaging were built [127] [128]. G. Rinard et al. described the practical experiences of resonators for *in vivo* imaging [129]. Digitizers for time-domain EPR were studied [130].

The Zweier group developed an EPR instrument capable of *in vivo* spectroscopy and imaging of free radicals in human skin [49]. A loop resonator for slice-selective *in vivo* EPR imaging in rats was reported later [45].

The Krishna group tested the suitability of the Litz foil coil resonator (LCR) for *in vivo* EPR/EPRI applications in the Time-domain (TD) mode and compared it with a parallel coil resonator (PCR). The result showed in TD mode, the sensitivity of LCR was lower than that of the PCR. However, in CW mode, the LCR showed better sensitivity [131].

The Swartz group reported techniques to use coils for electronic rotation of the gradient and computer control of the scan time to obtain CW EPR images of wet samples. Scan times were as short as 6 s per projection and the total time of one image was 132 s. Imaging experiments were performed on an X-band (9.5 GHz) Varian E-112 spectrometer with ¹⁵N PDT. Gradient strength was 100 G/cm (1 T/m) and 18~20 projections were taken. All nitroxide lines were used in the image reconstruction and resolution was 1 mm [132].

2.2.7 Other Subjects

Besides phantoms and *in vivo* experiments on small animals, researchers also studied various other subjects with EPRI and their work is described below briefly. These achievements indicated that the capability of EPRI can potentially be expanded to a wide variety of fields.

The Kurczewska group investigated the behavior of TEMPO-labeled polymer coated magnetite nanoparticles under different conditions (temperature and orientation in magnetic field). L-band (1 GHz) 2D CW images were taken. Maximum gradient used was 10 G/cm. The time required to take an image was 30 min, and all three nitroxide lines were used. Resolution was 1 mm [133]. The study showed that EPRI was effective for evaluation of changes in the spatial distribution of nanoparticles in the sample.

B. Fink et al. studied redox active minerals in dietary supplements on a Bruker L-band CW EPR-Spectrometer ELEXSYS E540. Nitroxide studied were CPH and 3-CP. Gradient strength was 24 G/cm. 31 projections were taken for a total of 28 min. The 2D EPR images were constructed employing FT deconvolution and filtered back projection [134]. Data showed that redox active metals, e.g. copper and iron, had reduced ability to catalyze free radical formation and associated detrimental oxidations when part of a multivitamin/multimineral formulation.

Lebedev et al. studied natural probes, the water-soluble fraction of soil humic substances, at X band (9.3 GHz) with an ERS-221 CW spectrometer. Magnetic field gradient was 100 G/cm. Image was reconstructed by a convolution-back projection algorithm on a 51×51 grid. Resolution was 2 ~ 3 mm [135]. The study showed that the

humic substances penetration into seeds and its distribution had important biological effects on the seeds.

The Sotgiu group applied two-dimensional EPR imaging experiments to alanine dosimeters at 1.5 GHz. Although the EPR spectrum was very broad and complex, the low frequency EPRI was able to give some spatial localization of the signals [136].

Fuchs and Parker group performed imaging experiments at X-band (9.5 GHz) and S-band (2.4 GHz). Radicals used were TEMPO, PCA, PCM. Objects studied included hairless mice, human skin and phantom. At X-band, both 1D and 2D spatial image were acquired. Gradient strength was 400 G/cm (4 T/m). 72 projections were taken in 4 min. Resolution was 10~100 μm [137]. At S-band, field gradient strength was 100 G/cm (10 mT/cm). 2D image at 2.0 GHz (L-band) was measured over a time period of 4 min, with 72 projections. Resolution was 2 mm. Higher spatial resolution of 65 μm was reached when the field gradient was increased to 320 G/cm (32 mT/cm) [138]. Measurement of nitroxide reduction kinetics and spatial distribution in human skin using EPR imaging was demonstrated [139].

The Schlick group studied the degradation of polymers (ABS) from the spatial and temporal perspectives. Imaging experiments were performed on an X-band (9.7 GHz) Bruker EMX spectrometer using phantoms. The 1D images were obtained with a field gradient of 206 G/cm [22]. The 2D spectral-spatial images were taken using a gradient of 250 G/cm [140] and 320 G/cm. 128 projections were taken for gradients corresponding to equally spaced increments in the range -90° to $+90^\circ$, of which 83 real projections were used (the others were missing angles) [141]. The image reconstruction method was Fourier transform followed by optimization with the Monte Carlo (MC)

procedure [22]. Missing angles were obtained by the projection slice algorithm (PSA) with 2-10 iterations. The 2D image was saved as a 256 x 256 matrix [142] [143].

A. Blank performed CW EPR micro-imaging on LiNc-BuO crystals in PDMS. 2-D spatial and 2-D spatial 1-D spectral imaging experiments were carried out on a home built new CW EPR micro-imaging system with very small gradient coils. Microcrystals coated in a bio-compatible and oxygen permeable polymer matrix have the benefit of reduced cell toxicity thus are suitable for repetitive use. A 2-D spatial image was acquired with 256 projections, and the gradient magnitude was 4.9, 4.5, and 230 G/cm (2.3 T/m) for the X-, Y-, and Z-axis, respectively. MW frequency was 15.410 GHz, center field was 5447.2 G and sweep range was 22 G. Image resolution was in the μm -scale [144]. The group also detected, quantified and imaged superoxide in plant roots by spin-probe TEMPONE [145].

The Zhao group was the first to study endogenous NO free radicals generated in plants. The distributions of NO generation in different plants from different species with different shapes were studied. An X-band EPR Imaging system was developed. For the leaf *in vivo* EPR imaging, a zero-field gradient was measured first, a group of total $9 \times 9 \times 9$ projection spectra were acquired at gradient strength of 27 G/cm (2.7 mT/cm) with the gradient direction rotating in angle increments of 20° . Each projection took 40 s and the total time for acquiring one image was approximately 60 min. The 3D spatial image was reconstructed using two-stage back-projection reconstruction algorithm. Imaging resolution was better than 200 μm , which was 10 times higher than L-band (about 1–3 mm); the sensitivity was about 1000 times higher than L-band [146]. This study provided a convenient method to study the endogenous free radicals in plants.

2.3 Summary and Current Work

In the past thirty years, the EPR imaging technique went through fast development and numerous research articles have been published focusing on a variety of aspects. Currently EPR imaging using nitroxide probes can be performed at frequencies of VHF, UHF, L-band, S-band and X-band. The imaging subjects include phantoms, selected regions of biological samples, whole animal (rat and mouse), human skin, plants, nanoparticles, lipids and many more. Methods of CW, pulse and rapid-scan EPR imaging have been established. A variety of image types have also been explored, including spatial, spectral-spatial, 1D, 2D, 3D up to 4D EPR imaging. Research on EPR imaging technique has been extended to multiple disciplines, including oximetry, metabolism, spatial distribution, nitroxide properties, method development, instrumentation, materials science, etc. These contributions have been made by EPR scientists worldwide over the years, covering much wider application areas than the earlier years of EPR and bringing a prosperous future for the whole field of EPR.

My research work on VHF EPR imaging in the past few years has made a step beyond the prior work. An outline is provided here. Details are in subsequent chapters.

- (1) Imaging parameters are optimized, including gradient strength, gradient step, sweep width (Chapter 5).
- (2) A method has been developed to perform EPR imaging by field-stepped linear scan at VHF. This method does not perform as well as the sinusoidal single-sweep image (slower, poorer S/N, more complicated), still, it serves as an alternative and may be used when large sweep width is needed (Chapter 6).

- (3) Work has been done to decrease image time, including investigation of the digitizer behavior, optimization of the software, adopting various averages approach (Chapter 7).
- (4) A method has been shown to image different samples simultaneously with 2D spatial EPRI (Chapter 7).
- (5) Routines based on 'Python' software have been developed to run the EPR imaging, from data acquisition to image reconstruction. These procedures allow central control of EPRI experiment by connecting various parts in the imaging system, sending commands and monitoring equipment status. A novel method of using Python to record EPR spectra in a new data format ('csv') is provided, which is faster and more compact with easy access, to facilitate the efficient transport of data among various physical/virtual spaces (Chapter 7).

List of definitions of the abbreviations for the nitroxides and other radicals

3-CP	2,2,5,5-tetramethyl-1-pyrrolidinyloxy-3-carboxamide or 3-carbamoyl-proxyl
6-OHDA	6-hydroxydopamine
16-PC	1-palmitoyl-2-(16-doxyl stearoyl) phosphatidylcholine
ABS	acrylonitrile-butadiene-styrene
AMCPe	1-acetoxy-4-methoxycarbonyl-2,2,6,6-tetramethylpiperidine
AMCPy	1-acetoxy-3-methoxycarbonyl-2,2,5,5-tetramethylpyrrolidine
BDPA	α,γ -bis(diphenylene)- β -phenylallyl
BMPO	5-tert-butoxycarbonyl 5-methyl-1-pyrroline N-oxide
carbamoyl-PROXYL	3-carbamoyl-2,2,5,5-tetramethylpyrrolidine-1-oxyl
carboxy-PROXYL	3-carboxy-2,2,5,5-tetramethylpyrrolidine-1-oxyl
CAT-1	4-trimethylamino-2,2,6,6-tetramethylpiperidine-1-oxyl
COP	3-Carboxy-2,2,5,5-tetramethyl-pyrro lidine-1-oxyl
CP•	3-carboxy-2,2,5,5-tetramethyl-1-pyrrolidinyloxy
CPH	1-hydroxy-3-carboxy- 2,2,5,5-tetramethylpyrrolidine
CTPO	3-carbamoyl-2,2,5,5-tetramethylpyrrolidine-1-oxyl
CYPMPO	5-(2,2-dimethyl-1,3-propoxycyclophosphoryl)-5-methyl-1-pyrroline N-oxide
DACPy	1-acetoxy-3-(acetoxymethoxy)carbonyl-2,2,5,5-tetramethylpyrrolidine
DBNBS	3,5-dibromo-4-nitrosobenzene sulfonic acid
DEPMPO	5-diethoxyphosphoryl-5-methyl-1-pyrroline N-oxide
DETC	diethyldithiocarbamate
DMPO	5,5-dimethyl-1-pyrroline-N-oxide
DPPH	1,1-diphenyl-2-picrylhydrazyl
EMPO	5-(ethoxycarbonyl)-5-methyl-1-pyrroline N-oxide
HMP	3-hydroxymethyl-2,2,5,5-tetramethylpyrrolidine-1-oxyl

IPSL	3-(2-Iodoacetamido)-2,2,5,5-tetramethyl-1-pyrrolidinyloxy
LiNc-BuO	lithium octa-n-butoxynaphthalocyanine
LiPc	lithium phthalocyanine
MCP	3-methoxycarbonyl-2,2,5,5-tetra-methylpyrrolidine-1-yloxy
MC-PROXYL	3-methoxycarbonyl-2,2,5,5-tetramethylpyrrolidine-1-oxyl
mHCTPO	CTPO deuterated at all positions except the 4-H
NN1	2-(5-methyl-1H-imidazole-4-yl)-4,4,5,5-tetramethyl-4,5-dihydroimidazole-3-oxide-1-oxyl
NN2	2-(1H-imidazole-4-yl)-4,4,5,5-tetramethyl-4,5-dihydroimidazole-3-oxide-1-oxyl
NO•	nitric oxide
O2 •-	superoxide radical anion
PBN	N-tertbutyl- α -phenylnitrone
PCA	3-carboxy-2,2,5,5-tetramethylpyrrolidine-1-oxyl
PCAM	3-methoxycarbonyl-2,2,5,5-tetramethylpyrrolidin-1-yloxy
PDMS	poly-dimethyl-siloxane
PFR	Perfluoroalkyl radical
PDT	Per-deuterated tempone, tempone-d ₁₆
POBN	α -(4-pyridyl-1-oxide)-N-tert-butyl nitrone
PROXYL	pyrrolidine-1-oxyl
R-SG	2-(4-((2-(4-amino-4-carboxybutanamido)-3-(carboxymethylamino)-3-oxopropylthio) methyl) phenyl)-4-pyrrolidino-2,5,5-triethyl-2,5-dihydro-1H-imidazol-1-oxyl
TEEPONE	4-oxo-2,2,6,6-tetraethylpiperidine nitroxide
TEMPAMINE	4-amino-2,2,6,6-tetramethylpiperidine-1-oxyl
TEMPO	2,2,6,6-tetramethylpiperidine-1-oxyl
TEMPOL	4-hydroxy-2,2,6,6-tetramethylpiperidine-1-oxyl
TEMPONE	4-oxo-2,2,6,6-tetramethylpiperidine-1-oxyl

CHAPTER 3 : RELAXATION AND S/N MEASUREMENTS OF TRITYL RADICAL AT VARIOUS FREQUENCIES

Tissue pH (hydrogen ion concentration) and pO₂ (oxygen concentration) are among the most important parameters in physiology and pathophysiology of living organisms. Measurement tools are needed for diagnostics and optimization of treatment strategies for diseases such as cancer and ischemic heart disease [147]. Triaryl methyl-based radicals are promising probes to monitor pO₂ *in vivo*, because of their sharp, single-line EPR spectra and better stability *in vivo* compared to the traditional nitroxide-based radicals [148] [149]. Conventional oximetry is based on the linewidth changes of the spin probes. However, changes in relaxation time are more sensitive and accurate measures of pO₂ than linewidths [150]. Low observation frequency is used to maximize the tissue penetration depth to which the EPR technique is sensitive.

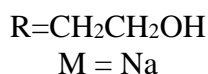
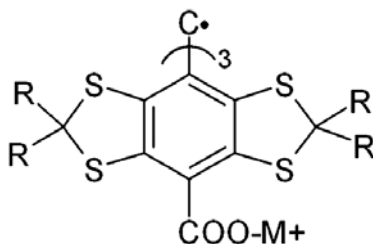
3.1 Introduction

The dependence of relaxation times of OX063 on observation frequency is investigated in this chapter and the results were reported in [151]. Longer relaxation time increases the sensitivity to oxygen concentration [152]. The experiments were carried out on a locally designed and constructed ultra-high frequency (UHF) pulse instrument. Relaxation times and S/N of the OX063 radical at frequencies between 0.4 ~ 1 GHz were measured. We seek to find the optimum frequency for pulse EPR in small animals.

3.2 Materials

3.2.1 Sample

The samples are solutions of OX063, a triarylmethyl based radical whose structure is shown below. The OX063 solid was provided by Dr. Howard J. Halpern (University of Chicago).



Six solutions of OX063 were prepared (Table 3.1). Five of the samples were in 10 mM pH = 7.4 HEPES buffer, with trityl concentrations ranging from 0.05 to 0.4 mM. The sixth sample was in deionized water. Of the five samples in HEPES buffer, four samples had NaCl added with a salt concentration of 0.9% weight/volume, as in normal saline. Samples in quartz tubes were de-oxygenated by bubbling with N₂. Tubes were flame sealed.

Table 3.1 Sample solutions of OX063

Sample #	OX063 concentration (mM)	Salt concentration	HEPES buffer
1	0.05	0.9% w/v	10 mM, pH=7.4
2	0.1	0.9% w/v	10 mM, pH=7.4
3	0.2	0.9% w/v	10 mM, pH=7.4
4	0.4	0.9% w/v	10 mM, pH=7.4
5	0.2	none	10 mM, pH=7.4
6	0.2	none	none

3.2.2 Instrument

1. Variable frequency pulse resonator

The cross-loop resonator (Figure D3 in Appendix D) that was used for the multifrequency measurements was designed such that the frequency can be adjusted between 400 MHz ~1 GHz with the same 16-mm o.d. sample and the same filling factor, thus maintaining all resonator characteristics, except resonance frequency and resonator Q, constant throughout the series of relaxation and S/N measurements. In many EPR experiments, S/N is limited by source noise. One of the advantages of using a CLR (a bimodal resonator) is to isolate the detected signal from the RF source noise.

To adjust the frequency, first connect the microwave source input port of the resonator with sample to the network analyzer (HP 8719D), then on the screen of network analyzer, move the marker tool to the desired frequency. Adjust the tuning screws at the front and back of the resonator to move the dip to the position of the marker, which is the desired frequency.

2. L-band pulse resonator

L-band (1.5 GHz) two pulse ESE and three pulse IR-ESE measurements were performed on a locally designed L-band spectrometer equipped with a reflection resonator (Figure D4 in Appendix D) designed for 4 mm o.d. tubes.

3.3 Method

The six OX063 samples were studied at room temperature, ca 20°C. T_2 was measured by two-pulse spin echo using a $\pi/2 - \tau - \pi - \tau -$ echo pulse sequence. The

initial value of τ was 2400 ns and data were acquired for 1024 60-ns increments of τ . T_1 was measured by inversion recovery with a $\pi - T - \pi/2 - \tau - \pi - \tau - \text{echo}$ pulse sequence. The initial value of T was 1200 ns and data were acquired for 1500 60-ns increments in T . The lengths of the $\pi/2$ pulses were 30 ns at 250 MHz, 80 ns at 400 MHz~1 GHz, and 90 ns at 1.5 GHz. At each frequency the attenuation of the output from the high power amplifier was adjusted to achieve $\pi/2$ and π pulses with the specified length. The fixed τ value in the inversion recovery sequence was 2400 ns at 400 MHz~1 GHz and 1500 ns at 1.5 GHz. Four-step phase cycling was used for the field sweep two-pulse spin echo experiment, and eight-step phase cycling was used for the echo decay and inversion recovery experiments. At 400 MHz~1 GHz the spin echo and inversion recovery data were not subjected to background subtraction since the off-resonance baselines were quite flat. For data acquired at 1.5 GHz, about 10 G off-resonance backgrounds were subtracted from the echo decays and inversion recoveries (i.e., the relaxation measures were usually done at 242 MHz at L-band, then a background was run at 230 MHz). S/N was calculated from the amplitude of field-swept 2-pulse echo detected spectra with a constant τ value of 2400 ns. For the relaxation rate and S/N measurements, five echoes were averaged at each time or field point.

Most of the experiments were performed at ambient temperature, which was about 19 °C. For 700 MHz experiments at 37 °C, a heating tape (Electrothermal®) was wrapped around the resonator. The voltage of the heating tape was controlled via a variable autotransformer (Powerstat®). A thermocouple was attached to the top of the resonator to monitor the temperature. Layers of cloth and aluminum foil insulated the resonator assembly.

Echo decay experiments were performed to measure T_2 . After background subtraction from the data, the fitting function in Xepr software is used to find the values of T_2 . The fitted value from Xepr is multiplied by 2 to give the true T_2 , since the software uses an x-axis of τ , although decay is occurring during the interval 2τ .

Inversion recovery experiments were performed to measure T_1 . After background subtraction, data were multiplied by -1 to provide a decaying signal as required by the software, then fitted with the exponential function in Xepr software, which gives T_1 directly.

3.4 Results for Relaxation Times

3.4.1 Measurement of Sample Resonator Q

The CLR is composed of two resonators, the excitation resonator #1 and the sample resonator (or detection resonator) #2. Q of the sample resonator was measured on the network analyzer (HP 8719D) and values are summarized in Table 3.2. The height of the liquid in the sample tube is 25~28 mm.

Table 3.2 Q of resonator#2 at different frequencies for 0.2 mM and 0.4 mM OX063

Frequency (MHz)	Q#2	
	0.2 mM	0.4 mM
990	12.1	10.4
900	19.1	11.0
800	19.5	14.2
700	21.9	17.7
600	25.6	23.5
500	30.1	27.8
440		32.7
410	43.2	
Uncertainty	5%	5%

3.4.2 Spin-lattice Relaxation Time (T_1)

The values of T_1 for the six OX063 samples as a function of frequency are summarized in Table 3.3 and plotted in Figure 3.1.

Table 3.3 Electron spin relaxation times (T_1 , μs) for OX063 solutions at room temperature

Sample #	OX063 concentration											
	1		2		3		4		5		6	
Frequency (MHz)	0.05mM+salt +HEPES		0.1mM+salt +HEPES		0.2mM+salt +HEPES		0.4mM+salt +HEPES		0.2mM +HEPES		0.2mM+water	
	$T_1(\mu\text{s})$	STD /Avg	$T_1(\mu\text{s})$	STD /Avg	$T_1(\mu\text{s})$	STD /Avg	$T_1(\mu\text{s})$	STD /Avg	$T_1(\mu\text{s})$	STD /Avg	$T_1(\mu\text{s})$	STD /Avg
1500	12.6		12.4	0.022	12.2	0.012	11.6	0.016	12.6	0.021	12.1	0.003
970			10.9	0.052	10.7		10.4		11.1			
900			10.6	0.020	10.4	0.052	10.1		10.8			
800			10.0	0.001	9.9		9.6	0.027	10.2			
700			9.5	0.063	9.4		9.0	0.006	9.7			
600			8.8	0.026	8.7	0.041	8.2	0.045	8.9			
500			8.2		8.0		7.6		8.3			

T_1 uncertainties are ~2 to 3% for 0.1 to 0.4 mM.

Empty cells: the corresponding experiment was not performed or STD (standard deviation) was not calculated because only one measurement was performed.

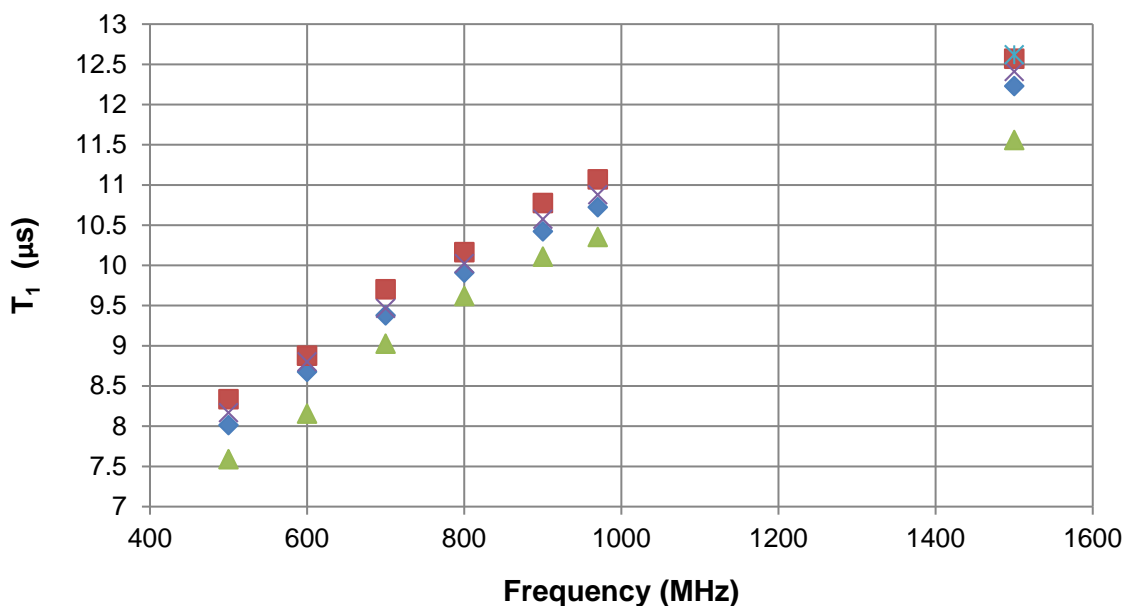


Figure 3.1 Microwave frequency dependence of T_1 for OX063 in HEPES buffer (■) 0.2 mM, (*) 0.05 mM + salt, (x) 0.1 mM + salt, (◆) 0.2 mM + salt, (▲) 0.4 mM + salt

For OX063 of a certain concentration, T_1 increases as frequency increases. At a certain frequency, T_1 decreases as OX063 concentration increases. Adding salt decreases T_1 by about 3% for 0.2 mM OX063.

3.4.3 Spin-spin Relaxation Time (T_2)

The values of T_2 for the six OX063 samples as a function of frequency are summarized in Table 3.4 and plotted in Figure 3.2.

Table 3.4 Spin-spin relaxation times (T_2 , μs) for OX063 at room temperature

Sample #	OX063 concentration											
	1		2		3		4		5		6	
Frequency (MHz)	0.05mM+salt +HEPES		0.1mM+salt +HEPES		0.2mM+salt +HEPES		0.4mM+salt +HEPES		0.2mM +HEPES		0.2mM+water	
	T_2 (μs)	STD /Avg	T_2 (μs)	STD /Avg	T_2 (μs)	STD /Avg	T_2 (μs)	STD /Avg	T_2 (μs)	STD /Avg	T_2 (μs)	STD /Avg
1500	6.6	0.028	5.9	0.081	5.7	0.065	4.72	0.002	6.0	0.034	6.9	0.027
970			6.6	0.137	6.0		5.1	0.003	6.7			
900			6.4	0.115	5.9	0.021	5.1		6.7			
800			6.4	0.029	5.8		5.0		6.6			
700			6.2	0.006	5.7		4.9		6.4			
600			6.2	0.013	5.7	0.027	4.7		6.3			
500			5.9		5.6		4.7		6.2			

55

T_2 uncertainties are ~2 to 3% for 0.2 to 0.4 mM, ~6% for 0.1 or 0.05mM.

Empty cells: the corresponding experiment was not performed or STD was not calculated because only one measurement was performed.

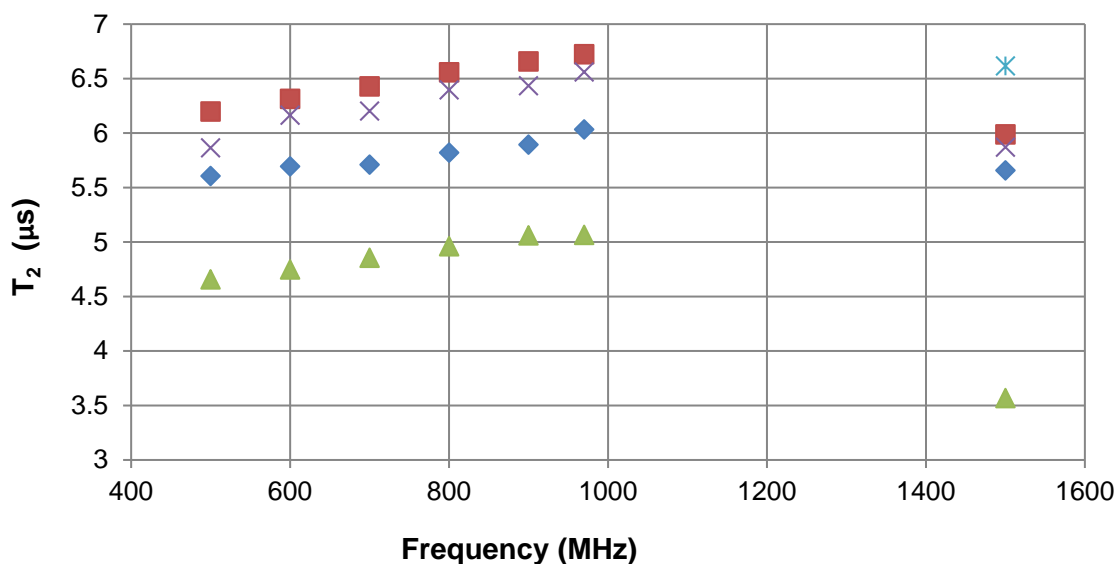
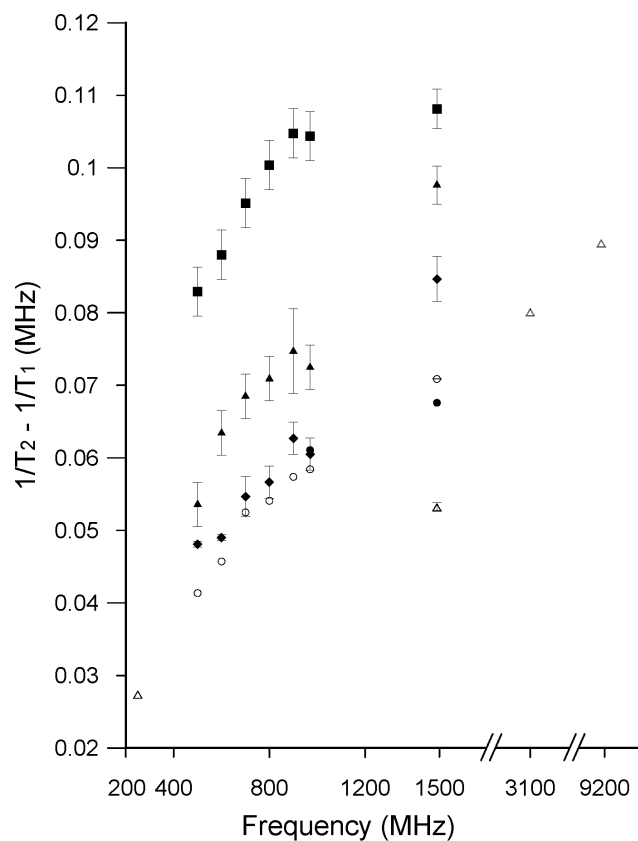


Figure 3.2 Microwave frequency dependence of T_2 for OX063 in HEPES buffer (■) 0.2 mM, (*) 0.05 mM + salt, (×) 0.1 mM + salt, (◆) 0.2 mM + salt, (▲) 0.4 mM + salt

In the UHF frequency range (0.4 ~ 1 GHz), at a certain OX063 concentration, T_2 increases as frequency increases, however, when frequency further increases to 1.5 GHz, T_2 drops. At a certain frequency, when OX063 concentration increases, T_2 decreases. The concentration dependence is larger for T_2 than for T_1 . HEPES buffer decreases T_2 for 0.2 mM OX063. Adding salt decreases T_2 by about 10% further for 0.2 mM OX063.

Since T_1 is much more frequency dependent than T_2 , the contribution of T_1 to T_2 changes substantially with frequency. To separate those two factors, $(1/T_2 - 1/T_1)$ as a function of frequency for each sample were calculated and plotted (Figure 3.3c). The contributions to T_2 increase as frequency increases.



(c)

Figure 3.3 Microwave frequency dependence of relaxation rates for OX063 in pH = 7.4 solution at ambient temperature (19 °C). (a) $1/T_1$, (b) $1/T_2$, (c) $1/T_2 - 1/T_1$ (●) 0.05 mM OX063 + 154 mM NaCl in 10 mM HEPES, (◆) 0.1 mM OX063 + 154 mM NaCl in 10 mM HEPES, (▲) 0.2 mM OX063 + 154 mM NaCl in 10 mM HEPES, (■) 0.4 mM OX063 + 154 mM NaCl in 10 mM HEPES, (○) 0.2 mM OX063 in 10 mM HEPES, and (Δ) 0.2 mM OX063 in water.

The plots in this Figure are reproduced from [151]. Data at 9.2 GHz is from [153].

The results show that, $1/T_1$ decreased by more than a factor of 2 as frequency is increased over this range. $1/T_2$ is less strongly frequency dependent than $1/T_1$. There is a significant contribution to $1/T_2$ from incomplete motional averaging of anisotropic interactions.

3.5.2 Dependence of Relaxation Rates on the Concentration of OX063

The results are summarized in Table 3.5.

Table 3.5 Dependence of Relaxation Rates for OX063 on Radical Concentration and Salt Concentration ^a

Relaxation Rate	Resonance Frequency (MHz)	Parameters held constant	Parameter Varied	Impact
1/T ₁	500 - 1500	10 mM HEPES, 154 mM NaCl	[OX063] = 0.1 to 0.4 mM	$(2.1 \pm 0.7) \times 10^{-2}$ MHz/mM ^b
1/T ₁	250	145 mM NaCl, 37°C,	[OX063] = 0.1 to 4.6 mM	3.6×10^{-2} MHz/mM ^c
1/T ₁	700	10 mM HEPES, [OX063] = 0.2 or 0.4 mM, T = 19 or 37°C	[NaCl] = 0, 77, or 154 mM	3.2×10^{-5} MHz/mM ^d
1/T ₂	500 - 1500	10 mM HEPES, 154 mM NaCl	[OX063] = 0.1 to 0.4 mM	0.15 ± 0.01 MHz/mM ^b
1/T ₂	250	Water	[OX063] = 0.2 to 15 mM	0.11 MHz/mM
1/T ₂	250	0.5 PBS	[OX063] = 0.2 to 5 mM	0.14 MHz/mM
1/T ₂	250	PBS	[OX063] = 0.2 to 15 mM	0.15 MHz/mM
1/T ₂	250	145 mM NaCl, 37°C	[OX063] = 0.1 to 4.6 mM	0.16 MHz/mM ^c
1/T ₂	250	10 PBS	[OX063] = 0.2 to 5 mM	0.20 MHz/mM
1/T ₂	700	10 mM HEPES, [OX063] = 0.2 or 0.4 mM, T = 19 or 37°C	[NaCl] = 0, 77, or 154 mM	1.9×10^{-4} MHz/mM ^d
1/T ₂	250	PBS, [OX063] = 1 mM	[NaCl] = 0, 77, 154 mM	7.0×10^{-4} MHz/mM
1/T ₂	250	PBS, [OX063] = 2 mM	[NaCl] = 0, 77, 154 mM	1.5×10^{-3} MHz/mM
1/T ₂	250	PBS, [OX063] = 5 mM	[NaCl] = 0, 77, 154 mM	4.0×10^{-3} MHz/mM
1/T ₂	250	PBS, [OX063] = 0.5 mM	pO ₂ = 0 to 21%	6.1×10^{-2} MHz/%O ₂
1/T ₂ – 1/T ₁	500 - 1500	10 mM HEPES, 154 mM NaCl	[OX063] = 0.1 to 0.4 mM	0.13 ± 0.01 MHz/mM ^b
1/T ₂ – 1/T ₁	700	10 mM HEPES, 0.2 or 0.4 mM OX063, T = 19 or 37°C	[NaCl] = 0, 77, or 154 mM	1.4×10^{-4} MHz/mM ^d

^a pH = 7.4, temperature = 19 – 21°C, unless noted. ^b Average at 7 resonance frequencies. ^c Data from ref. [154]. ^d Average for two concentration of OX063 at two temperatures.

The results show that, when radical concentration increases, relaxation rates increase. Concentration dependence is independent of frequency.

3.5.3 Dependence of Relaxation Rates on Salt Concentration

The concentration of other charged species in solution impacts both the relaxation rate of OX063 and the dependence of the relaxation rate on radical concentration.

The effect of ions in solution on relaxation rates is smaller for $1/T_1$ than for $1/T_2$ or $1/T_2 - 1/T_1$ (Figure 3.3). The average slope of plots of $1/T_1$ vs [NaCl] at 700 MHz is 3.2×10^{-5} MHz/mM, which is about a factor of six smaller than the dependence of $1/T_2$ on salt concentration under similar conditions (1.9×10^{-4} MHz/mM). The higher the concentration of ions in solution, the larger the slope of plots of $1/T_2$ vs. concentration of OX063, increasing from 0.11 MHz/mM in water to 0.2 MHz/mM in $10 \times$ PBS at 250 MHz (Table 3.5). The increase in the collisional contribution to relaxation as the concentration of counter-ions in solution increases is attributed to interactions of cations with the negatively charged radicals which decreases repulsion between trityl radicals. Relaxation rates increase when salt concentration increases.

3.5.4 Dependence of S/N on Resonance Frequency

The relationship between S/N and frequency is plotted in Figure 3.4. The S/N value was normalized by \sqrt{Q} where Q is the quality factor of the detection resonator.

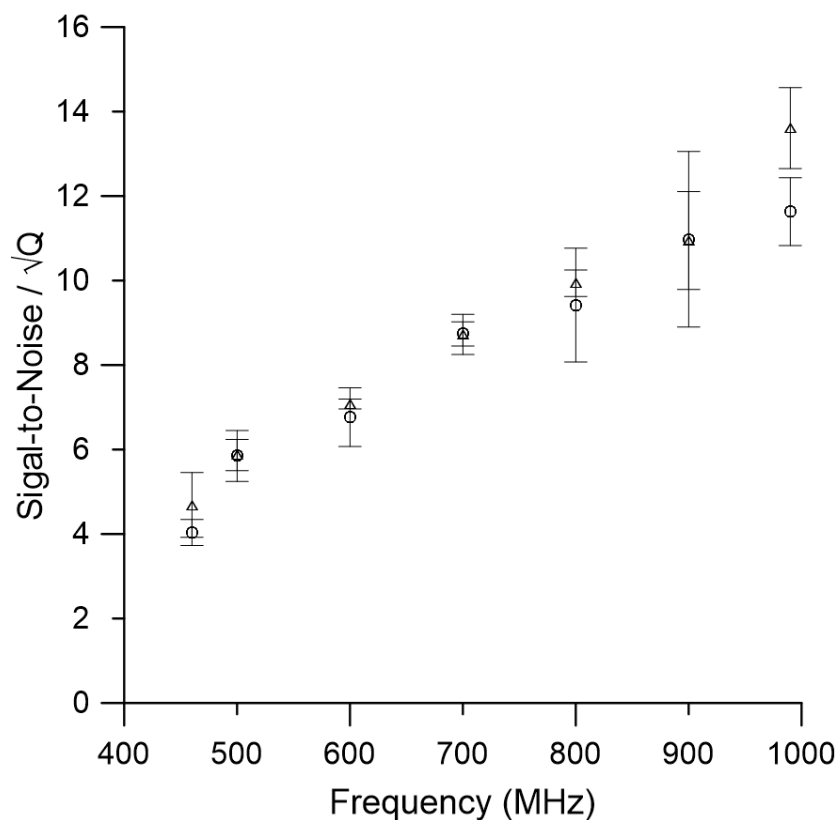


Figure 3.4 Frequency dependence of S/N (normalized by \sqrt{Q}) for OX063 in 10 mM HEPES buffer at 19 °C

(\circ) 0.2 mM OX063 + 154 mM NaCl in 10 mM HEPES, (Δ) 0.4 mM OX063 + 154 mM NaCl in 10 mM HEPES.

Values for the 0.4 mM solutions were divided by two to facilitate comparison.

Reproduced from [151].

The data shows that S/N increases as frequency increases. The decrease in resonator Q with increase in RF frequency is due predominantly to eddy current losses in the sample.

3.5.5 Dependence of S/N on Salt Concentration and Temperature at 700 MHz

The data are summarized in Table 3.6:

Table 3.6 Dependence of S/N (normalized by \sqrt{Q}) on salt concentration for OX063 solutions at 700 MHz

Temperature	OX063 concentration					
	0.2 mM, no salt	0.2 mM+ 77 mM NaCl	0.2 mM+ 154 mM NaCl	0.4 mM, no salt	0.4 mM+ 77 mM NaCl	0.4 mM + 154 mM NaCl
19 °C	7.1	4.9	5.0	13.1	8.7	8.7
37 °C	5.8	4.7	4.9	12.2	9.0	9.7

At constant radical concentration and temperature, S/N is lower at higher salt concentration, which is attributed to the lowering of Q by the salt.

The ratio of S/N at 37 °C to that at 19 °C varied from 0.81 to 1.1, with an average of 0.97. It is concluded that the S/N is insensitive to temperature over this narrow interval.

3.6 Conclusion

In summary, in the frequency range 0.4 ~ 1 GHz, $1/T_1$ and $1/T_2$ decrease as the frequency increases, which increases sensitivity to O₂. Q-normalized S/N increases as frequency increases, in an almost linear relationship. For the same frequency, relaxation rates increase as the OX063 concentration increases. Addition of NaCl to the solution to mimic *in vivo* ionic strength increases $1/T_2$ more than $1/T_1$. Adding salt to the radical solution decreases S/N at 700 MHz because salt lowers the resonator Q.

Consequently, selection of an optimum frequency for *in vivo* imaging depends on the desired depth of penetration for a particular physiological study [155]. Construction of a practical preclinical imager will also depend on availability of key spectrometer components.

CHAPTER 4 : L-BAND RAPID-SCAN EPR OF IRRADIATED SOLIDS

The radicals in six γ -irradiated solids: malonic acid, glycylglycine, 2,6 di-*t*-butyl 4-methyl phenol, L-alanine, dimethyl malonic acid, and 2-amino isobutyric acid, were studied by rapid scan EPR at L-band (1.04 GHz) using a customized Bruker Eleksys spectrometer and a locally-designed dielectric resonator. Sinusoidal scans with widths up to 182 G were generated with the recently described coil driver and Litz wire coils [126]. Power saturation curves show that the rapid scan signals saturated at higher powers than conventional CW signals [9]. The rapid scan data are deconvolved and background subtracted to obtain absorption spectra [8]. For the same data acquisition time, the S/N for the rapid scans is significantly higher than for conventional CW spectra [9] [156]. Information in this chapter was published in [157].

4.1 Introduction

Radiation-induced defects in organic solids have been studied extensively by CW EPR [158], and by pulsed EPR [159] [160] [161]. Rapid scan EPR has provided improved signal-to-noise (S/N) for many types of samples, including defects in solids [9] and spin-trapped radicals [162]. This study demonstrated that the rapid scan EPR technique developed in our laboratory [3] provides improved S/N at L-band for the radicals in six γ -irradiated organic solids with spectra ranging from two to seven lines and sweep widths of 72 to 182 G.

Especially in the field of radiation dosimetry, reliable recording of signals due to very low levels of radiation is desired. The improved S/N achieved with rapid scan EPR for very weak EPR signals suggests that rapid scan EPR may be useful in dosimetry.

4.2 Materials

4.2.1 Sample

The samples are from the same irradiation batches that were used in the papers by Harbridge and coworkers [159] [160] [161]. Samples of glycylglycine, 2,6 di-t-butyl 4-methyl phenol, dimethyl malonic acid, and 2-amino isobutyric acid are polycrystalline solids; the malonic acid sample consisted of several crystals; and the L-alanine sample is a single crystal. The samples were irradiated in 1995 and 1998, and the radiation doses were in the range of 50 to 100 kGy. Samples were transferred to 4 mm o.d. quartz sample tubes and studied in air at room temperature. The heights of the solids in the tubes were 5 to 33 mm. Radiation doses, mass of samples, and spins in the samples are summarized in Table 4.1. Samples were shorter than the active volume of the resonator.

Table 4.1 Radiation Doses and Spin Concentrations

Sample	Mass (mg)	Dose (kGy)*	Spins	Spin density (spins/g)
Glycylglycine	61.3	57	4.4×10^{17}	7.2×10^{18}
L-alanine	3.2	115	8.8×10^{16}	2.7×10^{19}
2-amino isobutyric acid	72.5	98	3.9×10^{17}	5.4×10^{18}
2,6 di-t-butyl, 4-methyl phenol	23.3	98	1.1×10^{17}	4.7×10^{18}
Malonic acid	72.3	115	1.2×10^{16}	1.6×10^{17}
Dimethyl malonic acid	60.3	57	2.8×10^{16}	4.6×10^{17}

* ^{60}Co γ -irradiation at ambient temperature

4.2.2 Instrument

X-band CW spectra were obtained using a Bruker EMX with ER4122SHQE resonator. X-band rapid scan spectra were obtained using a Bruker E500T prototype rapid scan spectrometer and an ER4118X-MD5 resonator.

L-band CW and rapid scan spectra were recorded on a customized Bruker E540 L-band (~1.039 GHz) spectrometer with many locally-designed and constructed components. The cylindrical dielectric resonator was constructed from a ceramic and the rapid scan coils were constructed with Litz wire (Figure D1 in Appendix D). The magnet is a water-cooled four-coil air-core system (Figure D2 in Appendix D). The bridge is similar to the 250 MHz bridge described in [163]. The sinusoidal rapid scans of the magnetic field were created by a coil current driver of the type described in [126]. Sinusoidal rapid scans had sweep widths up to 180 G wide.

4.3 Methods

4.3.1 Resonator Q, Signal and Resonator Bandwidth

The quality factor Q of resonator with sample loaded was measured on an HP network analyzer. The frequency of dip, 3 dB to the left and right of the dip from the baseline are recorded as f_0 , f_1 and f_2 correspondingly. The Q can be calculated as

$$Q = \frac{f_0}{f_2 - f_1} \quad (4.1)$$

To minimize broadening of the rapid-scan signal, the signal bandwidth should be less than the available resonator bandwidth, Eq. (4.1).

$$BW_{sig} < BW_{res} = \frac{\nu}{2Q} \quad (4.2)$$

This equation for BW_{res} includes a factor of $1/2$ because we use only half of the resonator bandwidth for rapid scan in each direction.

The signal bandwidths were estimated using Eq. (4.3-4)

$$scan\ rate = \pi \times w \times f \quad (4.3)$$

$$BW_{sig} = \frac{N \times scan\ rate}{\sqrt{3} \pi \times CW_{pp}} \quad (4.4)$$

where w is the sweep width in gauss, f is the scan frequency, and N is set to 5, CW_{pp} is the peak to peak linewidth of CW signal.

The calculation results are summarized in Table 4.2.

Table 4.2 Resonator Q values, available resonator bandwidths and signal bandwidths for each sample.

Sample	Q	BW _{res} (MHz)	BW _{sig} (MHz)
Malonic acid	546	0.95	0.77
Glycylglycine	624	0.83	0.68
2,6 di-t-butyl 4-methyl phenol	618	0.84	0.76
L-Alanine	618	0.84	0.64
Dimethyl malonic acid	484	1.07	0.41
2-amino isobutyric acid	617	0.84	0.48

Signal is defined by the peak amplitude of the lines, while noise is the standard deviation of baseline region (about 8~10 G wide).

4.3.2 CW EPR

The modulation amplitudes selected for the six samples were about 10% of ΔB_{pp} . The microwave powers were selected to be in the regime where there is no more than ~7% deviation of detected signal amplitude from that predicted by extrapolation from the linear region of the power saturation curves. Data were acquired with the Xep software

and a Bruker Signal Processing Unit (SPU). The filter parameter was set to 1. The modulation frequency was 100 kHz.

4.3.3 Rapid-scan EPR

Rapid-scan signals were recorded with a Bruker SpecJet-II digitizer. The time base and number of points are selected so that each individual scan included at least three complete sinusoidal cycles, which is required by the deconvolution program. The number of averages was selected so that the CW and rapid scan would have the same data acquisition time, for the purpose of comparison. The scan frequencies were selected so that the signal bandwidth would be less than the available resonator bandwidth, to minimize the broadening of the signal.

The slow-scan absorption spectra are calculated from the rapid-scan signals by Fourier deconvolution [8]. In the deconvolution procedure the signals from up-field and down-field scans were combined [164]. After phase correction the Hilbert transform of the dispersion signal is combined with the absorption signal, and the background signals from the sinusoidal scans are removed [165]. The deconvolution of the rapid scan data produces the absorption spectra. Numerical differentiation is used to calculate the first derivative spectra from the rapid scan absorption spectra, to compare with conventional CW EPR line shapes.

Filtering is done with the MATLAB 'mygaussian' routine and the values of the adjustable parameters, sH and FWHM, are selected to give less than 2% broadening. sH is the filter used for both CW and rapid scan, and a value of 0.3-0.5 G is typically used. FWHM is the post processing filter applied on the rapid scan data. It is the estimated full

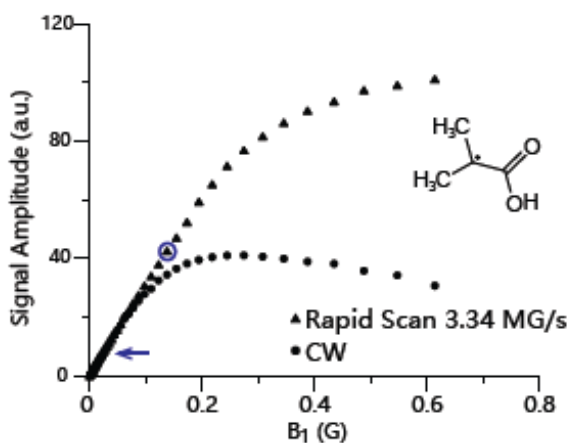
width at the half height of the narrowest line in the spectrum and is used for spectrum filtering with a Gaussian profile having 5% of FWHM. A value of 0~0.1 G is typically used.

4.4 Results

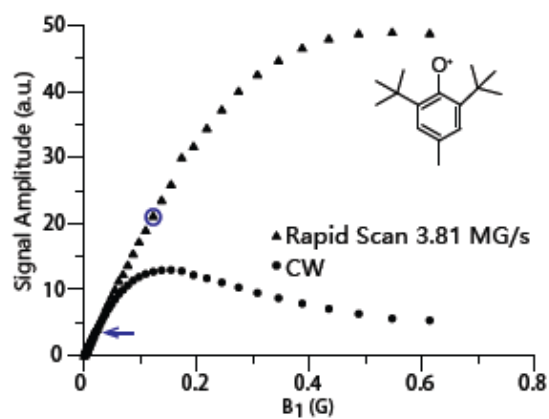
4.4.1 Power Saturation Curves

To determine the appropriate microwave power levels for recording spectra, power saturation curves are measured for each of the samples with both CW and rapid scan (Figure 4.1). For CW the peak-to-peak amplitudes of the first derivative spectra were measured. For the rapid scans the signal amplitudes after deconvolution are measured. To compare rapid-scan and CW saturation, the relative signal amplitudes are normalized to be the same at low B_1 , in the linear response region.

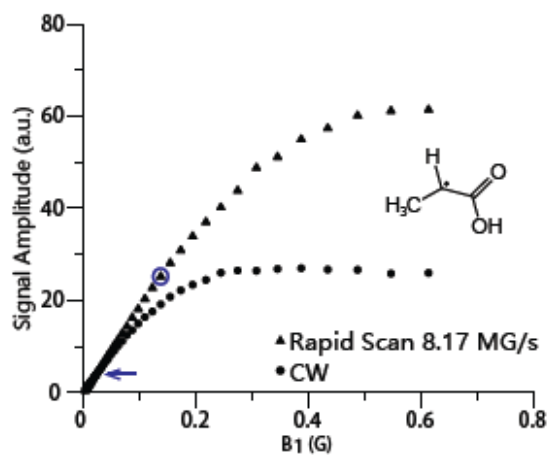
Post-acquisition digital filtering was applied to smooth noise, with the criterion that the line width will not be increased by more than 2% by the filtering.



(a) 2-amino isobutyric acid



(b) 2,6 di-t-butyl 4-methyl phenol



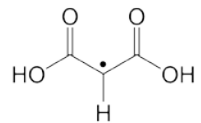
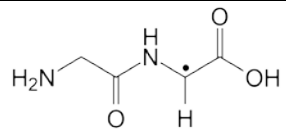
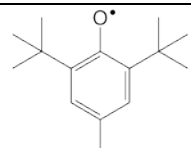
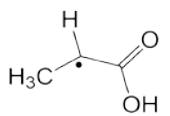
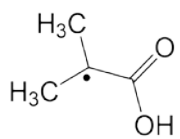
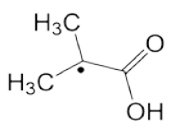
(c) L-Alanine

Figure 4.1 L-band Power Saturation Curves for 3 of the samples

The points that correspond to the acquisition conditions for the rapid-scan and CW spectra in Figure 4.1 are circled or marked with an arrow, respectively.

The results for all samples are summarized in Table 4.3.

Table 4.3 Summary of power saturation curves

#	Compound	State	Radical Structure	Power Saturation Curve Linear region B ₁ (G)	
				L-band CW	L-band Rapid Scan
1	Malonic Acid	11.5 Mrad Crystals (white)		0.012	0.087
2	Glycylglycine	5.7 Mrad polycrystalline (white)		0.019	0.097
3	2,6 di-t-butyl 4-methyl phenol	9.8 Mrad polycrystalline (blue)		0.019	0.123
4	L-Alanine	11.5 Mrad single crystal (yellow)		0.014	0.137
5	Dimethyl Malonic Acid	5.7 Mrad polycrystalline (white)		0.019	0.097
6	2-amino isobutyric acid	9.8 Mrad polycrystalline (white)		0.031	0.137

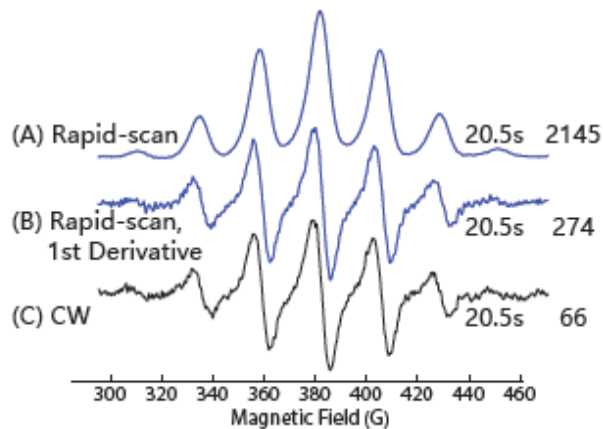
In summary, for each of the samples the linear region of the power saturation curve extends to higher B_1 for the rapid scan than for CW. The relative signal amplitude was substantially higher at the higher B_1 that can be used in rapid scan than for the same degree of power saturation for CW spectra. The ability to use higher B_1 without saturating the signal is a major advantage in improving S/N by rapid scan [3].

4.4.2 EPR Spectra

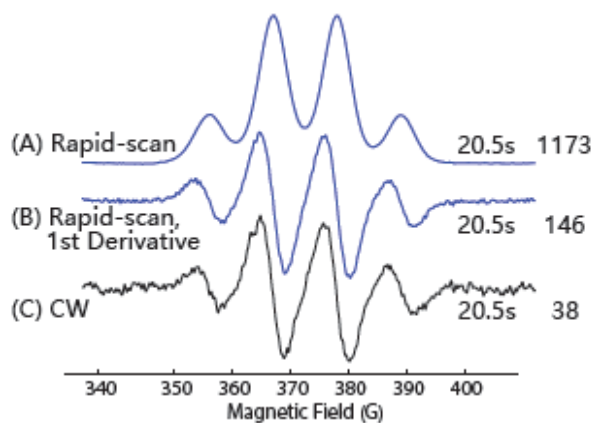
The parameters used during the measurement of each sample are listed in Table 4.4. The L-band spectra of three of the samples are shown in Figure 4.2.

Table 4.4 Parameters for CW and rapid scans

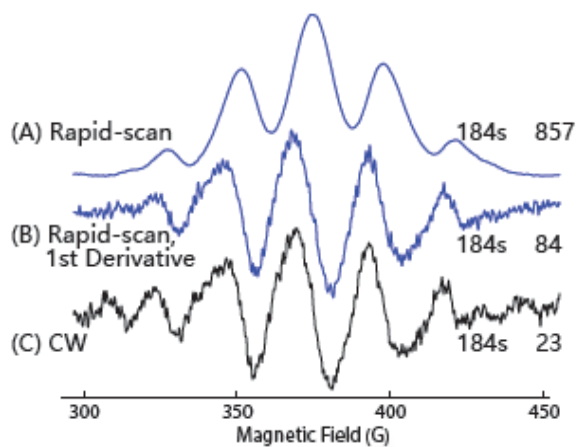
sample	ΔB_{pp} (mT)	CW	Rapid Scan			
		B_1 (μ T)	B_1 (μ T)	Sweep width (mT)	Scan frequency (kHz)	Scan rate (T/s)
malonic acid	0.47 (1 st peak)	1.2	8.7	7.2	17.35	392
glycylglycine	1.08 (1 st peak)	1.9	9.7	8.8	28.86	793
2,6 di-t-butyl 4-methyl phenol	0.46 (2 nd peak)	1.9	12.3	8.9	13.69	381
L-alanine	1.18 (central peak)	1.4	13.7	17.0	15.26	817
dimethyl malonic acid	0.70 (central peak)	1.9	9.7	17.0	5.83	312
2-amino isobutyric acid	0.64 (central peak)	3.1	13.7	18.2	5.85	334



(a) 2-amino isobutyric acid



(b) 2,6 di-t-butyl 4-methyl phenol



(c) L-Alanine

Figure 4.2 L-band spectra for 3 of the samples
 Data acquisition time and S/N are listed on each curve.

4.4.3 Line shapes

The line shapes obtained from rapid scan and CW EPR spectra are in good agreement with prior reports [159] [160] [161]. The hyperfine splittings in the spectra are consistent with the dominant hyperfine couplings reported in the literature [166] [167].

4.4.4 Signal-to-Noise Ratio (S/N)

S/N is the peak-to-peak signal amplitude (for CW) or absorption signal amplitude (for rapid scan) divided by RMS noise in a baseline region. The data acquisition times were selected to give workable S/N for the CW spectra. Spectra for the six irradiated organic solid samples showed significantly higher S/N for rapid scans than for CW obtained in the same amount of time (Table 4.5).

Table 4.5 Signal-to-Noise Ratios of Rapid Scan and CW Spectra

Sample Irradiated	Method	Data acquisition time (s)	S/N	S/N relative to CW
malonic acid	Rapid scan	164	300	23
	CW	164	13	
glycylglycine	Rapid scan	20.5	2500	25
	CW	20.5	105	
2,6 di-<i>t</i>-butyl 4-methyl phenol	Rapid scan	20.5	1173	31
	CW	20.5	38	
L-alanine	Rapid scan	184	857	37
	CW	184	23	
dimethyl malonic acid	Rapid scan	245	1200	25
	CW	245	48	
2-amino isobutyric acid	Rapid scan	20.5	2145	33
	CW	20.5	66	

The results show that, for the same data acquisition time, the S/N for the absorption spectra obtained in rapid scans are 23~37 times higher than for first-derivative spectra obtained by conventional CW EPR.

4.5 Conclusion

In summary, this study is a first demonstration of rapid scan EPR on defect centers in γ -irradiated organic solids at L-band. The results showed that the linear regions of the power saturation curves extend to higher B_1 for rapid scan than for CW.

Absorption spectra of irradiated organic solids obtained by rapid scan have substantially higher S/N at L-band than standard CW spectra when data are acquired for the same total time (Table 4.5). The improvements in S/N are large enough to open new vistas in measuring radiation defects in organic materials.

CHAPTER 5 : VHF RAPID-SCAN EPR SPECTRA AND IMAGING

Understanding tumor physiology is crucial to the development of improved cancer therapies. Small molecule probes with unpaired electrons are being developed to monitor properties of living systems. Because the large water content of living systems can greatly reduce radiofrequency penetration depth, these experiments are performed in relatively low magnetic fields. This makes the signal weaker than would be observed at higher magnetic fields. Our research group is developing an improved detection method, called rapid-scan EPR, where the magnetic field is scanned through the signal much faster than in conventional spectroscopy [3] (see Chapter 1, Section 1.2.3 for more details about the rapid-scan principles and technique). The goal is to design an instrument that can be used in clinical studies of small animal models of human disease.

5.1 Introduction

New probe molecules have been developed by our collaborators, Dr. Halpern et al. at the University of Chicago, Dr Rosen at University of Maryland, and Dr. Kao at University of Maryland. Probes are designed to measure biological properties in tumors, including local oxygen pressure, the acidity, and the oxidation/reduction status, which may vary with location in a tumor. To monitor these properties and the effects of therapeutic techniques, our group is developing an EPRI method to map the spatial variation of the spectral properties of the probe. This method is made possible by

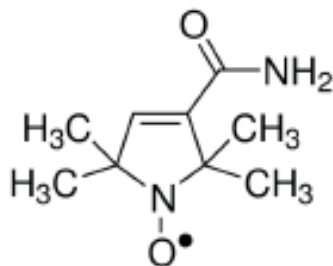
encoding spatial information of samples with spatial variations in magnetic field called gradients. Rapid-scan EPR techniques were applied to increase S/N. Different parameters were tested, including gradient strength, gradient step size, and rapid-scan frequencies. Among them, gradient strength will affect how well the features are separated along the spatial axis, and gradient step size affects the texture of the image. It is important to observe how these parameters impact the quality of the image and find the best experimental conditions.

Albeit being fast and high S/N, rapid-scan also produces a large background. The rapidly-changing magnetic field induces a background signal that may be larger than the EPR signal and increases with increasing scan width. The magnetic field-dependent component of the background is attributed to eddy currents induced in the resonator. A background correction method based on reversal of B_0 is being developed in our lab [168], and has been applied to rapid-scan experiments.

5.2 Materials

5.2.1 Sample

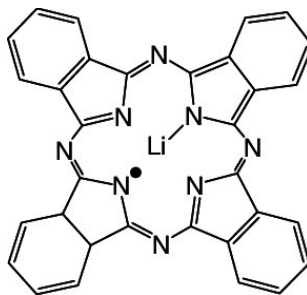
Many imaging experiments are done using nitroxide CTPO (3-Carbamoyl-2,2,5,5-tetramethyl-3-pyrrolin-1-oxyl) because it has a simple spectrum, is commercially available, and is structurally related to mHCTPO that is used for mouse studies in the Halpern lab at the University of Chicago [169]. The structure of CTPO is shown below: it has a five-member ring, and the spin density is predominantly on the NO portion of the molecule.



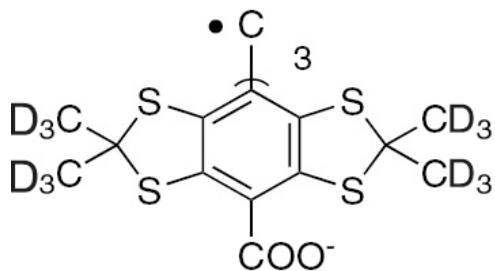
The CTPO solid was purchased from Sigma-Aldrich. The solid was dissolved in water to form solution with concentrations of 0.1 mM, 0.2 mM, and 0.5 mM. Sample solutions are de-oxygenated by bubbling with N₂ before the experiments start. Because ¹⁴N has nuclear spin $I = 1$, a typical EPR absorption spectrum of CTPO has 3 lines. The little shoulders caused by ¹³C hyperfine are also present flanking the main nitroxide lines (refer to Figure 6.1 in Section 6.1). The three ¹⁴N nitroxide hyperfine lines have an asymmetric splitting pattern at 250 MHz due to Breit-Rabi effects [170]. The splitting between low-field and center-field, and center-field to high-field lines was 14.8 and 17.6 G, respectively, for a total spacing of 32.4 G [11]. The splitting of the ¹⁵N ($I = 0.5$) low-field to high-field line is 22.6 G [11]. The linewidths at half height of the absorption rapid scan signal of 0.1 mM, 0.2 mM, and 0.5 mM CTPO are 1.25 G, 1.25 G, or 1.38 G respectively when no gradient is applied.

Sealed samples of deoxygenated 0.1 mM OX063 solution was also used, which has a single narrow line. The structure is shown in Section 3.2.1.

LiPc (lithium phthalocyanine) was used, which is a black polycrystalline solid with strong, narrow one-line spectrum. It is used as a very sensitive O₂ probe in *in vivo* oximetry [171]. The structure is shown below:



Sealed 0.2 mM trityl-CD3 water solution was also used, which has a single narrow line. Structure is shown below:



5.2.2 Instrument

The EPR imaging experiments were performed on a locally designed and constructed spectrometer [122] with a cross-loop resonator at VHF frequency.

The spectrometer uses a 4-coil magnet to produce the main static magnetic field and the Z-gradient coil is one pair, which produce magnetic field gradients (Figure D9 in Appendix D). B_0 is along the Z direction and gradients for images with single spatial dimension have a linear variation of B_0 along the Z direction [172] [173]. A home-built 16 mm cross-loop resonator (Figure D7 in Appendix D) for rapid scan is placed at the center of the coils. A home-built 25 mm cross-loop resonator is also used for imaging (Figure D10 in Appendix D). A home-built coil driver is used to generate either

sinusoidal or linear scans depending on what kind of scan is needed (Figure D8 in Appendix D). The block diagram of the EPR imaging system is shown in Figure 5.1.

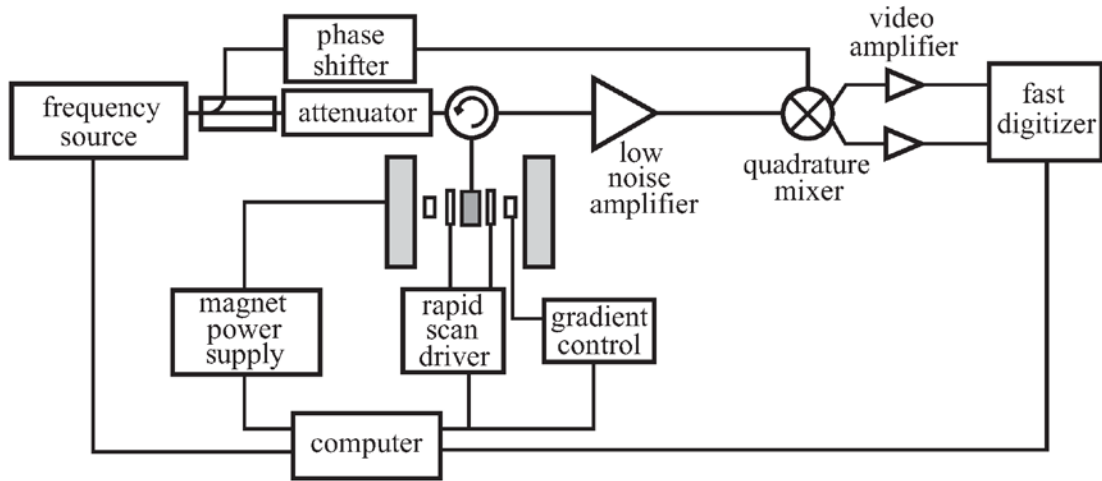


Figure 5.1 Block diagram of Rapid-scan imaging system, from [6]

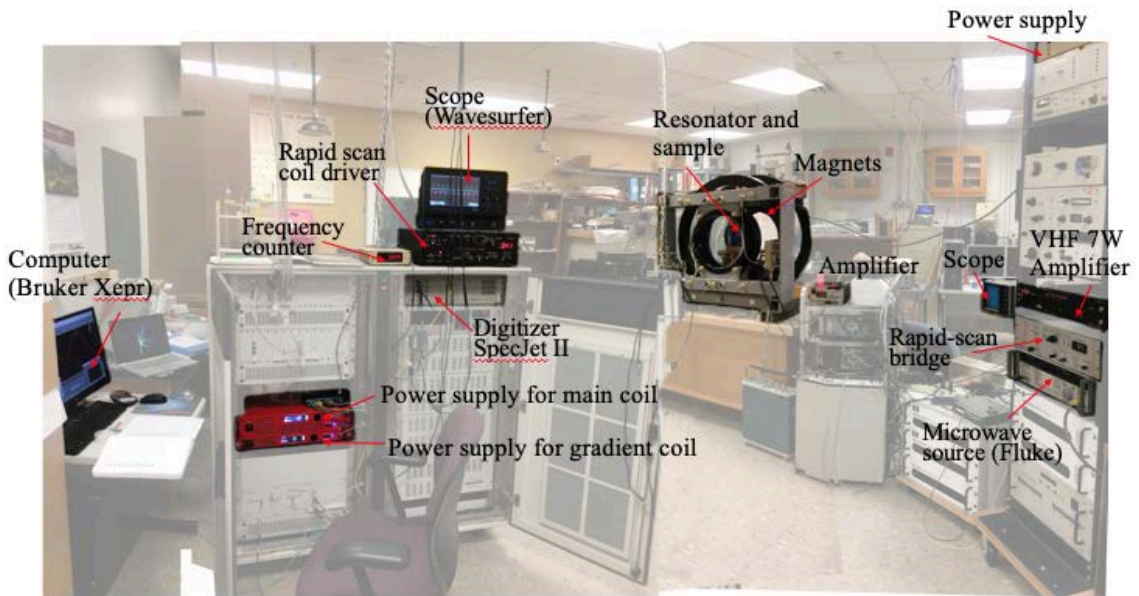


Figure 5.2 A functional EPRI system actively collecting data

The whole scene of the EPRI work station is captured in a photo (Figure 5.2). The equipment in use is annotated with arrows and names while the laboratory environment is in transparent background.

5.3 Method

5.3.1 Rapid-scan EPRI

The details of the rapid-scan technique are covered in Chapter 1, section 1.2.3. The phantom used is a 16 mm o.d. quartz tube, and has a divider of 1 or 2 mm thickness at the bottom part, which separates the tube into two compartments. In sinusoidal rapid-scan EPR, a fast, sinusoidal scan encompasses the whole spectrum by single sweeps. Data were deconvolved with algorithms developed previously in our lab [8]. A Gaussian filter equal to $0.05 \times$ full linewidth at half height is applied.

In an imaging experiment, EPR spectra are taken under a series of magnetic field gradients (called projections). The projections are first deconvolved individually then the image is reconstructed with an algorithm developed by Dr. Tseitlin et al. in our lab [11]. No additional filter was applied to the images. S/N, linewidths at half height (LWHH), and resolution are calculated. Resolution is defined as the ratio of valley/peak in the spatial slice that cut through the peak position. The valley is at the position of the divider. Acquisition conditions, including maximum gradient and gradient step size are studied and optimized.

5.3.2 Field-reversal Background Subtraction

The concept of field-reversal background subtraction method is illustrated in Figure 5.3. A regular EPR scan is first performed, denoted as Scan 1. Then the external field B_0 is reversed and the data acquisition trigger is offset by one half-cycle of the scan field relative to the settings used in Scan 1, and the acquired spectra is denoted Scan 2. Since the EPR signals in the Scan 1 and 2 are inverted but their backgrounds are same,

when Scan 2 is subtracted from Scan 1 (generating Scan3), the backgrounds cancel, and the signals add. The subtracted spectrum, Scan 3, has almost flat baseline (Figure 5.3). In an imaging experiment, a third parameter, gradient, is reversed as well. This method has been tested with 0.1 mM CTPO, 0.2 mM trityl-CD₃, 0.5 mM dinitroxide and effectively removes their backgrounds [168]. This method works for some contributions to background signals, but not others.

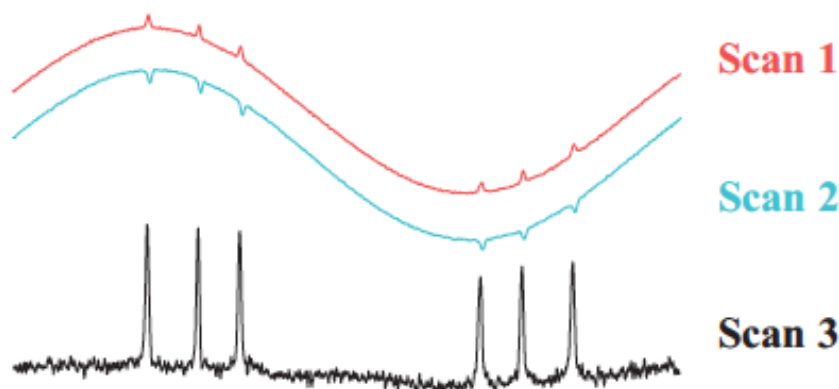


Figure 5.3 Illustration of field reversal background correction method.

Figure is similar to ones shown in Ref. [168]. One sinusoidal cycle of raw data is shown, for 0.5 mM CTPO.

5.3.3 MATLAB Program

In Dr. Tseitlin's image reconstruction program, a spectral-spatial image is reconstructed from projections with arbitrarily selected gradients, and each projection is defined as the sum of contributions at the set of locations in the object. This approach permits imaging wide spectra without the use of the very large sweep widths and gradients that would be required for spectral-spatial imaging with filtered back projection reconstruction [11].

Based on Dr. Tseitlin's image reconstruction MATLAB program, additions were made to accommodate more image analysis (code is provided in Appendix B):

(1) Codes for spectrum analysis was added, including calculating linewidth and S/N, plotting spatial and spectral slices at any locations. About 10 ~15 G length along the spectral axis and more than 1000 points are used to define noise.

(2) The zooming factor in image display is clarified. The spatial axis should have the same resolution (number of points) as the number of projections (gradients). Having more points in the spatial axis than the number of projections slows down calculation without improving resolution, but fewer points will blur the image and decrease spatial resolution.

(3) A method is proposed to remove bad projections at high gradients. Due to the instability of the instrument system, sometimes one projection turned out to be abnormal relative to others, e.g. exaggerated amplitude. If the bad projections only appear at the high gradients, data are still usable by discarding the bad projections and their counterparts at the other end of the gradient series, as long as the projections are still distributed symmetrically around the zero-gradient projection. This approach has an effect on image quality similar to reducing G_{max} . Taking out a few projections (up to 10%) does not affect the image substantially.

(4) As the MATLAB software was migrated from older version 2014 to newer version 2018, some syntax changes, and corresponding adjustments were made.

5.3.4 Use of Real and Imaginary Channels

The quadrature data have two channels that are designated I and Q. The phase can be adjusted such that one channel contains the real signal and the other is imaginary. The deconvolution program (which is used in both spectral and image reconstruction) written by Dr. Tseitlin [8] uses the signal in both the I and Q channels during the deconvolution process, but only exports data in one channel (the I channel). Revisions were made so one can choose to use information either in one channel or both channels (see Appendix A). The imaginary channel first undergoes Hilbert transformation, then its imaginary part is taken and added to the real channel to generate the final spectrum. Three types of experiments were performed with the CTPO phantom, sinusoidal single-sweep spectrum and imaging, field-stepped linear scan imaging. Each spectrum or image was analyzed twice, first with imaginary channel only, then with both channels. The results are summarized in Table 5.1.

Table 5.1 Comparison of spectra by using both I and Q channels versus only the I channel

Experiment type	CTPO concentration	Channel used	LWHH (G)	S/N	S/N increase	Resolution
Sinusoidal rapid-scan spectrum	0.5 mM	Q	1.31	509		N/A
		both	1.33	567	11%	
	0.2 mM	Q	1.27	169		
		both	1.27	190	12%	
	0.1 mM	Q	1.27	100		
		both	1.27	126	26%	
Sinusoidal single sweep imaging	0.5 mM	Q	1.19	131		0.37
		both	1.20	142	8%	0.37
	0.2 mM	Q	1.32	117		0.61
		both	1.32	132	13%	0.61
	0.1 mM	Q	1.20	60		0.47
		both	1.20	66	10%	0.47
Field-stepped linear scan imaging	0.5 mM	Q	1.13	142		0.43
		both	1.14	163	9%	0.33
	0.2 mM	Q	1.34	45		0.78
		both	1.30	53	17%	0.77
	0.1 mM	Q	1.26	29		0.54
		both	1.26	36	24%	0.54

One should only compare results within each experiment, as different experiment might have different numbers of averages. The results show that, compared to using data from only the imaginary channel, using both channels increase S/N by 5~25%, for rapid-scan spectra, sinusoidal single sweep imaging, or field-stepped linear scan imaging. The increase in S/N is more evident for weak samples. However, it does not affect line width or resolution.

5.3.5 Impact of 7 W Amplifier

The 7 W amplifier was used in the excitation pathway and is turned on in most EPR experiments. Its role was tested as well.

Table 5.2 Impact of 7W Amplifier

Attenuation	7W Amplifier	S/N	LWHH (G)
15 dB	OFF	69	0.57
35 dB	ON	68	0.58

Both experiments used 10240 averages. Sample is 0.1 mM OX063. Rapid scan frequency is 5 kHz.

The results show that, using high power or lower power plus amplifier produce similar results.

5.3.6 Measurement of Gradient Coil Constant

Since the magnets are all electromagnets, whose field strength is controlled by currents, it is important to know the coil constant (G/A) to allow accurate control of the magnetic field. Two methods are described for the measurement, both used a standard sample holder which contains two point samples of LiPc separated by 1 cm (Figure 5.4).

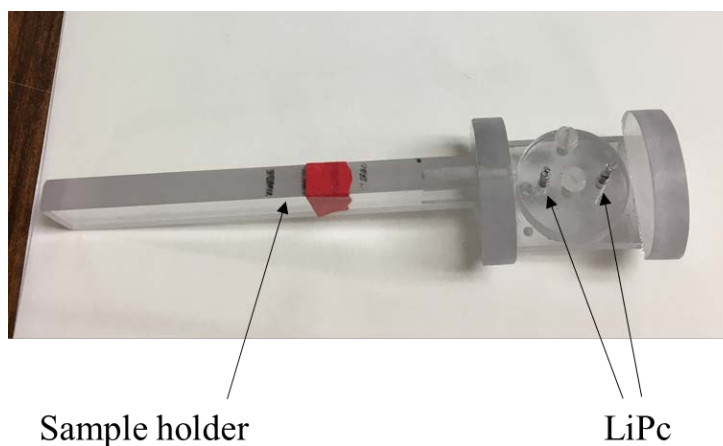


Figure 5.4 LiPc point sample

An estimated value for the coil constant is first used, for example 1 G/A (which usually can be estimated from coil size and material, or from manufacturer), then one applies gradient to calibrate this value.

1. Method 1: use high gradient spectrum

As gradient increases, the signal splits more; the splitting between two narrow-line LiPc samples at a series of gradients is measured below:

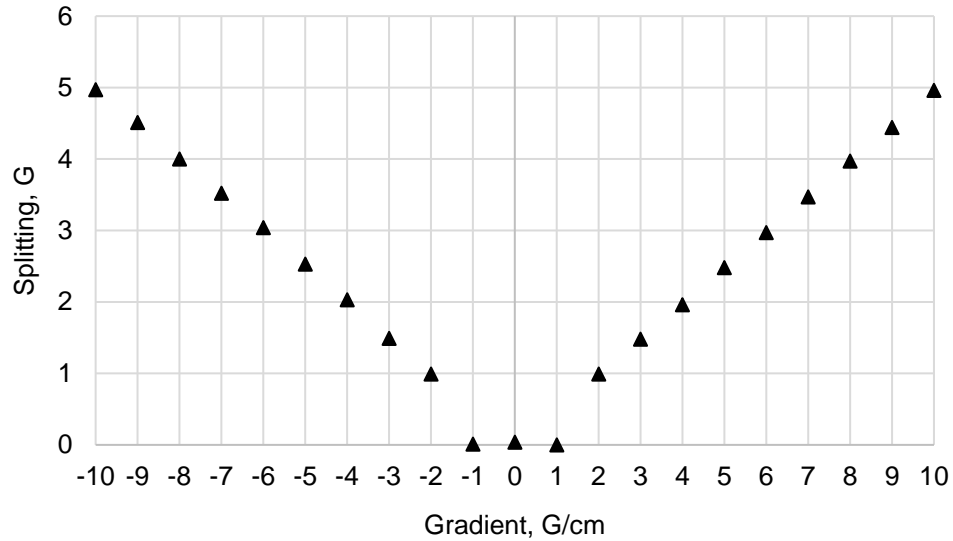


Figure 5.5 Signal splitting under various gradients for two LiPc samples

Parameters were: gradient strength is 10 G/cm with 1 G/cm step, 21 gradients, 100 ns time base, 8192 points; 4096 averages for each gradient, on-board average is 1024. Rapid-scan frequency is 8 kHz, sweep width is 40 G.

Fitting the negative gradient region, i.e. -10 ~ 0 G/cm, we got:

$$y = -0.499x + 0.018 \quad (5.1)$$

Fitting the positive gradient region, i.e., 0 ~ G/cm, we got:

$$y = 0.496x + 0.008 \quad (5.2)$$

Because the distance between the two samples is 1 cm, for 10 G/cm gradient one expects to get 10 G splitting, but one actually gets 5 G (Figure 5.5), which means the coil constant should be reduced by $5/10 = 0.5$, or the value of the slope. Thus, the gradient coil constant is 0.50 G/A.

2. Method 2: use image

One can also run an EPRI experiment and measure the splitting between the two dots on the image.

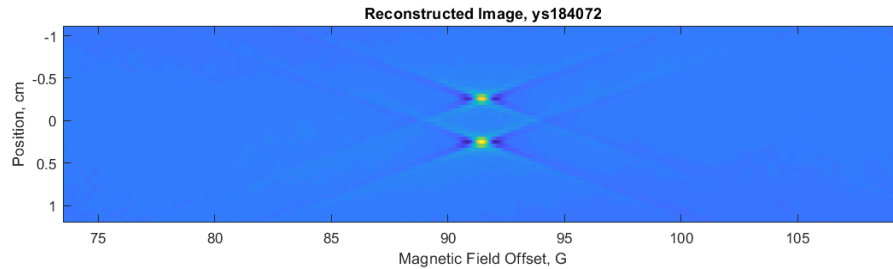


Figure 5.6 Test image with estimated coil constant, using LiPc

Parameters were: gradient strength is 10 G/cm with 0.2 G/cm step, 101 projections, 100 ns time base, 8192 points; 5120 averages for each projection, on-board average is 256. Rapid-scan frequency is 8 kHz, sweep width is 20 G.

The distance between the two dots in Figure 5.6 is 0.5 cm. The actual distance is 1 cm, so we should reduce the estimated coil constant by a factor of $1/0.5 = 2$, i.e., the actually coil constant should be 0.5 G/A. Use the adjusted value and run again, the image is shown in Figure 5.7:

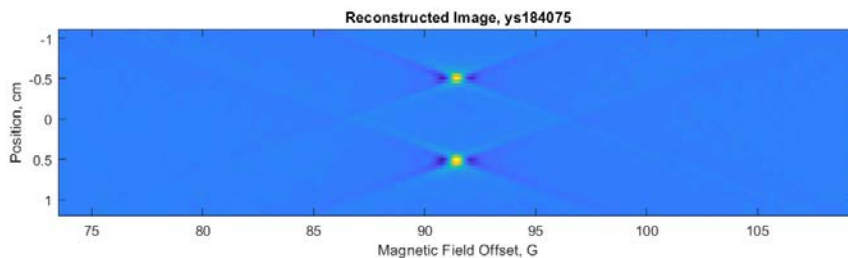


Figure 5.7 Verify coil constant with adjusted coil constant, using LiPc

Parameters were same as Figure 5.6.

The distance between the two dots in Figure 5.7 is 1 cm now, which is correct and verifies the calculation. For strong and narrow line sample, the high gradient spectrum is

clear, and the splitting can be measured accurately, so method 1 is faster. If the sample used has broader peak, one might want to run an image to get a more accurate distance since the high gradient spectrum is noisy.

5.3.7 Xepr and Python API

Before 2017, Bruker software used Xepr ‘version 2.6b.139, 2015-Oct-15 (11:38)’ (referred to as ‘old version’) on computers installed with ‘Open SUSE’ Linux distribution. Starting in 2017, a newer version of Xepr, ‘version 2.6b.167, 2017-Jul-17 (14:46)’ (referred to as ‘new version’), was installed on the Linux computer in the lab, which ran another Linux distribution, ‘Centos’ (version 7) and installed with Python 2.7. The new version includes an API (Application programming interface) that can run customized Python program, which greatly reforms/facilitates the way that people run experiments. With Xepr old version, ProDeL was the default programming language to run pulse or imaging experiments and was not very user-friendly. As Python became one of the most popular programming languages in recent years, people can write their own code and design their own experiments much more easily.

Python has an older version called Python 2 and a current version called Python 3. Dr. Ralph Weber from Bruker BioSpin highly recommended the use of Python 2 on the new Linux computers, because he was concerned that Python 3 may interfere with the Centos operating system which also uses Python. As the new developments today are all made in Python 3, and Python 2 will no longer be maintained after 2020, it is better to switch to Python 3.

The Centos Linux distribution works fine, which has a clean interface and easy to use. However, the Centos operation system crashes about once a month (which is a little too high). The whole system freezes and stops responding. Power off then cold start restores function. In contrast, the OpenSUSE Linux distribution seems more stable.

Based on previous Python scripts written by Dr. Laura Buchanan and Lukas Woodcock [128], a Python code was written to run all VHF Rapid-scan experiments, including EPR spectra, field-stepped linear scan and image, sinusoidal single-sweep image (code is provided in Appendix C(1)). Additions and improvements include:

(1) The old code was simplified and restructured. Changes include (a) adjusted the relationship between different modules to better accommodate different experiments; (b) the inputs are stored as one '.txt' file instead of multiple files; (c) the files are shown as names instead of folders for easier use; (d) it was found that the digitizer will automatically start averaging after the field is set, so pause during experiments is not needed; (e) one can choose either using field-reverse background subtraction method or not.

(2) A section was added that allows variable averages for different projections.

(3) The occasional failure of the CAEN power supply of the gradient coils is fixed; the program will set the z-gradient to zero as soon as it finishes with the high gradient spectrum (> 9 G/cm).

(4) The time usage of each section of the experiment is recorded.

5.4 Rapid-Scan Spectra

5.4.1 Resonator Q Measurement

To ensure that signal bandwidth will not exceed resonator bandwidth, the resonator Q, signal and resonator bandwidth for the 16 mm and 25 mm CLR (described in 5.2.2) were calculated using the method described in section 4.3.1 of Chapter 4. The results are summarized in Table 5.3.

Table 5.3 Summary of resonator Q, resonator and signal bandwidth

	Resonator	16mm CLR		25mm CLR
	Sample	0.1 mM CTPO	0.5 mM CTPO	0.1 mM OX063
Resonator#1 (excitation)	Q1	46	47	52
	Bandwidth BW1	2.8 MHz	2.8 MHz	2.5 MHz
Resonator#2 (sample)	Q2	94	93	60
	Bandwidth BW2	1.4 MHz	1.4 MHz	2.2 MHz
Maximum signal bandwidth		1.4 MHz	1.4 MHz	2.2 MHz
Maximum rapid-scan frequency		5.2 kHz *	5.2 kHz *	7.6 kHz** 30 kHz***

* for 70 G RS sweep width

** for 20 G RS sweep width

*** for 5 G RS sweep width

The uncertainty in Q measurement is 5%.

5.4.2 Power Saturation Curves

Before running a spectrum, power saturation curves were taken to find the highest power that can be used without saturating the signal. The power is selected to be within the linear response region.

1. Nitroxide

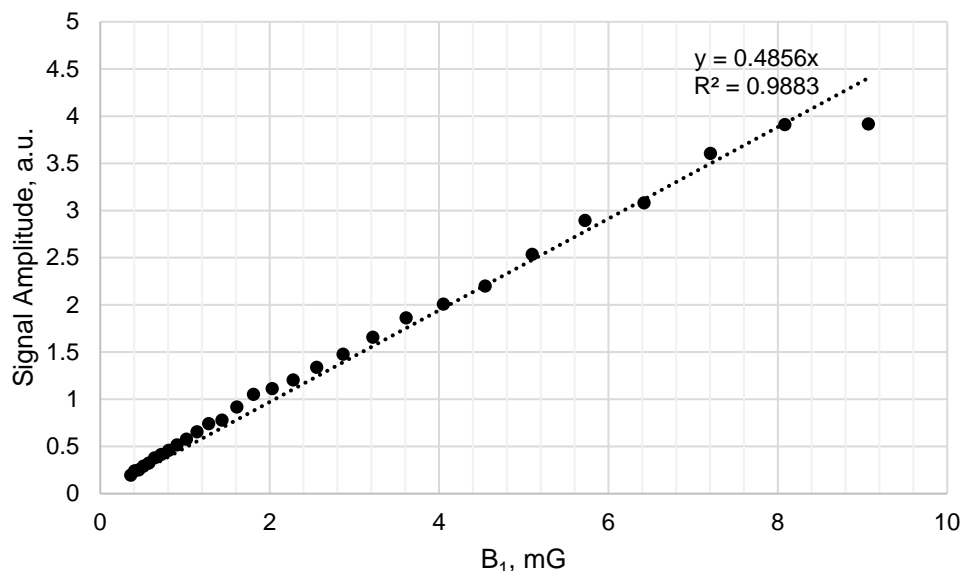


Figure 5.8 Power saturation curve of 0.1 mM CTPO at 5 kHz rapid-scan frequency

The resonator used is 16 mm CLR, resonator efficiency is $0.20 \text{ G}/\sqrt{\text{W}}$ [118].

Parameters: rapid-scan frequency is 5 kHz, RF frequency is 262 MHz, 100 ns time base, 8192 points, sweep width is 70 G, 5120 averages, 1024 on-board averages.

The rightmost point corresponds to 12 dB attenuation (equals to 2.06 mW in microwave or 9.07 mG in B_1), which is the smallest attenuation one can use while keeping the reflected power above zero dB. When using 11 dB attenuation (equals to 2.59 mW) or less (means more power), the reflected power goes above zero which means the isolation between excitation and sample resonator is very bad and one should not use such low attenuation.

The dotted line is the linear fitting for the lower power region. The linear region extends up to 15 dB attenuation (equals to 1.03 mW in microwave, or $B_1 = 6.42 \text{ mG}$).

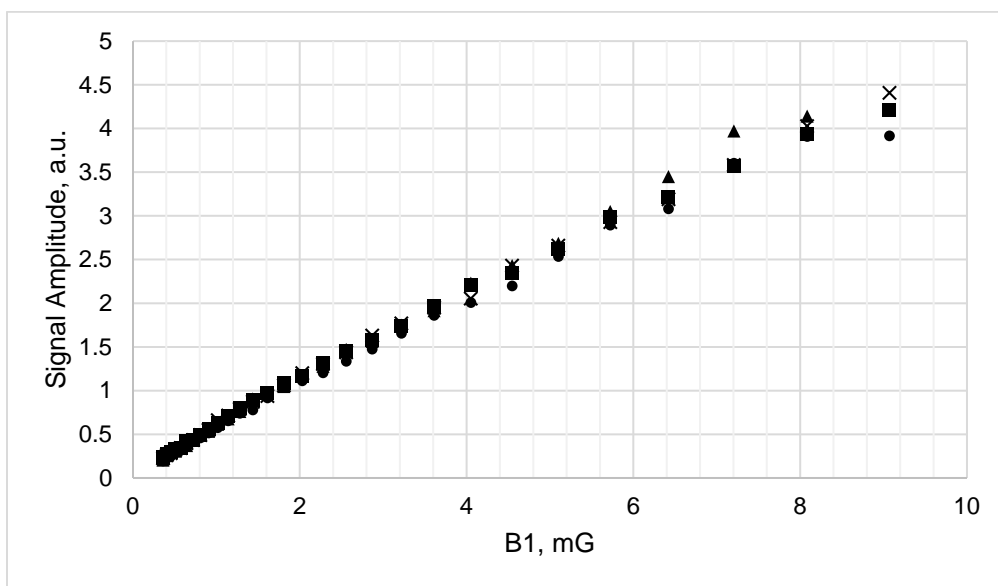


Figure 5.9 Power saturation curve of 0.1 mM CTPO, under various rapid-scan frequencies. (■) 3 kHz, (×) 4 kHz, (◆) 5 kHz, (▲) 6 kHz.

Resonator used is 16 mm CLR. Parameters: RF frequency is 262 MHz, 100 ns time base, 8192 points, sweep width is 70 G, 5120 averages, 1024 on-board averages.

The rightmost point is 12 dB attenuation (equals 2.057 mW in microwave power) for 3, 4, 5 kHz rapid-scan frequency, and 13 dB (equals 1.63 mW) for 6 kHz rapid-scan frequency. Using less attenuation (means more power) will have reflected power more than zero dB, which is not workable because isolation is bad.

CTPO shows little saturation within the power range that is used at 3~6 kHz rapid-scan frequencies. The power selected for the experiments was 15 dB attenuation (equals to 1.03 mW in microwave, or $B_1 = 6.42$ mG).

The weak dependence of saturation on scan frequency in Figure 5.9 means that the experiments are not in the rapid-scan region. T_1 and T_2 are around $0.5 \mu\text{s}$ for CTPO at 250 MHz [174], and these are shorter than for trityl.

2. Trityl OX063

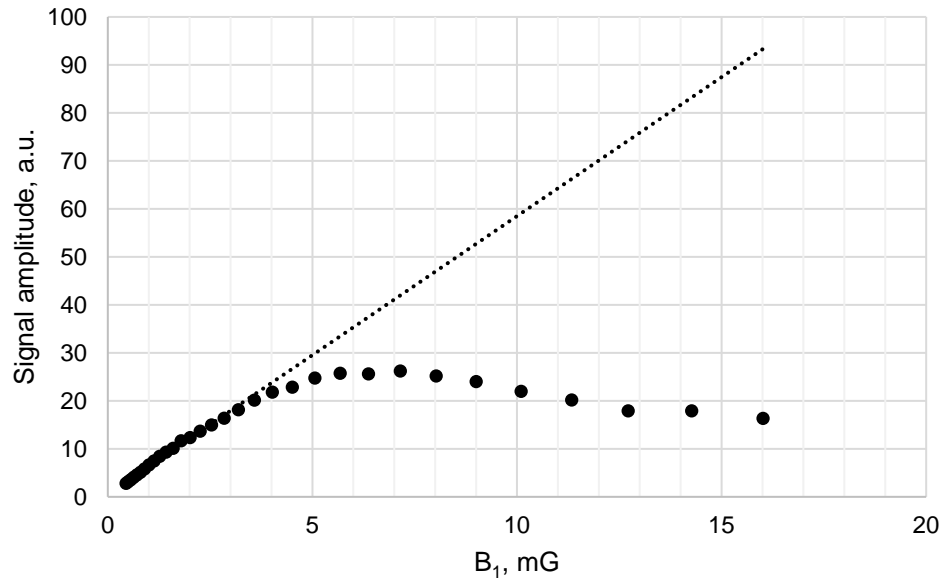


Figure 5.10 Power saturation curve of 0.1 mM OX063 at 5 kHz rapid-scan frequency. Resonator used is 25 mm cross-loop resonator, and resonator efficiency is 0.25 G/\sqrt{W} [118].

Parameters: rapid-scan frequency is 5 kHz, RF frequency is 262 MHz, 1024 on-board averages, 100 ns time base, 8192 points, sweep width is 20 G, 5120 averages.

The rightmost point corresponds to 9 dB attenuation (equals 4.10 mW in microwave power or 16.0 mG B_1), which is the smallest attenuation (highest power) one can use to keep the reflected power below zero dB. The dotted line is the linear fitting of the lower power region. The figure shows that trityl saturates quickly as power is increased and the linear region is up to 23 dB attenuation (equals 0.163 mW or $B_1 = 3.2$ mG). From Chapter 3.4, $T_1 = 12 \mu\text{s}$ and $T_2 = 6.5 \mu\text{s}$ and the relaxation rate $1/T_1 = 0.083$ MHz, $1/T_2 = 0.154$ MHz. These relaxation times are much longer than for CTPO, which

is why the power saturation curves show saturation at much lower B_1 for OX063 than for CTPO.

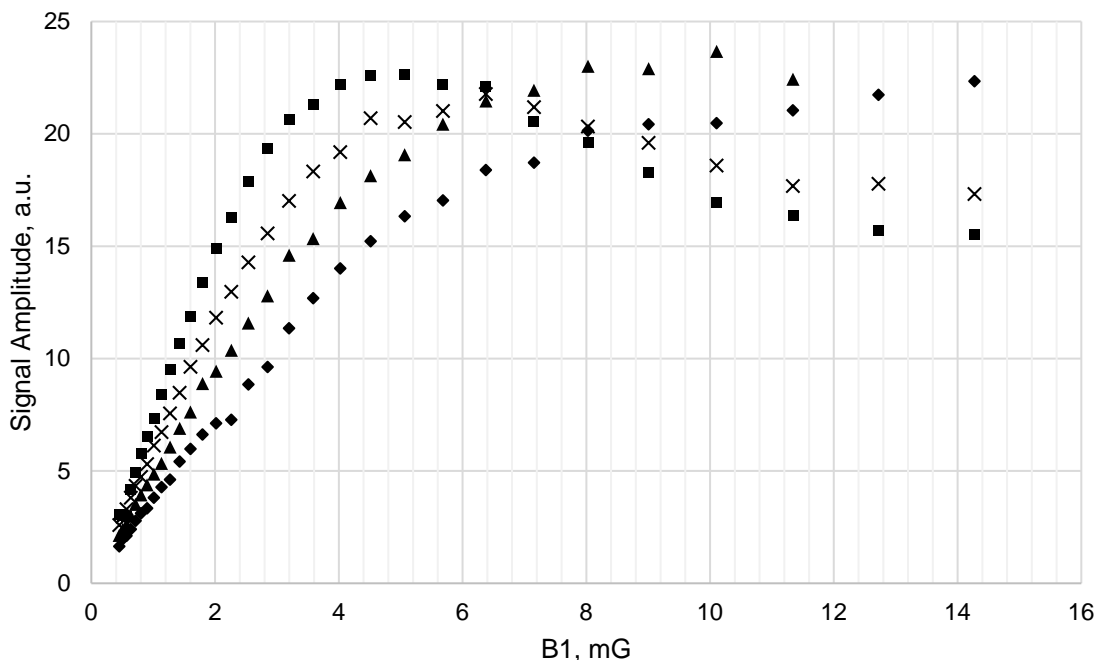


Figure 5.11 Power saturation curve of 0.1 mM OX063, for various rapid-scan frequencies (■) 3 kHz, (×) 4 kHz, (◆) 5 kHz, (▲) 8 kHz.

Resonator used is 25 mm CLR. Parameters: RF frequency is 262 MHz, 1024 on-board averages, 100 ns time base, 8192 points, sweep width is 20 G, 5120 averages.

Power saturation curves under different rapid-scan frequencies are shown in Figure 5.11. In the linear response region, high rapid-scan frequency actually decreases signal amplitude, although the maximum amplitude at high power increases. 5 kHz RS frequency was selected for most experiments carried out later and power selected was 25 dB attenuation (0.103 mW, or 2.54 mG B_1) for CTPO. From Table 5.3, signal bandwidth at this scan frequency does not exceed resonator band width, which is important to avoid signal broadening.

5.4.3 Background Study of Empty 16 mm CLR

Background signal amplitude was studied for the empty 16 mm cross-loop resonator, using both sinusoidal single sweep method and field-stepped linear scan method, which will be introduced in the next chapter. The data acquisition parameters are the same for sinusoidal and linear scans: rapid-scan frequency is 5 kHz, attenuation is 20 dB ($0.326 \text{ mW} = 4.514 \text{ G B}_1$), 4096 averages, 256 on-board averages, 100 ns time base and 8192 points.

1. Background and gradient

The amplitudes of backgrounds under different gradients (in the region of $-10 \sim +10 \text{ G/cm}$, stepping at 1 G/cm) were measured and plotted in Figure 5.12 for sinusoidal scan and Figure 5.13 for linear scan, respectively.

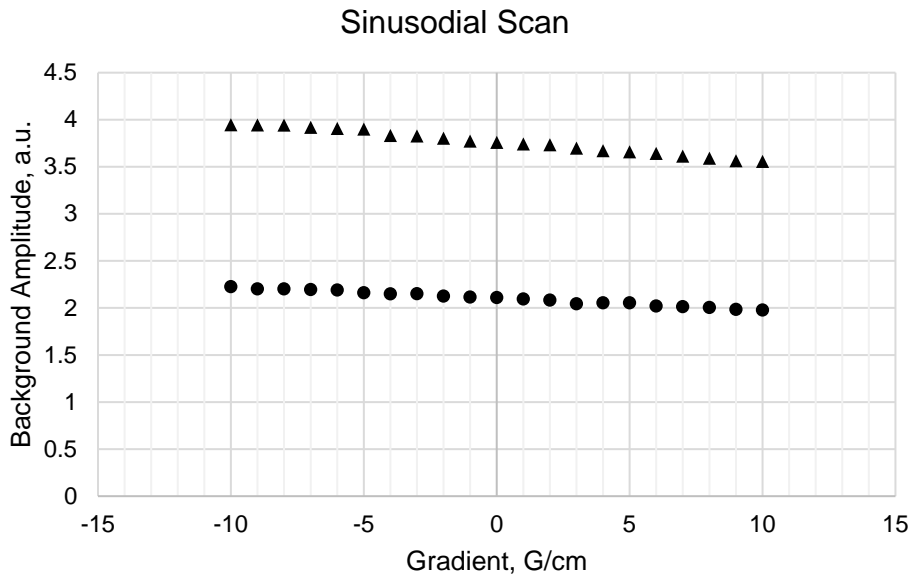


Figure 5.12 Background as a function of gradient for sinusoidal scans Real (▲) and imaginary (●) channel; sweep width is 20 G.

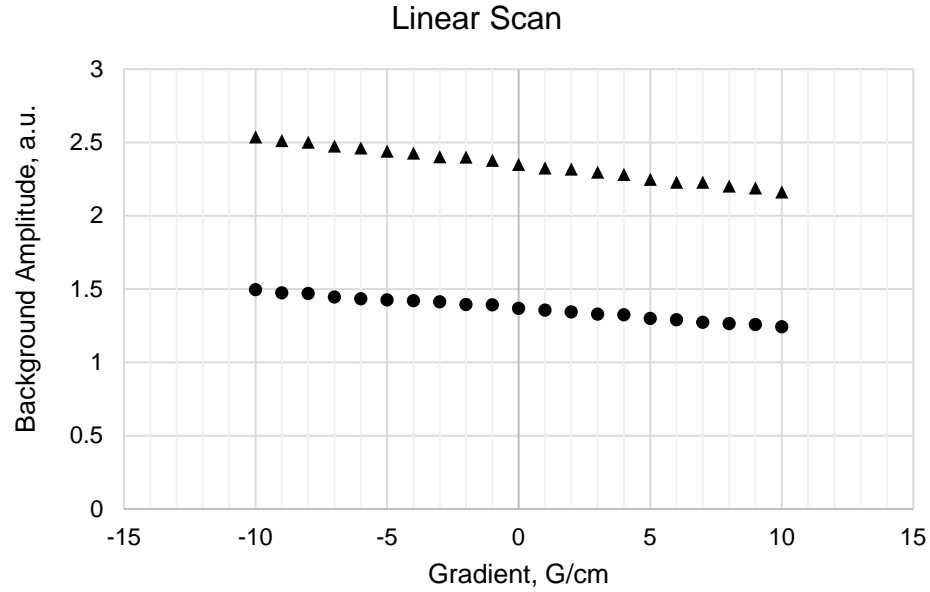


Figure 5.13 Background as a function of gradient for linear scan Real (\blacktriangle) and imaginary (\bullet) channel; sweep width is 70 G with 2 G field step.

Both sinusoidal and linear scans show the same trend: the background amplitude of the real channel is larger than that of the imaginary channel. At 250 MHz, $B_0 = 90$ G, when the gradient increases from -10 G/cm to +10 G/cm, the background amplitude is reduced by 12% for sinusoidal scan and by 16% for linear scan, in a linear fashion.

2. Background and B_0

The amplitudes of backgrounds with different center field positions (in the region of -90 ~ +90 G, stepping at 10 G) were measured and plotted in Figure 5.14 for sinusoidal scan and Figure 5.15 for linear scan, respectively.

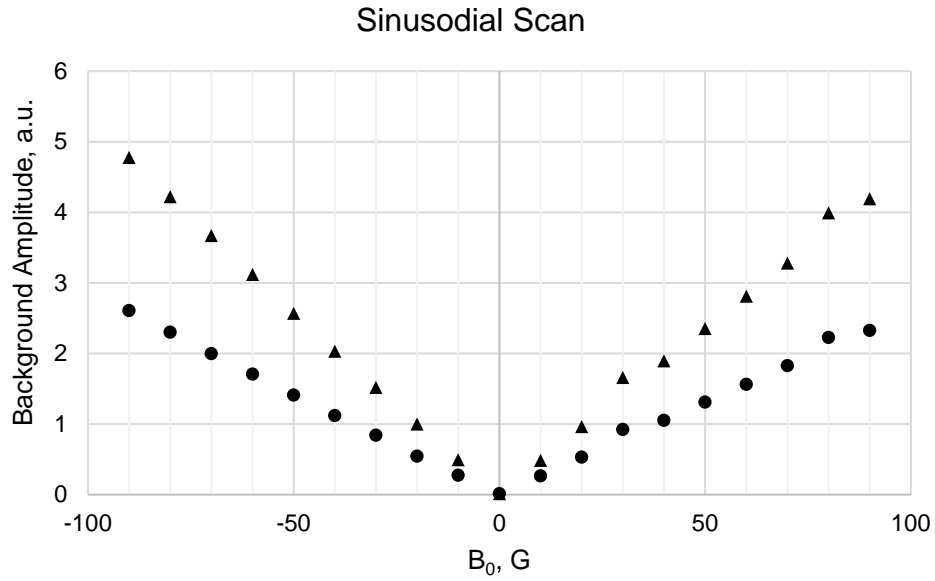


Figure 5.14 Background as a function of main magnetic field for sinusoidal scan Real (▲) and imaginary (●) channel; sweep width is 20 G.

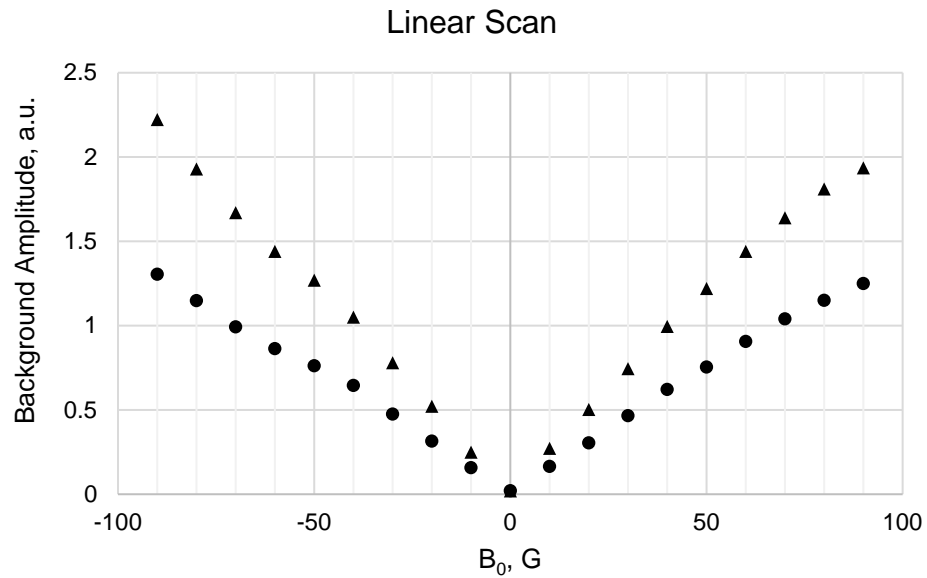


Figure 5.15 Background as a function of main magnetic field for linear scan Real (▲) and imaginary (●) channel. Sweep width is 70 G with 2 G field step

Both methods show similar trends: (1) The real channel has higher background than the imaginary channel; (2) The background is smallest at 0 G, and increases in a

linear fashion when the magnitude of the field strength increases; (3) for both methods, the background of the real channel grows faster, by 100% (i.e., background doubles as the field doubles), while background of the imaginary channel grows by 80%; (4) Comparing the two magnetic fields with same magnitude but opposite sign, their background amplitudes are close, while the negative field has slightly higher background.

The real channel contains information from the dispersion signal and the imaginary channel contains information from the absorption signal. The dispersion signal does not power saturate as readily as the absorption signal does. The background signal comes from the rapidly changing magnetic field in rapid-scan. It is proposed that the background is generated primarily from mechanical vibrations produced by the interaction between the current in the scan coils and B_0 (so-called motor effects), between the scanning field and any magnetic material, and between eddy currents and B_0 [168].

5.4.4 Rapid-scan Spectra acquired with Various Rapid-scan Frequencies

The knowledge learnt from previous sections, especially resonator Q from 5.4.1 and power saturation curves from 5.4.2, helps us select scan frequency and power. Rapid-scan EPR experiments were carried out with different scan frequencies and spectra were compared to select the scan frequency to work with. Both 16 mm and 25 mm CLR were tested.

The equations to calculate scan rate, signal bandwidth and resonator band width are equations (4.1~4.4) in Chapter 4, Section 4.3.1. The results for 16 mm CLR are summarized in Table 5.4. Sample used is 0.1 mM CTPO.

Table 5.4 EPR spectra of 0.1 mM CTPO with different rapid-scan frequencies for 16mm CLR

Scan Frequency (kHz)	Scan rate (MG/s)	Signal bandwidth (MHz)	Linewidth at half height (G)	S/N
3	0.67	0.76~0.89	1.25	65
4	0.90	1.02~1.19	1.25	58
5	1.10	1.25~1.46	1.25	58

Parameters: sweep width = 70 G, 8192 averages, the field-reversal background subtraction method is used.

Since the resonator bandwidth is 1.4 MHz (Table 5.3) and should be larger than the signal bandwidth, the rapid-scan frequency to work with for CTPO is 3~5 kHz.

The results for 25 mm CLR are summarized in Table 5.5. Sample is 0.1 mM OX063.

Table 5.5 EPR spectra of 0.1 mM OX063 with different rapid-scan frequencies for 25mm CLR

Scan Frequency (kHz)	Scan rate (MG/s)	Signal bandwidth (MHz)	Linewidth at half height (G)	S/N
2.5	0.039	0.18	0.178	90
3	0.047	0.22	0.173	96
4	0.063	0.29	0.164	105
5	0.079	0.36	0.157	116
6.2	0.097	0.45	0.155	117

Parameters: sweep width = 5 G; 20 ns time base, 1024 on-board average, 4096 averages.

The resonator bandwidth is 7.6 MHz (Table 5.3) and should be larger than the signal bandwidth to avoid signal broadening. Scan frequency too high showed line broadening, so a workable rapid-scan frequency to work with is 2.5~6.2 kHz.

5.4.5 Iron Signal Observed in Pyrex Tubes

During one of the imaging practices, a mistake of coil constant resulted in a wider rapid-scan width than was unintended. The spectrum is shown in Figure 5.16.

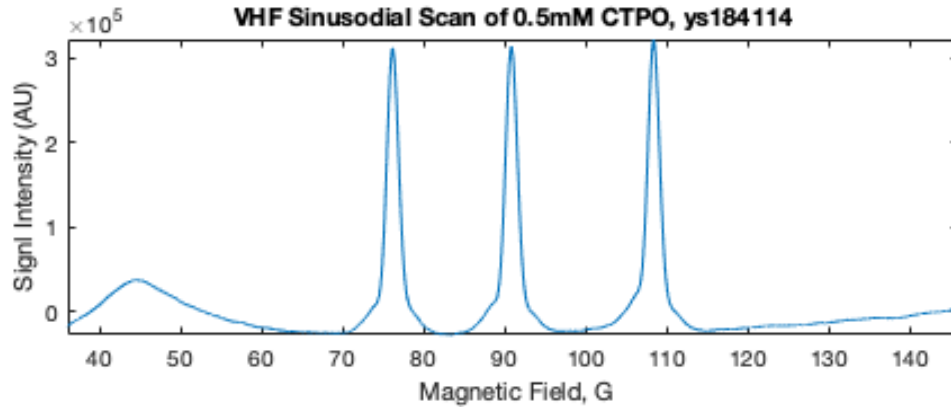


Figure 5.16 Sinusoidal EPR spectrum with wider sweep width

Sample is 0.5 mM CTPO, field-reversal background subtraction method is used.

Experimental parameters are: RS frequency 5.128 kHz, 8192 average, 100 ns time base, 8192 points. Actual sweep width is 110 G.

The 'bump' at ~45 G is caused by an iron signal in Pyrex glass, which could adversely impact imaging. In the experiments reported in this chapter sweep widths were limited to avoid including the iron signal.

5.5 Sinogram for Images

A sinogram is a useful way to diagnose potential problems in a set of projections. A sinogram is a whole set of projections, before deconvolution, stacked together, which allows one to predict the quality of the image. A sinogram can provide information regarding an image from four aspects.

5.5.1 Texture of the Sinogram

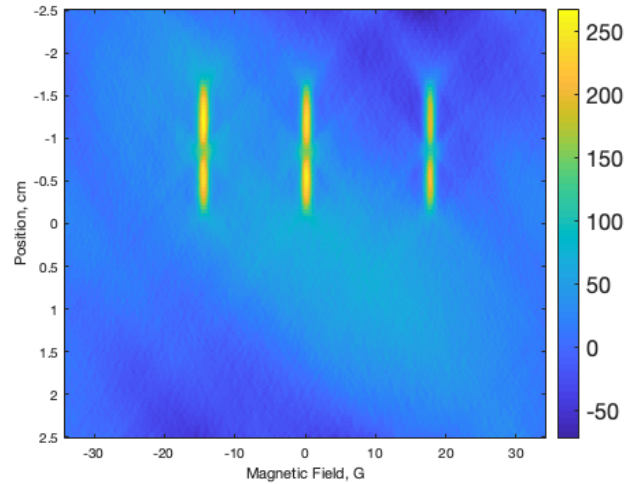
If the sinogram shows uniformed texture with clearly defined features, the deconvolved image usually has good quality too, see section 6.6~6.8 for more examples. Bad projections (e.g. abnormal amplitude or splitting) can be seen in the sinogram directly. The best and easiest way to avoid the occurrence of a bad projection is to allow system to run at least one hour before taking the data so it can warm up and stabilize.

5.5.2 Resolution of Signals from Compartments or Hyperfine Lines

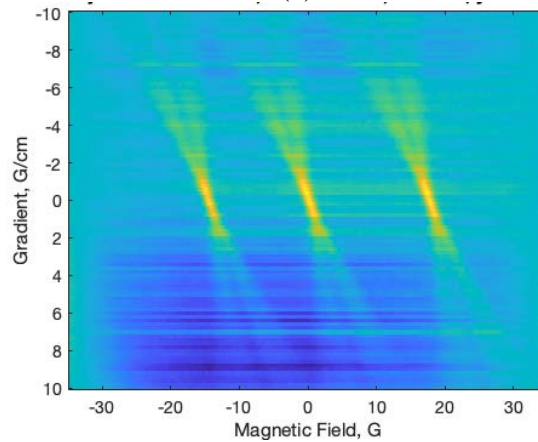
If the features on the sinogram show clear splitting, they will be better separated on the reconstructed image. See the summary in Table 6.10 in Section 6.6 ~6.8 for more examples. As radical concentration decreases, signal becomes weaker, the splitting becomes less evident; as a result, boundaries of different features smear together.

5.5.3 Resonator in Effective Space

The magnets are designed to provide a uniform magnetic field for a volume of a ball with diameter of 15 cm. Gradients also are linear within a finite range. As long as the sample and resonator are set within this region, the image is of good quality although the position may be shifted relative to the center of the magnet coils. If the sample is at the center, its reconstructed image will also be located at the middle of the spatial axis, and its sinogram will show spacings that vary linearly. Analysis of the positions of features in the sinogram can be used to adjust the sample position. An example is shown below:



(a)



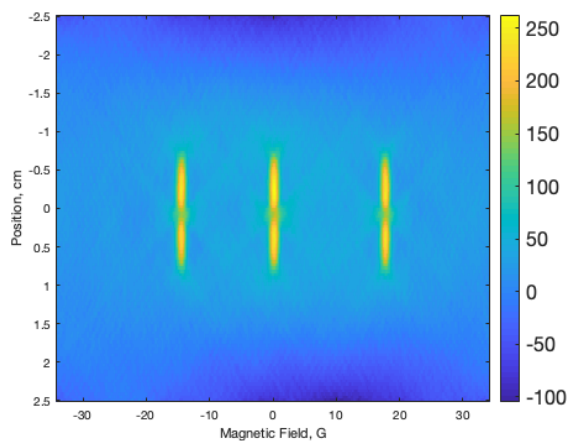
(b)

Figure 5.17 (a) Image (b) sinogram when resonator is not centered

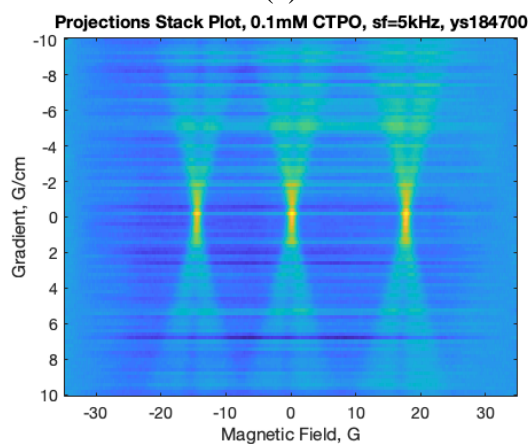
Parameters: sample is 0.1 mM CTPO, gradient strength is 10 G/cm with 0.2 G/cm step, 101 projections, 100 ns time base, 8192 points; 2048 averages for each projection, on-board average is 1024. Rapid-scan frequency is 5 kHz and sweep width is 70 G.

In Figure 5.17, the sample/resonator is centered at -0.8 cm, and the positions of resonances vary linearly in the sinogram. In the resulting image, the linewidth at half height = 1.31 G, S/N = 54, resolution = 0.58.

After adjusting the resonator position (back and forth several times):



(a)



(b)

Figure 5.18 (a) Image (b) sinogram when resonator is centered

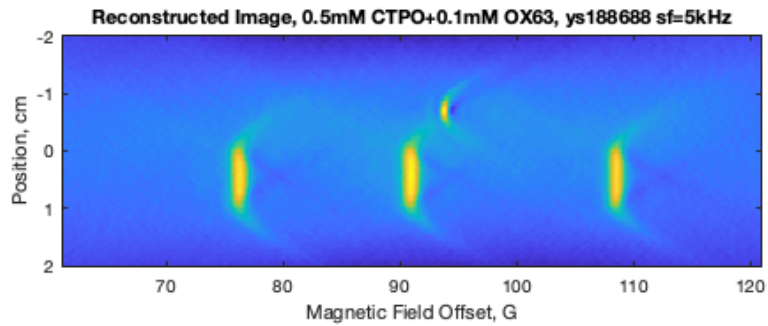
Parameters are same as those used in Figure 5.17.

Now the sample/resonator is located very close to 0 cm (Figure 5.18), and the positions of resonances are approximately vertically aligned. The linewidth at half height = 1.34 G, S/N = 50, resolution = 0.62.

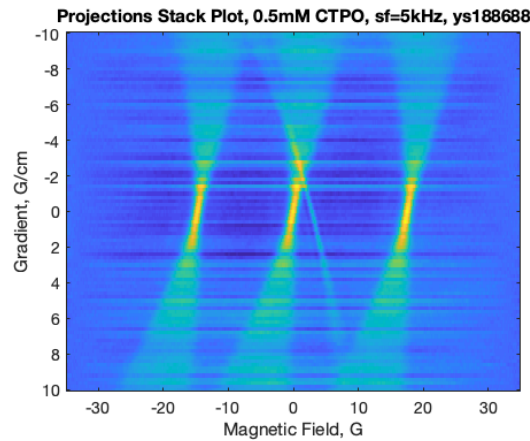
Obviously, changing the position within the effective space does not impact linewidth, S/N, and resolution.

5.5.4 Resonator Outside of Effective Space

If the resonator/sample is off center too much and is outside the effective space, a homogenous field and uniform gradients cannot be guaranteed. As a result, the image will show tailing edges at the end of the features (Figure 5.19a), and the lines in sinogram show curvature (Figure 5.19b).



(a)

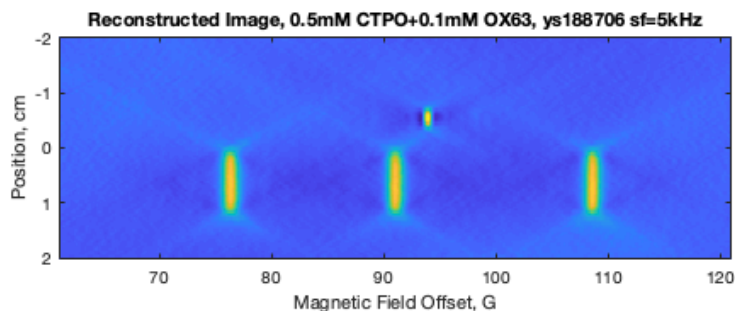


(b)

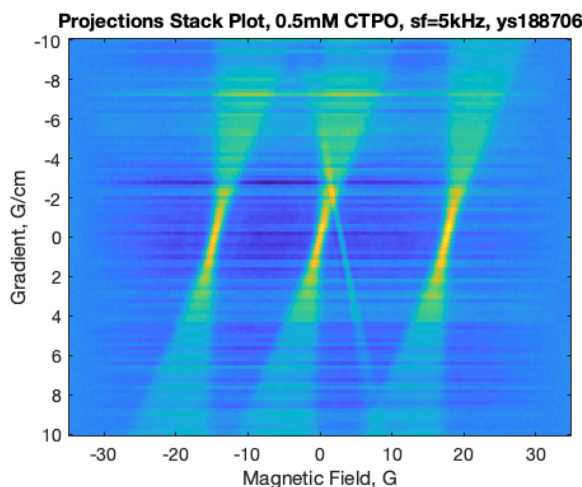
Figure 5.19 (a) Image and (b) sinogram when resonator and sample are off-center

Parameters: sample is 0.5 mM CTPO and 0.1 mM OX063, gradient strength is 10 G/cm with 0.2 G/cm step, 101 projections, 100 ns time base, 8192 points; 2048 averages for each projection, on-board average is 1024. Rapid-scan frequency is 5 kHz, sweep width is 70 G.

The curvature and tailing edge can be eliminated by adjusting the position of the resonator, both horizontally and vertically (Figure 5.20).



(a)



(b)

Figure 5.20 (a) Image and (b) sinogram when resonator and sample are centered

The parameters are same as those in Figure 5.19.

It is very important to have the resonator and sample centered within the magnet coils to get the spatial position correctly. As a result, color tapes have been marked on the frame and the distance from the magnets to the center are recorded to facilitate future experimental settings.

5.6 Rapid-Scan 2D Spectral-spatial Imaging

5.6.1 Criteria for Image Quality

Criteria used to evaluate the quality of the image include:

(1) S/N of a spectral slice with maximum signal intensity, defined as the ratio of signal amplitude to noise; amplitude is calculated by measuring peak height relative to baseline; noise is calculated as the average of two standard deviations taken from the start and end zones of the spectra. Each baseline zone typically includes more than 1000 points and has a length of 10 ~15 G along the spectral axis.

(2) Linewidth at half height of the absorption peak in the spectral slice.

(3) Spatial resolution, defined as the ratio of peak/valley in the spatial slice of the image at a field that corresponds to the peak of the nitroxide signal.

(4) The cleanness of the image, which means whether the image has uniform background color and less artifact (e.g. colored dots, star pattern), which can be easily done by visual inspection.

5.6.2 Rapid-scan Imaging with Various Parameters

Parameters of rapid-scan 2D spectral-spatial imaging, including maximum gradient strength G_{max} , gradient step size, and number of averages, S/N, linewidth and resolution were calculated as criteria of image quality. Samples were 0.1, 0.2 and 0.5 mM CTPO solutions. Experiments were run at 5 kHz rapid-scan frequency, 100 ns time base, 8192 points, 70 G rapid-scan width. Field-reversal background subtraction was used. The data acquisition time was recorded and listed as well. For fair comparison, only one variable under study was changed at a time.

1. Gradient step size

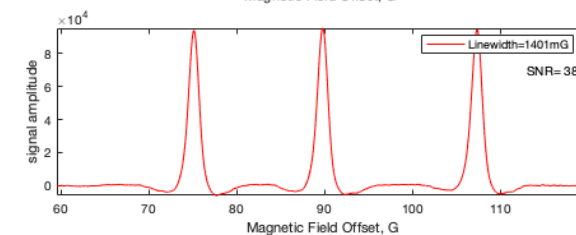
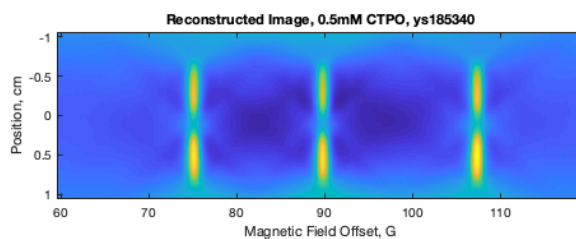
The results are summarized in Table 5.6 and the spectra are shown in Figure 5.21.

Table 5.6 Comparison of different gradient step size for CTPO

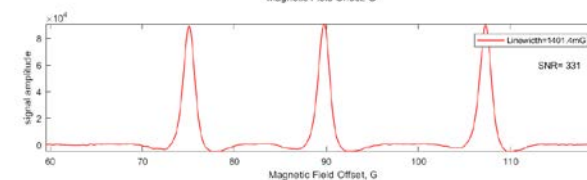
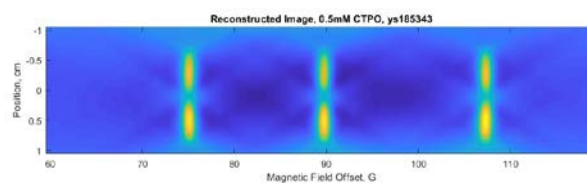
Sample conc., mM	Gmax, G	Gradient step, G/cm	Number of projections	LWHH, G	S/N for spectral slice	Spatial Resolution	Time*
0.5	10	0.2	101	1.37	380	0.35	37'25"
0.5	10	0.4	51	1.40	337	0.36	19'10"
0.5	10	0.5	41	1.41	286	0.39	15'20"

Sample is 0.5 mM CTPO, averages per projection is 2048.

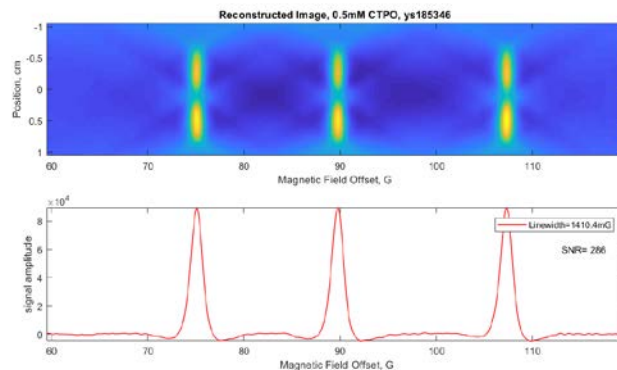
*Total experimental time, can be reduced further by programming; see chapter 7.



(a)



(b)



(c)

Figure 5.21 EPR images and spectral slices with different gradient steps

Parameters are: RS frequency is 5 kHz, 2048 averages for each projection, $G_{max} = 10$ G/cm. (a) Gradient step is 0.2 G/cm, 101 projections, (b) gradient step is 0.4 G/cm, 51 projections, (c) gradient step is 0.5 G/cm, 41 projections.

Since all experiments have the same maximum gradient (10 G/cm), the resolution is about the same. Smaller gradient step (more projections) have higher S/N, and narrower linewidth but similar spatial resolution.

2. Maximum gradient strength

Table 5.7 Comparison of different maximum gradient strength G_{max} and same gradient step size

#	Sample, conc.	G_{max} , G	Gradient step, G/cm	Number of Projections	Average for each projection	LWHH, G	S/N	Resolution	Time*
1	0.5	10	1	21	1024	1.47	157	0.38	3'33"
2	0.5	8	1	17	1024	1.52	121	0.51	2'49"
3	0.5	6	1	13	1024	1.46	72	0.62	2'10"
4	0.2	10	1	21	2048	1.39	125	0.42	5'3"
5	0.2	8	1	17	2048	1.39	86	0.54	4'6"
6	0.2	6	1	13	2048	1.36	86	0.65	3'9"

*total experiment time.

The results show that, with same gradient step size, larger Gmax provides higher resolution, but does not affect linewidth. Images created using more projections have higher S/N.

Table 5.8 Comparison of different maximum gradient strength Gmax and same number of projections

Gmax, G	Gradient step, G/cm	Number of Projections	Average for each projection	LWHH, G	S/N	Resolution	Time
10	0.4	51	2048	1.4	331	0.36	19'
5	0.2	51	2048	1.2	137	0.65	19'

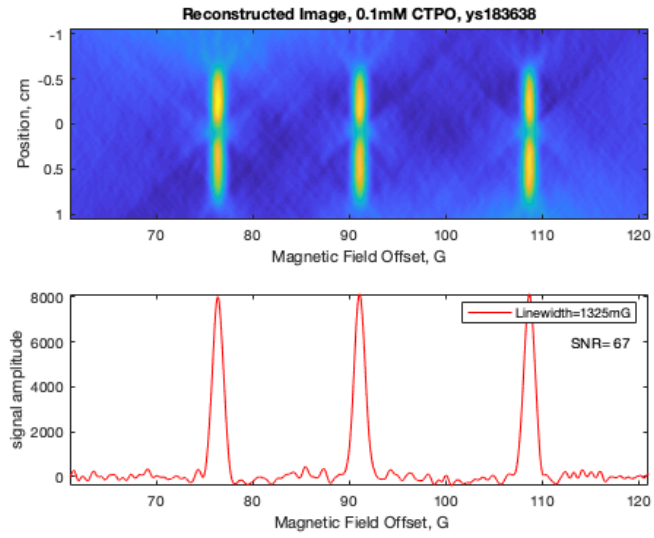
Sample is 0.5 mM CTPO.

The results show that, for the same number of projections, larger Gmax provides higher spatial resolution and higher S/N, but also broadens linewidth. Gmax of 10 G/cm was selected for most subsequent imaging experiments.

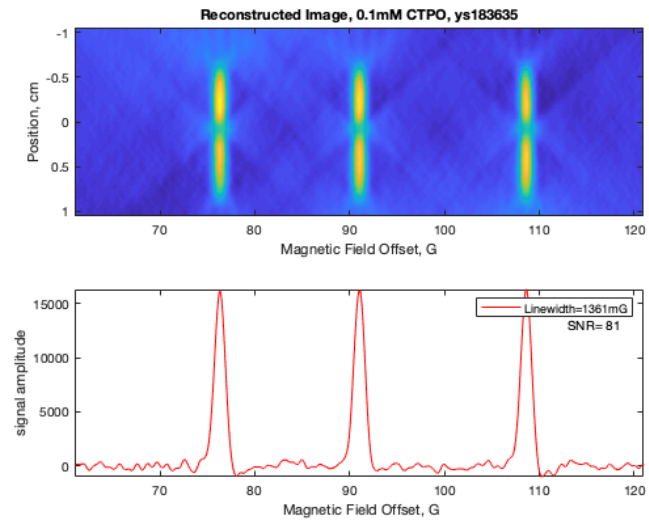
3. Average

Table 5.9 Comparison of different averages

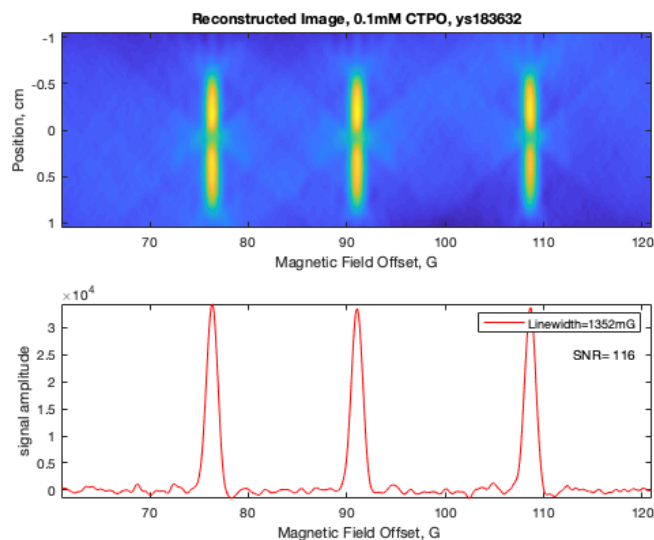
#	Sample, conc.	Gmax, G	Gradient step, G/cm	Average for each projection	LWHH, G	S/N	Resolution	Time
1	0.5	10	0.2	1024	1.24	58	0.35	11'4"
2	0.5	10	0.2	2048	1.28	98	0.31	20'
3	0.2	10	0.2	2048	1.22	76	0.33	30'42"
4	0.2	10	0.2	4096	1.23	144	0.37	42'42"
5	0.2	10	1	1024	1.39	84	0.50	4'1"
6	0.2	10	1	2048	1.39	125	0.42	5'3"
7	0.1	10	1	1024	1.33	67	0.51	4'5"
8	0.1	10	1	2048	1.36	78	0.55	5'8"
9	0.1	10	1	4096	1.35	116	0.59	7'24"



(a)



(b)



(c)

Figure 5.22 EPR image and spectral slice with (a) 1024, (b) 2048, (c) 4096 averages for each projection

Sample is 0.1 mM CTPO, rapid-scan frequency is 5 kHz, scan width = 70 G, gradient strength = 10 G/cm with 1 G/cm step, 21 projections, 100 ns time base and 8192 points.

The results show that, more averages give higher S/N, but do not affect resolution or linewidth.

4. Sample concentration

Table 5.10 Comparison of different sample concentrations

#	Sample conc.	LWHH, G		S/N	Resolution
		Spectral slice	Zero-gradient spectrum		
1	0.1	1.26	1.24	86	0.56
2	0.2	1.32	1.32	151	0.48
3	0.5	1.37	1.37	380	0.35

RS frequency is 5 kHz, G_{\max} is 10 G/cm with 0.2 G/cm step, 101 projections, 2048 averages for each projection.

The results show that, the sample with higher concentration gives much higher S/N and resolution. The S/N increases approximately linearly with concentration, as expected. The less concentrated sample has narrower linewidth because the inherent linewidth at zero-gradient is different for different concentrations.

In conclusion, higher gradient strength gives better resolution; a smaller gradient step size or more diluted sample gives narrow linewidth; a more concentrated sample or more average gives better S/N.

5.6.3 Trade off Among Different Parameters

1. Number of projections vs. gradient step size

These two parameters are inversely related; more projections means smaller gradient step size if G_{\max} is constant. So, what is a practically good number for the projections that is enough to provide all the features? A possible scenario is, for broad line samples, such as CTPO, gradient strength $G_{\max} = 10$ G/cm with 1 G/cm step, which is a total of 21 projections. This is enough for more concentrated sample like 0.5 mM CTPO. For diluted sample like 0.1 mM CTPO, this gradient setting is still enough to provide adequate features like resolution and S/N, although the background may not be very smooth.

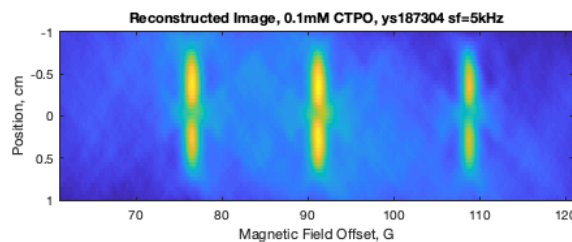
Another scenario with gradient strength $G_{\max} = 10$ G/cm with 0.2 G/cm step, which is a total of 101 projections, is a more conservative combination one can use; image texture is finer, but data acquisition time is also significantly increased.

Because spatial resolution depends on maximum gradient strength G_{max} , increasing projection number does not get better resolution (but does improve S/N and narrower linewidth). The system currently can produce a G_{max} of 10 G/cm, which is the maximum value that the CAEN power supply can produce. For strong samples, signal is strong even with less averages, and the high gradient spectrum is also defined better (i.e. peak splitting due to gradient is clear). But for weaker samples, signal is weaker, and spectrum of individual projection is noisy, more averages are needed to better describe the high gradient spectra.

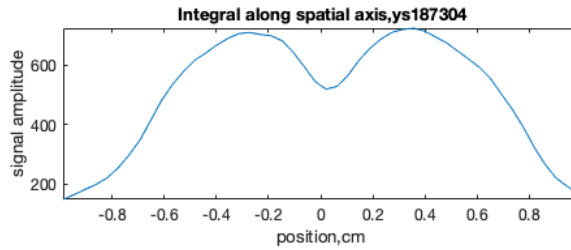
2. Number of projections vs. number of averages

Another question is, for a weak sample, is it more efficient to do more averages for a smaller number of projections or do fewer averages for more projections. If one is more interested in spatial information, it is more efficient to take more averages for a smaller number of projections.

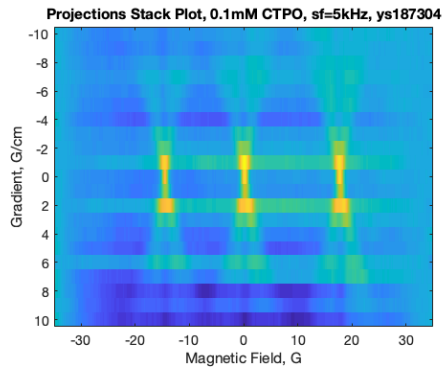
The first example is comparison under the same data acquisition time (Figure 5.23 and Figure 5.24), using 0.1 mM CTPO:



(a)



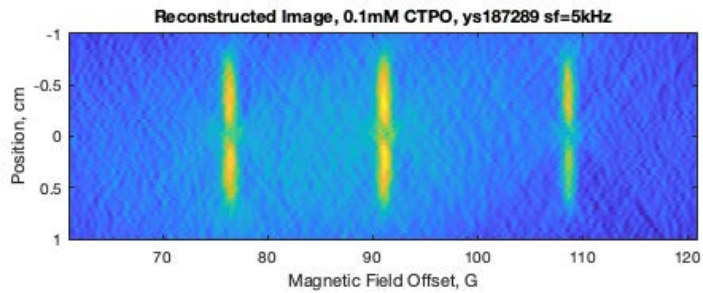
(b)



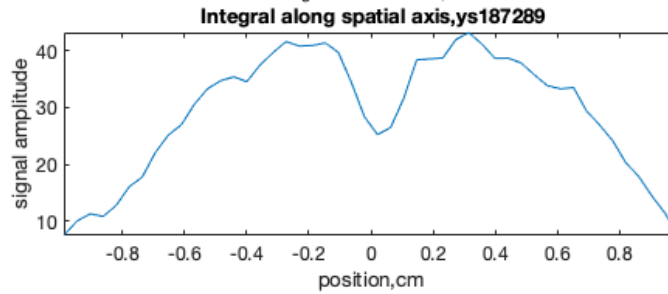
(c)

Figure 5.23 Imaging with more averages, same data acquisition time
(a) Reconstructed image, (b) spatial slice, (c) sinogram

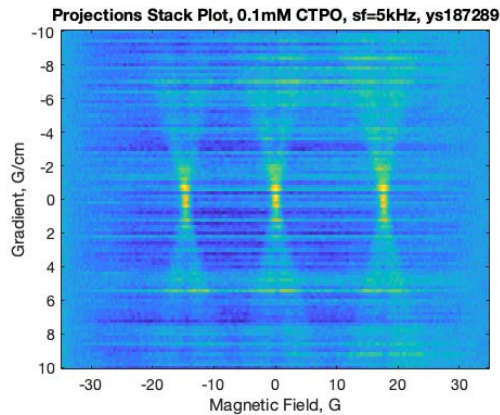
Parameters are: gradient strength $G_{max} = 10 \text{ G/cm}$ with 1 G/cm step, 21 projections, 8192 averages for each projection, took 11'2". Linewidth = 1.48 G , $S/N = 35$. The linewidth of zero-spectrum is only 1.26 G , so the broadened line might be caused by the image reconstruction process or the limited number of projections.



(a)



(b)



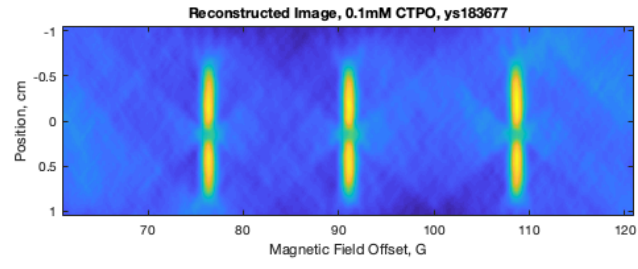
(c)

Figure 5.24 Imaging with more projections, same data acquisition time
(a) Reconstructed image, (b) spatial slice, (c) sinogram

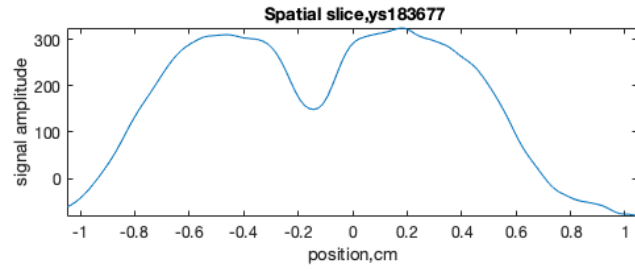
Parameters are: gradient strength $G_{max} = 10 \text{ G/cm}$ with 0.2 G/cm step generates 101 projections, 1024 averages for each projection, took 11'5". Linewidth = 1.15 G, $S/N = 15$.

Both methods take the same amount of time, about 11 minutes, but the one with larger averages (Figure 5.23) is much better than the one had more projections (Figure 5.24), which can be clearly seen from the images, spatial slices or sonograms, although the linewidth was narrower in the image with more projections.

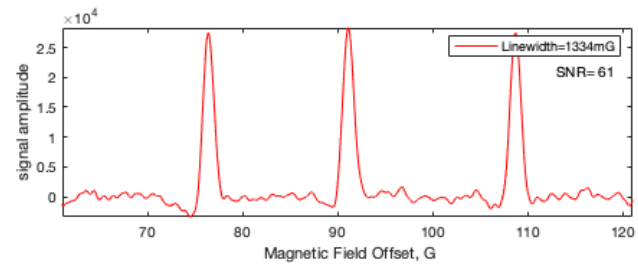
The second example is comparison with same total averages (Figure 5.25 and Figure 5.26), and it was found that more averages can compensate for fewer projections in aspect of S/N and linewidth. Sample is 0.1 mM CTPO.



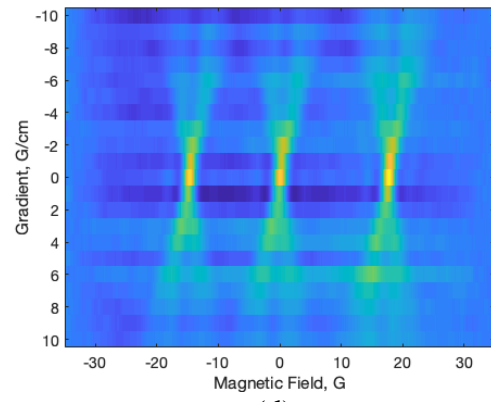
(a)



(b)



(c)



(d)

Figure 5.25 Imaging with more averages for individual projections, same total averages

Parameters are: gradient strength $G_{max} = 10 \text{ G/cm}$ with 1 G/cm step, 21 projections, 8192 averages for each projection, took 12' 14". Linewidth = 1.33 G , $S/N = 61$, resolution is 0.47 .

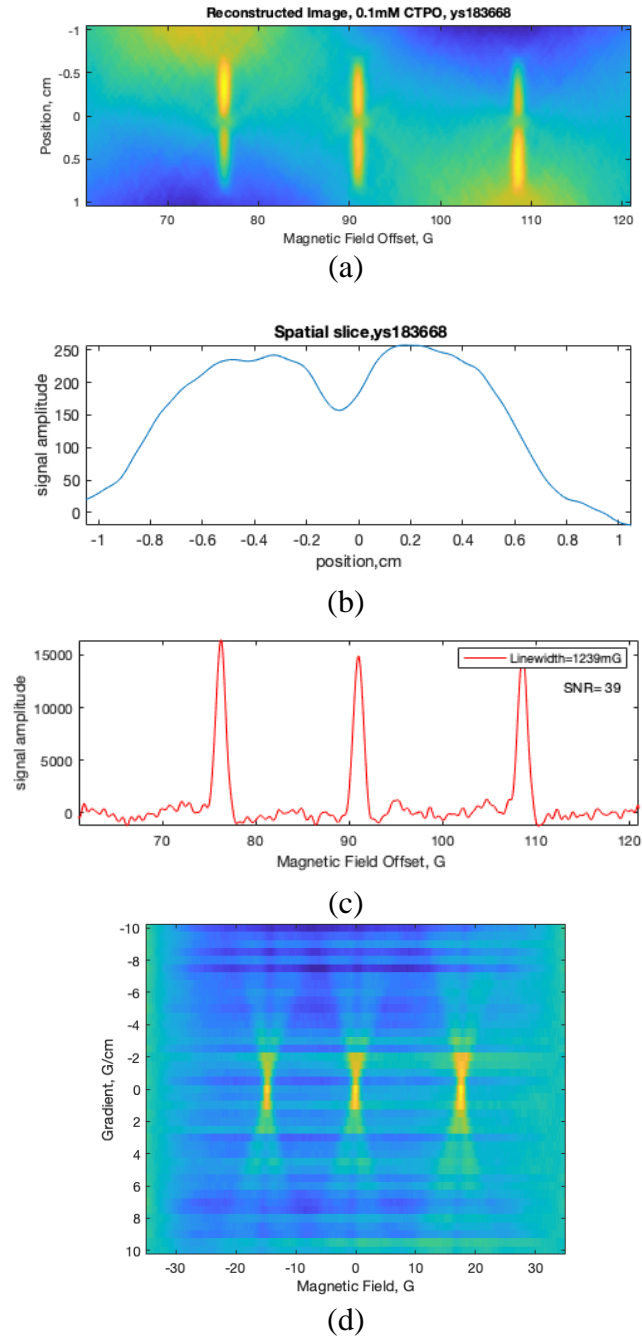


Figure 5.26 Imaging with more projections, same total averages
(a) Reconstructed image, (b) spatial slice, (c) spectral slice, (d) sinogram

Parameters are: gradient strength $G_{\max} = 10 \text{ G/cm}$ with 0.5 G/cm step, 41 projections, 4096 averages for each projection, took 15'. Linewidth = 1.24 G , $S/N = 39$, resolution is 0.61 .

Additionally, for weak samples, like the 0.1 mM CTPO solution, the spectrum of an individual projection is noisier, and the texture of the image is rough. Reconstruction may bring in artifacts as well. The 'uneven' baselines could be mistaken for weaker features in the spectral dimension. When taking the spectral slice, one should avoid regions where artifacts are too strong. Also, carefully adjusting phase and applying background correction functions and smoothing function will improve baseline for the spectral slice.

In conclusion, with same data acquisition time or same total averages, for a weaker sample, it is better to average more for a smaller number of projections, so that each projection (especially the high gradient ones) can be defined better. On the other side, more projections give narrower linewidth, because more information is provided, at the cost of more data acquisition time.

5.6.4 Image with Other Samples

1. CTPO with inorganic salts

The broadening caused by NiCl₂ is shown in Figure 5.27.

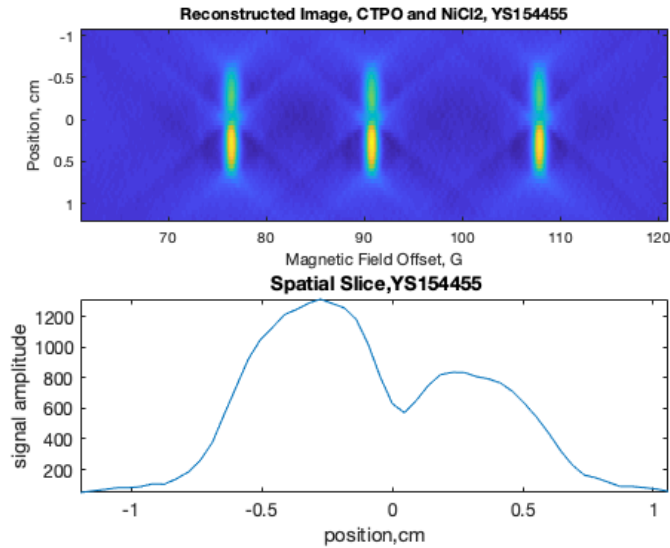


Figure 5.27 EPR image and spatial slice of CTPO and Ni²⁺ salt

The samples are 0.5 mM CTPO and 0.5 mM CTPO + 1.25 mM NiCl₂.

Experimental parameters are: G_{max} = 10 G/cm, gradient step = 0.2 G/cm, 101 projections, 5120 averages for each projection. RS frequency is 15.4 kHz.

For CTPO, S/N of spectral slice is 160, linewidth is 1.14 G; for CTPO and NiCl₂, S/N is 90, linewidth is 1.32 G. Resolution of spatial slice is 0.44. The NiCl₂ broadens the CTPO signal, so the peak amplitude decreases.

2. 3-compartment phantom

A three-compartment phantom was imaged (Figure 5.28). Each compartment had a length along the spatial axis of 4 mm, and the thickness of the spacer was 1 mm.

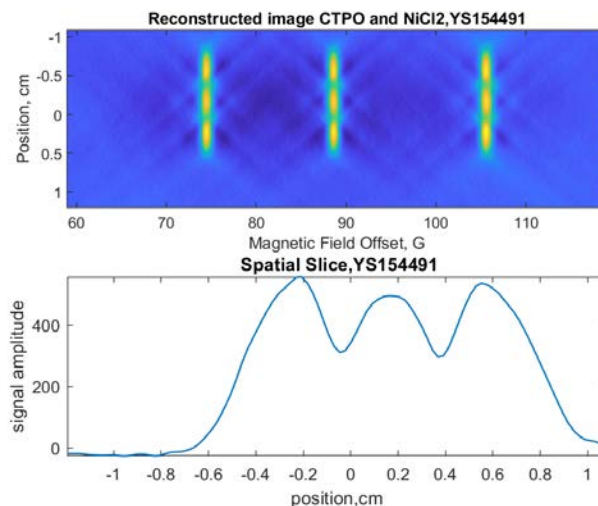


Figure 5.28 EPRI of a 3-compartment phantom and its spatial slice

The samples are 0.5 mM CTPO, 0.5 mM CTPO + 1.25 mM NiCl₂, and 0.5 mM CTPO. Experimental parameters are: G_{max} = 10 G/cm, gradient step = 0.1 G/cm, 201 projections, 5120 averages for each projection. RS frequency is 15.3 kHz.

For the two CTPO samples, linewidths are 1.15 G and 1.17 G, S/N is 98 and 101 respectively; for CTPO and NiCl₂, linewidth is 1.27 G and S/N is 68. The resolution is 0.56 and the three compartments are resolved. The dimensions in the image are in good agreement with the known geometry of the sample.

3. OX063 image

Sample used is 0.1 mM OX063 in the 25 mm CLR. Sweep width is reduced to 5 G, just covering the central line to minimize the broadening. The ¹³C line is not imaged in this region. There are about 560 points to define the peak in an individual projection.

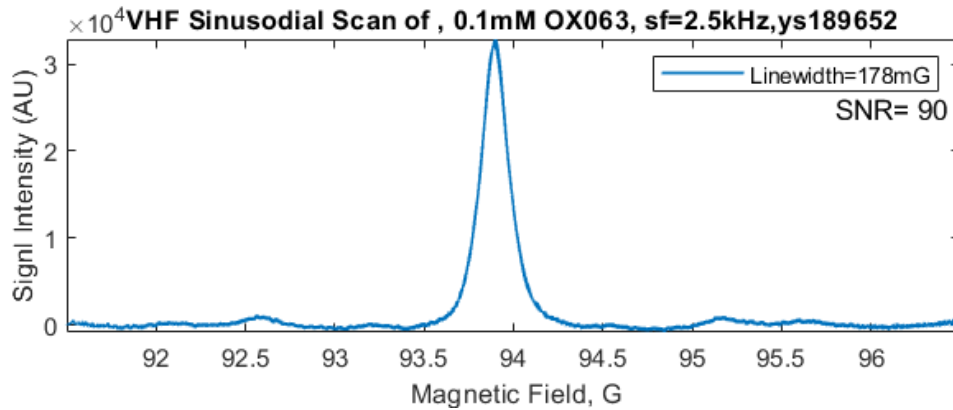


Figure 5.29 Sinusoidal single sweep EPR spectra of 0.1 mM OX063

Parameters are: RS frequency= 2.5 kHz, 4096 averages, 20 ns time base, 65536 points, sweep width is 5 G. Linewidth is 178 mG.

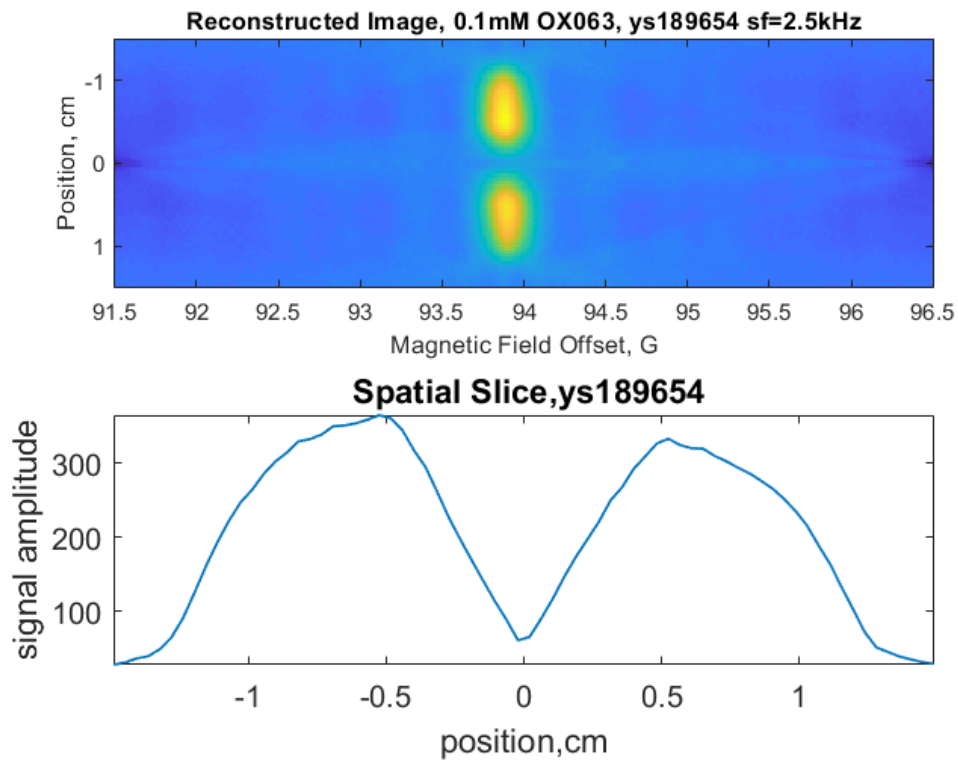


Figure 5.30 Sinusoidal single sweep EPR imaging of 0.1 mM OX063

Parameters are: RS frequency = 2.5 kHz, 4096 averages, 20 ns time base, 4096 points. Gradient strength $G_{max} = 10$ G/cm with 0.1 G/cm step, 201 projections. To

minimize line broadening, a sweep width of 5 G was. Linewidth of spectral slice is 271 mG. The two compartments are very well resolved.

5.7 Field-Reversal Background Subtraction

The field-reversal background subtraction method has been used for EPR spectroscopy and imaging at VHF [168]. To make comparison, both methods are run under parallel conditions and S/N, linewidth and resolution are calculated. The image and spectral slice are shown in Figure 5.31 without using field reversal background subtraction method, and in Figure 5.32 with the method.

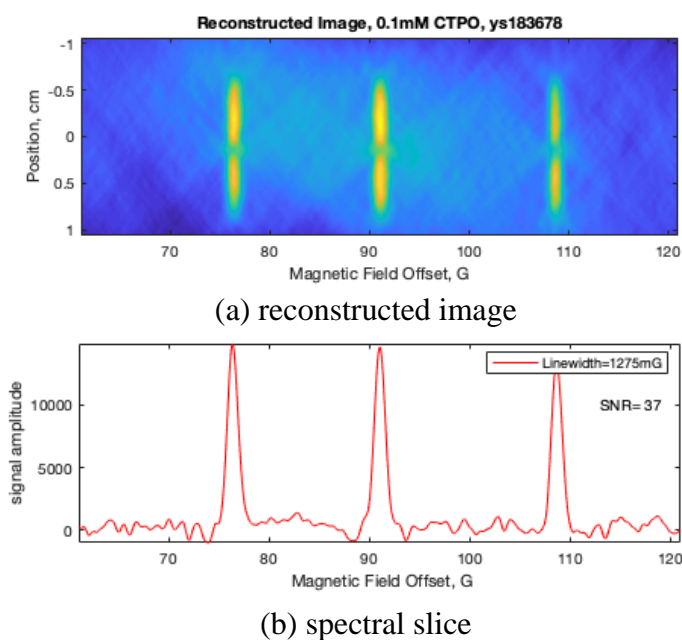
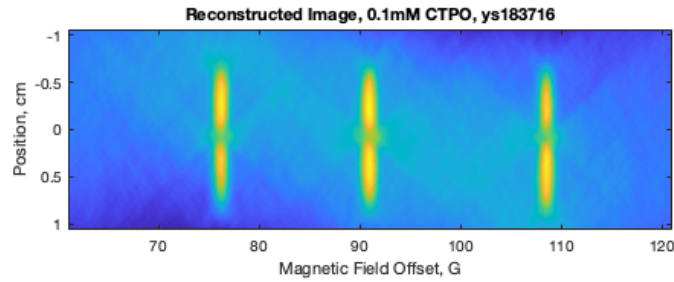
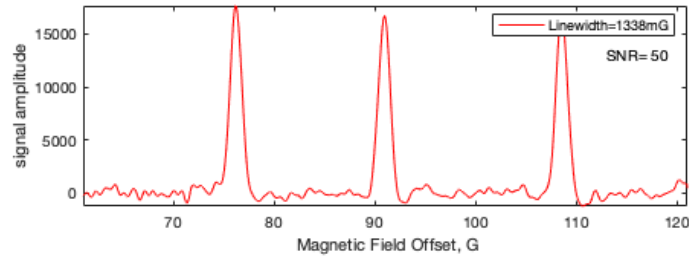


Figure 5.31 Rapid-scan image without field-reversal background subtraction method, 8192 averages per projection



(a) reconstructed image



(b) spectral slice

Figure 5.32 Rapid-scan image with field-reversal background subtraction method, 4096 averages per projection

For both Figure 5.31 and Figure 5.32, sample is 0.1 mM CTPO; parameters are: RS frequency is 5 kHz, gradient strength 10 G/cm with 1 G/cm step, 21 projections, 100 ns time base, 8192 points.

Note: The spectrum in Figure 5.31 has twice as many averages as the spectrum in Figure 5.32 for fair comparison, since Figure 5.32 is the sum of two scans. A MATLAB script named “backcor” [175] is used to flatten the base line for spectral slices of both images.

Results from both methods are compared and summarized in Table 5.11:

Table 5.11 Comparison of using field-reversal background reversal subtraction method or not

Sample	Resonator	Experiment	Field-reversal background subtraction	Line width (G)	S/N	resolution	Averages	Time
0.1 mM CTPO	16 mm CLR	EPRI [1]	No	1.28	37	0.65	8192	6'20"
			Yes	1.34	50	0.67	4096	7'34"
0.1mM OX063	25 mm CLR	EPR Spectrum [2]	No	0.178	90	N/A	4096	
			Yes	0.249	78	N/A	2048	
		EPRI [3]	No	0.271	67	0.18	4096	57'
			Yes	0.296	61	0.20	2048	1h55'

Experimental parameters are:

[1] same as Figure 5.31 and Figure 5.32

[2] RS frequency is 2.5 kHz, 20 ns time base, 65536 points

[3] RS frequency is 2.5 kHz, gradient strength 10 G/cm with 0.1 G/cm step, 201 projections, 20 ns time base, 65536 points.

The results show that, at VHF, for the 16 mm CLR with 0.1 mM CTPO sample, the field reversal background subtraction method improves S/N for weaker samples. For stronger samples, there is no difference between the two methods since the signals are already quite strong relative to the rapid-scan background. Also, the field-reversal method increase linewidth by 5% for CTPO and 10% for OX063, since the forward and backward scan may not overlap exactly. Finally, there is no difference in image resolution by both methods since the same gradient strength is used.

Comments: besides being more complicated in experimental procedures for the field-reversal background subtraction method, one still has good reasons to go back to the basic, simple, no reversal method. (1) In the field-reversal method, the backgrounds of

forward and backward scans may not be identical so there is background even after subtraction. (2) It takes at least 1 second to reverse the main field, the gradient and the trigger; this time is made use of to acquire more averages by the method that does not do field-reversal. (3) For each projection, data are exported from digitizer to computer twice (forward and backward scan) in the field-reversal method while only once in the method that does not do field-reversal. When data points are high, it takes a long time to export data (5 s for 32768 points and 10 s for 65536 points), see Table 5.11 and Table 7.6 (Chapter 7, Section 7.3), and this time can be made use of to take more averages. (4) Dr. Tseitlin's deconvolution code [8] is able to remove most background, and using the 'backcor' function [175] adds an extra layer of warranty; thus background can be removed pretty completely in post-experiment programming, because the backgrounds are usually stable and predictable.

5.8 Conclusion

In conclusion, the rapid-scan single-sweep spectra and imaging of 0.1 mM, 0.2 mM and 0.5 mM CTPO at room temperature, 250 MHz were performed. To minimize the rapid scan background, 3~5 kHz rapid scan frequency was used. Rapid-scan width of at least 70 G is needed to encompass the whole spectrum at high gradients. For EPR imaging, larger gradient strength gives better resolution, while a smaller gradient step size (means more projections) gives fine image texture. Larger gradient and bigger gradient step size broaden the linewidth. The field-reversal background subtraction method was performed, which improves S/N only for weak samples, but does not improve resolution or linewidth.

In addition, sinogram is described, which acts as an indicator for resonator position as well as image quality. Comparison is made between turning on and off the VHF power amplifier for the excitation resonator, which is basically very similar. Finally, two methods are demonstrated for how to measure coil constant.

CHAPTER 6 : VHF FIELD-STEPPED EPR SPECTRA AND IMAGING

While the sinusoidal single-sweep method works well, other efforts were devoted to decreasing the impact of interfering signals generated by the rapid field scans. Methods are being developed to acquire the spectrum of the probe molecules in segments and combine the segments to construct the complete spectrum [176]. This approach is denoted as ‘field-stepped’ rapid-scan EPR. Linear scan (also called triangular scan) was used. EPR spectra of CTPO solutions with a series of gradients were taken at room temperature at VHF. Images were reconstructed by the same home-written algorithm as in Chapter 5 [11]. Several parameters, including field sweep width, step size, number of averages, rapid scan frequency, rapid scan width, maximum gradient, and gradient step size, were varied to optimize acquisition conditions and improve image quality. The linewidths and resolutions were calculated and compared.

6.1 Field-Stepped EPR Introduction

The principle of field-stepped direct detection method is illustrated in Figure 6.1.

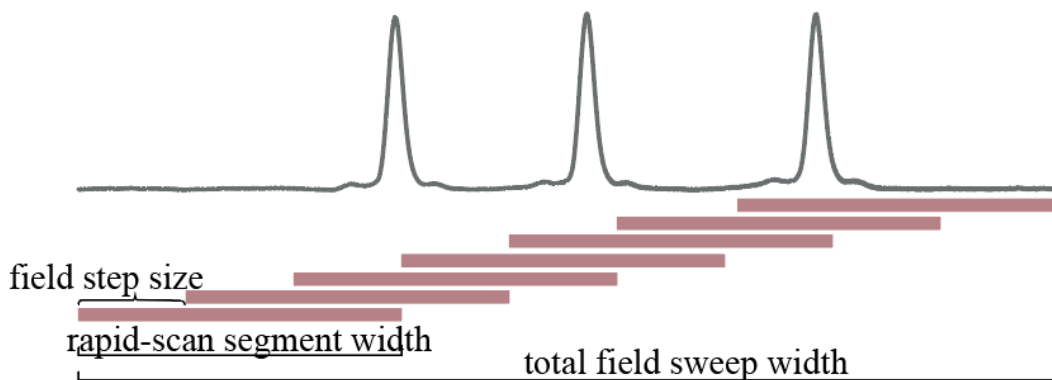


Figure 6.1 Illustration of the field-stepped method, sample is CTPO

Spectra are acquired in segments and each scan covers a portion of the total spectrum with overlapping regions; these segments are then combined by matching DC offset for the overlapping regions of successive scans, to construct the complete spectrum using a MATLAB program. The amplitude of the DC component of the EPR signal, caused by RF reflected from the resonator, is typically quite large compared to the detected EPR signal. The spectrometer has a low-pass filter to eliminate the high DC level of the recorded signal without impacting the EPR signal. Therefore, it is necessary to restore the relative DC level in each segment before combining them to obtain the complete spectrum. If no DC correction is applied, summation of the segments will cause discontinuities at the beginning of each segment [176].

6.2 Materials

6.2.1 Sample

Samples used are same as those used in sinusoidal single sweep experiments (see Chapter 5), which includes solutions of CTPO (degassed by nitrogen gas right before experiment), sealed samples of deoxygenated OX063 solution and sealed deoxygenated polycrystalline LiPc.

6.2.2 Instrument

The instruments are the same as those used in sinusoidal single-sweep rapid scan experiments. The experiments are performed at room temperature with a locally-built spectrometer operating at around 250 MHz (VHF). The phantom imaged is a 16 mm o.d. quartz tube with a divider 1 or 2 mm thick to separate the space into 2 compartments. The tube is inserted into a home-build 16 mm cross-loop resonator (Figure D7 in Appendix D) located at the center of the magnet (in Figure D9 Appendix D). See descriptions in Chapter 5, section 5.2.2.

6.3 Method

The CTPO solution was studied at room temperature, ca 19 °C. A linear scan generated by a rapid-scan coil driver is used [133]. Since the scan rate of a linear scan is constant across the spectrum, multiple segments can be pieced together (Figure 6.1), and linear deconvolution can then be applied to obtain the slow-scan absorption spectrum. Sinusoidal scan is not used in the field-step method, since the scan rate changes continuously during a scan and deconvolution of the combined segments will be

complicated by the scan rate that is not varying monotonically. According to Dr. Tseitlin's presentation at the 59th Rocky Mountain Conference on Magnetic Resonance (July 2018), he intends to develop a deconvolution method for the field-step spectrum using sinusoidal scans, but that is not yet available.

For the field-step experiment, the change of center field positions for the series of segments initially was implemented in Bruker Xepr old version software. Now this can be done in a home-written Python program. The rapid scan frequency used is around 5 kHz and the microwave power used is 20 dB attenuation (equals to 0.32 mW, or 4.51 mG B_1). For an imaging experiment, the field stepped rapid scan experiments are run sequentially under a series of gradients, then pieced together to generate a full spectrum by MATLAB program. These projections are combined together into a 2D file in the Xepr software, from which a final image is reconstructed with a revised version of Dr. Tseitlin's image reconstruction program. Major changes made to accommodate the field-step process include the following (code is provided in Appendix A):

(1) Correct the error: old field stepped program [176] has an error as it forgot to add to itself every time the loop executes. As a result, the old program uses only one cycle instead of adding up multiple cycles, and this will decrease S/N. The error has been corrected.

(2) Skip the linear interpolation part: in old program [176], linear interpolation was used, and the number of data points were increased by a factor of 10. This step was needed for LiPc data with extensive rapid-scan oscillations, but is not needed for nitroxide lines or for trityl in the presence of gradients. In field-stepped imaging, the linear interpolation was not used, and no difference was observed in the result. Deleting

linear interpolation reduces calculation time and is required to match the matrix dimension in the subsequent imaging reconstruction process.

(3) Improve the linear deconvolution program: in the old field stepped program [176], the linear deconvolution sometimes did not work. The raw deconvolved spectrum had oscillating tails that needed to be removed, but there was no quantitative way to determine how much data to be removed, which resulted in incorrect spectrum widths. A linear deconvolution MATLAB program written previously by Dr. Tseitlin worked better, resulting in no oscillating tails and narrower linewidth. Dr. Tseitlin's linewidth calculation function was incorporated into the updated code.

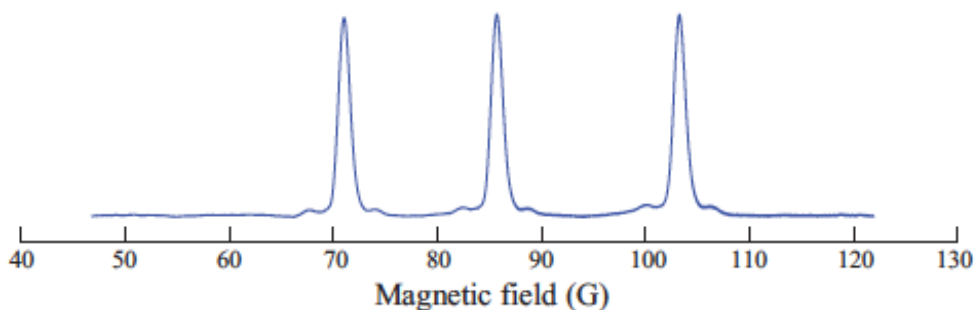
(4) Code was added to remove the glitches caused by stitching the segments.

(5) Section for CW comparison was added: the revised program can integrate CW spectra and take the derivative of rapid scans.

6.4 Field-Stepped Spectra

6.4.1 Comparison of Field-stepped Rapid-scan Spectrum with CW

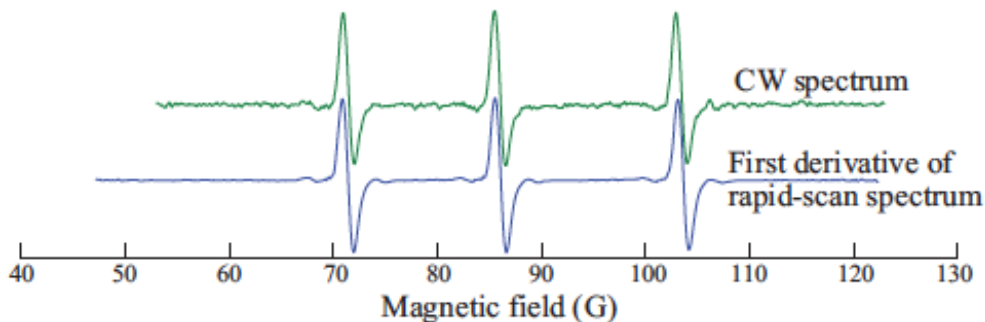
The field stepped rapid-scan spectrum of 0.5mM CTPO is shown in Figure 6.2a:



(a) Rapid-scan absorption spectrum

Parameters for RS: 10 ns time base, 65536 points; 2048 averages for each segment, on-board average is 1024. Rapid-scan frequency is 5 kHz, total field sweep

width is 70 G, field step size is 5 G, 15 segments, rapid-scan width for each segment is 10 G.



(b) First derivative of rapid-scan spectrum matches with CW spectrum

Figure 6.2 Field-stepped rapid-scan spectrum of 0.5mM CTPO

Parameters for CW: modulation frequency is 100 kHz, modulation amplitude is 1 G, conversion time is 10 ms, sweep time is 10.24 s, field-sweep width is 70 G, 1024 points and 10 scans.

Derivative of the absorption spectrum is taken and compared with the conventional CW spectrum (Figure 6.2b), which found to be matching well.

6.4.2 Optimization of Experimental Parameters for a Spectrum

1. Field step size

To make fair comparison, the number of averages was adjusted to compensate for different field step sizes. For the total sweep width a smaller field step means more overlapping segments, so the number of averages per segment is reduced accordingly.

Table 6.1 Comparison of field step size

Field step, G	Number of segments	Averages per segment	S/N	LWHH, G	Time
5	15	19456	69	1.24	8'38"
2	36	8192	131	1.31	8'53"
1	71	4096	128	1.33	10'
0.5	141	2048	109	1.32	11'44"

Parameters are: rapid scan sweep width = 10 G, total spectrum width is 70 G.

In consideration of S/N, field-step size of 1 and 2 G is highest. Large step almost comparable to the step size (rapid-scan width) may not provide enough region for overlap. However, working with very small field-step size also means a large number of spectra need to be pieced together in the program, and likely produce a lot of artifacts and broadens the line.

2. Rapid scan sweep width

The rapid-scan sweep width of each segment was varied while other parameters were kept the same. Sample is 0.5 mM CTPO, total sweep width = 70 G, rapid scan frequency = 5 kHz, field step size = 2 G, 36 segments, 8192 averages for each segment, data acquisition time is about 8'53". The results are summarized in Table 6.2.

Table 6.2 Comparison of different rapid scan sweep widths

Rapid-scan width, G	S/N	LWHH, G
20	111	1.33
10	74	1.35
5	55	1.33

The rapid-scan sweep width did not have much impact on linewidth. Since large rapid-scan width means more overlap, S/N is expected to be higher. Doubling the segment length approximately doubles the number of scans averaged at each point, so a $\sqrt{2}$ improvement is expected, which is approximately what is observed. The disadvantage of increasing the segment width is that the rapid scan background increases with increasing scan width. The software approaches to background correction assume baseline on both sides of a spectrum which is not generally applicable to the segments of a spectrum.

3. Rapid-scan frequency

Different rapid-scan frequencies were tested, and the results are summarized in Table 6.3. Sample is 0.5 mM CTPO, field sweep width is 80 G, field step size is 2 G, 41 segments; each segment has 10 G rapid scan sweep width, 4096 averages and 65536 points, time base is reduced as frequency goes up, so that the time windows all include 3 cycles.

Table 6.3 Comparison of different rapid scan frequencies

#	Rapid-scan Frequency, kHz	Time base, ns	Data acquisition time	S/N	LWHH, G	Signal Band width, MHz
1	15 *	10	3'37"	98	1.28	0.46
2	13	10	3'53"	116	1.28	0.50
3	12	10	3'16"	141	1.26	0.46
4	10	10	3'34"	136	1.26	0.38
5	9	20	5'14"	109	1.29	0.35
6	8	20	5'37"	105	1.29	0.31
7	7	20	6'18"	147	1.28	0.27
8	6	20	5'16"	103	1.26	0.23
9	5	20	5'58"	171	1.29	0.19
10	4	20	6'58"	153	1.29	0.15
11	3	20	5'02"	122	1.27	0.12
12	2	40	8'40"	87	1.28	0.08

* Rapid scan sweep width = 8 G due to hardware limitation of the coil driver. Uncertainty in S/N measurement is 7%.

Signal bandwidths did not exceed resonator bandwidth (1.4 MHz, from section 5.4.1). Each spectrum contains many segments and may not overlap exactly; as a result the S/N showed large variation. Based on S/N, linewidth and bandwidth, these are all workable rapid-scan frequencies.

6.5 Field-Stepped Linear Scan Imaging

The field-step size, gradient strength, and gradient step size were varied and the images were taken. Linewidth, S/N and resolution are compared in Table 6.4.

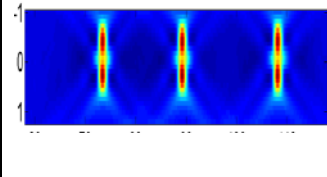
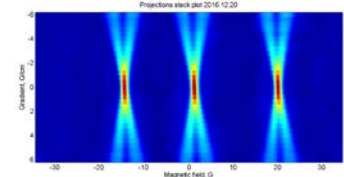
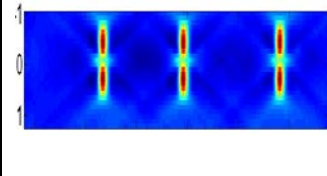
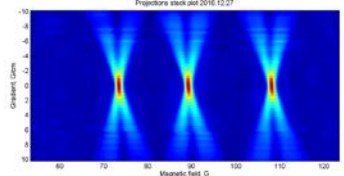
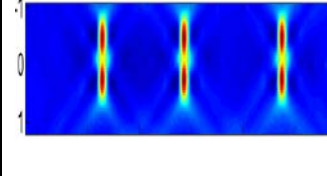
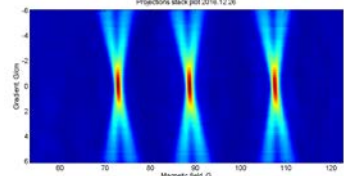
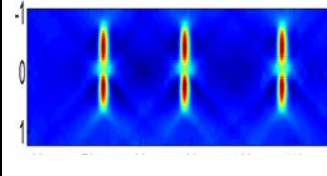
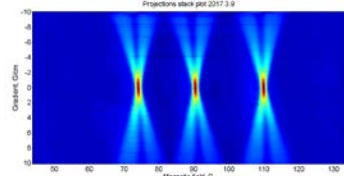
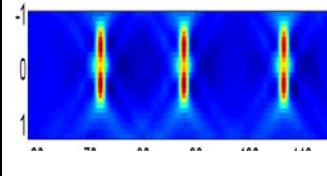
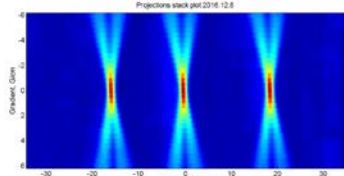
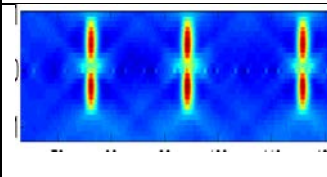
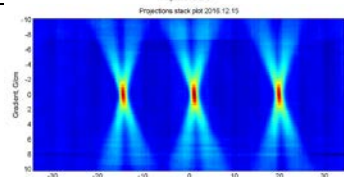
Table 6.4 Summary of field stepped imaging results

#	Field step, G	Gmax, G/cm	Gradient step size, G/cm	Spectral slice		Zero-gradient spectral		Resolution	Time
				S/N	LWHH, G	S/N	LWHH, G		
(a)	2	6	0.4	81	1.37	250	1.39	0.65	7h
(b)	2	10	0.4	109	1.39	250	1.39	0.44	11h
(c)	2	6	0.2	82	1.35	168	1.37	0.61	14h
(d)	2	10	0.2	136	1.32	168	1.37	0.44	22h
(e)	5	6	0.4	77	1.33	166	1.37	0.74	3h
(f)	5	10	0.4	104	1.38	128	1.38	0.47	6h

Sample is 0.5 mM CTPO, rapid-scan frequency is 5 kHz, field sweep width = 50 G, average for each segment is 5120, RS sweep width of 20 G for each segment is selected (one could use 10 G or other values, but this is fixed for comparison), 20 ns time base, 65536 points, which includes 6 rapid-scan cycles. A linear scan was used. The power used is 20 dB (equals to 0.33 mW, or 3.61 mG B₁). The noise is mostly random. Since the method requires more experimental procedures and more complicated reconstruction steps (compared to sinusoidal single-sweep method), each projection takes significant longer time to acquire and the whole experiment is extended so much that system instability could affect the result, which partially explains why (c) and (d) did not improve a lot compared to (a) and (b).

The reconstructed images and sinograms corresponding to Table 27 are plotted and listed in Table 6.5.

Table 6.5 Summary of results for various Gmax, gradient step and field step size

#	Field step size, G	Gmax, G/cm	Gradient step, G/cm	Reconstructed image (x-axis is field in G, y-axis is position in cm)	Sinogram for projections assembled from the segments (x-axis is field in G, y-axis is gradient in G/cm)
(a)	2	6	0.4		
(b)	2	10	0.4		
(c)	2	6	0.2		
(d)	2	10	0.2		
(e)	5	6	0.4		
(f)	5	10	0.4		

Parameters are same as those listed in Table 6.4.

The sinograms show that, high gradient strength Gmax gives large splitting, and small gradient step (means more projections) gives finer texture. Both are desired

characters for a better image. Field-step size seems not to affect the features of sinograms.

Summary for images of nitroxides. Results may differ for a probe with narrower lines:

1. Parameters that affect Resolution:

- (1) Gradient strength: larger gradient strength has better resolution; from 6 G/cm to 10 G/cm, there is an improvement of 41%.
- (2) Gradient step size: smaller gradient step slightly improves resolution; from 0.2 G/cm to 0.4 G/cm, there is an improvement of 6%. For samples with these relatively large linewidths the effect step size is smaller than the effect of increasing G_{max} .
- (3) Field step size: smaller field step slightly improves resolution; from 2 G to 5 G, there is an improvement of 5%; this is mainly due to more overlap thus more averages.

2. Parameters that affect linewidth at half height of the middle line:

- (1) Gradient step size: large gradient step size (means fewer projections) broadens linewidth; from 0.4 G/cm to 0.2 G/cm, line broadens about 5%.

3. Comparing the zero-gradient spectrum with the spectral slice of the reconstructed image, it is found that the linewidths are close, but the zero-gradient spectrum has higher S/N (twice as much). Possible source of noise comes from image reconstruction process since it uses zero-gradient spectrum as well as other gradient-broadened spectra.

6.6 Comparison of Field-Step Method with Single Sweep Method

Two data acquisition methods were compared: the single-sweep sinusoidal scan and the field-stepped linear scan. Both methods were tested under comparable conditions. The comparison is performed from four aspects: EPR spectra, EPR spectra under gradients, image and sinogram. Again, linewidths, S/N, and the resolution are used as criteria.

6.6.1 EPR Spectra

Comparison of rapid-scan spectra with both methods are summarized in Table 6.6:

Table 6.6 Comparison for Rapid-scan spectra

Sample	Method	Average	S/N	LWHH, G	Cut off*
0.2 mM trityl-CD3	Single sweep	20480	1650	0.087	no
	Field step	5120	1481	0.097	
0.5 mM CTPO	Single sweep	20480	482	1.32	0.1
	Field step	4096	441	1.33	
0.2 mM CTPO	Single sweep	20480	159	1.28	0.1
	Field step	4096	110	1.32	
0.1 mM CTPO	Single sweep	20480	166	1.25	0.1
	Field step	4096	135	1.25	

* Since the linear scan might be rounded off at the triangular edges, part of the spectrum is cut off; 0.1 cut off means 5% of the data at the beginning and the end of the spectrum are cut off.

Same parameters were used: rapid-scan frequency is 5 kHz, time base is 20 ns, 65536 points, filter used in post processing is 0.1 G. For the field stepped method, rapid-scan sweep width is 10 G, field step size is 2 G. The numbers of averages were adjusted, reflecting the fact that there is overlap in the field-step method.

The data shows that, for strong samples such as trityl-CD₃ and 0.5 mM CTPO, both methods give comparable S/N. At lower concentrations, 0.2 and 0.1 mM CTPO, single-sweep sinusoidal scan has better S/N than the field-stepped one.

In addition, lines get narrower when CTPO concentration drops. This trend is the same as the data shown in Table 5.9 in previous chapter, using the sinusoidal single-sweep method.

6.6.2 Spectra with Gradients

The S/N of EPR spectra with both methods are summarized in Table 6.7.

Table 6.7 Summary of S/N for EPR spectra under different magnetic gradients

Sample gradient (G/cm)	0.1mM CTPO		0.2mM CTPO	
	Field step [a]	Single sweep [b]	Field step [c]	Single sweep [d]
-10	2	21	7	29
-9	4	31	6	43
-8	3	19	9	39
-7	3	18	6	46
-6	4	16	6	66
-5	4	19	9	67
-4	7	26	17	58
-3	10	52	14	95
-2	14	62	22	154
-1	17	84	34	207
0	21	98	51	209
1	16	84	31	166
2	12	47	17	99
3	8	34	16	60
4	4	25	11	40
5	4	18	7	34
6	4	35	7	32
7	4	24	5	24
8	2	31	5	21
9	3	22	4	28
10	3	19	5	27

The parameters are:

[a] 0.1 mM CTPO field step spectra: rapid-scan frequency is 5 kHz, field sweep width is 80 G, field step size is 2 G; each segment has 10 G rapid-scan width and 5120 averages; time base is 20 ns, number of points is 65536.

[b] 0.1 mM CTPO single sweep spectra: rapid-scan frequency is 4.8 kHz, rapid-scan width is 77 G, time base is 20 ns and number of points is 65536, 20480 averages.

[c] 0.2 mM CTPO field step spectra: rapid-scan frequency is 4.8 kHz, field sweep width is 80 G, field step size is 2 G; each segment has 10 G rapid-scan width and 4096 averages; time base is 20 ns and number of points is 65536.

[d] 0.2 mM CTPO single sweep spectra: rapid-scan frequency is 4.7 kHz, rapid-scan width is 77 G, time base is 20 ns and number of points is 65536, 20480 averages.

Number of averages are compensated for spectra taken by the single sweep method, since there are overlapping regions in spectra taken by the field-step method.

The data in Table 6.7 are also plotted in Figure 6.3 and Figure 6.4.

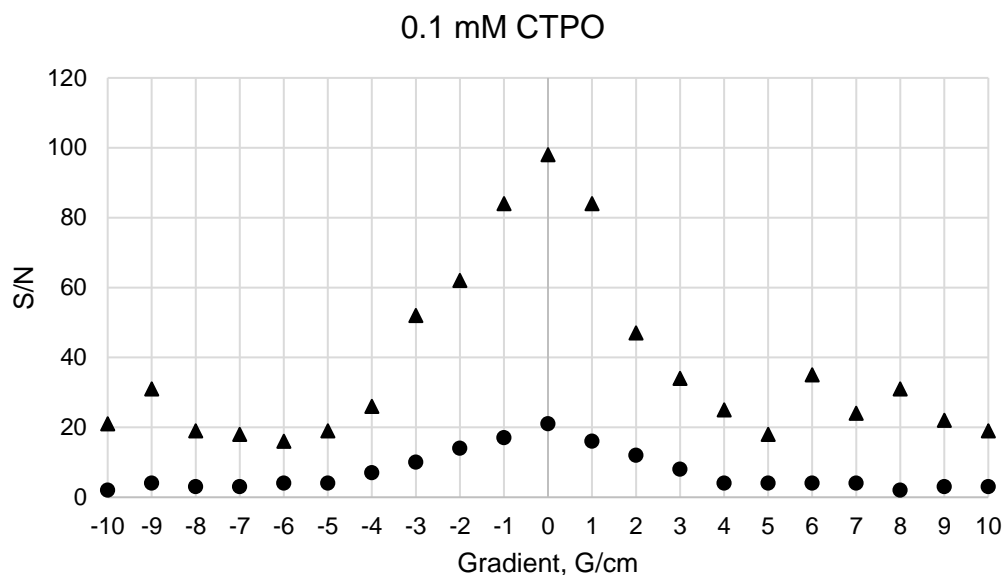


Figure 6.3 S/N for spectra under gradients, 0.1 mM CTPO
Single sweep method (▲) and field step method (●); for parameters see Table 6.7.

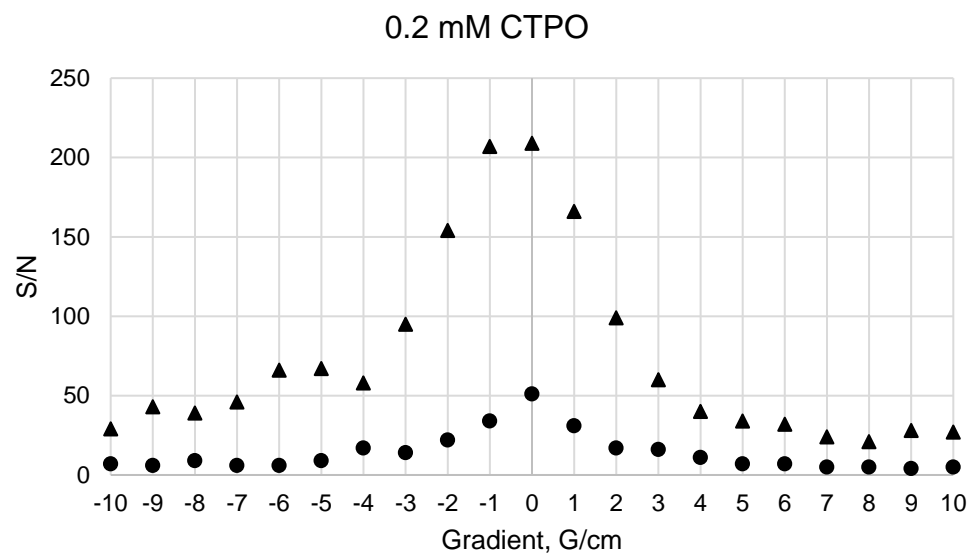


Figure 6.4 S/N for spectra under gradients, 0.2 mM CTPO
 Single sweep method (▲) and field step method (●); for parameters see Table 6.7.

The results show that the single sweep method has higher S/N than the field stepped method, at all gradients. Noise comes from both random and imperfect alignment of field step segments.

6.6.3 EPR Imaging

The comparison of EPR Images of different CTPO solutions are listed in Table 6.8.

Table 6.8 Comparison of field step with single sweep

CTPO Conc.	Method	Average	S/N	LWHH, G	Resolution	Cut off*
0.5 mM	Single sweep	20480	217	1.27	0.42	
	Field step	4096	81	1.21	0.42	0.1
0.2 mM	Single sweep	20480	180	1.25	0.55	
	Field step	4096	92	1.30	0.77	0.1
0.1 mM	Single sweep	20480	106	1.23	0.58	
	Field step	4096	79	1.19	0.69	0.2

*Cut off is the percentage of spectrum that is deleted as a result of rounding corners of triangular scans, refer to Table 6.6.

The comparison of both methods is performed with same parameters: rapid-scan frequency is 5 kHz, the gradient strength $G_{max} = 10$ G/cm with 0.2 G/cm step, 101 projections, 20 ns time base, 65536 points, filter used in post processing is 0.1 G. For the field stepped method, rapid-scan sweep width is 10 G, field step size is 2 G. The number of averages were adjusted so both methods have the same number of averages. Both channels are used.

The corresponding image and spatial slice are listed in Table 6.9.

Table 6.9 Summary of reconstructed images of CTPO with spatial slice cut at the middle peak

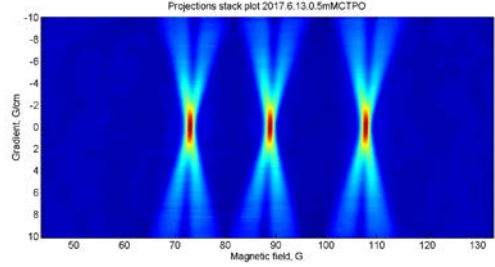
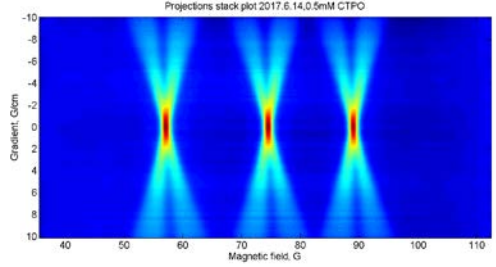
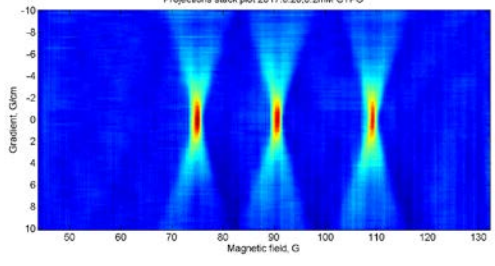
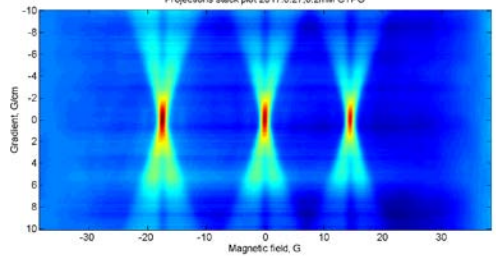
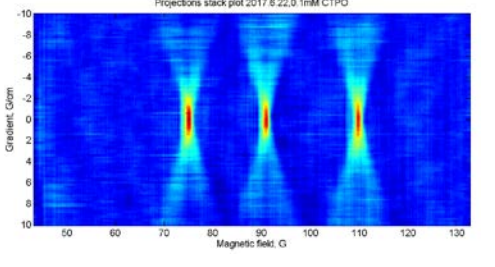
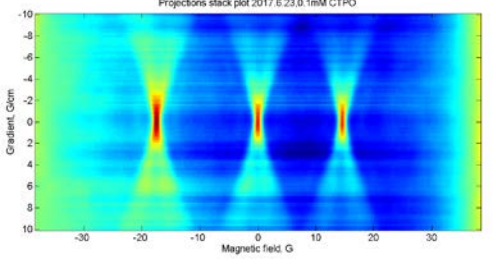
Sample concentration	Field-stepped linear scan	Single sweep sinusoidal scan
0.5 mM		
0.2 mM		
0.1 mM		

In summary, when radical concentration increases, S/N also increases. At high concentration, 0.5 mM, both methods give comparable S/N. At lower concentrations, 0.2 and 0.1 mM, single-sweep sinusoidal scan method gives 1.5 times better S/N than the field-stepped method. Line gets narrower as radical concentration decreases.

6.6.4 Sinogram

The sinograms for different CTPO solutions using both methods are listed in Table 6.10:

Table 6.10 Comparison of sinogram by both methods

Sam ple	Field-stepped linear scan	Sinusoidal single sweep
0.5 mM		
0.2 mM		
0.1 mM		

The experiments were run with comparable parameters: gradient strength $G_{\max} = 10$ G/cm, gradient step = 0.2 G/cm. For field step images, field step size = 2 G, rapid-scan sweep width = 10 G, 4096 averages; For sinusoidal single sweep images, 20480 averages, so both methods have same averages.

Table 6.10 shows that, with same experimental parameters, when the sample concentration goes down, the spectra become noisier and the high gradient spectrum of the field-stepped scans is weak, and the sinusoidal single sweep method defines EPR feature more clearly.

6.7 Conclusion

In conclusion, to get better image resolution, large gradient, small gradient step size and small field step size should be used. Exemplary parameters are, gradient strength $G_{\max} = 10$ G/cm, gradient step = 0.2 G/cm, 101 projections and field step size = 2 G.

For the 0.5 mM CTPO sample, the single sweep sinusoidal scan method and the field-stepped linear scan method produce comparable results; For low concentrations sample, 0.1 and 0.2 mM CTPO, the single sweep method produce better results, since there is no need to piece together segments.

Being significantly faster, simpler and higher S/N, the sinusoidal single sweep method should be the default way to take spectra as well as imaging. The rapid-scan coil driver is able to produce ~5A current, which corresponds to 110 G sweep width, and is far more than needed (for trityl 20 G sweep width is enough; for CTPO 70 G sweep width is enough). Sinusoidal scan is much faster in data acquisition and analysis. When

sinusoidal single sweep is not able to cover the full scan width, linear scan can be used instead, which is more complicated in data acquisition and analysis.

Excess sweep width is not only unnecessary but also potentially problematic. High sweep width will produce a lot of heat, increase the temperature of resonators and sample, which might be difficult to cool. Besides, since most of our imaging tubes are made of Pyrex glass, sweeping too wide will incur the iron signal in the glass.

CHAPTER 7 : NEW DEVELOPMENTS IN VHF RAPID-SCAN EPR IMAGING

Based on the above knowledge about the rapid-scan imaging, new improvements have been made to accommodate needs of EPRI, such as decrease data acquisition time, quantify image features, increase instrument efficiency, simplify experimental procedures from data acquisition to spectral analysis. Programming language Python is also introduced and integrated into the EPRI experiments, in the hope of making EPRI more user-friendly for a larger potential user group.

7.1 EPR Imaging with Various Averages

For weaker samples, noise is high so it may be necessary to average more at higher gradient, however, this increases data acquisition time, which is unfavorable for tracking *in vivo* kinetic processes or for medical diagnosis. In order to reduce imaging time, a first attempt was made to skip some of the intermediate projections, as shown in the distribution listed in Table 7.1.

Table 7.1 Projection distribution

Gradient region, G/cm	Number of projections
[-10, -5.5]	46
(-5.5, -0.5)	none
[-0.5, 0.5]	11
(0.5, 5.5)	none
[5.5, 10]	46

[] means the value is included; () means the value is not included.

The image is shown in Figure 7.1.

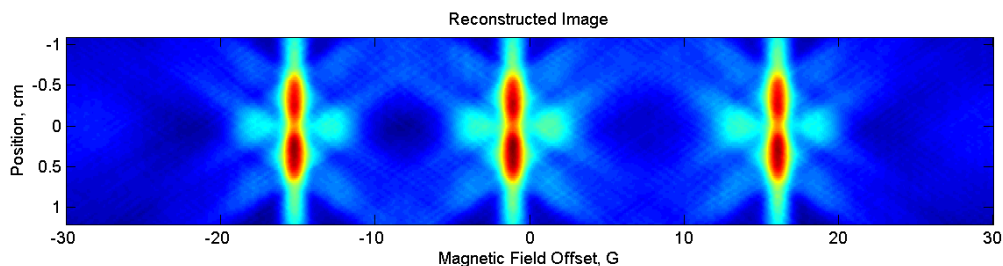


Figure 7.1 Sectioned EPR image

The sample used is 0.5 mM CTPO; parameters are: rapid-scan frequency is 15 kHz, rapid sweep width is 77 G, Gmax is 10 G/cm with 0.1 G/cm step, 201 projections, 5120 averages, 5 ns time base, 65536 points.

The artifacts turn out to be so strong that it decreases image quality. It was learned that the contributions from those missing projections cannot be omitted.

Then a second attempt was made to still run a whole set of projections while selectively reducing the averages of projections in intermediate region, whose contributions are less but cannot be eliminated. This approach was found to preserve image quality while significantly reducing imaging time.

Several combinations of parameters have been tried for averaging a larger number of scans at higher gradients. Some empirical norms used are:

- (1) The number of averages was usually set as integer multiple of 1024, which is a power of 2 since Fourier transform routines are faster for powers of 2.
- (2) The numbers of averages for different gradients were symmetrically distributed around 0 gradient.

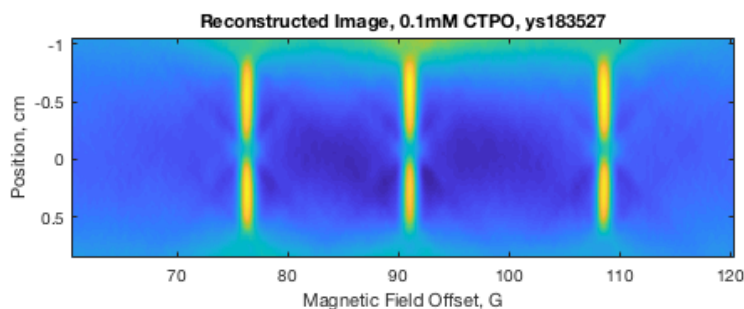
(3) The number of averages at higher gradients can be set 2~4 times the number of averages at lower gradients. The definition of ‘higher gradient’ is flexible, and can be viewed as the region of 6~10 G, or 8~10 G, which does not make much difference. The definition of ‘lower gradient’ is not strict either, and can be set as the region of 0~2 G. In my Python program, one can customize these regions by entering the values in the graphic user interface.

Sample settings for an imaging experiment with variable averaging is shown in Table 7.2 and Table 7.3, and a python program is written to realize this.

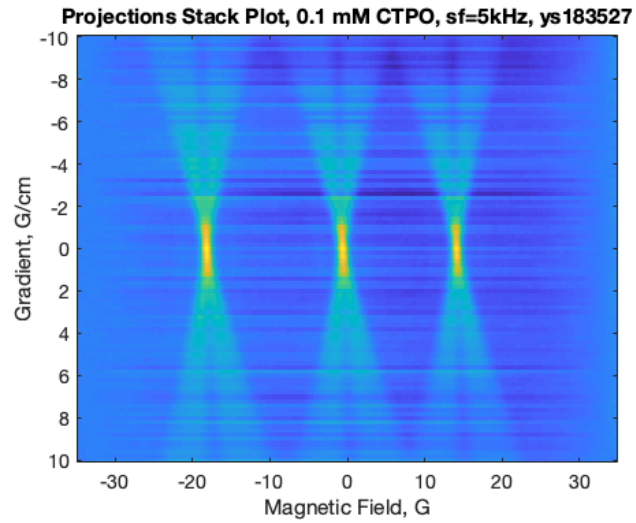
Table 7.2 Comparison of EPR imaging of 0.1 mM CTPO with various averages

#	Gradient Range G	Averages	LWHH G	S/N	Resolution	Time
1	All	8192	1.20	110	0.36	57'17"
2	-10 ~ -8.2	8192	1.21	95	0.35	37'11"
	-8 ~ 2.2	4096				
	-2 ~ 0 ~ 2	2048				
	2.2 ~ 8	4096				
	8.2 ~ 10	8192				

EPR images are compared in Figure 7.2 and Figure 7.3.



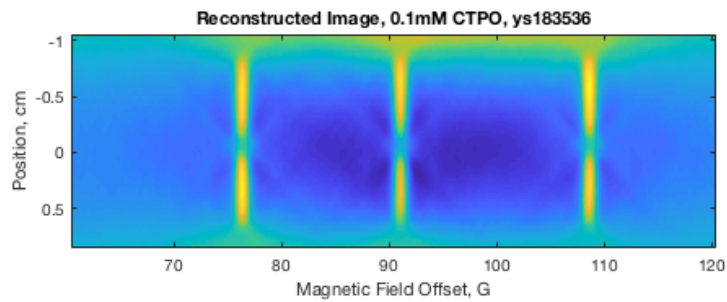
(a)



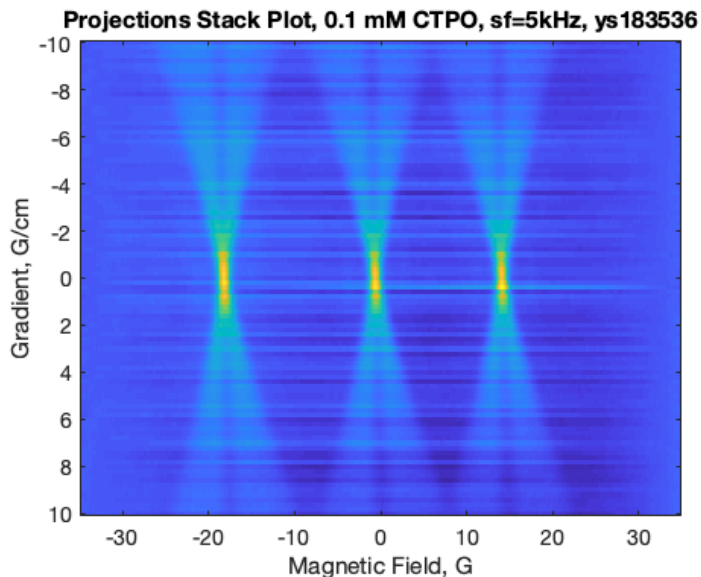
(b)

Figure 7.2 EPR image (a) and sinogram (b) using variable averages

Parameters are: $G_{max} = 10$ G/cm with gradient step size = 0.2 G/cm, 101 projections, 256 on-board averages. Rapid-scan width = 70 G, rapid scan frequency = 5 kHz. 100 ns time base and 8192 points. Digitizer used is SpecJet-II. Averages are listed in Table 7.2, #2.



(a)



(b)

Figure 7.3 EPR image (a) and sinogram (b) using uniform averages
Parameters are same as Figure 7.2. 8192 averages for each projection.

Note:

1. The signal amplitudes of different projections are normalized, so that intensity is that which would be obtained for 8192 averages.
2. The gradient range -8 G/cm and -2 G/cm were selected based on the analysis of previous data of S/N calculation.

Table 7.3 Comparison of EPR imaging of 0.2 mM CTPO with various averages

#	Gradient Range G	Averages	LWHH G	S/N	Resolution	Time
1	All	4096	1.24	170	0.48	35'44"
2	-10 ~ -6.2	4096	1.26	165	0.51	27'30"
	-6 ~ 2.2	2048				
	-2 ~ 0 ~ 2	1024				
	2.2 ~ 6	2048				
	6.2 ~ 10	4096				

Other experimental parameters are: $G_{max} = 10$ G/cm, with gradient step size = 0.2

G/cm, 101 projections, rapid-scan width = 70 G, rapid scan frequency = 5 kHz.

Table 7.2 and Table 7.3 are summarized below:

Table 7.4 Comparison of using variable averages or not

Sample	Method	Averages	LWHH G	S/N	Resolution
0.1 mM CTPO	Uniform averages	4096	1.20	110	0.36
	Variable averages		1.21	95	0.35
0.2 mM CTPO	Uniform averages	8192	1.24	170	0.48
	Variable averages		1.26	165	0.51

The results show that the variable average method is able to reduce experimental time while preserving image quality.

7.2 EPR Image Quantification

7.2.1 Dimension of the Subject

In a 2D spectral-spatial image, both the line shape and 1D spatial information are provided. While the spectral slice provides line shape information, the spatial axis provides dimension of the subjects along the Z-axis (the main magnetic field direction). This information can be used to back-calculate the sample size.

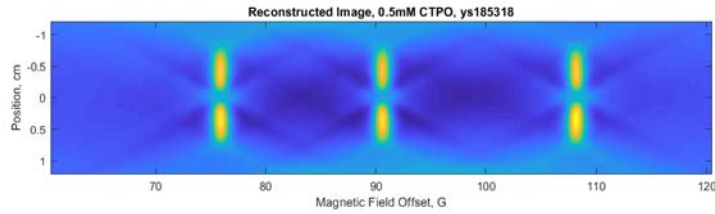
The size of the feature on image can be identified in three ways:

(1) by colors seen by eyes:

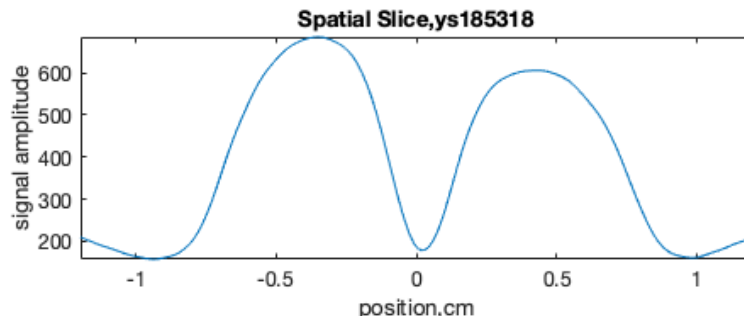
Since colors in a spectral-space image represent signal amplitude, regions with different colors from the background are where signal is located.

(2) by taking a first derivative of the spatial slice:

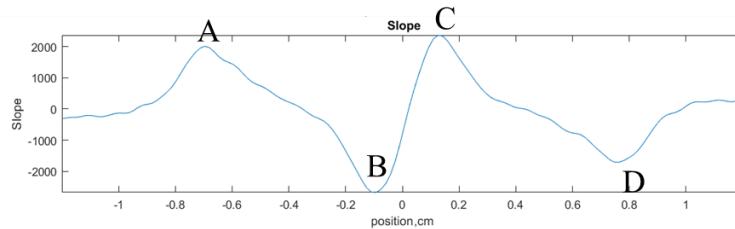
An example is shown below. Phantom is a 16 mm o.d. tube with 2 mm thick divider in the middle. EPR image, spatial slice and its first derivative is taken sequentially (Figure 7.4):



(a)



(b)



(c)

Figure 7.4 Spatial analysis of image
 (a) reconstructed image; (b) spatial slice; (c) first derivative of (b).

Experimental parameters are: $G_{max} = 10 \text{ G/cm}$, with gradient step size = 0.2 G/cm , 101 projections, 2048 averages for each projection. Rapid-scan width = 70 G , rapid scan frequency = 5 kHz .

On the first derivative curve of the spatial slice, positions are recorded at the peaks or valleys, i.e. where the second derivative equals 0. They are called inflection points where the concavity changes and are used to define the width of the peak. The inflection points in Figure 7.4c corresponding to where the feature starts and ends. There is a total of 4 inflection points, at positions (cm):

$A = -0.696, B = -0.092, C = 0.126, D = 0.763.$

The length of the compartment in the tube along the z -axis is 6 mm, corresponding to

$$|A-B| = 0.604$$

$$|C-D| = 0.637$$

The thickness of the divider = 2 mm, corresponding to

$$|C-B| = 0.21$$

The calculated values from the image match pretty well with the actual physical dimensions of the phantom. This spatial information can be extracted to create a 2D spatial image, see Section 7.2.2 for an example.

(3) By setting the threshold value for the features:

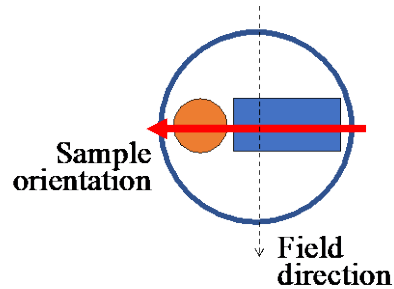
If the image is derived from a 2D matrix of amplitude values, the region of the feature can be bounded by using a threshold value defining the peaks (refers to Section 7.2.2), and its length along the spatial axis is obtained.

7.2.2 Radical Quantification

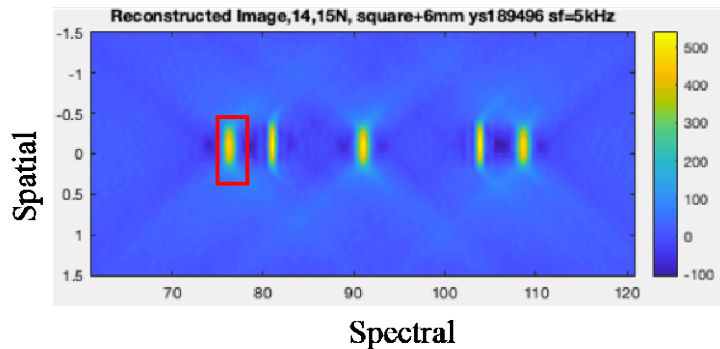
The power of the EPR technique includes its ability to quantify radicals [1]. The integral under a rapid-scan absorption spectrum, or the double integral under a CW derivative spectrum is linearly proportional to the number of spins in the system. In a 2D spatial-spectral image, the quantity of spins in different regions can be measured. There are two ways to quantify an image: the numerical approach, and the raster-image approach.

1. Numerical approach

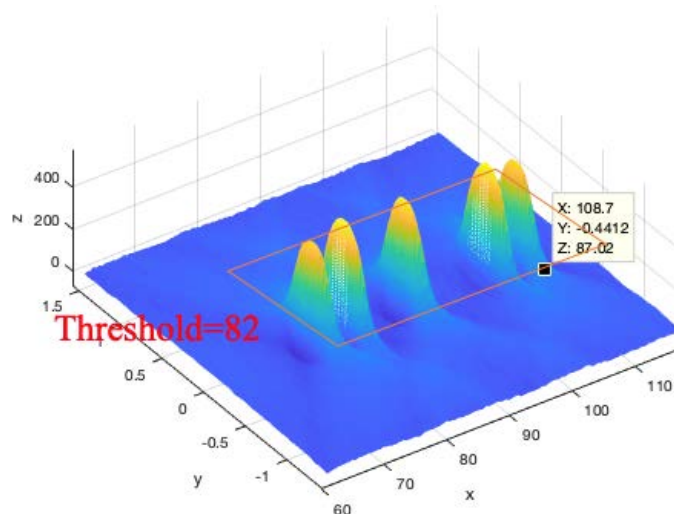
The image is actually a 2D matrix of numbers representing signal amplitudes, with one dimension for field and the other for space. The numbers become significantly larger when they enter a zone with an EPR feature. As a result, a threshold value is set to identify the region; any numbers above this threshold value is regarded as an EPR feature, while numbers that do not reach this standard are regarded as background. Figure 7.5a is the diagram of one phantom, a 6 mm tube with 0.53 mM ^{15}N -PDT and a 12×6 square tube with 0.5 mM CTPO that are imaged together (see Figure 7.13 in Section 7.6 for tube details). They are inserted in the 3D printed sample holder then put into the 25 mm resonator as shown in Figure 7.5a. The gradient is along the magnetic field direction and does not distinguish between the samples in the two tubes.



(a) Diagram of the phantom, not to scale



(b) 2D spatial-spectral image. The red box roughly identifies a feature.



(c) 3D representation of the image. X-axis is spectral, Y-axis is spatial, Z-axis is signal amplitude, so the volume of the ‘hills’ represents spin concentration.

Figure 7.5 Steps for image quantification

Experimental parameters are: $G_{\max} = 10$ G/cm, with gradient step size = 0.4 G/cm, 51 projections, 2048 averages for each projection. Rapid-scan width = 70 G, rapid scan frequency = 5 kHz.

The reconstructed image is shown in Figure 7.5b and a square box is used to roughly define a feature. Since the two samples have different hyperfine splittings, they are easily separated. To calculate the volume of each of the feature region, since the amplitude of the foot of the ‘hill’ is measured to be 87, a threshold value of 82 (or some other values close to 87) is selected (Figure 7.5c), and a numerical integral under a 2D surface defined by the square box is carried out for each of the 5 ‘hills’, using the threshold value to separate ‘hill’ from ‘background’. The volumes of these ‘hills’ are, 5.0, 3.4, 5.1, 3.6, 5.2 in arbitrary units.

Obviously, the first, third and last hill are together generated by CTPO, while the second and fourth hills are together generated by ^{15}N PDT. Adding this up volume we can calculate the ratio of spins in these two samples,

$$\frac{14\text{N CTPO}}{15\text{N PDT}} = \frac{5.0 + 5.1 + 5.2}{3.4 + 3.6} = 2.2$$

To verify the answer, the ratio of radicals was calculated from concentration and liquid volume. The CTPO solution has a concentration of 0.5 mM and volume of 1.48 mL, while the ^{15}N PDT solution has a concentration of 0.53 mM and volume of 0.68 ml, thus the ratio of spin is,

$$\frac{14\text{N CTPO}}{15\text{N PDT}} = \frac{0.5 \times 1.48}{0.53 \times 0.68} = 2.1$$

This is in good accordance with the results from image quantification.

A rapid-scan EPR absorption spectrum was also performed for the whole system (Figure 7.6):

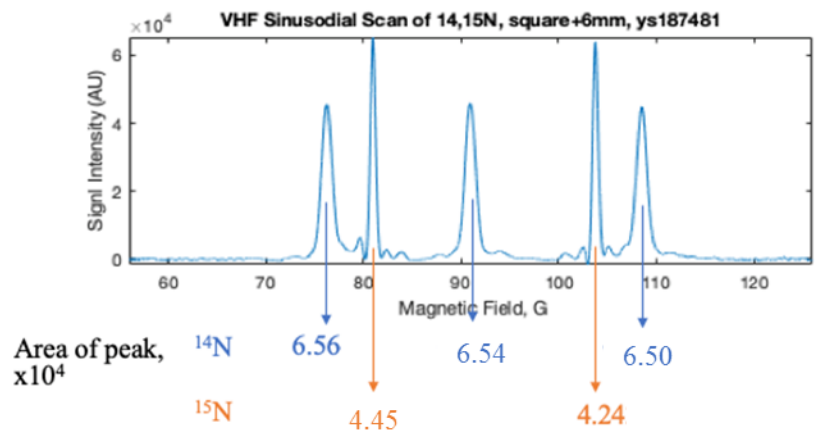


Figure 7.6 Rapid-scan EPR absorption spectrum of the system

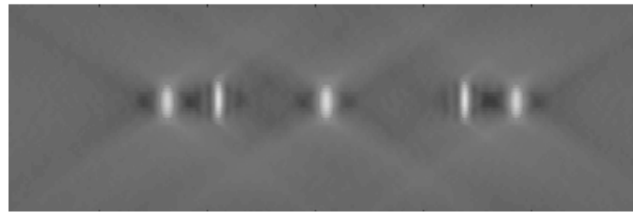
Parameters are: rapid scan frequency = 5 kHz, 10240 averages, Rapid-scan width = 70 G. 100 ns time base, 8192 points, 1024 on-board averages.

The integral under the absorption line is proportional to the total spin. With the use of a standard, we are able to get the absolute value. Two different species can be identified as belonging to ^{14}N CTPO and ^{15}N PDT. If these lines are separated far away from each other, we can integrate under each of the line and get the values separately (values listed at the bottom of Figure 7.6). The ratio of ^{14}N CTPO / ^{15}N PDT is 2.25, also in accordance with above calculations. Usually, an EPR spectrum is used to get the total number of spin while the image can define different sub-regions. For regions that are spectrally overlapped (e.g., contain same species), only a 2D spatial-spectral image can distinguish them by separating them along the spatial axis.

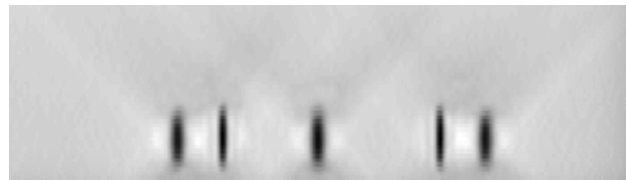
2. The raster image approach

If the matrix that generates the image is not available, and only a raster image (usually in 'jpg', 'png' or other format) is available, we can still quantify the EPR features by reading the intensity. A java-based, NIH developed, free image processing software called 'ImageJ' (version Fiji [177]) was used for quantification and the powerful image processing software Photoshop (version CC2018) is used for image preparation. ImageJ has been used intensively in many biology applications such as quantifying PAGE gel bands, fluoresce intensity, and counting cells. It has been extended to quantify EPR bands as well as reading the intensity.

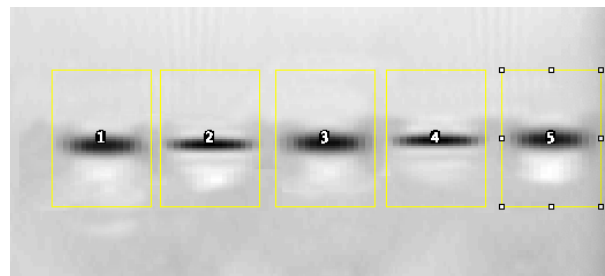
An example is shown below (same image as in Figure 7.5b is used):



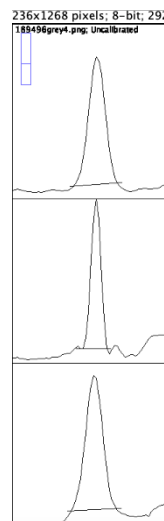
(a)



(b)



(c)



(d)

5748.205
3960.163
6262.619
4002.284
5677.548

(e) Table of peak areas generated in ImageJ (only 4 significant figures were used later)
Figure 7.7 Quantify EPR features by ImageJ

The procedures are:

- I. Convert color to grey scale by either MATLAB, ImageJ, or Photoshop; alternatively, one can plot an image in grey scale directly in MATLAB (Figure 7.7a).
- II. Reverse the color so that darker color represents higher intensity (Figure 7.7b). This is the requirement for using ImageJ. This can be done in Photoshop, just by selecting 'reverse color' option.
- III. Reorient the EPR bands so they lay horizontally (Figure 7.7c). Since the ImageJ quantification tool was originally designed for PAGE gels, the protein bands are laid horizontally, so the ImageJ reads bands in a horizontal position. This can also be done with Photoshop by rotating the bands by 90°.
- IV. Then use the rectangular tool to put boxes around each of the EPR bands (Figure 7.7c). These boxes all have the same dimension automatically, so the comparison is done based on the same area. The box should be drawn in the manner that the height is larger than the width, which is also a requirement of ImageJ because of its original design for PAGE gel lanes.
- V. ImageJ then automatically plots the profiles for each EPR band as peaks representing the band intensity (the first 3 bands are show in Figure 7.7d). The

areas of the peaks in Figure 7.7d are first defined by the user by drawing the base lines then calculated and listed as in Figure 7.7e by ImageJ.

We can check the accuracy of this method by taking the ratio of the two bands. As already pointed above, the first, third and last EPR bands belongs to one radical species (^{14}N CTPO), the second and fourth bands belongs to the other species (^{15}N PDT), so the spin ratio of them are (only 4 significant figures in Figure 7.7e were used):

$$\frac{14N \text{ CTPO}}{15N \text{ PDT}} = \frac{5748 + 6262 + 5677}{3960 + 4002} = 2.22$$

This result is also in good accordance with actual value and this method is simpler.

The numeric approach is more accurate since the original result matrix is used. The raster-image approach is less accurate since some information is lost when converting matrix to raster image, and it relies on subjective human judgement. However, the raster-image approach is more general and is the only option when only a raster image is available.

Some other researches also used image software in EPR image processing. For example, R. Krzyminiewski [54], F. Hyodo [85], K. Matsumoto [178] [122] et al. used ImageJ to quantify signal intensity; S. Burks et al. used Photoshop in their EPR image [179].

In summary, from an EPR spectrum we can find the total number of spins in the system if we use a standard with known number of spins. From the 2D spatial-spectral image, we know how many different samples and different regions are there and the ratio

of the spins for each region, so it is possible to calculate the relative spin concentrations in each region.

7.3 Time Distribution in an Imaging Experiment

In the Python code, the ‘time()’ function is used to track the time used by each section of the experiment.

For an experiment of 4096 averages, $G_{max} = 10$ G/cm with 0.2 G/cm gradient step, the time used by each section is summarized in Table 7.5.

Table 7.5 Time distribution in an imaging experiment of 4096 averages using the field reversal background correction method

#	Step	Sub-step	Achievement	Time(s)
1	Set up experiment			0.06
2	Imaging (Loop through the projections)	Scan1	Set up instrument	0.10
			Sleep	0
			Data acquisition (Equals pressing Xepr “Play” button)	8.04
			Data export	1.52
		Scan2		9.7
			Total time of 1 projection	18.69
3	Save data			3.75
			Total time of whole experiment	1906” = 31’46”

From Table 7.5, to finish 1 projection (scan 1), theoretical time = $100 \text{ ns} \times 8192 \text{ points} \times 4096 \text{ averages} = 3.35 \text{ s}$, but it actually takes 8.04 s, so the efficiency is $3.35 \text{ s} / 8.04 \text{ s} = 42\%$. The remaining 4.7 s, which accounts for more than half the experiment process, is instrument overhead time. The cause of overhead time is discussed in Section 7.4.3. Since Xepr controls the digitizer SpecJet-II, it might be difficult to get rid of the overhead time unless a different digitizer is used.

Three of the major procedures - data acquisition, data export from digitizer to computer and data saving, were studied further for different numbers of data points (Table 7.6).

Table 7.6 Time (s) needed for each procedure (same time window)

Points	Procedure	Data Acquisition	Data Export from digitizer to computer	Data Saving	
	Software Time base	Xepr (controls SpecJet-II)	Xepr	Xepr	Python
65536	12 ns	4.51	9.3~9.9	N/A *	0.50~0.53
32768	25 ns	7.96	4.4~4.8	N/A *	0.25~0.28
16384	50 ns	8.01	2.2~2.5	4.24	0.125~0.15
8192	100 ns	8.03	1.1~1.2	2.08	0.06~0.07
Behavior		Discontinuous	linear	linear	Linear

* The Xepr new version is unable to take points more than 16384.

The data acquisition and transfer are performed using the SpecJet-II digitizer, which can only be done by the Xepr software. For data saving, an alternative is proposed using Python (Section 7.5) which is much faster than Xepr. While the data acquisition time shows a discontinuous behavior (see Section 7.3 on the discussion about digitizer), the export and saving time are linearly increased with number of points, which can be explained as the quantity of data increased.

Table 7.6 also reveals that data export becomes unreasonably long as the number of data points increases. However, this procedure can only be done by digitizer (SpecJet-II) controlled through Xepr, so it's unlikely to get shortened until the digitizer is changed.

In addition, turning the computer off then on, and restarting the Xepr software or Python program can effectively reduce data acquisition time, by cleaning cache and releasing memory space.

7.4 Limitations

7.4.1 Software Limitations

1. Number of projections

For the imaging reconstruction program, which is written in MATLAB, there is a limitation on the number of projections that a computer can handle: for a laptop (SONY model: SVF142C29L, intel core i7), the maximum is 201; for a desktop (DELL model: Precision T3610) the maximum is 401. That puts some limitation when one decides how many projections to use.

2. Number of points

The Xepr ‘version 2.6b.139, 2015-Oct-15 (11:38)’ (referred to as ‘old version’) can save a maximum of 65536 points, for either EPR spectra or imaging. Xepr ‘version 2.6b.167, 2017-Jul-17 (14:46)’ (referred to as ‘new version’), can save a maximum of 65536 points for spectra, but only a maximum of 16384 points for imaging (the size limit of Xepr 2D dataset). As a result, time base has to be increased in order to cover the same width of time window.

3. Maximum averages

Due to the limitations on the CAEN power supply, the maximum averages that can be done for the high gradients, i.e. 9.45~10 G/cm (in magnitude), is 10240. Larger values trigger a fault. For gradient values equal to or smaller than 9.4 G/cm (in magnitude), there is no limitation on the number of averages.

7.4.2 CAEN Power Supply Limitations

Two CAEN power supplies are used in the image experiment: the FAST-PS-1K5 30-50 module is used to control the main magnet current; the FAST-PS 2040-600 module is used to control the gradient coil current. For the Z-coils shown in Figure D9 in Appendix D the FAST-PS 2040-600 module can provide a maximum gradient of 10 G/cm. Through practice it is found that the maximum time the FAST-PS 2040-600 module can stay at high gradient (magnitude > 9.4 G/cm) is around 20 s; otherwise it will trigger an error (Figure 7.8) and the limitation is likely on over-power. Smaller gradients do not have such limit.



Figure 7.8 Error message shown on CAEN

The FAST-PS-1K5 30-50 module responsible for producing the main field is fairly reliable and does not have limitation for the coils of the 250 MHz spectrometer.

The old imaging system with other gradient coils used a Bruker BMC-20 to control gradient values and did not have the same limitations as the CAEN supplies, but could not be controlled over the ethernet.

7.4.3 SpecJet-II Digitizer

Many studies have been performed on the SpecJet-II digitizer (Bruker), to understand its behavior and find the cause of instrument overhead time. It was found that the data acquisition time in SpecJet-II is discontinuous in a stepwise manner shown in Figure 7.9. Here the number of points = 16384 and the number of averages = 4096 is fixed, while the time base is varied from 10 to 180 ns in 10 ns steps (scan frequency is 5 kHz, 4 cycles per trigger). One would intuitively think that with the same number of points, larger time base means longer time window, and subsequently more time is needed to finish the process. In reality, the time needed is divided into a series of steps; within each step, it always takes the same time no matter how large the time base is. The value of time base where a new step rises, is in a binary fashion, which means the next step is always twice as long as its predecessor.

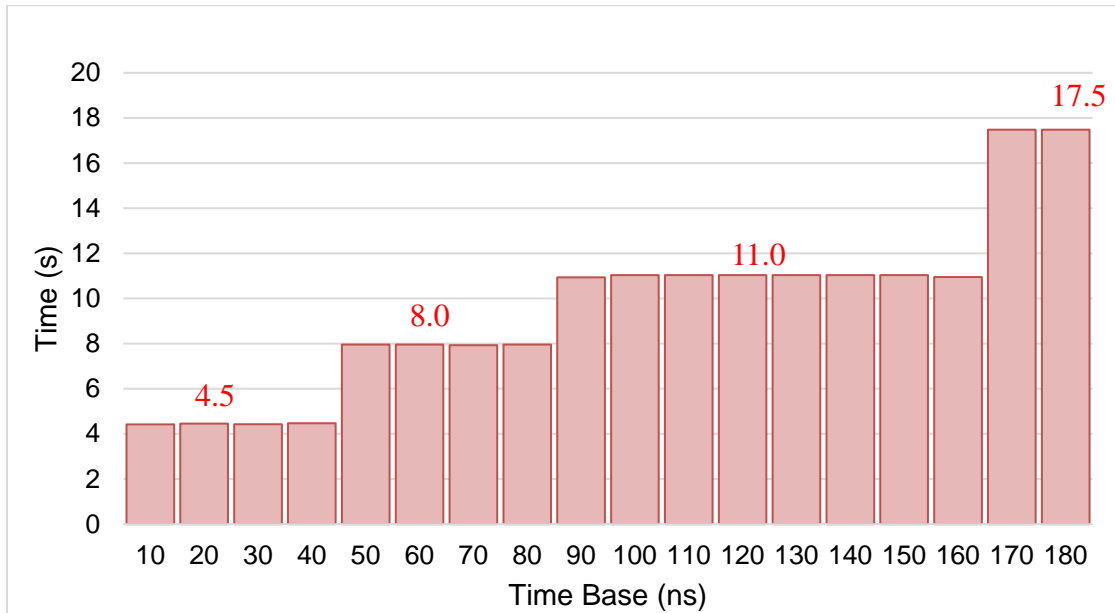


Figure 7.9 SpecJet-II data acquisition time

Through multiple testing it was found that the heights of the steps (the data acquisition times) are fixed, being 3.0 s (not shown in Figure 7.9), 4.5 s, 8.0 s, 11.0 s, 17.5 s. Originally my colleague Joseph suspected the stepwise behavior was caused by on-board average, i.e. data are passed in bundles of 256 or 1024, or any values equals to number of on-board average; however it is found that on-board average does not affect data acquisition time (see Table 7.9). It's likely an intrinsic property of the internal firmware of the SpecJet-II.

The widths of the steps (range of time base) vary as the number of averages or points changes. For the example shown in Figure 7.9, the first step ends at 40 ns, the second step ends at 80 ns, and third step ends at 160 ns, the fourth step ends at 320 ns (not shown). If more points are used such as 32768, the first step ends at 20 ns, the second step ends at 40 ns, and the third and fourth step ends at 80 ns and 160 ns. Four cases with different data points are shown together in Figure 7.10 for comparison.

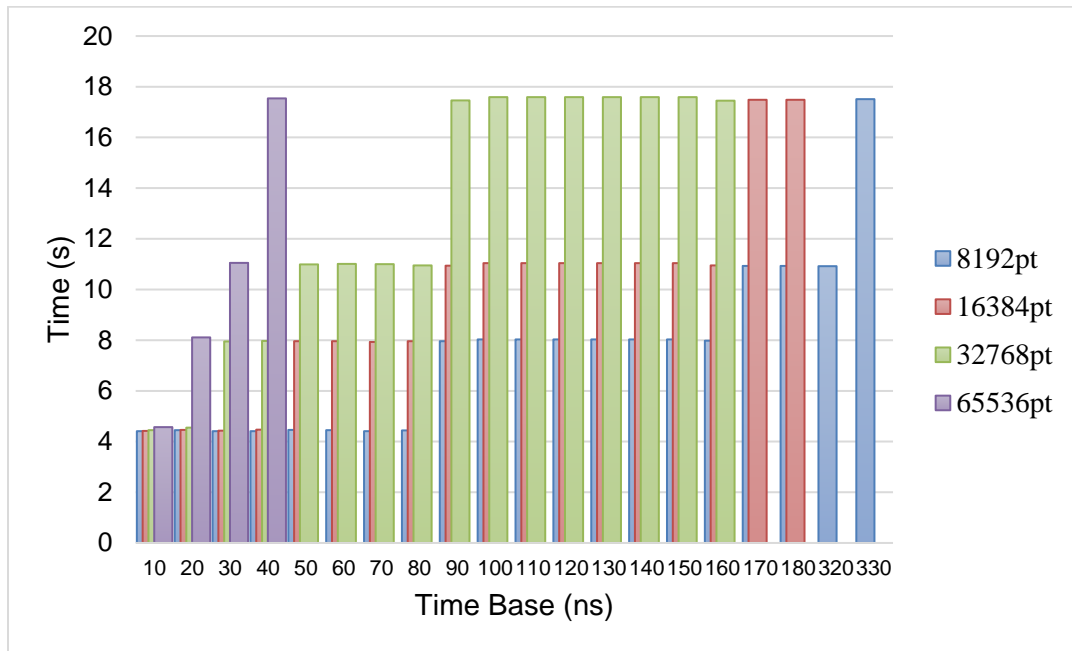


Figure 7.10 Data acquisition time with different points (same averages)

Other parameters in all cases are same: 4096 averages, rapid scan frequency is 5 kHz, 4 triggers per cycle.

The information in Figure 7.10 is summarized in Table 7.7.

Table 7.7 Summary of the step boundaries for different points

Points	Binary	Time base (ns) where the step ends			
		Step1	Step2	Step3	Step4
65536	2^{16}	16	22	32	
32768	2^{15}	20	40	80	
16384	2^{14}	40	80	160	
8192	2^{13}	80	160	320	
Data acquisition time (s)		4.45	8.0	11.0	17.45

Together, Figure 7.10 and Table 7.7 show the following trends:

- (1) Using more averages or more points tend to squeeze the region of time base into prior steps;
- (2) Although the widths of the steps are doubled for neighboring steps, the heights of the steps increase less than doubled, which means that using later steps within a 'block' is more time-efficient. See calculations below as well.

The SpecJet-II digitizer efficiency is calculated as follows:

$$\text{Digitizer efficiency} = \frac{\text{Theoretical data acquisition time}}{\text{Actual data acquisition time}} \quad (7.1)$$

$$\text{Theoretical data acquisition time} = \text{time base} \times \text{number of points} \times \text{averages} \quad (7.2)$$

As the example shown in Table 7.5 in the previous Section 7.3, using 100 ns time base, the digitizer efficiency is as low as 42%. However, if we shorten the time base to 80 ns, the theoretical data acquisition time shortens to 2.68 s (80 ns × 8192 pt × 4096 avg.), while the actual time shortens to 4.45 s (by checking either Figure 7.10, or Table 7.7, to

find out the time base region where 80 ns belongs to), the digitizer efficiency can actually be increased to 62% (= 2.68 s / 4.45 s).

The digitizer efficiency for other steps is summarized in Figure 7.11.

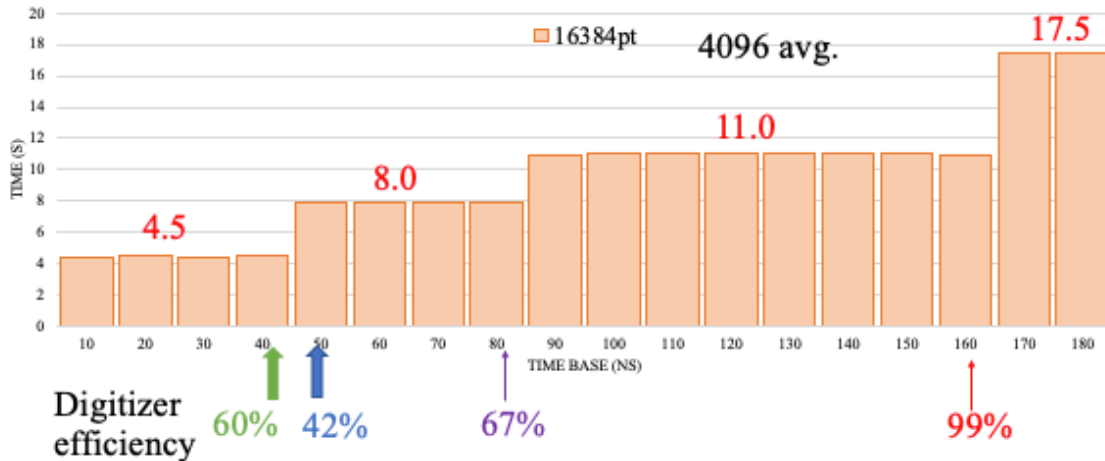


Figure 7.11 SpecJet-II Digitizer efficiency using different time base

Experimental parameters were: 16384 points, 4096 averages, rapid-scan frequency is 5 kHz, 4 triggers per cycle.

From Figure 7.11 two strategies can be applied to improve SpecJet-II digitizer efficiency by selecting time base and points.

- (1) Within a step, choosing larger time base, since any time base within that step takes the same actual data acquisition time.
- (2) Selecting later steps (means larger time base), since the height of the step (actual data acquisition time) grows slower than the width, as a consequence of the trend 2 mentioned above. When choosing 160 ns time base, the digitizer efficiency can be as high as 99%.
- (3) The time window should contain at least 3 cycles due to the deconvolution program. For example, for a rapid scan frequency of 5 kHz, 1 period is

2×10^{-4} s. For 16384 points, using either 40 ns or 50 ns time base will cover at least 3 cycles, but the 40 ns time base case is more efficient.

As an extension to Figure 7.11, the maximum digitizer efficiency for other points are calculated as well (Table 7.8)

Table 7.8 Maximum digitizer efficiency and the time base to get there

Points	Maximum digitizer efficiency	Time base (ns) when maximum efficiency is achieved	Current efficiency
65536	92%	15	N/A *
32768	98%	80	N/A *
16384	99%	160	42%
8192	98%	320	40%

* The Xepr new version is not able to run at that many points

The data in Table 7.8 shows that SpecJet-II can be very efficient as long as proper parameters are chosen which was unnoticed to the lab previously. However, it is not always realistic to using large time base in order to achieve high digitizer efficiency. Firstly, large time resolution means fewer points to define a feature which is undesirable. Practically time base should not go beyond 100 ns. Secondly, SpecJet-II is a fast digitizer with 1 ns time resolution, always using large time base does not take full advantage of the instrument, and a lower resolution digitizer is usually cheaper.

A solution to this paradox is going up in the number of points, as the trend (1) revealed in Figure 7.11, so that higher efficiency (> 90%) will appear even with smaller time base. This solution also provides extra benefit of increased time resolution and better usage of expensive instrument. However, the Xepr 'new version' is not able to go beyond 16384 points, which means the digitizer efficiency that can be achieved practically is only 40~60 %. An alternative is created by using Python, which allows going up to 65536 points. The Python approach will be described in Section 7.5.

Besides time base, average and points, a fourth parameter in SpecJet-II, the on-board average, can also affect the digitizer efficiency. On-board average is the quantity of data sent to the computer at a time. One of the advances of the SpecJet-II was an increase from 1024 on-board averages in SpecJet I to a maximum of 65536 on-board averages in SpecJet-II. For an experiment with same number of averages (4096), data acquisition times were recorded when choosing different on-board averages, see Table 7.9.

Table 7.9 On-board averages and data acquisition time (s)

On-board averages	256	512	1024	2048	4096
Data acquisition time (s)	4.40	4.42	4.43	4.43	3.98

Other parameters are same: 4096 averages, rapid-scan frequency 5 kHz, 8192 points, 80 ns time base.

Table 7.9 reveals that, if the number of on-board averages equals the total number of averages, data acquisition time will be reduced; this may provide another approach for shortening the experiment. If on-board averages is selected to be smaller than total averages, the data acquisition time are the same.

7.5 3D-Printed Sample Holder

Glass or quartz tubes are good for imaging but are fragile and may be difficult to use for some shapes of phantoms. With the development of 3D printing technology, custom-shaped containers can now be used. Three examples are shown in Table E1 in Appendix E.

7.5.1 How to Create 3D-prints

First, the 3D model is drawn using software such as Sketchup (Trimble Inc., <https://www.sketchup.com>), Solid works or 3dMax. The model should be created in a way that will facilitate 3D printing. A few tips are listed here. If a model is composed of different parts, they should be drawn separately then installed together after the printing is finished. If a shape contains concave spaces, try to re-orientate the object to avoid the addition of unwanted supporting materials (see example #2 in Table E1 in Appendix E). All the objects should be closed 3D objects. The models created in software are exported in a general format of 'stl', which are opened in computers connected to 3D printers. Models are printed on the 3D-printers in the Richie School of Engineering and Computer Science. The layer thickness and wall thickness can be controlled through fiber extrusion diameter. For example, to get finer texture one should use thinner layers, but this also consumes more material and requires much longer printing time. It is necessary to check the printer once in a while as errors might occur. A test tube for EPRI takes 2~3 hours to print.

7.5.2 3D-print Material

The technique of 3D printing has improved in a short time. There are a huge variety of printers as well as materials to choose from. For our experiment purpose, the material must not have an EPR signal. Several common plastic materials are used here.

1. ABS (Acrylonitrile butadiene styrene)

This plastic is high in strength and easy to modify by acetone bath. However, due to the toxic gas released during the filament heating process, it has been gotten rid of by

the Ritchie School of Engineering and Computer Science (RSECS) and is no longer available there. This material has many selections of color and can be glowing/fluorescent and transparent.

2. PLA (Polylactic acid)

This is environmentally friendly and is the only option now at the RSECS. PLA provides fine texture, but is less strong than ABS.

3. HIPS (High Impact Polystyrene)

Dr. George Rinard printed HIPS, which is the only material that was found to be water-proof.

7.5.3 Waterproof

The 3D-printed objects are usually not water tight. For liquid sample holders, it has to be water proof. There may be 3 ways to make a 3D printed object water proof.

1. Control the layer thickness

It is hard to conclude what thickness is needed, since there is a tradeoff between layer thickness and the number of layers. Thicker layers mean a smaller number of gaps, while thinner layers mean smaller gaps, both of which contribute positively to being water proof. Also, it takes longer to print with thinner layers. It might be better to try a few layer thicknesses then find the one that is not leaking.

2. Acetone Bath

This method only works for ABS. This method is used to smooth the surface of ABS material and can create water proof materials. From my experience, the procedures are: first wrap the inner surface of a beaker with paper towel, next use a wash bottle to spray acetone on the paper towel until it is fully soaked, then put the ABS 3D printed object in the middle of the beaker and cover with glass lid. After exposure to the acetone vapor for 2-3 hours, the object will become smooth and shiny. One should watch the process occasionally and use the tweezers to take the 3D printed object out to check, since exposure for too long will cause the melting and deformation of ABS plastic. There are some other ways to do the acetone bath, which can be found online with Google and YouTube. The acetone over-treated ABS tubes sometimes show cracks after one year because the treatment made them crispy (Figure 7.12).



Figure 7.12 Acetone over-treated ABS tubes have shiny finish but may develop cracks after one year.

3. Waxing

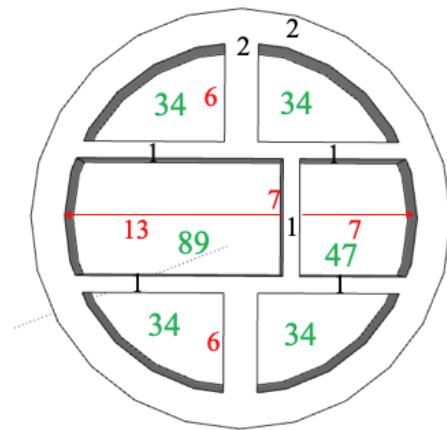
This is more laborious and was not attempted. It would be difficult to do inside intricate designs. Again, the wax should neither react with the sample, nor generate EPR signal.

7.6 Imaging with Multiple Samples

The ability of EPRI to image multiple samples simultaneously is demonstrated. This may serve as a prototype of imaging multiple organs/tissues *in vivo*. First, a specially designed sample holder was 3D printed; then samples were imaged separately to record their signal intensities; finally, samples whose intensity do not diverge too much were used to image together.

1. Sample holder

A 3D printed sample holder for the 25 mm CLR that was designed in Sketchup software (Trimble Inc., <https://www.sketchup.com>) is shown in Figure 7.13. It was purposefully created with 6 compartments of 3 different sizes to hold samples of different sizes and shapes.



(a)



(b)

Figure 7.13 Sample holder for 25 mm CLR.

(a) Section of the model, units are mm or mm² (b) photograph of 3D prints, sample holder and lid, in HIPS material

The round sample holder has an o.d. of 25 mm. The red numbers (mm) are the length of the divider or dimension of the compartments; the black numbers (mm) are the divider or wall thickness; the green numbers are the cross-section area (mm²) of each compartment, which can be derived directly from the Sketchup model. The height of the printed sample holder was either 45 mm or 75 mm. The 45 mm one can be included in the resonator cavity, while the 75 mm one extends the whole length of the resonator cavity. The model is 3D printed either in HIPS (High Impact Polystyrene) or PLA (Polylactic acid) plastic with extrusion width of 0.5 mm or 0.25 mm. After a water proof test, only the HIPS prints are found to able to hold liquids.

2. Sample selection

Different samples in different tubes that were already available in the Eaton lab were selected and the EPRI intensity was measured and summarized in Table 7.10. All samples were sealed.

Table 7.10 Summary of EPRI results of samples in the Eaton lab

Sample	Number of lines in EPR spectrum	External tube dimension (mm)	S/N	Signal Amplitude (a. u.)
0.5 mM CTPO	3	12 × 10 Square tube	152	1167
0.2 mM Trityl-CD3	1	4 mm	72	736
0.2 mM CTPO	3	5 mm	52	291
0.5 mM Trityl-CD3	1	4 mm	150	568
0.53 mM CTPO	3	4 mm	69	272
LiPc, polycrystalline	1	4 mm	62	376
¹⁵ N mH CTPO-d ₁₃	3	4 mm	61	428
0.53 mM PDT	3	6 mm	271	1331
0.2 mM ¹⁵ N CTPO-d ₁₂ in ethanol	2	4 mm	71	377
¹⁴ N mono radical	3	4 mm	24 *	90
0.2mM OX063+HEPES	1	4 mm	55	768
0.4mM ¹⁴ N PDT in Toluene	3	4 mm	18 *	118
0.5mM ¹⁵ N-Proxyl d ₁₅	2	4 mm	22 *	213
0.5mM ¹⁵ N-Proxyl d ₁₅	2	4 mm	36	156
Tempone d ₁₆ in sucrose octaacetate	1	4 mm	4 *	31
BDPA, solid	1	4 mm	305	19,620
1mM ¹⁴ N Proxyl	3	5 mm	29	103
1mM Tempol	3	5 mm	38	442

* Signal is too weak relative to rapid scan background, or the sample is too weak to produce a clear image.

Samples are listed in arbitrary sequence.

Samples with very weak signals were excluded from the study. Samples with similar signal amplitude were selected for simultaneous imaging so that they can be seen together, and the following 6 samples were selected (Table 7.11). The linewidth of each

sample is measured individually using slow scan frequency and small sweep width so signal bandwidth is smaller than resonator bandwidth for all samples.

Table 7.11 Linewidth of each sample by itself at 2.2 kHz, no gradient

#	Sample	Sweep width (G)	LW (mG)	BW _{sig} (MHz)	Literature value for LW (mG)
(a)	0.53 mM CTPO in H ₂ O	50	1300	0.42	1200
(b)	0.2 mM CTPO in H ₂ O	50	1200	0.46	
(c)	0.2 mM ¹⁵ N CTPO-d ₁₃ in ethanol	50	400	1.38	
(d)	0.2 mM trityl-CD ₃ in H ₂ O	5	40	1.38*	50 [168]
(e)	0.5 mM ¹⁵ N mHCTPO-d ₁₂ in H ₂ O	50	900	0.61	
(f)	particles of LiPc	5	83	0.66*	38 [176]

Parameters used: rapid-scan frequency is 2.2 kHz, time base 20 ns, 65536 points, 20480 averages.

* The bandwidth would be 15 and 6.3 MHz for (e) trityl and (f) LiPc respectively, if 50 G sweep width were used.

3. Images

The data acquisition parameters are: RF = 262 MHz since the home-built resonator is tuned to around 260 MHz. Rapid-scan frequency = 2.454 kHz, which is the lowest frequency one can get. The capacitors are parallel connected, each branch has three spots. Since the largest capacitors in the lab are 1 μF, this required 3 μF in each branch, and the total capacitance is 1.5 μF.

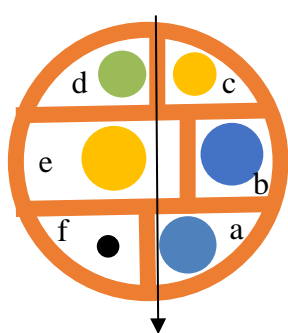
$$f = \frac{1}{2\pi\sqrt{LC}} \quad (7.3)$$

Inductance $L = 3.43$ mH, capacitor $C = 1.5$ μF, so rapid-scan frequency is around 2.2 kHz and the coil driver was tuned to be 2.454 kHz.

Rapid-scan sweep width is 50 G to cover all 3 lines of the nitroxides; center field = 94 G, on-board averages = 1024. Incident RF power was selected (25 dB attenuation,

equals to 0.103 mW, or 2.54 mG B_1) such that all signals were in the linear response regime.

Since the 2D spatial-spectral image only distinguishes regions along the direction of magnetic field, samples with the same kind of hyperfine splitting patterns were arranged along the Z -axis so they can be separated. Samples with different hyperfine splitting patterns were put at the same Z -axis position, because they have already been separated spectrally. A sample arrangement is shown in Figure 7.14.



Samples (from left to right)

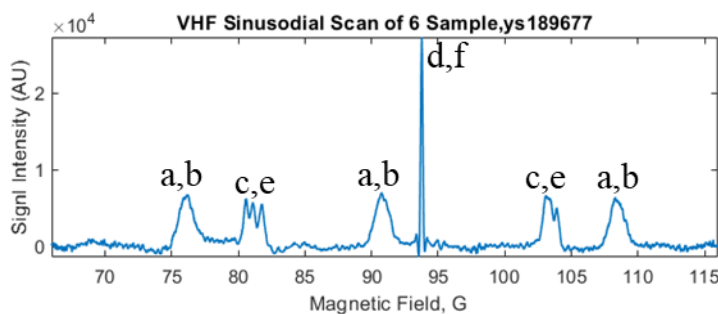
(d) 0.2 mM Trityl-CD₃; (c) 0.2 mM ¹⁵N CTPO-d₁₃ in EtOH

(e) 0.5 mM ¹⁵N mHCTPO-d₁₂; (b) 0.2 mM CTPO

(f) LiPc; (a) 0.53 mM CTPO

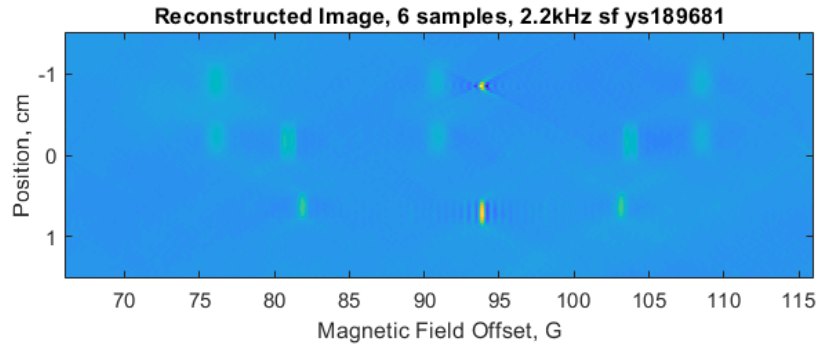
Magnetic field direction

(a) diagram, not to scale

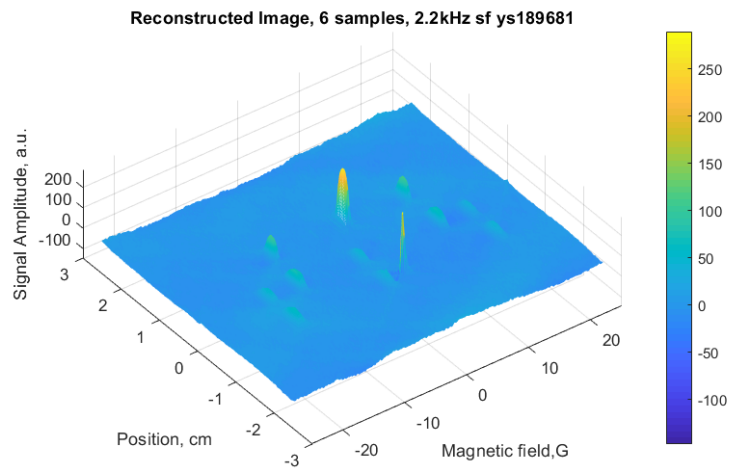


(b) zero-gradient spectrum of six samples.

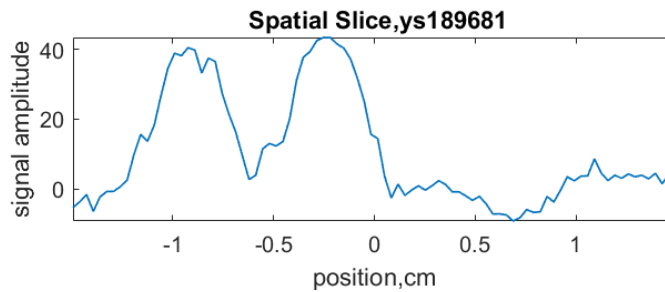
The peaks in this spectrum are labeled with letters that designate tubes in above figure (a).



(c)



(d)



(e)

Figure 7.14 Spectral-spatial image with 6 samples all be seen (a) sample arrangement diagram, (b) zero-gradient spectrum, (c) 2D spectral-spatial image in which all 6 samples all be distinguished, (d) 3D plot of (c), (e) spatial slice of (c) at field position 90.8 G (corresponding to the ^{14}N nitroxide middle line), two samples are fully separated.

Parameters: rapid-scan frequency is 2.2 kHz, sweep width is 50 G, 20 ns time base and 65536 points. For spectrum (b) number of averages is 20480. For image (c), 8192 averages for each projection, $G_{\text{max}} = 10 \text{ G/cm}$ with 0.05 G/cm step, total 401 projections.

On image Figure 7.14 (c) color represents signal intensity. For this set of sealed samples that had been prepared previously in the Eaton lab, the intensity of nitroxide signals are weaker than trityl and LiPc, so they may be a little hard to see on image (c). (d) is a 3D plot of (c) and may display the features more clearly.

The linewidth of each sample is:

Table 7.12 Linewidth Summary

#	Sample	LW (mG)
(a)	0.53 mM CTPO in H ₂ O	1250
(b)	0.2 mM CTPO in H ₂ O	1200
(c)	0.2 mM ¹⁵ N CTPO-d ₁₃ in ethanol	530*
(d)	0.2 mM trityl-CD ₃ in H ₂ O	340*
(e)	0.5 mM ¹⁵ N mHCTPO-d ₁₂ in H ₂ O	960
(f)	particles of LiPc	320*

* Linewidth is broadened by wide sweep width (50 G).

Comments:

(1) On the zero-gradient spectrum, sample (a) and (b), (e) and (f) have the exact same splitting pattern, so their signals overlapped. Sample c and d have slightly different splitting patterns, so the signals are not quite overlapped and resulted in a broad peak.

(2) Samples that could not be distinguished on the EPR spectrum (Figure 7.14b) can now be distinguished on the 2D spectral-spatial image (Figure 7.14c), due to the separation on the spatial axis.

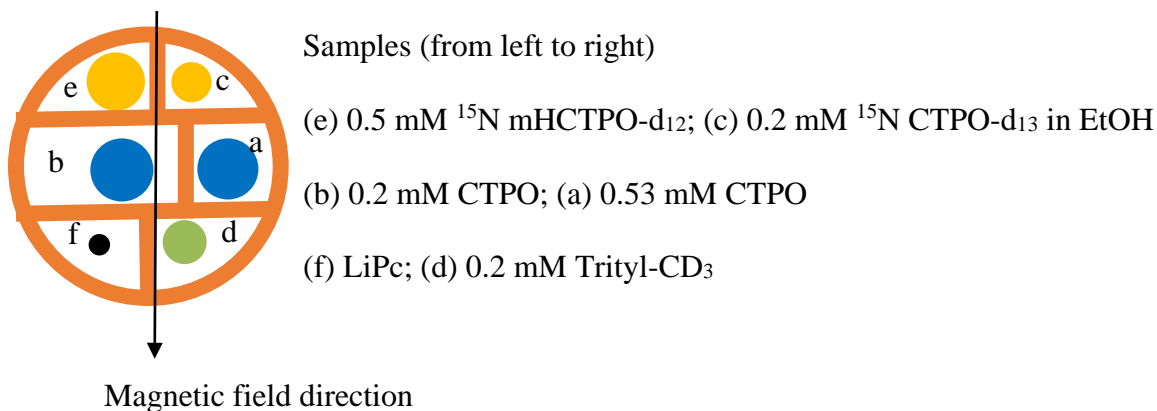
(3) The signal bandwidth should be less than resonator bandwidth to avoid linewidth broadening, which is the case for the 4 nitroxide samples (a~d) imaged with 50 G sweep. For the trityl and LiPc samples, the spectra were broadened by the 50 G sweep width used to image the full nitroxide spectra. This effect is demonstrated by comparing the deconvolved line widths for Trityl and LiPc individually at three selected scan widths (Table 7.13).

Table 7.13 Sweep width and full linewidth at half height of absorption spectra

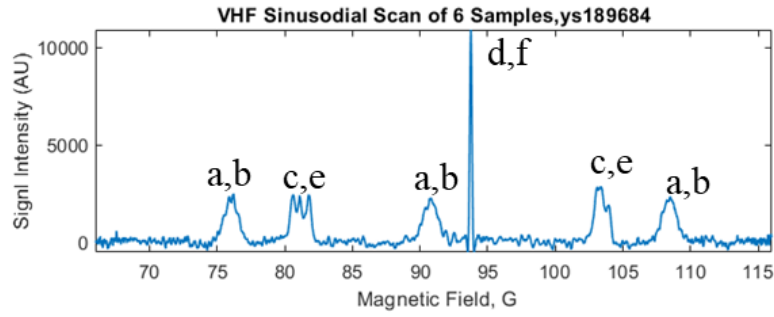
Sweepwidth	BW _{res} (MHz)	Trityl-CD ₃		LiPc	
		BW _{sig} (MHz)	linewidth, mG	BW _{sig} (MHz)	linewidth, mG
5 G	1.9	1.5	40	0.63	82
20 G	1.9	6	82	2.5	108
50 G	1.9	15	187	6.3	220

Parameters used: rapid-scan frequency is 2.5 kHz, time base 20 ns, 22686 points, 4096 averages.

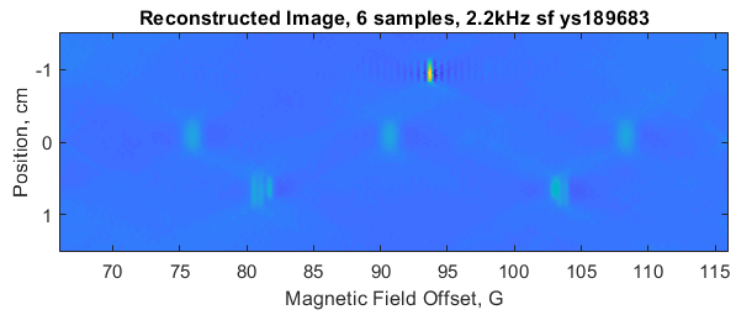
If the same samples are used but the arrangement is changed (Figure 7.15a) in such a way that samples with same hyperfine splitting pattern are at the same Z-axis position, then they cannot be distinguished. As a result, only 3 samples are seen in the spectral-spatial image.



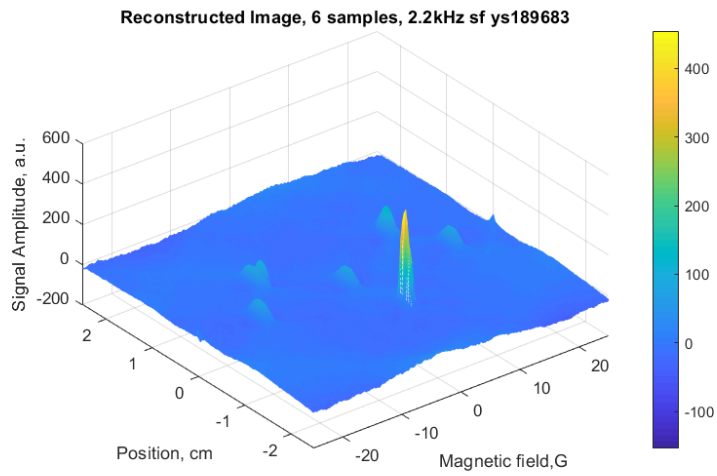
(a) diagram, not to scale



(b)



(c)



(d)

Figure 7.15 Spectral-spatial image of 6 samples with overlaps
 (a) sample arrangement diagram, (b) zero-gradient spectrum, (c) 2D spectral-spatial image, (d) 3D plot of (c).

Parameters used are same as Figure 7.14: rapid-scan frequency is 2.2 kHz, time base 20 ns, 65536 points, 8192 averages for each projection; $G_{\text{max}} = 10 \text{ G/cm}$ with 0.05 G/cm step, total 401 projections.

Figure 7.14b and Figure 7.15b shows the same spectrum, since the same set of samples is used. In the image (Figure 7.15d) the trityl and LiPc overlap at about -0.96 cm, the spectra of the two CTPO samples overlap at the 0.08 position; the two ^{15}N samples show a small difference in hyperfine splitting patterns due to the different solvents, at position about 0.62 cm. If 3D or 4D imaging were performed, all six samples would be distinguished in this case also.

In order to avoid line broadening, we need small sweep widths for narrow signals. EPR spectrum for a 5 G sweep width was performed to acquire one line of the nitroxide spectrum in the same scan as the trityl and LiPc spectra. The zero-gradient spectrum is shown in Figure 7.16.

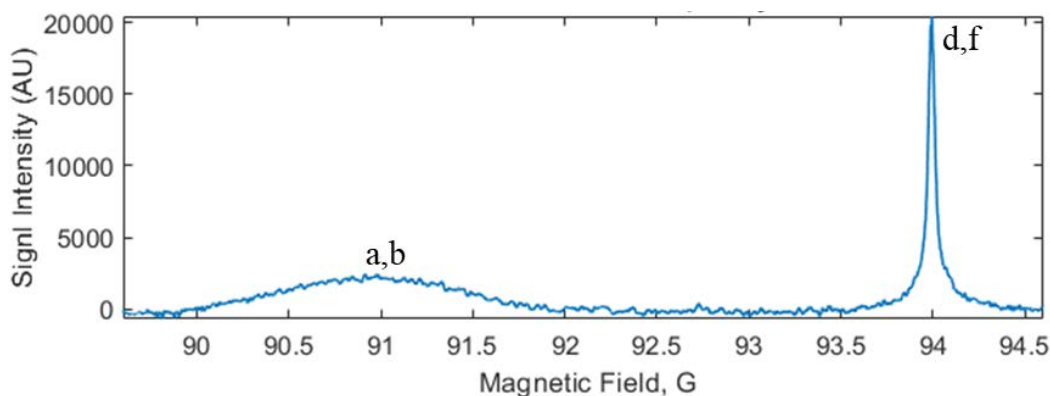


Figure 7.16 EPR spectrum of 5 G wide

Parameters used: rapid-scan frequency is 2.45 kHz, time base 20 ns, 65536 points, 10240 averages.

With the center field at 92.1 G, a 5 G rapid scan sweep at 2.45 kHz was just enough to encompass the trityl and LiPc samples (which superimpose) and the middle line of the nitroxide spectrum. The linewidth for trityl and LiPc is 44 mG, for ^{14}N nitroxide is 1100 mG.

EPR imaging for a 5 G sweep width was performed to capture only the trityl and LiPc signals (Figure 7.17).

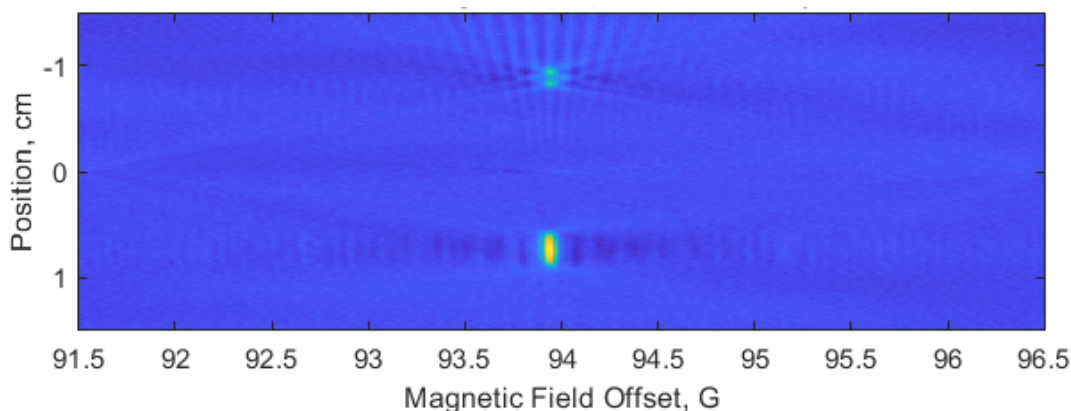


Figure 7.17 EPR image of 5 G wide

Parameters are: center field is selected to be 94 G to put trityl and LiPc signal at the middle, RS sweep width is 5 G, $G_{\text{max}} = 10$ G/cm with 0.05 G/cm step, 401 projections. 8192 averages for each projection, 20 ns time base and 22686 points.

The bright feature at spatial position 0.74 cm, field position 94 G comes from trityl; the other feature at 94 G is LiPc. The middle line of ^{14}N nitroxide was removed in deconvolution, and other lines of nitroxide were not shown in this image because they are outside this spectrum window (91.5~96.5 G).

From the spectral slices, linewidth for LiPc is 67 mG, for trityl- CD_3 is 69 mG; they are narrower than the 50 G wide image (Table 7.12). The linewidth can be further narrowed by increasing the number of projections. Under current hardware limitation,

one can get a maximum of 2001 projections (because CAEN power supply provides maximum gradient strength of 10 G/cm and a minimum gradient resolution of 0.01 G/cm) and 65536 points (the maximum number of points SpecJet-II digitizer offers).

Table 7.14 Linewidth of spectral slice of image with different numbers of projections

Number of Projections	Gradient step(G/cm)	Observed FWHH (mG)		Total data acquisition time
		Trityl-CD ₃	LiPc	
201	0.1	93	83	1h33'24"
401	0.05	69	67	3h6'8"
2001	0.01	55	67	14h38'15"

LW: linewidth of half height of absorption signal

Rapid-scan sweep width is 5 G, frequency is 2.5 kHz; 20 ns time base, 65536 points and 8192 averages; gradient strength $G_{max} = 10$ G/cm.

For the total data acquisition time listed in Table 7.14, 53% of the time is used by the digitizer to acquire data, 47% of the time is used for exporting data from the digitizer to the computer. For each projection it takes 14.52 s to acquire data, while the theoretical time = $20 \text{ ns} \times 65536 \text{ points} \times 8192 \text{ averages} = 10.74 \text{ s}$, so the digitizer efficiency is $10.74/14.52 = 74\%$. The overhead time is due to the way the digitizer is designed and built.

7.7 2D Spatial Imaging

The spatial information in the 2D spectral-spatial imaging can be abstracted and used to reconstruct a 2D spatial image. Since the spectral-spatial image only has spatial axis in one dimension, with only one pair of gradient coils being used, one can get a second spatial axis by rotating the sample. Alternatively, a second set of gradient coils could be added.

7.7.1 Principle

Suppose we have a round tube as the phantom, and the left half of the tube is filled with sample solution. The original point of the coordinate system for the phantom is set at the point of rotation. The tube was rotated for a series of degrees clockwise, from 0° to 180° , in a step of 10° (practically, 30° step may be enough). Because of the symmetry of the gradient, the tube only needs to be rotated 180° . The 2D phantom will always project onto the X -axis (axis perpendicular to field direction) and reveal itself as a line whose length corresponds to the length of the EPR feature along the spatial axis in the 2D spectral-spatial image.

The procedures are as follows, which takes advantage of the known geometry of the phantom. Firstly, take images at positions 0° and 90° relative to the field direction and get the lines projected on the X -axis, which represent the two physical dimensions of the phantom depicted as the blue box in Figure 7.18, this is where we start to compose the shape. Next, the phantom is rotated for a known degree δ , as the blue box is now at the position of the green box. However, the real shape of the phantom is a half-circle, so its shape should stay within the region defined by the two dashed red lines, and any areas that are outside the red boundaries (the dotted area) are wrong, otherwise their 'shadow' projected onto the X -axis will go beyond the boundaries. The dotted area in the green box is thus deleted and our shape is refined once. Then, we keep rotating in steps of δ and repeat the boundary check and delete processes until a total of 180° is reached. The shape is refined gradually after each rotation operation until a final shape is reached which is closer to the real shape.

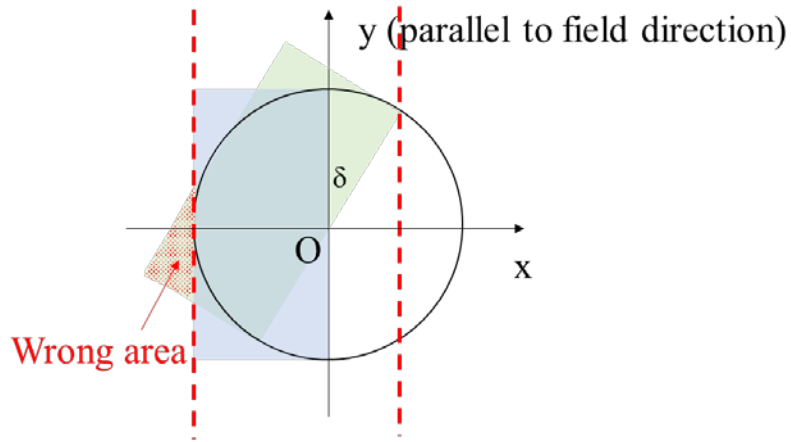


Figure 7.18 Illustration of the principle

The rotation operation is realized by using complex numbers and transformation between rectangular and polar coordinates (Figure 7.19).

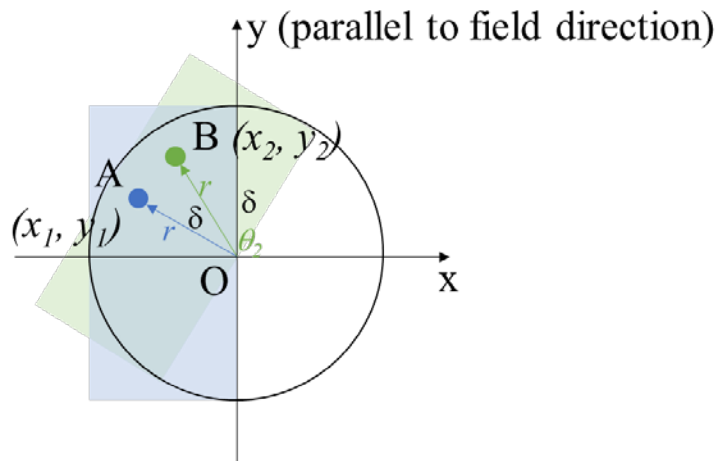


Figure 7.19 Illustration of the rotation operation

Continued from the scenario in Figure 7.18, a matrix of a certain amount of numbers composed of x, y coordinates (can be the pixel resolution) is used to represent the box. An arbitrary point A on the blue box with rectangular coordinates (x_1, y_1) can be represented by a complex number z_1 :

$$z_1 = x_1 + i * y_1 \tag{7.4}$$

which can be transformed into polar coordinates (r_1, θ_1) :

$$z_1 = r_1 * e^{i*\theta_1} \quad (7.5)$$

When the blue box rotates clockwise round the original point O to the position of green box by δ degree, point A becomes point B as (r_2, θ_2) in polar coordinates:

$$z_2 = r_2 * e^{i*\theta_2} \quad (7.6)$$

Similarly, its transformation back to rectangular coordinates is (x_2, y_2) :

$$z_2 = x_2 + i * y_2 \quad (7.7)$$

Since the magnitude of the rotation vector does not change, we have

$$r_2 = r_1 \quad (7.8)$$

$$\theta_2 = \theta_1 - \delta \quad (7.9)$$

which allows us to generate point B's x, y coordinates from its predecessor point A. The coordinate x_2 is thus used as the criteria to decide if point B is valid and should be retained or not.

The benefit of using complex numbers are: (1) much simpler equations for rotation compared to the rectangular coordinates, (2) avoid special situations such as negative magnitude or infinity (e.g., $\tan 90^\circ$) brought by sign change of sine and cosine functions in different quadrants, since the complex function in MATLAB will automatically categorize those situations.

7.7.2 2D Spatial Image with One Sample

The above scenario is put into practice here. The phantom is a 16 mm quartz tube with one chamber filled with 1 mM CTPO solution, imaged in the 16 mm CLR at VHF. Parameters are: rapid scan frequency is 5 kHz, rapid scan sweep width is 70 G, gradient

strength is 10 G/cm with 1 G/cm gradient step, number of averages is 2048. One image takes 2'23". Collecting all the rotations is completed in 45 mins.

The reconstructed 2D spatial image is shown in Figure 7.20.

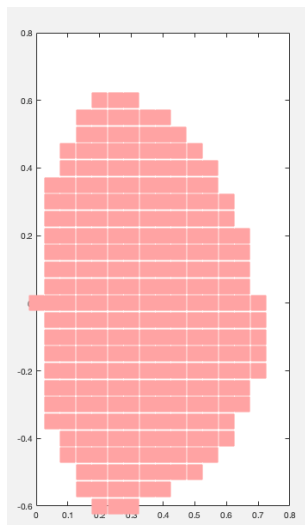


Figure 7.20 2D Spatial image using one-dimension gradient

Experimental parameters are: for each angle position, $G_{max} = 10$ G/cm, with gradient step size = 1 G/cm, 21 projections, 2048 averages for each projection, on-board average is 1024 and took 2'23". Phantom was rotated from 0° to 180° with 30° step, which took 18 min total. Rapid-scan width = 70 G, rapid scan frequency = 5 kHz.

The image depicts the phantom shape fairly accurately.

7.7.3 Image with More Samples Simultaneously

The same sample holder described in Figure 7.13 was used, and 2 tubes with different shapes and radicals were put along the magnetic field. The tube arrangement and dimensions are marked in Figure 7.21.

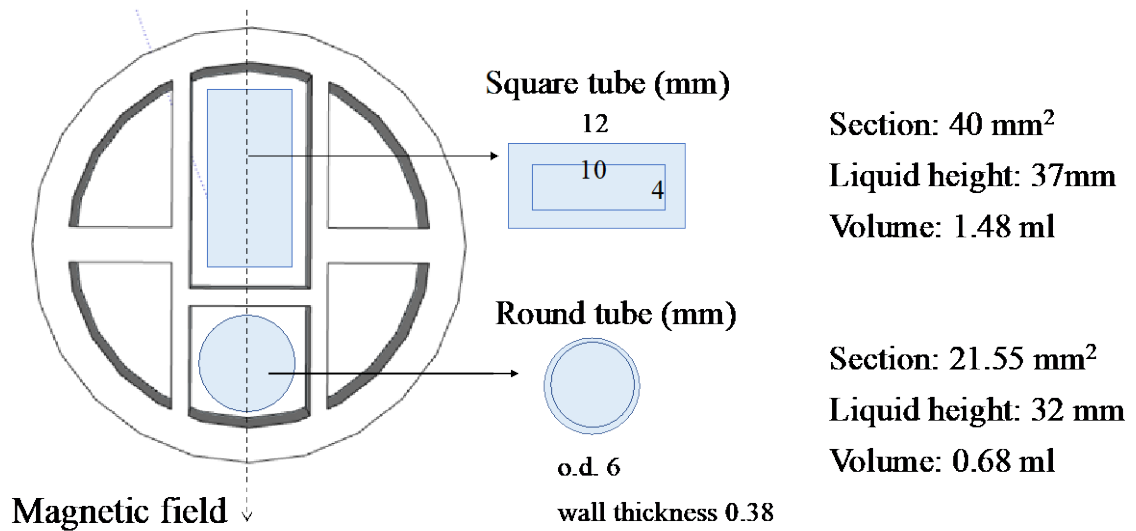


Figure 7.21 Tube arrangement and dimensions

The phantom is rotated in 30° steps for a total of 180° and spatial-spectral images were taken at each position. One of them (at start position 0°) is shown in Figure 7.22.

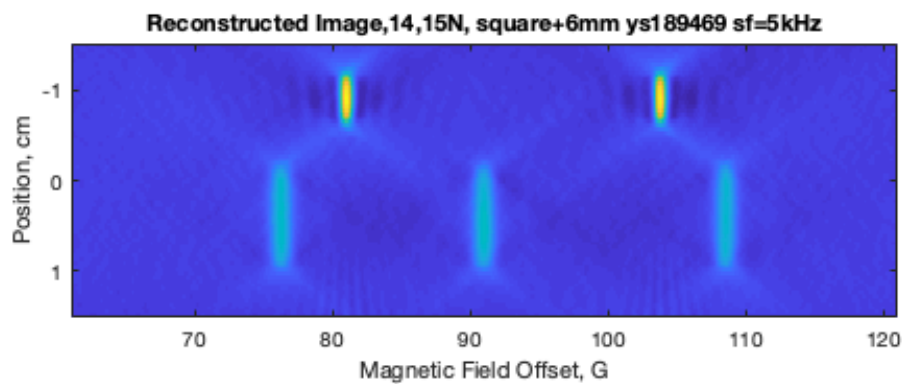


Figure 7.22 Spatial-spectral image taken at the starting position during rotation

Experimental parameters are: for each angle position, $G_{max} = 10$ G/cm, with gradient step size = 0.4 G/cm, 51 projections, 2048 averages for each projection, on-board average is 1024 and took 10' 12". Rapid-scan width = 70 G, rapid scan frequency = 5 kHz.

The reconstructed 2D spatial image is shown in Figure 7.23.

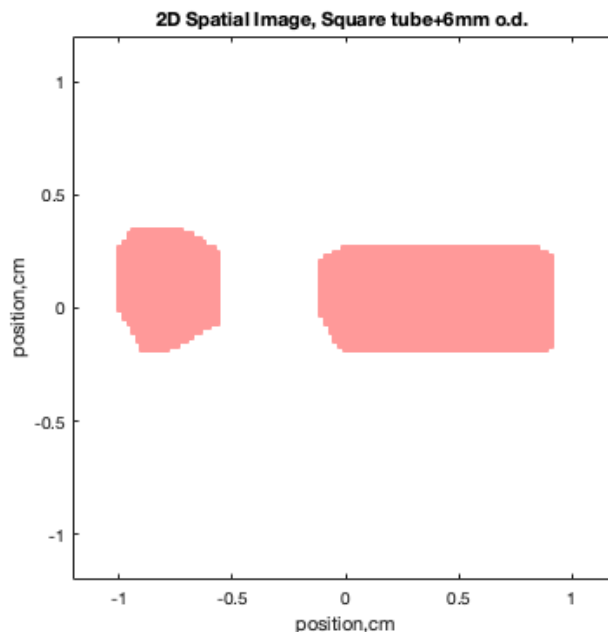


Figure 7.23 2D spatial image of two tubes with different shape and sample

This example shows that two tubes with different shape and samples can be imaged together fairly accurately at the same time in a 2D spatial-spatial image.

7.8 Python as a New Way of Performing EPRI

7.8.1 New Spectra Data Format

On a Bruker spectrometer, the data is saved by the Xepr software in the format of a 'DTA' file which stores the spectral information and a 'DSC' file which stores the parameters. For a 2D experiment (such as field-step or imaging), a third file in the format of 'YGF' is also added which appears neither readable nor needed in subsequent calculation. It might just be Bruker software specific.

In the Xepr new version, a Python API is added allowing the use of Python programming within Xepr, which provides many opportunities about what can be done with data acquisition, transfer and analysis. Since the spectra are merely a matrix of field

positions or points of time versus signal amplitudes, it is natural to use matrices to store spectra, which can be realized very easily in Python. For data storage, more generic formats are used to ensure more people can open and read, such as ‘csv’ (comma separated values), ‘txt’ (tab delimited text file), or ‘rtf’ (rich text format). A good choice is the ‘csv’ file, which can be easily opened and read using a spreadsheet and quite small in file size. Also, by using Python or spreadsheet software, the maximum number of points can be restored to 65536, which is the upper limit of the SpecJet II digitizer, while the Xepr new version only allows a maximum of 16384 points. A comparison of both spectra recording methods (running under same conditions) is shown in Table 7.15.

Table 7.15 Comparison of spectra saving method of Xepr and Python

Method	Bruker Xepr	Python language, spreadsheet	Experiment brief
Format	DTA, DSC, YGF	csv	
Maximum point	16384	65536	
Creating space for data storage	30s	0.1s	65536 points, 801 projections
Spectra saving time	4.24s	0.13s	5 projections, 16384 points, 50ns time base, 4096 averages
Data Size	13.2 MB	8.6 MB	101 projections, 8192 points 100 ns time base, 2048 averages
How to use data	Extra software required, such as ‘Easy-spin’	Directly open and import	

The comparison shows that, for allocating storage space and saving data, using a spreadsheet is much faster than Xepr’s dataset, and the file size of a spreadsheet is only 63% of Xepr’s data format. The use of a spreadsheet as a new format to store spectra should be promoted.

7.8.2 Spectral Analysis

In addition to recording spectra, the Python script can analyze the spectral data with the help of multiple packages/libraries, such as SciPy and NumPy, which are similar to using the tool boxes in MATLAB software. Dr. Tseitlin's MATLAB code for Rapid-scan deconvolution (Figure 7.24) and image reconstruction (Figure 7.25) have been re-written in Python and produced the same results (code is provided in Appendix C(2)).

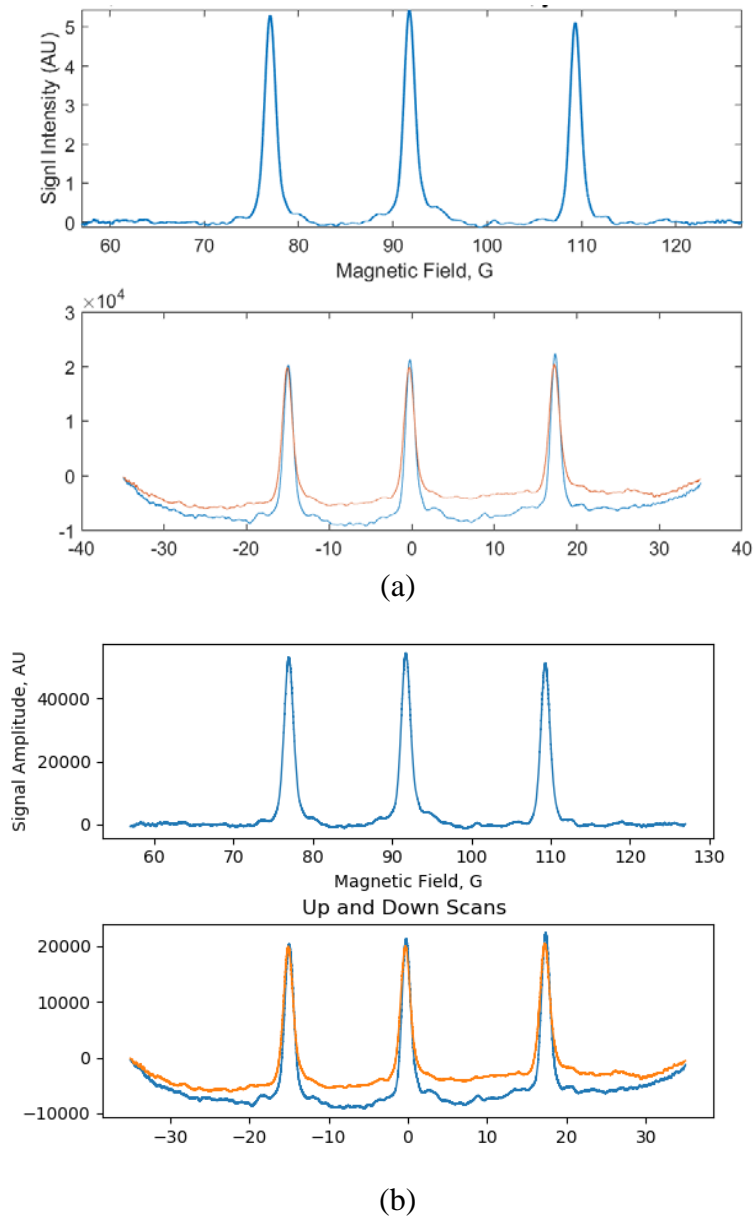
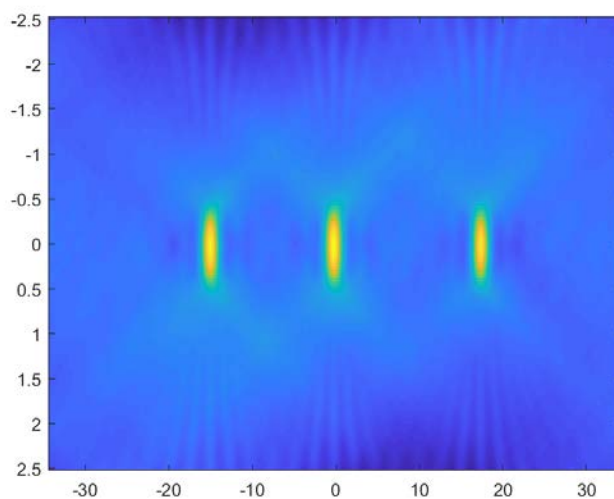


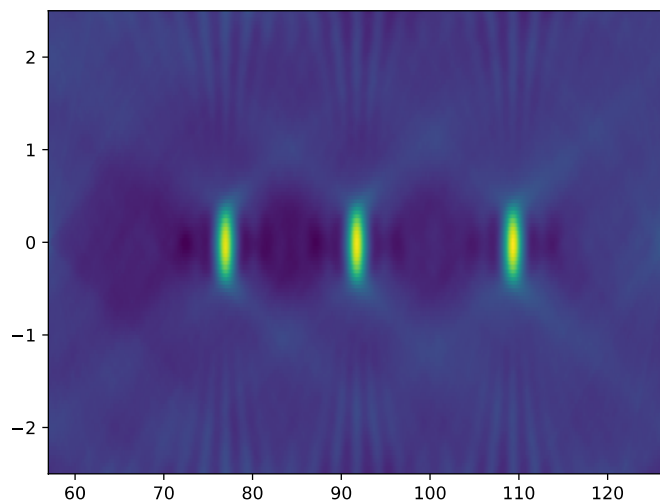
Figure 7.24 EPR spectrum deconvolved by (a) MATLAB code and (b) Python script

Sample is 1 mM CTPO. Experimental parameters are: $G_{\max} = 10$ G/cm, with gradient step size = 1 G/cm, 21 projections, 1024 averages for each projection, on-board average is 1024. Rapid-scan width = 70 G, rapid scan frequency = 5 kHz.

The top panel is the reconstructed EPR spectrum, the bottom panel is the up (blue) and down (orange) scans, since in one rapid-scan cycle the field is swept back and forth and 2 signals are acquired.



(a)



(b)

Figure 7.25 EPR image reconstructed by (a) MATLAB and (b) Python language

Parameters are the same as in Figure 7.24.

The color scales and apparent linewidth may be different in MATLAB and Python, which can be adjusted if necessary, but the results are shown to be the same after carefully checking. During each intermediate step as well as the final results for spectrum and image, the parameter matrices have been pulled out from both MATLAB and Python, and they were found to be equal, even 8 digits after the decimal point. Python scripts are sufficient to run EPR analysis and the code for achieving this has been finished.

7.8.3 Python Language as an All-in-one Solution for EPR

The previous way of doing an EPR experiment is summarized in Table 7.16, and four different software packages are needed.

Table 7.16 Procedures and software needed in an EPR experiment

#	Procedure	Software needed
1	Run experiment	ProDeL (by Bruker)
2	Save data	Xepr (by Bruker)
3	Read spectra	Easy-spin (a MATLAB tool box)
4	Get results	MATLAB

With the Python approach, the four software packages can be bypassed, and Python scripts alone can accomplish all procedures as an integrated process (Table 7.17).

Table 7.17 Python language used as central control in EPR

Hardware	Instrument name	Equipment controlled
	Bruker SpecJet II digitizer *	
	CAEN FAST-PS-1K5 30-50	Main magnet
	CAEN FAST-PS 2040-600	Gradient coils
	Homebuilt RS coil driver	Rapid-scan coils
Software	Run experiment and save data	
	Read spectra and get results	

* Connected to Python through Xepr API

The conceptual design of the UI (user interface) for EPR imaging is shown in Figure 7.26.



Figure 7.26 EPR Imaging UI design

UI includes four panels. On the leftmost one can select from 3 types of rapid-scan experiments: rapid-scan spectrum, sinusoidal single sweep imaging, field-step spectrum and image. In the next panel one can type in customized parameters, and the software retains input values from the previous experiment. The central panel is the most important part, which contains buttons to run and stop an experiment, two windows for plots such as raw data, image, spectrum, and a command line window to monitor equipment status. The rightmost panel is expandable and contains a little chat box, to

answer questions users may have. People here at Denver EPR center will answer the questions; if no one is available, the chat box will display 'offline' to users.

There are several benefits of using the Python language in EPR imaging.

(1) The faster data reading and writing is shown in Table 7.6 and Table 7.15.

(2) Python language allows more points and projections, which takes full advantage of the capacity of the digitizer.

(3) It is fairly easy to implement parallel computing in Python, which takes advantage of the full capacity of CPU and can be much faster. In the image reconstruction process, the number of projections can vary from 20 to 2000. In the current MATLAB approach one projection after another is deconvolved, which takes a significant amount of time to compute. However, in Python the deconvolution process is performed at the same time, which greatly reduces the calculation time. In MATLAB, an additional tool box is needed to implement parallel computing with an extra fee.

(4) The data analysis part of the Python script (read spectra and get results in Table 7.17) has been tested across the major platforms: Windows, Mac and Linux, and it works in all of these environments. Xepr is installed on Linux, so it is able to run the whole program on Linux. Running MATLAB software on Linux is complicated compared to just running a Python script.

(5) Other programming language, such as C++, or Java might perform the same job as Python, however, Xepr only offers API in Python, so it is natural to use Python. (Additional comments: one can also try to re-write in C++, but the learning curve is much steeper and takes longer to write than Python. However, C++ is 400 times faster than Python, so there may still be an impetus to use C++).

(6) Another important aspect is that, Python (as well as C, C++, C#, Java, et al.) is open source and free, but MATLAB software comes with an expensive annual license (student version is \$99 per year with limited features, in 2019).

Thus, Python language is an all-in-one solution for EPR imaging experiments. The development of Python scripts for EPRI is designed to move the data quickly among different physical/virtual spaces. This can be understood from three aspects: (1) move quickly between digitizer and PC, (2) circulate easily between different people through the adoption of open source free software Python and non-proprietary format 'csv', and (3) pass from raw data to the results easily, by removing the barriers involved in using multiple software packages.

CHAPTER 8 : CONCLUSIONS AND FUTURE WORK

Conclusions

Throughout this dissertation, various EPR methods have been used to investigate the properties of different radicals.

The first project performed relaxation measurements of OX063 radical from 400 MHz to 1.5 GHz, to assist in the selection of an optimum frequency for oximetry. Electron spin relaxation rates for the triarylmethyl radical OX063 as a function of radical concentration, salt concentration, and resonance frequency were measured by electron spin echo 2-pulse decay and 3-pulse inversion recovery. At constant OX063 concentration, $1/T_1$ and $1/T_2$ decreases with increasing frequency. $1/T_2 - 1/T_1$, the incomplete motional averaging contribution to $1/T_2$, increases with increasing frequency. At constant frequency, relaxation rates increase with increasing radical concentration due to contributions from collisions that are more effective for $1/T_2$ than $1/T_1$. S/N of field-swept echo-detected spectra of OX063 were measured in the frequency range of 400 MHz – 1 GHz. S/N values, normalized by \sqrt{Q} , increase as frequency increases. Adding salt to the radical solution decreased S/N because salt lowers the resonator Q. Changing the temperature from 19 to 37 °C caused little change in S/N at 700 MHz. Both slower relaxation rates and higher S/N at higher frequencies are advantageous for oximetry.

The second project involves comparison of rapid-scan and CW spectra of irradiated solids at L-band. The radicals used were: malonic acid, glycylglycine, 2,6 di-t-

butyl 4-methyl phenol, L-alanine, dimethyl malonic acid, and 2-amino isobutyric acid. Sinusoidal scans of 182 G were used. Power saturation curves show that the rapid scan signals saturated at higher powers than conventional CW signals. The rapid scan data were deconvolved and background subtracted to obtain absorption spectra. For the same data acquisition time the S/N for the absorption spectra obtained in rapid scans were 23-37 times higher than for first-derivative spectra obtained by conventional CW electron paramagnetic resonance.

The third project studied EPR imaging at VHF by both sinusoidal single sweep method and field stepped linear scan method. Several parameters, including field sweep width, stepping size, number of averages, rapid scan frequency, rapid scan width, maximum gradient, and gradient step size, were varied to optimize acquisition conditions and improve image quality. The linewidths and resolutions were calculated and compared. It is found that, to minimize the rapid scan background, 3~5 kHz rapid scan frequency is used and a rapid-scan width of at least 70 G is needed to encompass the whole ^{14}N nitroxide spectrum at high gradients. Smaller scans could be used for radicals with smaller hyperfine splittings such as ^{15}N nitroxides or trityls. For EPR imaging, larger gradient strength gives better resolution, while a smaller gradient step size (more projections) gives higher S/N and finer image texture. Larger gradient and bigger gradient step size broaden the linewidth. When radical concentration increases, S/N increases and line are broadened. A comparison of both methods was made: at high concentration, 0.5 mM, both methods give comparable S/N. At lower concentrations, 0.2 and 0.1 mM, the single-sweep sinusoidal scan method gives much better S/N than the field-stepped method.

It is important to have signal bandwidth less than the resonator bandwidth, which limits how wide (sweep width) and how fast (scan frequency) we can use. For narrow line samples (such as Trityl or LiPc), 5 G sweep width and 2.5 kHz scan frequency were used to minimize the broadening. For the spectral slice of a 2D spectral-spatial image, more projections helps reducing linewidth, especially for narrow line samples. For the field sweep method, the final result comes from a combination of many individual spectra, as a result, the S/N showed larger uncertainty and may not fit with expectations concerning dependence of S/N on number of scans averaged.

New developments in EPRI were also reported. The time used in each step of EPRI experiment is recorded. The behavior of a CAEN power supply for gradient coils and of a digitizer SpecJet-II were described, to make the system more stable and reduce data acquisition time. Two methods were demonstrated to quantify features in EPR 2D spectral-spatial image: a numerical approach by MATLAB software and a raster-image approach by ImageJ software. 3D-print tubes and sample holder were demonstrated. The Python language was used to write experiment procedures, store data and create spectra and images and the results were same as the previous approach by MATLAB software. A non-proprietary data format, 'csv', was introduced to make access easier from a diversity of platforms. The new Python script is a comprehensive approach for EPRI compared to our previous, more fragmented routines.

Future work

Some imaging experiments should be repeated since the linewidth taken from spectral slice shows larger variation than expected.

A high-dimensional EPRI methodology is under development, with the testing of more samples simultaneously.

Other information brought in by the spin probes (e.g., radical may also act as pH probe, oximetry probe) can be incorporated into the 2D spatial image, combined with the quantitative method described earlier, and gives EPR functional image.

There is an urgent need to reduce the time of transferring data from digitizer to the computer, which can be even longer than the actual data acquisition time. We have heard unofficially that Bruker will be introducing a new SpecJet with much more efficient data transfer. It will be useful to see its impact on our experiments.

A Python UI (user interface) is currently under development, which allows users to run three different kinds of EPRI experiments, input parameters, display data, deconvolve data and reconstruct image. The function part and the UI part has been finished separately, but a connection between them has not been established and is still under construction at this time. A basic UI can be generated by PAGE software (<http://page.sourceforge.net/>), while more elaborated UI (like the one shown in Figure 7.26) can possibly be generated by Qt software (<https://www.qt.io/>); both approaches are currently under testing.

BIBLIOGRAPHY

- [1] G. R. Eaton, S. S. Eaton, D. P. Barr and R. T. Weber, *Quantitative EPR*, New York: Springer, 2010.
- [2] E. Duin, "Auburn University," [Online]. Available: http://webhome.auburn.edu/~duinedu/epr/1_theory.pdf. [Accessed 2019].
- [3] S. S. Eaton, R. W. Quine, M. Tseitlin, D. G. Mitchell, G. A. Rinard and G. R. Eaton, "Rapid Scan Electron Paramagnetic Resonance," in *Multifrequency Electron Paramagnetic Resonance: Data and Techniques*, Wiley-VCH, 2014, pp. 3-67.
- [4] N. Bloembergen, E. Purcell and R. Pound, "Relaxation Effects in Nuclear Magnetic Resonance Absorption," *Physical Review*, vol. 73, pp. 679-712, 1948.
- [5] M. Klein and B. Barton, "Enhancement of signal-to-noise ratio by continuous averaging: application to magnetic resonance," *Rev Sci Instrum.*, vol. 34, no. 7, pp. 754-759, 1963.
- [6] S. S. Eaton, Y. Shi, L. Woodcock, L. A. Buchanan, J. McPeak, R. W. Quine, G. A. Rinard, B. Epel, H. J. Halpern and G. R. Eaton, "Rapid-scan EPR imaging," *Journal of Magnetic Resonance*, vol. 280, pp. 140-148, 2017.
- [7] M. Tseitlin, G. A. Rinard, R. W. Quine, S. S. Eaton and G. R. Eaton, "Rapid Frequency Scan EPR," *Journal of Magnetic Resonance*, vol. 211, no. 2, pp. 156-161, 2011.
- [8] M. Tseitlin, G. Rinard, R. Quine, S. Eaton and G. Eaton, "Deconvolution of Sinusoidal Rapid EPR Scans," *J. Magn. Reson*, vol. 208, pp. 279-283, 2011.
- [9] D. G. Mitchell, M. Tseitlin, R. W. Quine, V. Meyer, M. Newton, A. Schnegg, B. George, S. S. Eaton and G. R. Eaton, "X-Band Rapid-scan EPR of Samples with Long Electron Relaxation Times: A Comparison of Continuous Wave, Pulse, and Rapid-scan EPR," *Molecular Physics*, vol. 111, pp. 2664-2673, 2013.
- [10] G. Eaton and S. Eaton, "Introduction to EPR Imaging using magnetic-field gradients," *Concepts in Magnetic Resonance*, vol. 7, no. 1, pp. 49-67, 1995.
- [11] M. Tseitlin, J. R. Biller, H. Elajaili, V. V. Khramtsov, I. Dhimitruka, G. R. Eaton and S. S. Eaton, "New spectral-spatial imaging algorithm for full EPR spectra of multiline nitroxides and pH sensitive trityl radicals," *Journal of Magnetic Resonance*, vol. 245, pp. 150-155, 2014.
- [12] A. Iannone, A. Tomasi and V. Quaresima, "Nitroxides as metabolic and EPR imaging probes in biological model systems," *Research on Chemical Intermediates*, vol. 19, p. 715, 1993.
- [13] A. Sotgiu, S. Colacicchi, G. Placidi and M. Alecci, "Water soluble free radicals as biologically responsive agents in electron paramagnetic resonance imaging," *Cellular and Molecular Biology*, vol. 43, no. 6, pp. 813-23, 1997.
- [14] K. Yasukawa and K. Ichikawa, "Imaging in vivo redox status in high spatial resolution with OMRI," *Free Radical Research*, vol. 46, no. 8, pp. 1004-1010, 2012.

- [15] S. Subramanian and M. C. Krishna, "Electron Paramagnetic Resonance Imaging," *Resonance*, vol. 21, no. 8, pp. 717-740, 2016.
- [16] C. L. Hawkins and M. J. Davies, "Detection and characterisation of radicals in biological materials using EPR methodology," *Biochimica et Biophysica Acta*, vol. 1840, pp. 708-721, 2014.
- [17] D. Grucker, "Oxymetry by magnetic resonance: applications to animal biology and medicine," *Progress in Nuclear Magnetic Resonance Spectroscopy*, vol. 36, pp. 241-270, 2000.
- [18] A. Anemone, L. Consolino, F. Arena, M. Capozza and D. L. Longo, "Imaging tumor acidosis: a survey of the available techniques for mapping in vivo tumor pH," *Cancer Metastasis Reviews*, pp. 1-25, 2019.
- [19] S. S. Eaton, G. R. Eaton and L. J. Berliner, Eds., *Biomedical EPR - Part A: Free Radicals, Metals, Medicine and Physiology*, vol. 23, Springer, 2005.
- [20] G. R. Eaton, S. S. Eaton and K. Salikhov, Eds., *Foundations of Modern EPR*, Singapore: World Scientific Publishing, 1998.
- [21] L. Berliner, Ed., *In vivo EPR (ESR): Theory and Applications.*, New York: Springer, 1993.
- [22] M. Lucarini, G. F. Pedulli, M. V. Motyakin and S. Schlick, "Electron spin resonance imaging of polymer degradation and stabilization," *Progress in Polymer Science*, vol. 28, pp. 331-340, 2003.
- [23] P. Kuppusamy and J. L. Zweier, "Cardiac applications of EPR imaging," *NMR in Biomedicine*, vol. 17, pp. 226-239, 2004.
- [24] U. Hochkirch, W. Herrmann, R. Stöber, H.-H. Borchert and M. W. Linscheid, "Electron paramagnetic resonance and mass spectrometry: Useful tools to detect ultraviolet light induced skin lesions on a molecular basis – A short review," *Spectroscopy*, vol. 20, pp. 1-17, 2006.
- [25] P. M. Plonka, "Electron paramagnetic resonance as a unique tool for skin and hair research," *Experimental Dermatology*, vol. 18, pp. 472-484, 2009.
- [26] G. He, A. Samouilov, P. Kuppusamy and J. L. Zweier, "In vivo imaging of free radicals: Applications from mouse to man," *Molecular and Cellular Biochemistry*, vol. 234/235, pp. 359-367, 2002.
- [27] L. Berliner and H. Fujii, "Magnetic resonance imaging of biological specimens by electron paramagnetic resonance of nitroxide spin labels," *Science*, vol. 227, no. 4686, pp. 517-9, 1985.
- [28] B. Epel, M. Kotecha and H. J. Halpern, "In vivo preclinical cancer and tissue engineering applications of absolute oxygen imaging using pulse EPR," *Journal of Magnetic Resonance*, vol. 280, pp. 149-157, 2017.
- [29] B. Epel, S. V. Sundramoorthy, M. Krzykawska-Serda, M. C. Maggio, M. Tseytlin, G. R. Eaton, S. S. Eaton, G. M. Rosen, J. P. Kao and H. J. Halpern, "Imaging thiol redox status in murine tumors in vivo with rapid-scan EPR," *Journal of Magnetic Resonance*, vol. 276, pp. 31-36, 2017.

- [30] J. Weaver, S. R. Burks, K. J. Liu, J. P. Kao and G. M. Rosen, "In vivo EPR oximetry using an isotopically-substituted nitroxide: Potential for quantitative measurement of tissue oxygen," *Journal of Magnetic Resonance*, vol. 271, pp. 68-74, 2016.
- [31] M. Ferrari, V. Quaresima, C. I. Ursini, M. Alecci and A. Sotgiu, "In Vivo Electron Paramagnetic Resonance Spectroscopy-Imaging in Experimental Oncology: The Hope And The Reality," *International Journal of Radiation Oncology, Biology, Physics*, vol. 29, no. 3, pp. 421-425, 1994.
- [32] M. C. Emoto, M. Yamato, H. Sato-Akaba, K.-i. Yamada and H. G. Fujii, "Brain redox imaging in the pentylenetetrazole (PTZ)-induced kindling model of epilepsy by using in vivo electron paramagnetic resonance and a nitroxide imaging probe," *Neuroscience Letters*, vol. 608, no. 3, pp. 40-44, 2015.
- [33] H. Fujii, H. Sato-Akaba, K. Kawanishi and H. Hirata, "Mapping of Redox Status in a Brain-Disease Mouse Model by Three-Dimensional EPR Imaging," *Magnetic Resonance in Medicine*, vol. 65, pp. 295-303, 2011.
- [34] M. C. Emoto, S. Sato and H. G. Fujii, "Development of nitroxide-based theranostic compounds that act both as anti-inflammatory drugs and brain redox imaging probes in MRI," *Magnetic Resonance in Chemistry*, vol. 54, pp. 705-711, 2016.
- [35] X. Wang, M. Emoto, A. Sugimoto, Y. Miyake, K. Itto, M. Amasaka, S. Xu, H. Hirata, H. Fujii and H. Arimoto, "Synthesis of ¹⁵N-labeled 4-oxo-2,2,6,6-tetraethylpiperidine nitroxide for EPR brain imaging," *Tetrahedron Letters*, vol. 55, pp. 2146-2149, 2014.
- [36] H. Sato-Akaba, H. Fujii and H. Hirata, "Improvement of temporal resolution for three-dimensional continuous-wave," *Review of Scientific Instruments*, vol. 79, no. 12, p. 123701, 2008.
- [37] H. G. Fujii, H. Sato-Akaba, M. C. Emoto, K. Itoh, Y. Ishihara and H. Hirata, "Noninvasive mapping of the redox status in septic mouse by in vivo electron paramagnetic resonance imaging," *Magnetic Resonance Imaging*, vol. 31, pp. 130-138, 2013.
- [38] D. A. Komarov, Y. Ichikawa, K. Yamamoto, N. J. Stewart, S. Matsumoto, H. Yasui, I. A. Kirilyuk, V. V. Khramtsov, O. Inanami and H. Hirata, "In Vivo Extracellular pH Mapping of Tumors Using Electron Paramagnetic Resonance," *Analytical Chemistry*, no. 90, pp. 13938-13945, 2018.
- [39] Y. Kawada, H. Hirata and H. Fujii, "Use of multi-coil parallel-gap resonators for co-registration EPR/NMR imaging," *Journal of Magnetic Resonance*, vol. 184, pp. 29-38, 2007.
- [40] M. C. Emoto, H. Sato-Akaba, H. Hirata and H. G. Fujii, "Dynamic changes in the distribution and time course of blood-brain barrier-permeative nitroxides in the mouse head with EPR imaging: visualization of blood flow in a mouse model of ischemia," *Free Radical Biology and Medicine*, vol. 74, pp. 222-228, 2014.

- [41] D. A. Komarov and H. Hirata, "Fast backprojection-based reconstruction of spectral-spatial EPR images from projections with the constant sweep of a magnetic field," *Journal of Magnetic Resonance*, no. 281, pp. 44-50, 2017.
- [42] M. Emoto, F. Mito, T. Yamasaki, K.-I. Yamada, H. Sato-Akaba, H. Hirata and H. Fujii, "A novel ascorbic acid-resistant nitroxide in fat emulsion is an efficient brain imaging probe for in vivo EPR imaging of mouse," *Free Radical Research*, vol. 45, no. 11-12, pp. 1325-1332, 2011.
- [43] V. V. Khramtsov, "Functional EPR Spectroscopy and Imaging of Nitroxides," *Supramolecular Structure and Function*, vol. 9, pp. 181-208, 2007.
- [44] M. C. Emoto, M. Yamato, H. Sato-Akaba, K. Yamada, Y. Matsuoka and H. G. Fujii, "Brain imaging in methamphetamine-treated mice using a nitroxide contrast agent for EPR imaging of the redox status and a gadolinium contrast agent for MRI observation of blood-brain barrier function," *Free Radical Research*, vol. 49, no. 8, pp. 1038-1047, 2015.
- [45] H. Hirata, G. He, Y. Deng, I. Salikhov, S. Petryakov and J. L. Zweier, "A loop resonator for slice-selective in vivo EPR imaging in rats," *Journal of Magnetic Resonance*, vol. 190, pp. 124-134, 2008.
- [46] G. He, Y. Deng, H. Li, P. Kuppusamy and J. L. Zweier, "EPR/NMR Co-imaging for Anatomic Registration of Free-Radical Images," *Magnetic Resonance in Medicine*, vol. 47, pp. 571-578, 2002.
- [47] P. Kuppusamy, M. Chzhan and J. L. Zweier, "Development and optimization of three-dimensional spatial EPR imaging for biological organs and tissues," *Journal of Magnetic Resonance, Series B*, vol. 106, pp. 122-130, 1996.
- [48] P. Kuppusamy, M. Chzhan, A. Samouilov, P. Wang and J. L. Zweier, "Mapping the spin-density and lineshape distribution of free radicals using 4D spectral-spatial EPR imaging," *Journal of Magnetic Resonance, Series B*, vol. 107, pp. 116-125, 1995.
- [49] G. He, A. Samouilov, P. Kuppusamy and J. L. Zweier, "In Vivo EPR Imaging of the Distribution and Metabolism of Nitroxide Radicals in Human Skin," *Journal of Magnetic Resonance*, vol. 148, pp. 155-164, 2001.
- [50] G. L. Caia, O. V. Efimova, M. Velayutham, M. A. El-Mahdy, T. M. Abdelghany, E. Kesselring, S. Petryakov, Z. Sun, A. Samouilov and J. L. Zweier, "Organ specific mapping of in vivo redox state in control and cigarette smoke-exposed mice using EPR/NMR co-imaging," *Journal of Magnetic Resonance*, vol. 216, pp. 21-27, 2012.
- [51] F. Hyodo, N. D. Shingo Matsumoto, C. Dharmaraj, S. Subramanian, J. B. Mitchell and M. C. Krishna, "Pulsed EPR imaging of nitroxides in mice," *Journal of Magnetic Resonance*, vol. 197, pp. 181-185, 2009.
- [52] K.-I. Yamada, P. Kuppusamy, S. English, J. Yoo, A. Irie, S. Subramanian, J. Mitchell and M. Krishna, "Feasibility and Assessment of Non-Invasive In Vivo Redox Status Using Electron Paramagnetic Resonance Imaging," *Acta Radiologica*, vol. 43, pp. 433-440, 2002.

- [53] F. Hyodo, B. P. Soule, K.-I. Matsumoto, S. Matusmoto, J. A. Cook, E. Hyodo, A. L. Sowers, M. C. Krishna and J. B. Mitchell, "Assessment of tissue redox status using metabolic responsive contrast agents and magnetic resonance imaging," *Journal of Pharmacy and Pharmacology*, vol. 60, pp. 1049-1060, 2008.
- [54] F. Hyodo, R. Murugesan, K.-I. Matsumoto, E. Hyodo, S. Subramanian, J. B. Mitchell and M. C. Krishna, "Monitoring redox-sensitive paramagnetic contrast agent by EPRI, OMRI and MRI," *Journal of Magnetic Resonance*, vol. 190, pp. 105-112, 2008.
- [55] S. Subramanian, J. W. Koscielniak, N. Devasahayam, R. H. Pursley, T. J. Pohida and M. C. Krishna, "A new strategy for fast radiofrequency CW EPR imaging: Direct detection with rapid scan and rotating gradients," *Journal of Magnetic Resonance*, vol. 186, pp. 212-219, 2007.
- [56] K.-I. Matsumoto, J. B. Mitchell and M. C. Krishna, "Comparative studies with EPR and MRI on the in vivo tissue redox status estimation using redox-sensitive nitroxyl probes: influence of the choice of the region of interest," *Free Radical Research*, vol. 52, no. 2, pp. 248-255, 2018.
- [57] P. Kuppusamy, H. Li, G. Ilangovan, A. J. Cardounel, J. L. Zweier, K. Yamada, M. C. Krishna and J. B. Mitchell, "Noninvasive Imaging of Tumor Redox Status and Its Modification by Tissue Glutathione Levels," *Cancer Research*, vol. 62, pp. 307-312, 2002.
- [58] K. Takeshita, K. Kawaguchi, K. Fujii-Aikawa, M. Ueno, S. Okazaki, M. Ono, M. C. Krishna, P. Kuppusamy, T. Ozawa and N. Ikota, "Heterogeneity of Regional Redox Status and Relation of the Redox Status to Oxygenation in a Tumor Model, Evaluated Using Electron Paramagnetic Resonance Imaging," *Cancer Research*, vol. 70, no. 10, pp. 4133-40, 2010.
- [59] S. S. Leonard, K. Mowrey, D. Pack, X. Shi, V. Castranova, P. Kuppusamy and V. Vallyathan, "In vivo bioassays of acute asbestosis and its correlation with ESR spectroscopy and imaging in redox status," *Molecular and Cellular Biochemistry*, vol. 234/235, pp. 369-377, 2002.
- [60] S. Som, L. C. Potter, R. Ahmad and P. Kuppusamy, "A parametric approach to spectral-spatial EPR imaging," *Journal of Magnetic Resonance*, vol. 186, pp. 1-10, 2007.
- [61] D. S. Vikram, B. K. Rivera and P. Kuppusamy, "In Vivo Imaging of Free Radicals and Oxygen," in *Free Radicals and Antioxidant Protocols, Methods in Molecular Biology*, Springer Science+Business Media, LLC, 2010, p. 610.
- [62] A. Hirayama, K. Yoh, S. Nagase, A. Ueda, K. Itoh, N. Morito, K. Hirayama, S. Takahashi, M. Yamamoto and A. Koyama, "EPR Imaging of Reducing Activity in Nrf2 Transcriptional Factor-Deficient Mice," *Free Radical Biology & Medicine*, vol. 34, no. 10, pp. 1236-1242, 2003.
- [63] H. P. Kobayashi, T. Watanabe, S. Oowada, A. Hirayama, S. Nagase, M. Kamibayashi and T. Otsubo, "Effect of CV159-Ca²⁺/Calmodulin Blockade on Redox Status Hepatic Ischemia-Reperfusion Injury in Mice Evaluated by a Newly

- Developed In Vivo EPR Imaging Technique," *Journal of Surgical Research*, vol. 147, pp. 41-49, 2008.
- [64] S. Siepe, W. Herrmann, H.-H. Borchert, B. Lueckel, A. Kramer, A. Ries and R. Gurny, "Microenvironmental pH and microviscosity inside pH-controlled matrix tablets: An EPR imaging study," *Journal of Controlled Release*, vol. 112, pp. 72-78, 2006.
- [65] H. Yokoyama, T. Ogata, N. Tsuchihashi, M. Hiramatsu and N. Mori, "A Spatiotemporal Study on The Distribution of Intraperitoneally Injected Nitroxide Radical In The Rat Head Using An In Vivo ESR Imaging System," *Magnetic Resonance Imaging*, vol. 14, no. 5, pp. 559-563, 1996.
- [66] K. Oikawa, T. Ogata, H. Togashi, H. Yokoyama, H. Ohya-Nishiguchi and H. Kamada, "A 3D- and 4D-ESR Imaging System for Small Animals," *Applied Radiation and Isotopes*, vol. 47, no. 11/12, pp. 1605-1609, 1996.
- [67] Y. Lin, H. Yokoyama, I. Ishida, N. Tsuchihashi and T. Ogata, "In vivo electron spin resonance analysis of nitroxide radicals injected into a rat by a flexible surface-coil-type resonator as an endoscope- or a stethoscope-like device," *MAGMA (Magnetic Resonance Materials in Physics, Biology and Medicine)*, vol. 5, pp. 99-103, 1997.
- [68] H. Yokoyama, Y. Lin, O. Itoh, Y. Ueda, A. Nakajima, T. Ogata, T. Sato, H. Ohya-Nishiguchi and H. Kamada, "EPR Imaging For In Vivo Analysis of The Half-Life of A Nitroxide Radical In The Hippocampus And Cerebral Cortex Of Rats After Epileptic Seizures," *Free Radical Biology & Medicine*, vol. 27, no. 3/4, pp. 442-448, 1999.
- [69] H. Yokoyama, O. Itoh, M. Aoyama, H. Obara, H. Ohya and H. Kamada, "In vivo EPR imaging by using an acyl-protected hydroxylamine to analyze intracerebral oxidative stress in rats after epileptic seizures," *Magnetic Resonance Imaging*, vol. 18, pp. 875-879, 2000.
- [70] H. Yokoyama, M. Tada, O. Itoh and K. Fukui, "Reaction Kinetics Analysis To Estimate in Vivo Decay Rate of EPR Signals of a Nitroxide Radical in the Brain and the Inferior Vena Cava of Rats," *Applied Magnetic Resonance*, vol. 25, pp. 217-225, 2003.
- [71] A. Ueda, H. Yokoyama, S. Nagase, A. Hirayama, A. Koyama, H. Ohya and H. Kamada, "In vivo temporal EPR imaging for estimating the kinetics of a nitroxide radical in the renal parenchyma and pelvis in rats," *Magnetic Resonance Imaging*, vol. 20, pp. 77-82, 2002.
- [72] H. Yokoyama, O. Itoh, H. Ohya-Nishiguchi and H. Kamada, "Reducing Ability of the Striatum and Cerebral Cortex in Rats following Acute Administration of Risperidone or Haloperidol: An Estimation by in Vivo Electron Paramagnetic Resonance Imaging," *Neurochemical Research*, vol. 27, no. 3, pp. 243-248, 2002.
- [73] H. Yokoyama, O. Itoh, M. Aoyama, H. Obara, H. Ohya and H. Kamada, "In vivo temporal EPR imaging of the brain of rats by using two types of blood-brain barrier-permeable nitroxide radicals," *Magnetic Resonance Imaging*, vol. 20, pp. 277-284, 2002.

- [74] H. Yokoyama and T. Ono, "In Vivo Temporal EPR Measurements in the lung of mice by a selected-region intensity determination method," *Applied Magnetic Resonance*, vol. 33, pp. 197-205, 2008.
- [75] T. Ito, H. Yokoyama and T. Ogata, "Determination of Absolute Concentration of Nitroxide Radical by Radio-Frequency EPR Imaging," *Applied Magnetic Resonance*, vol. 20, pp. 257-263, 2001.
- [76] H. Yokoyama, Y. Ueda, O. Itoh, T. Ikeda, J. I. Noor and T. Ikenoue, "EPR imaging to estimate the in vivo intracerebral reducing ability of mature rats after neonatal hypoxic–ischemic brain injury," *Magnetic Resonance Imaging*, vol. 22, pp. 1305-1309, 2004.
- [77] H. Yokoyama, S. Morinobu and Y. Ued, "EPRI to Estimate the In Vivo Intracerebral Reducing Ability in Adolescent Rats Subjected to Neonatal Isolation," *Journal of Magnetic Resonance Imaging*, vol. 23, pp. 637-640, 2006.
- [78] H. Yokoyama, T. Sato, H. Ohya-Nishiguchi and H. Kamada, "In vivo 300 MHz longitudinally detected ESR-CT imaging in the head of a rat treated with a nitroxide radical," *Magnetic Resonance Materials in Physics, Biology and Medicine*, vol. 7, pp. 63-68, 1998.
- [79] M. Ferrari, S. Colacicchi, G. Gualtieri, M. T. Santini and A. Sotgiu, "Whole mouse Nitroxide Free Radical Pharmacokinetics by Low Frequency Electron Paramagnetic Resonance," *Biochemical and Biophysical Research Communications*, vol. 166, no. 1, pp. 168-173, 1990.
- [80] V. Quaresima, M. Alecci, M. Ferrari and A. Sotgiu, "Whole Rat Electron Paramagnetic Resonance Imaging Of A Nitroxide Free Radical By A Radio Frequency (280 MHz) Spectrometer," *Biochemical And Biophysical Research Communications*, vol. 183, no. 2, pp. 829-835, 1992.
- [81] S. Kempe, H. Metz and K. Mäder, "Application of Electron Paramagnetic Resonance (EPR) spectroscopy and imaging in drug delivery research – Chances and challenges," *European Journal of Pharmaceutics and Biopharmaceutics*, vol. 74, pp. 55-66, 2010.
- [82] F. Eisenächer, A. Schädlich and K. Mäder, "Monitoring of internal pH gradients within multi-layer tablets by optical methods and EPR imaging," *International Journal of Pharmaceutics*, vol. 417, pp. 204-215, 2011.
- [83] N. Charlier, A. M. Neyrinck, N. Beghein, N. M. Delzenne and B. Gallez, "Assessment of liver phagocytic activity using EPR spectrometry and imaging," *Magnetic Resonance Imaging*, vol. 27, pp. 565-569, 2009.
- [84] Y. Ueda, H. Yokoyama, H. Ohya-Nishiguchi and H. Kamada, "ESR Imaging of The Rat Brain with A Nitroxide Radical Perfused By In Vivo Microdialysis," *Magnetic Resonance Imaging*, vol. 15, no. 3, pp. 355-360, 1997.
- [85] S. R. Burks, L. F. Macedo, E. D. Barth, K. H. Tkaczuk, S. S. Martin, G. M. Rosen, H. J. Halpern, A. M. Brodie and J. P. Y. Kao, "Anti-HER2 immunoliposomes for selective delivery of electron paramagnetic resonance imaging probes to HER2-overexpressing breast tumor cells," *Breast Cancer Research and Treatment*, vol. 124, pp. 121-131, 2010.

- [86] H. J. Halpern, M. Peric, C. Yu, E. D. Barth, G. V. R. Chandramouli, M. W. Makinen and G. M. Rosen, "In Vivo Spin-Label Murine Pharmacodynamics Using Low-Frequency Electron Paramagnetic Resonance Imaging," *Biophysical Journal*, vol. 71, pp. 403-409, 1996.
- [87] B. B. Williams, H. A. Hallaq, G. Chandramouli, E. D. Barth, J. N. Rivers, M. Lewis, V. E. Galtsev, G. S. Karczmar and H. J. Halpern, "Imaging Spin Probe Distribution in the Tumor of a Living Mouse With 250 MHz EPR: Correlation with BOLD MRI," *Magnetic Resonance in Medicine*, vol. 47, pp. 634-638, 2002.
- [88] G. Redler, E. D. Barth, K. S. Bauer, J. P. Kao, G. M. Rosen and H. J. Halpern, "In Vivo Electron Paramagnetic Resonance Imaging of Differential Tumor Targeting Using cis-3,4-Di (Acetoxymethoxycarbonyl)-2,2,5,5-Tetramethyl-1-Pyrrolidinyloxy," *Magnetic Resonance in Medicine*, vol. 71, no. 4, pp. 1650-1656, 2014.
- [89] S. R. Burks, E. D. Barth, H. J. Halpern, G. M. Rosen and J. P. Kao, "Cellular uptake of electron paramagnetic resonance imaging probes through endocytosis of liposomes," *Biochimica et Biophysica Acta*, vol. 1788, pp. 2301-2308, 2009.
- [90] M. Velayutham, H. Li, P. Kuppusamy and J. L. Zweier, "Mapping Ischemic Risk Region and Necrosis in the Isolated Heart Using EPR Imaging," *Magnetic Resonance in Medicine*, vol. 49, pp. 1181-1187, 2003.
- [91] M. Alecci, M. Ferrai, V. Quresimna, A. Sotgiu and C. L. Ursini, "Simultaneous 280 MHz EPR Imaging of Rat Organs During Nitroxide Free Radical Clearance," *Biophysical Journal*, vol. 67, pp. 1274-1279, 1994.
- [92] Y.-K. Shin, U. Ewert, D. E. Budil and J. H. Freed, "Microscopic versus macroscopic diffusion in model membranes by Electron Spin Resonance spectral-spatial imaging," *Biophysical Journal*, vol. 59, pp. 950-957, 1991.
- [93] R. H. Crepeau, S. Saxena, S. Lee, B. Patyal and J. H. Freed, "Studies on lipid membranes by two-dimensional Fourier transform ESR: Enhancement of resolution to ordering and dynamics," *Biophysical Journal*, vol. 66, pp. 1489-1504, 1994.
- [94] L. A. Shundrin, I. A. Kirilyuk and I. A. Grigor'ev, "3-Carboxy-2,2,5,5-tetra(2H3)methyl-[4-2H(1H)]-3-pyrroline-(1-15N)-1-oxyl as a spin probe for in vivo L-band electron paramagnetic resonance imaging," *Mendeleev Commun.*, vol. 24, pp. 298-300, 2014.
- [95] H. Yokoyama, T. Ono and T. Yoshimura, "In Vivo EPR imaging of a perfluoroalkyl radical in mouse abdomen," *Applied Magnetic Resonance*, vol. 32, pp. 283-291, 2007.
- [96] R. K. Strizhakov, L. A. Shundrin, N. G. Kolosova, N. A. Stefanova, E. U. Fursova, V. I. Ovcharenko and E. G. Bagryanskaya, "Nitronyl Nitroxides as a Spin Probe in EPR Tomography In Vivo," *Applied Magnetic Resonance*, vol. 45, pp. 743-758, 2014.
- [97] S. S. Eaton and G. R. Eaton, "EPR Imaging," *Journal of Magnetic Resonance*, vol. 59, pp. 414-411, 1984.

- [98] M. M. Maltempo, S. S. Eaton and G. R. Eaton, "Spectral-Spatial Two-Dimensional EPR Imaging," *Journal of Magnetic Resonance*, vol. 72, pp. 449-455, 1987.
- [99] H. Fujii and L. J. Berliner, "Application of the Convolution Difference Resolution Method in Reconstruction Techniques in EPR Imaging," *Journal of Magnetic Resonance*, vol. 68, pp. 377-382, 1986.
- [100] M. Spitzbarth and M. Drescher, "Simultaneous iterative reconstruction technique software for spectral-spatial EPR imaging," *Journal of Magnetic Resonance*, vol. 257, pp. 79-88, 2015.
- [101] M. Alecci, S. Colacicchi, P. Indovina, F. Momo, P. Pavone and A. Sotgiu, "Three-Dimensional In Vivo ESR Imaging in Rats," *Magnetic Resonance Imaging*, vol. 8, pp. 59-63, 1990.
- [102] M. Ferrari, V. Quaresima and A. Sotgiu, "Present status of electron paramagnetic resonance (EPR) spectroscopy/imaging for free radical detection," *Pflügers Arch*, vol. 431, pp. 267-268, 1996.
- [103] Z. Chen, L. A. Reyes, D. H. Johnson, M. Velayutham, C. Yang, A. Samouilov and J. L. Zweier, "Fast Gated EPR Imaging of the Beating Heart: Spatiotemporally Resolved 3D Imaging of Free-Radical Distribution During the Cardiac Cycle," *Magnetic Resonance in Medicine*, vol. 69, pp. 594-601, 2013.
- [104] T. Czechowski, R. Krzyminiewski, J. Jurga and W. Chlewicki, "Two-Dimensional Imaging by the Continuous-Wave EPR," *Applied Magnetic Resonance*, vol. 29, pp. 335-349, 2005.
- [105] T. Czechowski, R. Krzyminiewski, J. Jurga and W. Chlewicki, "Two-dimensional imaging of two types of radicals by the CW-EPR method," *Journal of Magnetic Resonance*, vol. 190, pp. 52-59, 2008.
- [106] T. Czechowski, W. Chlewicki, M. Baranowski, K. Jurga, P. Szczepanik, P. Szulca, K. Tadyszak, P. Kedzia, M. Szostak, P. Malinowski, S. Wosinski, W. Prukala and J. Jurga, "Two-dimensional EPR imaging with the rapid scan and rotated magnetic field gradient," *Journal of Magnetic Resonance*, vol. 248, pp. 126-130, 2014.
- [107] K. Tadyszak, A. Boś-Liedke, J. Jurga, M. Baranowski, R. Mrówczyński, W. Chlewicki, S. Jurga and T. Czechowski, "Overmodulation of projections as signal-to-noise enhancement method in EPR imaging," *Magnetic Resonance in Chemistry*, vol. 54, pp. 136-142, 2016.
- [108] T. Czechowski, A. Samolej, M. Baranowski, A. Bos-Liedke, W. Chlewicki, J. Jurga and K. Tadyszak, "Adaptive Modulation Amplitude in 2D Spectral-Spatial EPR Imaging," *Acta Physica Polonica Series a*, vol. 133, no. 3, pp. 710-712, 2018.
- [109] K.-I. Matsumoto, M. Narazaki, H. Ikehira, K. Anzai and N. Ikota, "Comparisons of EPR imaging and T1-weighted MRI for efficient imaging of nitroxyl contrast agents," *Journal of Magnetic Resonance*, vol. 187, pp. 155-162, 2007.
- [110] K.-I. Matsumoto, K. Anzai and H. Utsumi, "Simple data acquisition method for multi-dimensional EPR spectral-spatial imaging using a combination of constant-time and projection-reconstruction modalities," *Journal of Magnetic Resonance*, vol. 197, pp. 161-166, 2009.

- [111] M. Hashem, M. Weiler-Sagie, P. Kuppusamy, G. Neufeld, M. Neeman and A. Blank, "Electron spin resonance microscopic imaging of oxygen concentration in cancer spheroids," *Journal of Magnetic Resonance*, vol. 256, pp. 77-85, 2015.
- [112] I. Katz, M. Fehr, A. Schnegg, K. Lips and A. Blank, "High resolution in-operando microimaging of solar cells with pulse deelectrically-detected magnetic resonance," *Journal of Magnetic Resonance*, vol. 251, pp. 26-35, 2015.
- [113] I. Kissos, M. Levit, A. Feuer and A. Blank, "Statistical reconstruction algorithms for continuous wave electron spin resonance imaging," *Journal of Magnetic Resonance*, vol. 231, pp. 100-116, 2013.
- [114] N. Devasahayam, R. Murugesan, K. Matsumoto, J. Mitchell, J. Cook, S. Subramanian and M. Krishna, "Tailored sinc pulses for uniform excitation and artifact-free radio frequency time-domain EPR imaging," *Journal of Magnetic Resonance*, vol. 168, pp. 110-117, 2004.
- [115] C. D. Dharmaraj, M. C. Krishna and R. Murugesan, "A Feature Identification System for Electron Magnetic Resonance Tomography: Fusion of Principal Components Transform, Color Quantization and Boundary Information," *Journal of Mathematical Imaging and Vision*, vol. 30, pp. 284-297, 2008.
- [116] M. Tseitlin, T. Czechowski, S. S. Eaton and G. R. Eaton, "Regularized optimization (RO) reconstruction for oximetric EPR imaging," *Journal of Magnetic Resonance*, vol. 194, no. 2, pp. 212-221, 2008.
- [117] M. Tseitlin, T. Czechowski, R. W. Quine, S. S. Eaton and G. R. Eaton, "Background Removal Procedure for Rapid Scan EPR," *Journal of Magnetic Resonance*, vol. 196, no. 1, pp. 48-53, 2009.
- [118] J. R. Biller, M. Tseitlin, R. W. Quine, G. A. Rinard, H. A. Weismiller, H. Elajaili, G. M. Rosen, J. P. Kao, S. S. Eaton and G. R. Eaton, "Imaging of nitroxides at 250 MHz using rapid-scan electron paramagnetic resonance," *Journal of Magnetic Resonance*, vol. 242, pp. 162-168, 2014.
- [119] H. Sato-Akaba, M. C. Emoto, H. Hirata and H. G. Fujii, "Design and testing of a 750 MHz CW-EPR digital console for small animal imaging," *Journal of Magnetic Resonance*, vol. 284, pp. 48-58, 2017.
- [120] H. Yokoyama, T. Sato, T. Oteki, H. Ohya and T. Akatsuka, "Estimation of the In Vivo Decay Rate of EPR Signals for a Nitroxide Radical in Rat Brains by a Region-Selected Intensity Determination Method," *Applied Magnetic Resonance*, vol. 29, pp. 363-373, 2005.
- [121] G. A. Rinard, R. W. Quine, G. R. Eaton, S. S. Eaton, E. D. Barth, C. A. Pelizzari and H. J. Halpern, "Magnet and Gradient Coil System for Low-Field EPR Imaging," *Concepts in Magnetic Resonance (Magnetic Resonance Engineering)*, vol. 15, no. 1, pp. 51-58, 2002.
- [122] R. W. Quine, G. A. Rinard, S. S. Eaton and G. R. Eaton, "A Pulsed and Continuous Wave 250 MHz Electron Paramagnetic Resonance Spectrometer," *Concepts in Magnetic Resonance (Magnetic Resonance Engineering)*, vol. 15, no. 1, pp. 59-91, 2002.

- [123] R. W. Quine, S. S. Eaton and G. R. Eaton, "Pulsed Saturation Recovery 250 MHz Electron Paramagnetic Resonance Spectrometer," *Concepts in Magnetic Resonance Part B (Magnetic Resonance Engineering)*, vol. 268, no. 1, pp. 23-27, 2005.
- [124] L. A. Buchanan, G. A. Rinard, R. W. Quine, S. S. Eaton and G. R. Eaton, "Tabletop 700 MHz electron paramagnetic resonance imaging spectrometer," *Concepts Magn Reson Part B*, vol. 48B(2): e21384, 2018.
- [125] R. W. Quine, T. Czechowski and G. R. Eaton, "A Linear Magnetic Field Scan Driver," *Concepts in Magnetic Resonance Part B: Magnetic Resonance Engineering*, vol. 35B, no. 1, pp. 44-58, 2009.
- [126] R. W. Quine, D. G. Mitchell, M. Tseitlin, S. S. Eaton and G. R. Eaton, "A Resonated Coil Driver for Rapid Scan EPR," *Concepts in Magnetic Resonance Part B (Magnetic Resonance Engineering)*, vol. 41B, no. 4, pp. 95-110, 2012.
- [127] G. A. Rinard, R. W. Quine, J. R. Biller and G. R. Eaton, "A Wire Crossed-Loop-Resonator for Rapid Scan EPR," *Concepts in Magnetic Resonance Part B: Magnetic Resonance Engineering*, vol. 37B, no. 2, pp. 86-91, 2010.
- [128] L. A. Buchanan, L. B. Woodcock, G. A. Rinard, R. W. Quine, Y. Shi, S. S. Eaton and G. R. Eaton, "250 MHz Rapid Scan Cross Loop Resonator," *Applied Magnetic Resonance*, vol. 50, no. 1-3, pp. 333-345, 2019.
- [129] G. A. Rinard, R. W. Quine, L. A. Buchanan, S. S. Eaton, G. R. Eaton, B. Epel, S. V. Sundramoorthy and H. J. Halpern, "Resonators for In Vivo Imaging: Practical Experience," *Applied Magnetic Resonance*, vol. 48, pp. 1227-1247, 2017.
- [130] G. R. Eaton and R. W. Quine, "Comparison of Four Digitizers for Time-Domain EPR," *Applied Spectroscopy*, vol. 54, no. 10, pp. 1543-1545, 2000.
- [131] F. Hyodo, S. Subramanian, N. Devasahayam, R. Murugesan, K. Matsumoto, J. Mitchell and M. Krishna, "Evaluation of sub-microsecond recovery resonators for in vivo electron paramagnetic resonance imaging," *Journal of Magnetic Resonance*, vol. 190, pp. 248-254, 2008.
- [132] F. Demsar, T. Walczak, P. D. Morse II, G. Bacic, Z. Zolnai and H. M. Swartz, "Detection of Diffusion and Distribution of Oxygen by Fast-Scan EPR Imaging," *Journal of Magnetic Resonance*, vol. 76, no. 1, pp. 224-23, 1998.
- [133] R. Krzyminiewski, T. Kubiak, B. Dobosz, G. Schroeder and J. Kurczewska, "EPR spectroscopy and imaging of TEMPO-labeled magnetite nanoparticles," *Current Applied Physics*, vol. 14, pp. 798-804, 2014.
- [134] A. B. Rabovsky, G. R. Buettner and B. Fink, "In vivo imaging of free radicals produced by multivitamin-mineral supplements," *BMC(Bio Med Center) Nutrition*, pp. 1-32, 2015.
- [135] A. I. Smirnov, O. E. Yaiumchenko, H. A. Golovina, S. Kh. Bekova and Y. S. Lebedev, "EPR Imaging with Natural Spin Probes," *Journal of Magnetic Resonance*, vol. 91, pp. 386-391, 1991.

- [136] S. Colacicchi, S. Onori, E. Petetti and A. Sotgiu, "Application of Low Frequency EPR Imaging to Alanine Dosimetry," *Applied Radiation and Isotopes*, vol. 44, no. 1-2, pp. 391-395, 1993.
- [137] J. Fuchs, N. Groth, T. Herrling, R. Milbradt, G. Zimmer and L. Packer, "EPR imaging in skin: biophysical and biochemical microscopy," *Journal of Investigative Dermatology*, vol. 98, pp. 713-719, 1992.
- [138] J. Fuchs, N. Groth, T. Herrling and L. Packer, "In Vivo Electron Paramagnetic Resonance Imaging of Skin," *Methods in Enzymology*, vol. 233, pp. 140-149, 1994.
- [139] T. Herrling, J. Fuchs, J. Rehberg and N. Groth, "UV-Induced Free Radicals In The Skin Detected By ESR Spectroscopy And Imaging Using Nitroxides," *Free Radical Biology & Medicine*, vol. 35, no. 1, pp. 59-67, 2003.
- [140] M. Lucarini, G. F. Pedulli, M. V. Motyakin and S. Schlick, "Electron spin resonance imaging of polymer degradation and stabilization," *Progress in Polymer Science*, vol. 28, pp. 331-340, 2003.
- [141] M. V. Motyakin and S. Schlick, "Spectral Profiling by 1D and 2D Electron Spin Resonance Imaging: Nitroxide Radicals in UV and Thermal Degradation of Poly(acrylonitrile-butadiene-styrene) Containing a Hindered Amine Stabilizer," *Macromolecules*, vol. 34, pp. 2854-2864, 2001.
- [142] K. Kruczala, W. Aris and S. Schlick, "Stabilization and Early Degradation of UV-Irradiated Heterophasic Propylene-Ethylene Copolymers Based on ESR, ESR Imaging, UV-Vis, and DSC: Effect of Ethylene Content and UV Wavelength," *Macromolecules*, vol. 38, pp. 6979-6987, 2005.
- [143] S. Schlick and K. Kruczala, "Spatially Resolved Degradation in Heterophasic Polymers by ESR Imaging and FTIR: The Case of Propylene-Ethylene Copolymers," *Journal of Coatings Technology and Research*, vol. 2, no. 5, pp. 389-397, 2005.
- [144] A. Blank, R. Halevy, M. Shklyar, L. Shtirberg and P. Kuppusamy, "ESR imaging of LiNc-BuO crystals in PDMS: Spatial and spectral grain distribution," *Journal of Magnetic Resonance*, vol. 203, pp. 150-155, 2010.
- [145] N. Warwar, A. Mor, R. Fluhr, R. P. Pandian, P. Kuppusamy and A. Blank, "Detection and Imaging of Superoxide in Roots by an Electron Spin Resonance Spin-Probe Method," *Biophysical Journal*, vol. 101, pp. 1529-1538, 2011.
- [146] Y. Cao, Y. Chen, Q. Wan, J. Hu and B. Zhao, "Three-dimensional electron spin resonance imaging of endogenous nitric oxide radicals generated in living plants," *Biophysics Reports*, vol. 4, no. 3, pp. 133-142, 2018.
- [147] I. Dhimitruka, A. Bobko, T. Eubank, D. Komarov and V. Khramtsov, "Phosphonated Trityl Probes for Concurrent in Vivo Tissue Oxygen and pH Monitoring Using Electron Paramagnetic Resonance-Based Techniques," *J. Am. Chem. Soc.*, vol. 135, pp. 5904-5910, 2013.
- [148] A. Bobko, I. Dhimitruka, J. Zweier and V. Khramtsov, "Trityl Radicals as Persistent Dual Function pH and Oxygen Probes for in Vivo Electron

- Paramagnetic Resonance Spectroscopy and Imaging: Concept and Experiment," *J. Am. Chem. Soc.*, vol. 129, pp. 7240-7241, 2007.
- [149] B. Epel, M. K. Bowman, C. Mailer and H. J. Halpern, "Absolute Oxygen R1e Imaging In Vivo with Pulse Electron Paramagnetic Resonance," *Magn. Reson. Med.*, vol. 72, pp. 362-368, 2014.
- [150] L. Yong, J. Harbridge, R. Quine, G. Rinard, S. Eaton, G. Eaton, C. Mailer, E. Barth and H. Halpern, "Electron Spin Relaxation of Triarylmethyl Radicals in Fluid Solution," *Journal of Magnetic Resonance*, vol. 152, pp. 156-161, 2001.
- [151] Y. Shi, R. W. Quine, G. A. Rinard, L. Buchanan, S. S. Eaton, G. R. Eaton, B. Epel, S. W. Seagle and H. J. Halpern, "Triarylmethyl Radical: EPR Signal to Noise at Frequencies between 250 MHz and 1.5 GHz and Dependence of Relaxation on Radical and Salt Concentration and on Frequency," *Z. Phys. Chem.*, vol. 231, no. 4, pp. 923-937, 2017.
- [152] A. Kuzhelev, D. Trukhin, O. Krumkacheva, R. Strizhakov, O. Rogozhnikova, T. Troitskaya, M. Fedin, V. Tormyshev and E. Bagryanskaya, "Room-Temperature Electron Spin Relaxation of Triarylmethyl Radicals at the X- and Q-Bands," *J. Phys. Chem.*, vol. 119B, pp. 13630-13640, 2015.
- [153] R. Owenius, G. R. Eaton and S. S. Eaton, "Frequency (250 MHz to 9.2 GHz) and Viscosity Dependence of Electron Spin Relaxation of Triarylmethyl Radicals at Room Temperature," *J. Magn. Reson.*, vol. 172, pp. 168-175, 2005.
- [154] E. Epel, M. Bowman, C. Mailer and H. J. Halpern, "Absolute oxygen R1e imaging in vivo with pulse electron paramagnetic resonance," *Magn. Reson. Med.*, vol. 27, pp. 362- 368, 2014.
- [155] H. Halpern and M. Bowman, "Low-frequency EPR spectrometers: MHz range, in EPR Imaging and In Vivo EPR," in *EPR imaging and in vivo EPR*, vol. ch. 6., G. Eaton, S. Eaton and K. Ohno, Eds., Boca Raton, CRC Press, 1991.
- [156] Z. Yu, R. W. Quine, G. A. Rinard, M. Tseitlin, H. Elajaili, V. Kathirvelu, L. J. Clouston, P. J. B. 'ski, A. Rajca, R. Stein, H. Mchaourab, S. S. Eaton and G. R. Eaton, "Rapid-scan EPR of immobilized nitroxides," *Journal of Magnetic Resonance*, vol. 247, pp. 67-71, 2014.
- [157] Y. Shi, G. A. Rinard, R. W. Quine, S. S. Eaton and G. R. Eaton, "Rapid scan electron paramagnetic resonance at 1.0 GHz of defect centers in γ -irradiated organic solids," *Radiation Measurements*, vol. 85, pp. 57-63, 2016.
- [158] G. R. Eaton and S. S. Eaton, "Electron spin relaxation times for the alanine radical in two dosimeters," *Applied Radiation and Isotopes*, vol. 62, no. 2, pp. 129-132, 2005.
- [159] J. R. Harbridge, S. S. Eaton and G. R. Eaton, "Electron spin-lattice relaxation in radicals containing two methyl groups, generated by γ -irradiation of polycrystalline solids," *J. Magn. Reson.*, vol. 159, pp. 195-206, 2002.
- [160] J. R. Harbridge, S. S. Eaton and G. R. Eaton, "Electron Spin-Lattice Relaxation Processes in Irradiated Crystalline Organic Compounds," *J. Phys. Chem.*, vol. 107, pp. 598-610, 2003.

- [161] J. R. Harbridge, S. S. Eaton and G. R. Eaton, "Electron spin relaxation of radicals in gamma-irradiated malonic acid and methyl malonic acid," *Appl. Magn. Reson.*, vol. 24, pp. 261-276, 2003.
- [162] D. G. Mitchell, G. M. Rosen, M. Tseitlin, B. Symmes, S. S. Eaton and G. R. Eaton, "Use of Rapid-Scan EPR to Improve Detection Sensitivity for Spin-Trapped Radicals," *Biophys J.*, vol. 105, pp. 338-342, 2013.
- [163] R. Quine, G. Rinard, S. Eaton and G. Eaton, "Quantitative Rapid Scan EPR Spectroscopy at 258 MHz," *J. Magn. Reson.*, vol. 205, no. 1, pp. 23-27, 2010.
- [164] M. Tseitlin, R. Quine, G. Rinard, S. Eaton and G. Eaton, "Combining Absorption and Dispersion Signals to Improve Signal-to-noise for Rapid Scan EPR Imaging," *J. Magn. Reson.*, vol. 203, pp. 305-310, 2010.
- [165] M. Tseitlin, D. Mitchell, S. Eaton and G. Eaton, "Corrections for sinusoidal background and non-orthogonality of signal channels in sinusoidal rapid magnetic field scans," *J. Magn. Reson.*, vol. 223b, pp. 80 - 84, 2012.
- [166] S. Clough and F. Poldy, "Study of Tunneling Rotation of Methyl Groups by Electron Spin Resonance and Electron Nuclear Double Resonance," *J. Chem. Phys.*, vol. 51, pp. 2076-2087, 1969.
- [167] M. Katayama and W. Gordy, "Electron Spin Resonance of γ -Irradiated Glycylglycine," *J. Chem. Phys.*, vol. 35, pp. 117-122, 1961.
- [168] L. A. Buchanan, L. B. Woodcock, R. W. Quine, G. A. Rinard, S. S. Eaton and G. R. Eaton, "Background correction in rapid scan EPR spectroscopy," *Journal of Magnetic Resonance*, vol. 293, pp. 1-8, 2018.
- [169] H. J. Halpern, C. Yu, M. Peric, E. D. Barth, G. S. Karczmar, J. N. River, D. J. Grdina and B. A. Teicher, "Measurement of Differences in pO₂ in Response to Perfluorocarbon/Carbogen in FSa and NFSa Murine Fibrosarcomas with Low-Frequency Electron Paramagnetic Resonance Oximetry," *Radiation Research*, vol. 145, no. 5, pp. 610-618, 1996.
- [170] D. Gillies, L. Sutcliffe and M. Symms, "Effects encountered in EPR spectroscopy and imaging at small magnetic fields," *JCS Faraday Trans.*, vol. 90, pp. 2671-2675, 1994.
- [171] F. Hyodo, S. Matsumoto, E. Hyodo, A. Matsumoto, K. Matsumoto and M. Krishna, "In Vivo Measurement of Tissue Oxygen Using Electron Paramagnetic Resonance Spectroscopy with Oxygen-Sensitive Paramagnetic Particle, Lithium Phthalocyanine," *Free Radicals and Antioxidant Protocols*, vol. 610, pp. 29-39, 2009.
- [172] G. Rinard, R. Quine, S. Eaton, G. Eaton, E. Barth, C. Pelizzari and H. Halpern, "Magnet and Gradient Coil System for Low-Field EPR Imaging," *Magnetic Resonance Engineering*, vol. 15, pp. 51-58, 2002.
- [173] R. Quine, G. Rinard, S. Eaton and G. Eaton, "Quantitative Rapid Scan EPR Spectroscopy at 258 MHz," *Journal of Magnetic Resonance*, vol. 205, pp. 23-27, 2010.

- [174] J. R. Biller, H. Elajaili, V. Meyer, G. M. Rosen, S. S. Eaton and G. R. Eaton, "Electron spin–lattice relaxation mechanisms of rapidly-tumbling nitroxide radicals," *Journal of Magnetic Resonance*, vol. 236, pp. 47-56, 2013.
- [175] V. Mazet, C. Carteret, D. Brie, J. Idier and B. Humbert, "Background removal from spectra by designing and minimising a non-quadratic cost function," *Chemometrics and Intelligent Laboratory Systems*, vol. 76, no. 2, pp. 121-133, 2005.
- [176] Z. Yu, T. Liu, H. Elajaili, G. A. Rinard, S. S. Eaton and G. R. Eaton, "Field-stepped direct detection electron paramagnetic resonance," *Journal of Magnetic Resonance*, vol. 258, pp. 58-64, 2015.
- [177] J. Schindelin, I. Arganda-Carreras, E. Frise and e. al., "Fiji: an open-source platform for biological-image analysis," *Nature methods*, vol. 9, no. 7, pp. 676-682, 2012.
- [178] K.-I. Matsumoto, M. Narazaki, H. Ikehira, K. Anzai and N. Ikota, "Comparisons of EPR imaging and T1-weighted MRI for efficient imaging of nitroxyl contrast agents," *Journal of Magnetic Resonance*, vol. 187, pp. 155-162, 2007.
- [179] S. R. Burks, L. F. Macedo, E. D. Barth, K. H. Tkaczuk, S. S. Martin, G. M. Rosen, H. J. Halpern, A. M. Brodie and J. P. Y. Kao, "Anti-HER2 immunoliposomes for selective delivery of electron paramagnetic resonance imaging probes to HER2-overexpressing breast tumor cells," *Breast Cancer Res Treat.*, vol. 124, no. 1, pp. 121-131, 2010.
- [180] R. W. Quine, G. A. Rinard, Y. Shi, L. Buchanan, J. R. Biller, S. S. Eaton and G. R. Eaton, "UHF EPR spectrometer operating at frequencies between 400 MHz and 1 GHz," *Concepts Magn Reson Part B*, vol. 46B, pp. 123-133, 2016.
- [181] M. Tseitlin, J. Biller, H. Elajaili, V. Khramtsov, I. Dhimitruka, G. Eaton and S. Eaton, "New spectral-spatial imaging algorithm for full EPR spectra of multiline nitroxides and pH sensitive trityl radicals," *Journal of Magnetic Resonance*, vol. 245, pp. 150-5, 2014.

APPENDICES

Appendix A: MATLAB Code for Field-Stepped Linear Scan EPR

```
%% Field-stepped linear scan spectra reconstruction
% Created by Yilin Shi, on December 20, 2017.      220 lines
% Combined codes by Mark, Jason
% includes: real+imaginary channels, up+down scans, SNR, linewidth calculation
% How to use: 3 check points @ line109/110, 124, 162

%% Data loading: field stepped 2D data
clear all; clc;
fn='ys163652';
[tt rs pars] = eprload(fn);
t=tt{1,1};
B0=tt{1,2};
% pltc(rs(:,21)); return

%% Experimental Parameters
sf=5.017e3; % scan frequency / Hz
rs_width=0.376*27.6*1.085; % scan width / Gauss
sw=80; % Sweep width / Gauss, NOT use
cf=88.3; % Center field /Gauss
step_wise=2; % field resolution /Gauss
tb=(t(2)-t(1))/1e9; % time base / second
fp=535; % first point
cutoff=0.01; % cutoff/2 of data at both the beginning and the end were cut
% to maintain all the data for data reconstruction have the same scan rate
Ph_corr=215; %phase

%% Signal channels balance and orthogonality correction
% Since the quadrature channels are not perfect, a correction is performed
% before the D.C offset correction
Acorr=1; % Amplitude correction
Ph_corr_Ortho=0; % Phase correction
Ph_exp_Ortho=exp(1i*Ph_corr_Ortho/180*pi);
rs_corr_Ortho=Acorr*real(rs*Ph_exp_Ortho)+1i*imag(rs);%the corrected result

%% MW Phase correction
Ph_exp=exp(1i*Ph_corr/180*pi);
rs_phc=(rs_corr_Ortho*Ph_exp);

%% Multiple cycles combination. Up and down scans are processed separately then
combine.
Nc=round(1/(tb*sf)); % number of points per cycle
NC_hc=round(Nc/2); % number of points per half cycle
rs_width_per_ti=rs_width/NC_hc; % rs scan width per point
nop_left=round(NC_hc*(cutoff/2));
nop_right=round(NC_hc*(1-cutoff/2));

rs_phc_hc=rs_phc((fp):(fp+NC_hc),:); %uphalf
AAA=rs_phc((fp+NC_hc):(fp+Nc),:); %downhalf

cyc=floor((t(end)/1e9)/(1/sf))-1; %so down scan won't exceed matrix limit
for k=2:cyc
    rs_phc_hc=rs_phc_hc+rs_phc((fp+(k-1)*Nc):(fp+NC_hc+(k-1)*Nc),:);%uphalf
    AAA=AAA+rs_phc((fp+NC_hc+(k-1)*Nc):(fp+Nc+(k-1)*Nc),:); %downhalf
end

rs_phc_hc=(fliplr(rs_phc_hc'))'; % up
```

```

% AAA=(fliplr(AAA'))'; %down, use either line,depends on up or down scan

%% Spectral reconstruction
a=rs_phc_hc(nop_left:nop_right,1); %for up-scan
rs_cor(:,1)=a;
A=AAA(nop_left:nop_right,1); %for down-scan
AA(:,1)=A;

shift=round(step_wise/rs_width_per_ti*0.922);
sw_total=rs_width+(length(B0)-1)*shift*rs_width_per_ti;

for k=2:length(B0) %Baseline correction by matching overlap regions,up-scan
    b=rs_phc_hc(nop_left:nop_right,k);
    sq=0;
    for m=shift+1:(length(b))
        sq=(a(m)-b(m-shift))+sq;
    end
    dif=sq/(length(b)-shift);
    b=b+dif;
    a=b;
    rs_cor(:,k)=b;
end

for k=2:length(B0) % Baseline correction,down-scan
    B=AAA(nop_left:nop_right,k);
    sq=0;
    for m=shift+1:(length(B))
        sq=(A(m)-B(m-shift))+sq;
    end
    dif=sq/(length(B)-shift);
    B=B+dif;
    A=B;
    AA(:,k)=B;
end

% create zeros matrix for data averaging
rs_cor_zero=zeros((length(B0)-1)*shift+length(b),length(B0));
rs_cor_zerol=rs_cor_zero;

for k=1:length(B0) % Combine segments into a single 2D array, up scan
    bb=rs_cor(:,k);
    startP=(shift)*(k-1)+1;
    rs_cor_zero(startP:length(bb)+startP-1,k)=bb;
end

for k=1:length(B0) % Combine segments into a single 2D array, down scan
    BB=AA(:,k);
    startP=(shift)*(k-1)+1;
    rs_cor_zerol(startP:length(BB)+startP-1,k)=BB;
end
% RE=real(rs_cor_zero); pltc(RE); return %check#1, adjust cut off %
% REl=real(rs_cor_zerol); pltc(REl); return

%% Data averaging to a single 1D array
for k=1:length(rs_cor_zero)
    sum_rs(k,:)=sum(rs_cor_zero(k,:))/length(nonzeros(rs_cor_zero(k,:)));
    sum_rsl(k,:)=sum(rs_cor_zerol(k,:))/length(nonzeros(rs_cor_zerol(k,:)));
end
% pltc(sum_rs); return
% pltc(sum_rsl); return

sum_rs=(fliplr(sum_rs'))'; %up

```

```

% sum_rs1=(fliplr(sum_rs1))'; %down, use either line,correspond to ln 57/58

rs_new=[sum_rs;sum_rs1]; %creat one full cycle
pltc(rs_new); return %check#2

%% linear deco from Mark
sf=1/(tb*length(rs_new));
ph=155;
L=length(rs_new);
ft_sp=fft(rs_new);
d=1.4211e-008/rs_width/sf*0.1;
w=(1:L)*2*pi*sf;
AF = exp(-li*d*w.^2); % analytical function
L2=floor(L/2);
A1=AF(1:L2);
A2=fliplr(conj(A1));
if 2*length(A1)<length(rs_new)
    B=[A1 A1(end) A2];
else
    B=[A1 A2];
end
B=transpose(B);
ss=ifft(ft_sp./B); % slow scan spectrum
ss=ss*exp(li*ph/180*pi); % fine phase correction
% pltc(ss); title(fn); return

%% separate up and down, the add
set(gca,'FontSize',14);
M=length(ss);
ss=ss/max(imag(ss));
spU=ss(1:M/2);
spD=ss(M/2+1:M);

h=(0:(M/2-1))/(M/2-1)-.5;
h=-h; % may need to flirp spectrum left and right
h=h*sw_total+cf;
spD=flipud(spD);
% spU=-spU;spD=-spD;
plot(h,spU,h,spD);
% return %check#3: first point 'fp'

abso=spU+spD;
abso=zeroLine(abso,0.01);
% pltc(abso); return

Re=real(abso);
Im=imag(abso);
Imh=imag(hilbert(Im));
% plot(h,Re,h,Imh); return %check#4:see if use + or - in next line
RI=Re-imag(Imh); % may be + or -, depends
% pltc(RI); return
[BG]=backcor(h,RI,9,0.01,'atq');
% [BG]=backcor(h,RI); %one can adjust
RI=RI-BG;
% pltc(RI); return
%% filter, from Mark
sH=0.1; % filter in G
x=xForInterp(h(end)-h(1),length(RI));
filterH=mygaussian(x,sH);
RI=conv(RI,filterH,'same');

plot(h,RI);

```

```

axis tight;
title('VHF 0.5mM CTPO Field-Step Linear Scan');
xlabel('Magnetic Field (G)');
ylabel('Signal Intensity (AU)');
text(115,7100,fn); %adjust based on axis to make it show on plot

%% calculate linewidth of any peak
step=abs(h(2)-h(1));
m=find(abs(h-81)<step) % select area contain middle peak
n=find(abs(h-95)<step)
midpeak=RI(n:m); %region with middle peak. can be m:n or n:m,depends on h
sw_mp=length(midpeak)*abs((h(end)-h(1)))/length(RI);
Lw(midpeak,sw_mp);

%% calculate SNR
p=find(abs(h-110)<step)
q=find(abs(h-126)<step)
noise=std(RI(q:p)) % noise as base line. p:q or q:p,depends on h.
peak_mp=max(midpeak); % signal as middle peak
SNR=peak_mp/noise
text(115,6600,['SNR= ' num2str(floor(SNR))]);
return

%% for imaging experiment, save complex spectrum
% a1=real(abso);
% b1=imag(abso);
% cut=2;
% a1=a1(cut:end-cut);
% b1=b1(cut:end-cut);
% h=h(cut:end-cut);
% [BG1]=backcor(h,a1,5,0.01,'sh');
% [BG2]=backcor(h,b1,5,0.01,'sh');
% % [BG1]=backcor(h,a1); %one can adjust
% % [BG2]=backcor(h,b1);
% abso=(a1-BG1)+1i*(b1-BG2);
% % pltc(abso);
% % eprsave('ys161969g',h,abso);

```


Appendix B: MATLAB Code for Rapid-Scan EPR Analysis

Based on Dr. Mark Tseitlin's MATLAB code

(1) Spectrum deconvolution

```
clear all; clc;
% May 2019

%% load data

fn='ys188382';
CF = 92;

% for Bruker files:
% [t rs ppp]=eprload(fn);

% for csv files:
R = csvread(strcat(fn,'r.csv'));
I = csvread(strcat(fn,'i.csv'));
RS = R+1i*I;

% for projection in 2D dataset
k=11;
rs=RS(:,k);
% pltc(rs); return

%% input parameters
p.hm=70;
p.Vm=5.020e3;
p.fp=9.28;
p.ph=-155;
p.dt=100e-9;      % time base
p.up=1;           % up must be '1' for up or '-1' for down scan.

% usually fixed
p.bw=10e6;        %
p.fwhm=0;         % post -processing filter, in G
p.Nh=1;           % number of BG harmonics

p.fig=0;          % 1 to show Figure, 0 not to show; should be used to speed
up computaion
Acorr=1;
Ph_corr=0;
Ph_exp=exp(1i*Ph_corr/180*pi);

p.rs=Acorr*real(rs*Ph_exp)+1i*imag(rs);
p.method='fast';
% p.method='slower-better';

%% Deconvolution
[h A B]=sinDecoBG(p);
% show==1
%xlim([-0.3 0.4])
if p.fig==0
    subplot(2,2,[3 4]);
    plot(h,A,h,B);
end
% return
h = h+CF;
```

```

AB = A+B;

%% filter
% sH=50; % Filter in [mG]
% x=xForInterp(h(end)-h(1),length(AB));
% filterH=mygaussian(x,sH/1000);
% AB=conv(AB,filterH,'same');

subplot(2,1,1);
set(gca,'FontSize',12);

%% background correction
BG=backcor(h,AB,6,0.01,'ah');
% [z,a,it,ord,s,fct]=backcor(h,AB,6,0.01,'ah');
% BG=backcor(h,AB);
AB=AB-BG';

%% plot
plot(h,AB,'linewidth',1);
axis tight;
xlabel 'Magnetic Field, G'
ylabel('Signal Intensity (AU)');
title(['VHF Sinusoidal Scan of 1mM CTPO, ', fn])
% return

%% calculate linewidth of any peak
step=abs(h(2)-h(1));
m=find(abs(h-84)<step) % select area contain middle peak
n=find(abs(h-96)<step)
midpeak=AB(m:n); %region with middle peak. can be m:n or n:m,depends on h
sw_mp=length(midpeak)*abs((h(end)-h(1)))/length(AB);
Lw(midpeak,sw_mp);
% return
%% calculate SNR
p=find(abs(h-60)<step)
q=find(abs(h-70)<step)
noise1=std(AB(p:q)) % noise as base line. p:q or q:p,depends on h.
p=find(abs(h-116)<step)
q=find(abs(h-126)<step)
noise2=std(AB(p:q))
noise=(noise1+noise2)/2
peak_mp=max(midpeak) % signal as middle peak
SNR=peak_mp/noise
text(115,4e4,['SNR= ' num2str(floor(SNR))]);
return

```

(2) Image reconstruction

Step 1: deconvolution

```
clear all; clc;

%% check if file exists
par.fn='ys188382'; %file name, must be a 2D file
CF = 92;

% Bruker data format
[xy RS p]=eprload(fn);

% csv format
% RSr=[par.fn 'r.csv'];
% RSi=[par.fn 'i.csv'];
%
% if exist(RSr)&& exist(RSi);
%     disp(RSr);disp(RSi);
% else
%     disp(' file location is not correct');
%     disp(RSr);disp(RSi);     return
% end

%% Generate parameters
% R=csvread(RSr);
% I=csvread(RSi);
% RS=R+li*I; %create spectra in complex numbers
% disp(size(RS));

par.Gmax=10;
par.gstep=0.2;
par.grad=-par.Gmax:par.gstep:par.Gmax;
par.hm=70;
par.Vm=5020; %Scan Frequency, in Hz
par.up=1;     %+1 for up scan, -1 for down
par.ph=-155;
par.fp=9.28;
par.dt=100e-9; % time base

%Usually Fixed Parameters
par.fwhm=0.025; % Post-filtering with Gaussian profile
par.bw=10e6; % >= Resonator BW
par.fig=1;     % ON/OFF figure
par.method='fast';
par.msg=0;     % ON/OFF message
% pars(k).skip=25;
par.fn_out=[par.fn 'data']; % mat-file name w/projections
Ng=length(par.grad);
ii=(1:Ng)/Ng*29;
par.decay_corr=ii*0+1;
save PARS par

%%
Nh=round(2*par.hm/par.fwhm);
h_i=linspace(-par.hm/2,+par.hm/2,Nh);
AA=zeros(length(par.hm),Nh);
BB=AA;

%% addition for variable averages
```

```

%     n=1;
%     gr=zeros(1,101); gr(1)=1;
%     a1=par.Gmax; %Gmax
%     a2=7;
%     a3=2;
%     a4=par.gstep; % gradient step
%     b1=8192; %average in each section
%     b2=4096;
%     b3=4096;

for k=11 % : length(par.grad)
    % - epr read
    %     Nperiod=round(1/par.Vm/par.dt);
    %     skip=round(par.skip*Nperiod/100);
    par.rs=RS(:,k);

    %     par.rs=par.rs*n;
    % %     gr(k)=n; %check if times correct coefficiency
    %     if abs((a1-a2)/a4-k)<0.001
    %         n=b1/b2;
    %     elseif abs((a1-a3)/a4-k)<0.001
    %         n=b1/b3;
    %     elseif abs((a1+a3)/a4-k+1)<0.001
    %         n=b1/b2;
    %     elseif abs((a1+a2)/a4-k+1)<0.001
    %         n=1;
    %     end

    %% deconvolution
    q=par;
    q.hm=par.hm;
    [h A B rs_out bg_out]=sinDecoBG(q);
    plot(h,A,h,B)
    A1=transpose(A);

    if l==1 %plot derivative figure1; no plot 0
        dA=gradient(A); dA=ConvSmooth(dA',180)';
        dB=gradient(B); dB=ConvSmooth(dB',180)';
        in=abs(h)<34;
        plot(h(in),dA(in),h(in),dB(in),'--','linewidth',2); axis tight;
        grid minor

    break %When Active This Break Will Display Derivitave to Fix Phase and FP

    end
    %%
    q.ph=par.ph+90;
    [h Ax Bx rs_out bg_out]=sinDecoBG(q);
    A2=transpose(Ax);

    A=A+1i*Ax;
    B=B+1i*Bx;
%     A=zeroLine(A,0.05);
%     B=zeroLine(B,0.05);
    Ai=interpl(h,A,h_i);
    Ai(isnan(Ai))=0;
    Bi=interpl(h,B,h_i);
    Bi(isnan(Bi))=0;

    AA(k,:)=Ai;
    BB(k,:)=Bi;
    pltc(Ai);

```

```

end

save([par.fn_out], 'h_i', 'AA', 'BB', 'par');

```

Step 2: reconstruction

```

clear all; clc;
%%
load PARS par
%% CORR
ph(1)=0;
CF=92;

% method='pen-rose' %
% tol_pen=1.5
method='tikh_0'
tol_tikh=40;
% image_poly_fit=0;
Max_harm=100;
cut=1; % percent of projection to cut out
app=2; % percent Appodization
PFfactor=4; % polynomial factor for BG removal
h_max=30; %spectrum window/2
zlim=[-1.5 1.5];

%%
for nn=1
    fn_out=par(nn).fn_out;
    %disp(pars(nn).comm);
    load([fn_out], 'h_i', 'AA', 'BB', 'par');
    h=h_i; % newer format
    % z=pars(nn).z; % spatial axis [cm]
    fov=5; % Field of view in [cm] , <= resonator size tube
    Gmax=par.Gmax;
    Lw_min=0.5; % The smallest linewidth in G, 0.02 improves LW, but took 1h
    calculate
        dz=Lw_min/Gmax;
        Npoints=round(1.2*fov/dz); % x1.2, a little larger
        z=linspace(-fov/2,+fov/2,Npoints);

        g=par.grad;
        Nh=length(h);
        Nz=length(z);
        Ng=length(g);
        decay_corr=par(nn).decay_corr;

        %%
        AB=1*AA+1*BB;
        CC=AB*exp(1i/180*pi*ph(nn));
        R=real(CC); % pltc(R(51,:)); return
        % I=imag(CC); % pltc(I(51,:)); return
        % hb=(hilbert(I'))'; % pltc(hb(51,:)); return
        % % reH=real(hb); % pltc(reH(51,:)); return
        % imH=imag(hb); %pltc(imH(51,:)); return
        % % plot(h,imH(51,:),h,R(51,:)); return %check
        % RI=R-imH;
        % R=RI;

```

```

% for k=1:101
% %
%     BG=backcor(h,R(k,:));
%
%     BG=backcor(h,R(k,:),4,0.01,'ah');
%     R(k,:)=R(k,)-BG';
% end
% pltc(R(45,:)); return

R=transpose(R);

%% RECONSTRUCTION
hc=h;
Rc=R;
Nhc=length(hc);

SW=hc(end)-hc(1);
TT=zeros(Ng,Nz,Nhc);

for n=1:Ng
    % frequency-domain method to make phantom
    [v A]=fftM(hc,hc);
    w=ifftshift(2*pi*v); % w= DC ... wmax/w -wmax/2 ... -dw.
    [W,Z] = meshgrid(w,z);
    T=exp(+1i*Z*g(n).*W); TT(n,:,:)=T; % f-domain shift matrix
end

%% Reconstruction
PR=fft(Rc',[ ],2);
x_PH=zeros(Nz,Nhc);

%% Regul operatotrs
v0=ones(1,Nz);
v1=ones(1,Nz-1);
D0=diag(v0,0);
D1=diag(v1,-1)+diag(-v1,+1);
DD1=D1'*D1;
DD0=D0'*D0;

%%
fH=1; % first harmonic
switch method
case 'pen-rose'
    for m=fH:Max_harm %length(w)
        L=TT(:, :, m);
        b=PR(:, m);
        xx=pinv(L,tol_pen)*b;
        x_PH(:, m)=xx;
    end
case 'tikh_0'
    for m=fH:Max_harm %length(w)
        L=TT(:, :, m);
        b=PR(:, m);
        LL=L'*L;
        xx=(LL+tol_tikh*DD0)\L'*b;
        x_PH(:, m)=xx;
    end
case 'tikh_1'
    for m=fH:Max_harm %length(w)
        L=TT(:, :, m);
        b=PR(:, m);
        LL=L'*L;

```

```

                xx=(LL+tol_tikh*DD1)\L'*b;
                x_PH(:,m)=xx;
            end
        end

        %%
        subplot(1,1,1);
        x_Ph=real(iff(x_PH,[],2));
        imagesc(hc,z,x_Ph); %tag=colorbar; %colormap gray
    %     set(tag,'FontSize',16);
        %xlim([-20 23])
        %ylim([-0.75 0.55])
        xlabel 'Magnetic Field, G'
        ylabel 'Position, cm'
    %     return

        %% h cut
        inx=abs(hc)<h_max;
        jnx=(z>zlim(1)&(z<zlim(2)));
        I=x_Ph(jnx,inx);
        h=hc(inx);
    %     if 'cw'=='xx'
    %         for k=1:length(z(jnx))
    %             cw=I(k,:);
    %             rs=cumsum(cw);
    %             I(k,:)=zeroLine(rs,0.05);
    %         end
    %     end
    %     end

        %%
        subplot(2,1,1);
        set(gca,'FontSize',16);
        zj=z(jnx);
        h=h+CF;
        imagesc(h,zj,I); %tag=colorbar;
        title(['Reconstructed Image, 1mM CTPO, ', par.fn, ' sf=5kHz'])
        xlabel 'Magnetic Field Offset, G'
        ylabel 'Position, cm'
    %     return

        subplot(2,1,2);set(gca,'FontSize',16);
        z1=-0.2731; % slice 1 positions
        [vv jn1]=min(abs(zj-z1));
        z2= 0.02101; %0.2731; % slice 2 positions 0.9872
        [vv jn2]=min(abs(zj-z2));

        s11=I(jn1,:);
        s12=I(jn2,:);
        plot(h,s11,h,s12,'-r','linewidth',1)
        xlabel 'Magnetic Field Offset, G'
        axis tight
    %     saveas(gcf,['JPG\' fn_out'],'jpg')
    %     save(['MAT\'fig_' fn_out'],'h','zj','I');
    %     return
end
% plot(h,s12); return
%% background correction
BG=backcor(h,s12,4,0.01,'sh');
% BG=backcor(h,s12);
s12=s12-BG';
% plot(h,s12); return

%% filter, from Mark

```

```

% sH=0.05; % filter in G
% x=xForInterp(h(end)-h(1),length(s12));
% filterH=mygaussian(x,sH);
% s12=conv(s12,filterH,'same');

%% plot
plot(h,s12,'-r','linewidth',1)
xlabel 'Magnetic Field Offset, G'
ylabel 'signal amplitude'
axis tight
% return

%% calculate linewidth of any peak
step=abs(h(2)-h(1));
m=find(abs(h-87)<step) % select area contain middle peak
n=find(abs(h-95)<step)
midpeak=s12(m:n); %region with middle peak. can be m:n or n:m,depends on h
sw_mp=length(midpeak)*abs((h(end)-h(1)))/length(s12);
Lw(midpeak,sw_mp);

%% calculate SNR
p=find(abs(h-63)<step)
q=find(abs(h-70)<step)
noise1=std(s12(p:q)) % noise as base line. p:q or q:p,depends on h.
p=find(abs(h-113)<step)
q=find(abs(h-120)<step)
noise2=std(s12(p:q))
noise=(noise1+noise2)/2
peak_mp=max(midpeak) % signal as middle peak
SNR=peak_mp/noise
text(114,800,['SNR= ' num2str(floor(SNR))]);
% return

%% spatial slice
% subplot(2,1,1);

field=91.74; % pick this field value on image by cursor 90.53
[vv posit]=min(abs(h-field));
spat_amp=I(:,posit); %y-axis
spat=transpose(zj); %x-axis
% spat=-spat;
% BG=backcor(h,AB,4,0.01,'sh');
% BG=backcor(spat,spat_amp);
% spat_amp=spat_amp-BG';

plot(spat,spat_amp,'linewidth',1);
set(gca,'FontSize',12);
title(['Spatial Slice,', par.fn])
xlabel 'position,cm'
ylabel 'signal amplitude'
axis tight
return

```

Appendix C: Python Code for VHF Experiments

(1) Run experiment, Python 2.7 on Linux (version Centos 7)

```

#python 2.7
import ttk
from Tkinter import *
from ttk import *

```



```

import tkinter as tk
import XeprAPI # Load the XeprAPI Module
import numpy as np
import math
import time
import platform
import binascii
import serial
import socket
from function1 import * #import functions
import tkinter.messagebox
import os
import sys
import gc

Xepr=XeprAPI.Xepr()
Xepr.XeprCmds.aqExpSelect(1,'Experiment')

root=tk.Tk()
root.title('Rapid Scan Experiment Control')

grad_B0Offset=0
path='/home/xuser/Desktop/VHFSerial/temp/'

## 3 FUNCTIONS FOR RUN ##

def runRS():

    Xepr.XeprCmds.aqExpSelect(1,'Experiment')

    RSCD(float(e104.get()),float(e102.get()),90,int(e103.get()),float(e402.get()))
    MainMag(float(e101.get()),float(e401.get()))
    ZGrad(float(e105.get()),float(e403.get()))
    cur_exp=Xepr.XeprExperiment() # Get current experiment
    #ExperimentName = cur_exp.aqGetExpName() # Get experiment name

    hidden=Xepr.XeprExperiment('AcqHidden')
    #Xepr.XeprCmds.aqExpDesc("AcqHidden")
    #xPts=hidden['NoOfPoints'].value #int(cur_exp['NbPoints'].value) # Get
number of points
    #hidden['NoOfAverages'].value=4096
    #cur_exp.aqSetIntParValue(cur_exp,"NoOfPoints",0,None,4096)

    a1=hidden['NoOfAverages'].value # Get number of averages
    a2=hidden['NOnBoardAvg'].value # Get number of on-board averages
    a3=hidden['TimeBase'].value # Get time base
    a4=hidden['NoOfPoints'].value # Get number of points
    pts=int(a4)

    with open (path+'parameters.txt','a') as f:
        f.write(str(a1)+'\n')
        f.write(str(a2)+'\n')
        f.write(str(a3)+'\n')
        f.write(str(a4)+'\n')

    specr=np.zeros(pts)
    speci=np.zeros(pts)
    tic1 = time.time() #####
    cur_exp.aqExpRunAndWait() # Equivalent to pressing 'play'
    toc1 = time.time() #####
    print (toc1-tic1)

```

```

dset = Xepr.XeprDataset()
specr=dset.O[:].real
speci=dset.O[:].imag

with open(path+'address.txt', 'r') as f:
    fold = f.read()
    title3=e108.get()
    filename3=fold+'/' + title3 #location
    np.savetxt(filename3+"r.csv",specr, delimiter=",",fmt="%d")
    np.savetxt(filename3+"i.csv",speci, delimiter=",",fmt="%d")

#Xepr.XeprCmds.vpSave('Current', 'Primary', title3, filename3)
toc3 = time.time() ###$$$
print (toc3-tic1)

if(abs(float(e105.get()))>9.9):
    ZGrad(0,1)

def runRSFSDD(): #use field reversal background subtraction
Xepr.XeprCmds.aqExpSelect(1,'Experiment')
ZGrad(float(e105.get()),float(e403.get()))

    stepnum = int (float(e201.get())/float(e202.get()) +1)
    FSarray=np.linspace(float(e101.get())-
(float(e201.get())/2),float(e101.get())+(float(e201.get())/2), stepnum)
    q=0
    cur_exp=Xepr.XeprExperiment() # Get current experiment
    hidden=Xepr.XeprExperiment('AcqHidden')
    #ExperimentName=cur_exp.aqGetExpName() # Get experiment name
    xPts=hidden['NoOfPoints'].value #int(cur_exp['NbPoints'].value) # Get
number of points
    dset2D1=Xepr.XeprDataset(size=(int(xPts),int(len(FSarray))),xeprset =
'primary',iscomplex = True) # Create 2D dataset
    dset2D2=Xepr.XeprDataset(size=(int(xPts),int(len(FSarray))),xeprset =
'secondary',iscomplex = True)

    # Loop Through Field Values
    for i in FSarray:
        print i
        # Scan 1
        MainMag(float(i),float(e401.get()))

RSCD(float(e104.get()),float(e102.get()),90,int(e103.get()),float(e402.get()))
    time.sleep(1)
    cur_exp=Xepr.XeprExperiment() # Get current experiment
    ExperimentName=cur_exp.aqGetExpName() # Get experiment name
    cur_exp.aqExpRunAndWait() # Equivalent to pressing 'play'
    dset1D1=Xepr.XeprDataset()
    dset2D1.O[q] [:]=dset1D1.O[: ]
    Xepr.XeprCmds.aqExpSelect(1,'Experiment')

    # Scan 2
    MainMag(-float(i),float(e401.get()))

RSCD(float(e104.get()),float(e102.get()),270,int(e103.get()),float(e402.get()))
    time.sleep(1)
    cur_exp=Xepr.XeprExperiment() # Get current experiment
    ExperimentName=cur_exp.aqGetExpName() # Get experiment name
    cur_exp.aqExpRunAndWait() # Equivalent to pressing 'play'
    dset1D2=Xepr.XeprDataset()

```

```

dset2D2.O[q] [:]=dset1D2.O[:]

# Up the index counter 'q'
q=q+1

dset2D1.X=dset1D1.X
dset2D1.Y=FSarray
dset2D1.update(refresh=True)
dset2D1.setXprSet('primary')

with open(path+'address.txt', 'r') as f:
    fold = f.read()
    title1=e106.get()
    filename1=fold+'/'+ title1 #location
    Xpr.XexprCmds.vpSave('Current', 'Primary', title1, filename1)

dset2D2.X=dset1D2.X
dset2D2.Y=FSarray
dset2D2.update(refresh=True)
dset2D2.setXprSet('secondary')

title2=e107.get()
filename2=fold+'/'+ title2 #location
Xpr.XexprCmds.vpSave('Current', 'Secondary', title2, filename2)

Xpr.XexprCmds.prDiff('Current', 'Primary', 'All', 'Current', 1,0,1)

title3=e108.get()
filename3=fold+'/'+ title3 #location
Xpr.XexprCmds.vpSave('Current', 'Result', title3, filename3)

def runRSgrad():
    tic = time.time() #####
    Xpr.XexprCmds.aqExpSelect(1, 'Experiment')
    gstep=float(e302.get())
    Gmax= float(e301.get())
    Ng = int(2*Gmax/gstep+1)
    Garray=np.linspace(-Gmax, Gmax, Ng)
    #Garray=np.linspace(9.2, Gmax, 81)

    q=0
    cur_exp=Xpr.XexprExperiment() # Get current experiment
    hidden=Xpr.XexprExperiment('AcqHidden')
    #ExperimentName=cur_exp.aqGetExpName() # Get experiment name
    a1=hidden['NoOfAverages'].value # Get number of averages
    a2=hidden['NonBoardAvg'].value # Get number of on-board averages
    a3=hidden['TimeBase'].value # Get time base
    a4=hidden['NoOfPoints'].value # Get number of points

    pts=int(a4)

    with open (path+'parameters.txt', 'a') as f:
        f.write(str(a1)+'\n')
        f.write(str(a2)+'\n')
        f.write(str(a3)+'\n')
        f.write(str(a4)+'\n')

    hidden=Xpr.XexprExperiment('AcqHidden')
    if Avg.get()==1:
        hidden['NoOfAverages'].value=int((e305.get()))
    toc6 = time.time() #####

```

```

print (toc6-tic)

specr=np.zeros(( pts,Ng ))
speci=np.zeros(( pts,Ng ))

# Loop Through Gradient Values
for g in Garray: # g is gradient value
    if Avg.get()==1:

        if ( abs(g+float(e303.get()))<0.001 ):
            hidden['NoOfAverages'].value=int((e306.get()))
            #hidden['NonBoardAvs'].value=256
        elif( abs(g+float(e304.get()))<0.001 ):
            hidden['NoOfAverages'].value=int((e307.get()))
            #hidden['NonBoardAvs'].value=256
        elif( abs(g-float(e304.get()))-gstep<0.001 ):
            hidden['NoOfAverages'].value=int((e306.get()))
            #hidden['NonBoardAvs'].value=256
        elif( abs(g-float(e303.get()))-gstep<0.001 ):
            hidden['NoOfAverages'].value=int((e305.get()))
            #hidden['NonBoardAvs'].value=256

        print str(g)+' , avg.: '+str(hidden['NoOfAverages'].value)

        else:
            print g

        tic1=time.time()

        MainMag(float(e101.get())-
(grad_B0Offset*(float(g)*float(g)),float(e401.get()))
        ZGrad(float(g),float(e403.get()))

RSCD(float(e104.get()),float(e102.get()),90,int(e103.get()),float(e402.get()))
#toc5 = time.time() #####
#print (toc5-tic1)

cur_exp=Xepr.XeprExperiment() # Get current experiment
#ExperimentName=cur_exp.aqGetExpName() # Get experiment name

tic3=time.time()
cur_exp.aqExpRunAndWait() # Equivalent to pressing 'play'
toc3 = time.time() #####
print (toc3-tic3)

#if ( abs(g+10)<0.6 ) or (abs(g-10)<0.6):
if ( abs(g+10)<1 ) or (abs(g-10)<1):
    ZGrad(0, 1)

### zero at high gradient
if abs(g+9)<0.001:
    ZGrad(0, 1)
elif abs(g+8)<0.001:
    ZGrad(0, 1)
elif abs(g+7)<0.001:
    ZGrad(0, 1)
elif abs(g+6)<0.001:
    ZGrad(0, 1)
elif abs(g-6)<0.001:
    ZGrad(0, 1)
elif abs(g-7)<0.001:
    ZGrad(0, 1)

```

```

elif abs(g-8)<0.001:
    ZGrad(0, 1)
elif abs(g-9)<0.001:
    ZGrad(0, 1)

tic4 = time.time()
    dset1D1=Xepr.XeprDataset()
#print (type (Xepr.XeprDataset()))
#print (type (dset1D1))
specr[:,q]=dset1D1.O[:].real
speci[:,q]=(dset1D1.O[:]).imag

    toc1 = time.time() #####
    print (toc1-tic4)
print (toc1-tic1)

gc.collect()
del dset1D1
#del dset1D2
    q=q+1 # index counter 'q'

ZGrad(0, 1)
tic4=time.time() #####

with open(path+'address.txt', 'r') as f:
    fold = f.read()

title3=e108.get()
filename3=fold+'/' + title3 #location

np.savetxt(filename3+"r.csv",specr, delimiter=",",fmt="%d")
np.savetxt(filename3+"i.csv",speci, delimiter=",",fmt="%d")

toc4 = time.time() ####$$
print (toc4-tic4) ####$$
toc = time.time()
print (toc-tic)

#####
##### Experiment GUI #####
#####

nb=ttk.Notebook(root)
nb.grid(row=0, column=0, columnspan=50, rowspan=49, sticky='NESW')

frame1 = ttk.Frame(nb) #experiment settings
frame2 = ttk.Frame(nb)
frame3 = ttk.Frame(nb)
frame4 = ttk.Frame(nb)
nb.add(frame1, text=' Experiment Settings ')
nb.add(frame2, text=' Field Step Settings ')
nb.add(frame3, text=' Z Gradient Settings ')
nb.add(frame4, text=' Spectrometer Settings ')

f = open(path+'parameters.txt', "r")
temp = f.read().splitlines()
i=0

### frame1

```

```

eL101 = Label(frame1, text="Main Field (G)" #, font=("Helvetica", 16))
eL101.grid(row=1, column=1, sticky=E)
e101 = Entry(frame1)
e101.insert(0, temp[i]) #1: 91
i+=1
e101.grid(row=1, column=2,padx = 5,pady = 5)

eL102 = Label(frame1, text="Rapid Scan Width (G)")
eL102.grid(row=2, column=1, sticky=E)
e102 = Entry(frame1)
e102.insert(0, temp[i]) #2: 70
i+=1
e102.grid(row=2, column=2,padx = 5,pady = 5)

eL103 = Label(frame1, text="Cycles per Trigger")
eL103.grid(row=3, column=1, sticky=E)
e103=Spinbox(frame1, from_=1, to=10, increment=1)
e103.delete(0,"end")
e103.insert(0,temp[i]) #3: 4
i+=1
e103.grid(row=3, column=2,padx = 5,pady = 5)

eL104 = Label(frame1, text="Scan Frequency (Hz)")
eL104.grid(row=4, column=1, sticky=E)
e104 = Entry(frame1)
e104.insert(0, temp[i]) #4: 5070
i+=1
e104.grid(row=4, column=2,padx = 5,pady = 5)

eL105 = Label(frame1, text="Gradient (G/cm) ")
eL105.grid(row=5, column=1, sticky=E)
e105 = Entry(frame1)
e105.insert(0, temp[i]) #5: 0
i+=1
e105.grid(row=5, column=2,padx = 5,pady = 5)

eL106 = Label(frame1, text="Scan 1 name: ")
eL106.grid(row=1, column=3, sticky=E)
e106 = Entry(frame1)
e106.insert(0, temp[i]) #6: ys1
i+=1
e106.grid(row=1, column=4,padx = 5,pady = 5)

eL107 = Label(frame1, text="Scan 2 name: ")
eL107.grid(row=2, column=3, sticky=E)
e107 = Entry(frame1)
e107.insert(0, temp[i]) #7: ys2
i+=1
e107.grid(row=2, column=4,padx = 5,pady = 5)

eL108 = Label(frame1, text="Spectrum name: ")
eL108.grid(row=3, column=3, sticky=E)
e108 = Entry(frame1)
e108.insert(0, temp[i]) #8: ys3
i+=1
e108.grid(row=3, column=4,padx = 5,pady = 5)

l11 = Label(frame1, text="Fold to store files: ")
l11.grid(row=4, column=3, sticky=E)

with open(path+'address.txt', 'r') as f:

```

```

    name=f.read()
l12 = Label(frame1, text = "Current fold is: ")
l12.grid(row=5, column=3, sticky=E)
l13 = Label(frame1, text = name)
l13.grid(row=6, column=3, columnspan=2)

def foldin():
    fold = fd.askdirectory()
    with open (path+'address.txt','w') as f:
        f.write(fold)

    with open (path+'address.txt', 'r') as f:
        name = f.read()
        l13['text'] = name

b11 = Button(frame1, text = " Change ", command=foldin)
b11.grid(row=4,column=4)

l14 = Label(frame1, text = " ")
l14.grid(row=7, column=1, columnspan=2, sticky=W)

### frame2
eL201 = Label(frame2, text="Field Step Scan Width (G)")
eL201.grid(row=2, column=1, sticky=E)
e201 = Entry(frame2)
e201.insert(0, temp[i])    #9: 40
i+=1
e201.grid(row=2, column=2,padx = 5,pady = 5)

eL202 = Label(frame2, text="Field Step Size (G)")
eL202.grid(row=3, column=1, sticky=E)
e202 = Entry(frame2)
e202.insert(0, temp[i])    #10: 5
i+=1
e202.grid(row=3, column=2,padx = 5,pady = 5)

eL203 = Label(frame2, text=" ")
eL203.grid(row=5, column=1, sticky=E)

### Use Field Step Toggle
def FStog():
    if FS.get()==1:
        for child in frame3.wininfo_children():
            child.configure(state='disabled')
    else:
        for child in frame3.wininfo_children():
            child.configure(state='normal')
        avgoff()

FS=IntVar()
FSDDCheck=Checkbutton(frame2, text='Field Step', variable=FS, onvalue=1,
offvalue=0, command=FStog)
FSDDCheck.grid(row=6, column=1, sticky=E)

### frame 3
eL301 = Label(frame3, text="Maximum Gradient (G/cm)")
eL301.grid(row=2, column=1, sticky=E)
e301 = Entry(frame3)
e301.insert(0, temp[i])    #11: 10
i+=1
e301.grid(row=2, column=2,padx = 5,pady = 5)

```

```

eL302 = Label(frame3, text="Gradient Step Size (G/cm)")
eL302.grid(row=3, column=1, sticky=E)
#e302 = Entry(frame3)
e302=Spinbox(frame3, from_=0.1, to=10, increment=0.01)
e302.delete(0,"end")
e302.insert(0, temp[i]) #12: 0.2
i+=1
e302.grid(row=3, column=2,padx = 5,pady = 5)

l301 = Label(frame3, text="                ")
l301.grid(row=4, column=1, sticky=E)
l302 = Label(frame3, text="                ")
l302.grid(row=8, column=1, sticky=E)

# Use Z Gradient Toggle
def Ztog():
    if ZG.get()==1:
        e105.configure(state='disabled')
    for child in frame2.wininfo_children():
        child.configure(state='disabled')
    else:
        e105.configure(state='enabled')
    for child in frame2.wininfo_children():
        child.configure(state='enabled')
ZG=IntVar()
ZGradCheck=Checkbutton(frame3, text='Z Gradient', variable=ZG, onvalue=1,
offvalue=0, command=Ztog)
ZGradCheck.grid(row=5, column=1, sticky=E)

### Use Average Toggle
def avgon():
    l303.configure(state='normal')
    l304.configure(state='normal')
    l305.configure(state='normal')
    l306.configure(state='normal')
    l307.configure(state='normal')
    l308.configure(state='normal')
    eL303.configure(state='normal')
    e303.configure(state='normal')
    eL304.configure(state='normal')
    e304.configure(state='normal')
    eL305.configure(state='normal')
    e305.configure(state='normal')
    eL306.configure(state='normal')
    e306.configure(state='normal')
    eL307.configure(state='normal')
    e307.configure(state='normal')

def avgoff():
    l303.configure(state='disabled')
    l304.configure(state='disabled')
    l305.configure(state='disabled')
    l306.configure(state='disabled')
    l307.configure(state='disabled')
    l308.configure(state='disabled')
    eL303.configure(state='disabled')
    e303.configure(state='disabled')
    eL304.configure(state='disabled')
    e304.configure(state='disabled')

```



```

eL305.configure(state='disabled')
e305.configure(state='disabled')
eL306.configure(state='disabled')
e306.configure(state='disabled')
eL307.configure(state='disabled')
e307.configure(state='disabled')

def avgtog():
    if Avg.get()==1:
        l305['text']= e301.get()
        avgon()
    else:
        avgoff()

Avg=IntVar()
AvgCheck=Checkbutton(frame3, text='Variable Averages', variable=Avg, onvalue=1,
offvalue=0, command=avgtog)
AvgCheck.grid(row=2, column=4, columnspan=4,sticky=E)

w = Canvas(frame3, width=300, height=150)
w.create_rectangle(10, 10, 300, 150, outline = 'white')
w.grid(row=3, column=3,columnspan=10, rowspan=5)

l303 = Label(frame3, text="      Gradient Range (absolute values, G/cm) ")
l303.grid(row=3, column=4, columnspan=7)

l304 = Label(frame3, text=" |-----|-----|-----|
-----| ")
l304.grid(row=4, column=4, columnspan=7)

l305 = Label(frame3, text=" ", width=4) #same as Gmax: 10
l305.grid(row=5, column=4,)

eL303 = Label(frame3, text=" ", width=5)
eL303.grid(row=5, column=5)
e303 = Entry(frame3, width=2)
e303.insert(0, temp[i]) #13: 6
i+=1
e303.grid(row=5, column=6)

eL304 = Label(frame3, text=" ", width=5)
eL304.grid(row=5, column=7)
e304 = Entry(frame3, width=2)
e304.insert(0, temp[i]) #14: 2
i+=1
e304.grid(row=5, column=8)

l306 = Label(frame3, text=" ", width=5)
l306.grid(row=5, column=9)
l307 = Label(frame3, text="0", width=2)
l307.grid(row=5, column=10)

eL305 = Label(frame3, text="Avg.: [", width=5)
eL305.grid(row=7, column=4, sticky=E)
e305 = Entry(frame3, width=5)
e305.insert(0, temp[i]) #15: 2048
i+=1
e305.grid(row=7, column=5)

eL306 = Label(frame3, text=") [", width=2)

```

```

eL306.grid(row=7, column=6)
e306 = Entry(frame3, width=5)
e306.insert(0, temp[i]) #16: 1024
i+=1
e306.grid(row=7, column=7)

eL307 = Label(frame3, text="[" , width=2)
eL307.grid(row=7, column=8)
e307 = Entry(frame3, width=5)
e307.insert(0, temp[i]) #17: 512
i+=1
e307.grid(row=7, column=9)
l308 = Label(frame3, text="]", width=2)
l308.grid(row=7, column=10)

avgoff()

### frame 4
eL401 = Label(frame4, text="Main Magnet Coil Constant (G/A)")
eL401.grid(row=1, column=1, sticky=E)
e401 = Entry(frame4)
e401.insert(0, temp[i]) #18: 4.74
i+=1
e401.grid(row=1, column=2, padx = 5, pady = 5)

eL402 = Label(frame4, text="Rapid Scan Coil Constant (G/A)")
eL402.grid(row=2, column=1, sticky=E)
e402 = Entry(frame4)
e402.insert(0, temp[i]) #19: 27.7
i+=1
e402.grid(row=2, column=2, padx = 5, pady = 5)

eL403 = Label(frame4, text="Z Gradient Coil Constant (G/A)")
eL403.grid(row=3, column=1, sticky=E)
e403 = Entry(frame4)
e403.insert(0, temp[i]) #20: 0.5
i+=1
e403.grid(row=3, column=2, padx = 5, pady = 5)

l401 = Label(frame4, text=" ")
l401.grid(row=4, column=1, sticky=E)
l402 = Label(frame4, text=" Check Serial Port (Rapid Scan Coil Driver)")
l402.grid(row=5, column=1, sticky=E)
l403 = Label(frame4, text=" Check...")
l403.grid(row=7, column=1, sticky=W)

def checkRSCD():
    a=checkcd()
    l403['text']=a

b401=Button(frame4, text='Check', command=checkRSCD)
b401.grid(row=6, column=1)

def CheckNRun():
    if os.path.isfile(path+'parameters.txt'):
        os.remove(path+'parameters.txt')
    with open (path+'parameters.txt','a') as f:
        f.write(e101.get()+'\n')
        f.write(e102.get()+'\n')

```

```

        f.write(e103.get()+'\n')
        f.write(e104.get()+'\n')
        f.write(e105.get()+'\n')
        f.write(e106.get()+'\n')
        f.write(e107.get()+'\n')
        f.write(e108.get()+'\n')
        f.write(e201.get()+'\n')
        f.write(e202.get()+'\n')
        f.write(e301.get()+'\n')
        f.write(e302.get()+'\n')
        f.write(e303.get()+'\n')
        f.write(e304.get()+'\n')
        f.write(e305.get()+'\n')
        f.write(e306.get()+'\n')
        f.write(e307.get()+'\n')
        f.write(e401.get()+'\n')
        f.write(e402.get()+'\n')
        f.write(e403.get()+'\n')

    if FS.get()==1 and ZG.get()==0:
        runRSFSDD()
    elif FS.get()==0 and ZG.get()==1:
        runRSgrad()
#     elif FS.get()==1 and ZG.get()==1:
#         tkMessageBox.showinfo('Warning','Cannot run field step and gradient step
at the same time. \n Please select only one check-box.')
    else:
        runRS()

b1=Button(root, text='Send', command=CheckNRRun)
b1.grid(row=50, column=1)

l1 = Label(root, text=" ")
l1.grid(row=50, column=2)

# 0 Buttons
def zero1():
    MainMag(0, 1)
b2 = Button(root, text =" Set Main Magnet to 0 G ", command=zero1)
b2.grid(row=50,column=3)

l2 = Label(root, text=" ")
l2.grid(row=50, column=4)

def zero2():
    RSCD(1000, 0, 90, 1, 1)
b3 = Button(root, text =" Set RSCD to 0 A ", command=zero2)
b3.grid(row=50,column=5)

l3 = Label(root, text=" ")
l3.grid(row=50, column=6)

def zero3():
    e105.delete(0,"end")
    e105.insert(0, 0)
    ZGrad(0, 1)
b4=Button(root, text='Set Z Gradient to 0 G/cm', command=zero3)
b4.grid(row=50, column=7, sticky=E)

l4 = Label(root, text=" ")
l4.grid(row=50, column=8)

```

```

b5=Button(root, text='Close', command=root.quit)
b5.grid(row=50, column=9)

l5 = Label(root, text=" ", font=("Helvetica", 8))
l5.grid(row=51, column=1)

root.mainloop()

```

(2) Data analysis, Python 3.6

Script 1: Spectrum Deconvolution

```

##### Rapid-scan EPR spectrum code #####
# Yilin Shi, May 2019, shiyilin890@gmail.com
# choose 0: False, function skipped; 1: True, function performed
# Read Bruker data or csv; 1D or 2D data
# Reference [1,2,3]

import os
import numpy as np
import scipy as sp
import matplotlib.pyplot as plt
import csv
from tkinter import *
import math
import cmath
import struct
import numpy.matlib
from rs3func import *

if __name__ == '__main__':

    ##### Input parameters
    fn = 'ys188382' # filename
    sample = '1mM CTPO, sf=5kHz, ' # in title
    tb = 100 * 10 ** -9 # time base, ns
    pts = 8192 # known from data
    CF = 92 # center field
    sw = 70 # sweep width
    sf = 5020 # scan frequency, Hz
    fp = 9.28 # first point, value must exist in (-1,1), ADJUST
    ph = -155 # phase

    # function options
    use2d = 1 # use 2D image data, also need Gmax, gstep, n
    below
    useBruker = 0 # use Bruker format data DTA and DSC
    plotraw = 0 # plot raw data
    adjustspectrum = 0 # I need to adjust parameters (first point and
    phase) (0: don't need)
    usefilter = 0 # use filter or not
    sH = 50 # filter, [mG]
    usebackcor = 1 # use backcor function
    backcorpar = 0 # I know what backcor parameters to use! (0:
    don't know)
    uselw = 1 # calculate linewidth, input peak and baseline
    position below

```

```

useSNR = 1                # calculate S/R
                          # field range: [G], use cursor to pick values on
the plot
peakrange = [84, 96]     # includes the line, [G]
noiserange1 = [60, 70]   # includes noise section 1, [G]
noiserange2 = [116, 126] # includes noise section 2, [G]

if use2d:                 # use 2D image data
    Gmax = 10            # Maximum gradient, G/cm
    gstep = 1           # gradient step, G/cm
    Ng = int(2 * Gmax / gstep + 1) # number of projections/gradients
    n = 11              # which projection to use
else:                    # use 1D spectrum data
    Ng = 1
    n = 1

##### calculation starts, usually don't require input
##### import data
if useBruker:           # use Bruker format data DTA and DSC
    # check if files exist
    if os.path.isfile(fn + '.DTA') and os.path.isfile(fn + '.DSC'):
        print('Bruker file ' + fn)
    elif os.path.isfile(fn + '.DTA') and (os.path.isfile(fn + '.DSC') ==
0):
        print('Bruke data file \'DTA\' is present, but the parameter file
\'DSC\' is missing.')
    else:
        print('Bruker file does not exist!')
        exit()
    # exit()

Bruker = []
fin = open(fn + '.DTA', 'rb')
with open(fn + '.DTA', 'rb') as inh:
    indata = inh.read()
    for i in range(0, len(indata), 8):
        pos = struct.unpack('>d', indata[i:i + 8])
        Bruker.append(pos[0]);
fin.close()

if not len(Bruker) == pts*Ng*2: # Imaginary and Real data, so X2
    print('Input wrong! check number of points, Gmax, Gstep ')
    exit()

Bkre = np.zeros((pts, Ng), dtype=int)
Bkim = np.zeros((pts, Ng), dtype=int)
for i in range(Ng):
    for j in range(pts):
        Bkre[j][i] = Bruker[i * pts * 2 + j * 2]
        Bkim[j][i] = Bruker[i * pts * 2 + j * 2 + 1]
np.savetxt(fn + "r.csv", Bkre, delimiter=",", fmt="%d")
np.savetxt(fn + "i.csv", Bkim, delimiter=",", fmt="%d")
# exit()

# use csv format
# check if file exist
if os.path.isfile(fn + 'r.csv') and os.path.isfile(fn + 'i.csv'):
    print(fn)
else:
    print('csv file does not exist!')
    exit()

```

```

reader = csv.reader(open(fn + 'r.csv', "r"), delimiter=",")
x = list(reader)
R = np.array(x).astype("int")
reader = csv.reader(open(fn + 'i.csv', "r"), delimiter=",")
x = list(reader)
I = np.array(x).astype("int")

# check if input correct
pts1 = R.shape[0]
Ng1 = R.shape[1]
if not pts1 == pts:
    print('Input wrong! Check number of points ')
    exit()
elif not Ng1 == Ng:
    print('Input wrong! Check Gmax, gstep ')
    exit()

t = np.arange(pts) * tb
rr = R[:, n - 1]
ii = I[:, n - 1]

if plotraw:      # plot raw data
    plt.plot(t, ii, t, rr)
    plt.show()
    exit()

bw = 10 ** 6 # bandwidth
fwhm = 0.025 # post processing filter
Acorr = 1
Phcorr = 0
Ph_exp = cmath.exp(1j * Phcorr / 180 * math.pi)
rs = rr + 1j * ii
rs = Acorr * (rs * Ph_exp).real + 1j * rs.imag
method = 'fast'
# method='slower'
np.savetxt("temp/rsr.csv", rs.real, delimiter=",", fmt="%d")
np.savetxt("temp/rsi.csv", rs.imag, delimiter=",", fmt="%d")
np.savetxt("temp/t.csv", t, delimiter=",")

### save parameter file
if os.path.isfile('temp/parfix.txt'):
    os.remove('temp/parfix.txt')
with open ('temp/parfix.txt','a') as f:
    f.write(str(sw)+'\n')
    f.write(str(sf)+'\n')
    f.write(str(tb)+'\n')
    f.write(method+'\n')
    f.write(str(pts)+'\n')
    f.write(str(CF)+'\n')

if adjustspectrum:
    window = Tk()
    window.title("Up and Down Scan Adjust")
    window.geometry("400x250+900+200")
    start = adjust(window)
    window.mainloop()

    f = open('temp/parvary.txt', "r")
    temp = f.read().splitlines()
    ph = float(temp[0])
    fp = float(temp[1])
    f.close()

```

```

h, A, B = sinDecoBG(sw,sf,tb,t,rs,ph,fp,method)
AB = A+B
h = h+CF

if usefilter:          # Filter
    x = xForInterp(h[-1] - h[0], len(AB))
    filterH = mygaussian(x, sH / 1000)
    AB = np.convolve(AB, filterH, 'same')

if usebackcor:        # use 'backcor' background correction
    if backcorpar:     # I known what parameters to use!
        BG = backcor(h, AB, 6, 0.01, 'ah')
        AB = AB-BG

    else:            # try different parameters with GUI
        np.savetxt("temp/xdata.csv", h, delimiter=",")
        np.savetxt("temp/ydata.csv", AB, delimiter=",")
        window = Tk()
        window.title("backcor")
        window.geometry("300x250+900+200")
        start = mclass(window)
        window.mainloop()

        reader = csv.reader(open('temp/ybackcor.csv', "r"), delimiter=",")
        x = list(reader)
        AB1 = np.array(x).astype("float")
        AB = AB1[:,0]

plt.subplot(211)
plt.plot(h, AB, linewidth=1)
plt.xlabel('Magnetic Field, G')
plt.ylabel('Signal Amplitude, AU')
plt.title('VHF rapid-scan of ' + sample + fn)

plt.subplot(212)
plt.plot(h, A, h, B, linewidth=1)
plt.title('Up and Down Scans ')
plt.show()
# exit()

step = abs(h[1] - h[0])
m = np.where(abs(h - peakrange[0]) < step)[0][0] # define peak
n = np.where(abs(h - peakrange[1]) < step)[0][0]
peak = AB[m:n]

### Calculate linewidth
if uselw:
    swpeak = len(peak) * abs((h[-1] - h[0])) / len(AB)
    pphh = LW(peak,swpeak)
    print('linewidth,mG: ', pphh, '(lw at half height of absorption
signal)')

### Calculate SNR
if useSNR:
    p = np.where(abs(h-noiserange1[0])<step)[0][0] # define baseline
    q = np.where(abs(h-noiserange1[1])<step)[0][0]
    noise1 = np.std(AB[p:q]) #p:q or q:p if h reverses
    p = np.where(abs(h-noiserange2[0])<step)[0][0]
    q = np.where(abs(h-noiserange2[1])<step)[0][0]
    noise2 = np.std(AB[p:q]) #p:q or q:p if h reverses
    noise = (noise1 + noise2) / 2

```

```

    peak_amp = max(peak)           #signal
    SNR = peak_amp / noise
    print('S/N: ', SNR)

```

Script 2: Image Reconstruction

```

##### Rapid-scan EPR Imaging code #####
# Yilin Shi, May 2019, shiyilin890@gmail.com
# choose 0: False, function skipped; 1: True, function performed
# Read Bruker data or csv; 2D data only
# Reference [1,2,3]

import os
import numpy as np
import scipy as sp
import matplotlib.pyplot as plt
import csv
from tkinter import *
import math
import cmath
import struct
import numpy.matlib
from rs3func import *

if __name__ == '__main__':

    ##### Input parameters
    # adjust spectrum parameters (phase and first point) in step1
    'rs1spectrum.py'
    # Bruker file converted to csv in step 1
    fn = 'ys188382'
    sample = '1mM CTPO, sf=5kHz, ' #in title
    tb = 100 * 10 ** -9 # time base
    pts = 8192 # known from data
    Gmax = 10 # Maximum gradient, G/cm
    gstep = 1 # gradient step, G/cm
    CF = 92 # center field
    sw = 70 # sweep width
    sf = 5020 # scan frequency,Hz
    fp = 9.28 # first point (value must exist in (-1, 1)
    ph = -155 # phase
    h_max = 30 # final plot half field range
    zlim = [-1.5, 1.5] # final plot spatial range
    fov = 5 # field of view
    Lw_min = 0.5 # minimal line width
    Ng = int(2 * Gmax / gstep + 1) # number of projections/gradients

    # function options
    plotraw = 0 # plot raw data
    step2 = 1 # I need to deconvolve projections (0: prj
already deconvolved)
    plotsino = 0 # plot sinograph
    usebothch = 0 # use real and imaginary channels
    rawimg = 0 # plot raw image
    spat1 = 1 # plot spatial slice of the image
# for spectral slice:
    specs1 = 1 # plot spectral slice of the image
    usebackcor = 1 # use backcor function

```



```

backcorpar = 1          # I know what backcor parameters to use! (0:
don't know)
uselw = 1              # calculate linewidth, input peak and baseline
position below
useSNR = 1             # calculate S/R
# position of spectral and spatial slice pick on image and input at the
bottom

##### calculation starts, usually don't require input
# check if file exist
if os.path.isfile(fn + 'r.csv') and os.path.isfile(fn + 'i.csv'):
    print(fn)
else:
    print('File not exit!')
    exit()

# import data in csv format
reader = csv.reader(open(fn + 'r.csv', "r"), delimiter=",")
x = list(reader)
R = np.array(x).astype("int")
reader = csv.reader(open(fn + 'i.csv', "r"), delimiter=",")
x = list(reader)
I = np.array(x).astype("int")

# check if matrix dimension match
pts1 = R.shape[0]
Ng1 = R.shape[1]
if not pts1 == pts:
    print('Input wrong! check number of points ')
    exit()
elif not Ng1 == Ng:
    print('Input wrong! check Gmax, gstep ')
    exit()
elif Ng1 == 1:
    print('Need 2D dataset, but 1D data is given')
    exit()

t = np.arange(pts) * tb

if plotraw: # plot raw data
    n = 11
    rr = R[:, n - 1]
    ii = I[:, n - 1]
    plt.plot(t, ii, t, rr)
    plt.show()
    exit()

bw = 10 ** 6 # bandwidth
fwhm = 0.025 # post processing filter
method = 'fast'
# method='slower'

Nh1 = round(2 * sw / fwhm)
h_i = np.linspace(-sw / 2, +sw / 2, Nh1)

AA = np.zeros((Nh1, Ng), dtype=complex)
BB = np.zeros((Nh1, Ng), dtype=complex)

# Step2: projection deconvolution
# if you have deconvolved the data, you can skip.
if step2:
    for k in range(Ng):

```

```

rr = R[:, k]
ii = I[:, k]
rs = rr + 1j * ii

if (0): # if one wants channel balance
    Acorr = 1
    Phcorr = 0
    Ph_exp = cmath.exp(1j * Phcorr / 180 * math.pi)
    rs = Acorr * (rs * Ph_exp).real + 1j * rs.imag

h, A, B = sinDecoBG(sw, sf, tb, t, rs, ph, fp, method)
h, Ax, Bx = sinDecoBG(sw, sf, tb, t, rs, (ph + 90), fp, method)

A = A + 1j * Ax
B = B + 1j * Bx
Ai = np.interp(h_i, h, A) # Xquery,x,y,
cnt = len(Ai)
if Ai[-1] == 0:
    check = Ai[0]
    for i in range(round(cnt / 2)): # 37782
        if Ai[i] == check:
            Ai[i] = 0
else:
    check = Ai[-1]
    for i in range(cnt - 1, round(cnt / 2), -1): # 37782
        if Ai[i] == check:
            Ai[i] = 0

Bi = np.interp(h_i, h, B) # Xquery,x,y,
cnt = len(Bi)
if Bi[-1] == 0:
    check = Bi[0]
    for i in range(round(cnt / 2)): # 37782
        if Bi[i] == check:
            Bi[i] = 0
else:
    check = Bi[-1]
    for i in range(cnt - 1, round(cnt / 2), -1): # 37782
        if Bi[i] == check:
            Bi[i] = 0

AA[:, k] = Ai
BB[:, k] = Bi

AB = AA + BB
np.savetxt("ABr.csv", AB.real, delimiter=",", fmt="%d")
np.savetxt("ABi.csv", AB.imag, delimiter=",", fmt="%d")
print('Deconvolved projections is saved as ABr, ABi.csv ')

else:
    if os.path.isfile('ABr.csv') and os.path.isfile('ABi.csv'):
        print('Use saved deconvolved projections.')
    else:
        print('Deconvolved projections not exit!\n Please deconvolve
projections first.')
        exit()
    reader = csv.reader(open('ABr.csv', "r"), delimiter=",")
    x = list(reader)
    ABR = np.array(x).astype("int")
    reader = csv.reader(open('ABi.csv', "r"), delimiter=",")
    x = list(reader)
    ABI = np.array(x).astype("int")
    AB = ABR+1j*ABI

```

```

method1 = 'tikh_0'
tol_tikh = 40
Max_harm = 100
h = h_i
dz = Lw_min/Gmax
Npoints = round(1.2*fov/dz)
z = np.linspace(-fov/2,+fov/2, Npoints)
g = np.linspace(-Gmax, +Gmax, Ng)
Nh = len(h)
Nz = len(z)

if plotsino: #plot sinogram
    sino = (AB.real).T
    imgplot = plt.imshow(sino, aspect='auto', extent=[h[0] + CF, h[-1] +
CF, g[0], g[-1]])
    plt.ylabel('Gradient, G/cm')
    plt.xlabel('Magnetic Field, G')
    plt.title('Projections Stack Plot of ' + sample + fn)
    plt.show()
    exit()

phnn = 0 # phase adjust if want
CC = AB*cmath.exp(1j/180*math.pi*phnn)
CC[0, :] = 0
CC[-1, :] = 0
RR = CC.real
Rc = RR

if usebothch: #use real and imaginary channel
    II = CC.imag
    temp = II.conj().T
    hb = sp.signal.hilbert(temp)
    hb = hb.conj().T
    imH = hb.imag
    # plt.plot(h,imH[:,10],h,RR[:,10])
    # plt.plot(h,imH[10,:],h,RR[10,:])
    # plt.show()
    RI = RR-imH
    Rc = RI

hc = h
Nhc = len(hc)
SW = hc[-1]-hc[0]
TT = np.zeros((Ng, Nz, Nhc), dtype=complex)

for n in range(Ng):
    v, A = fftM(hc, hc)
    w = np.fft.ifftshift(2*math.pi*v)
    W, Z = np.meshgrid(w, z)
    temp = np.multiply(Z,W)
    T = np.exp(1j*temp*g[n])
    TT[n, :, :] = T

PR = np.fft.fft(Rc.conj().T)
x_PH = np.zeros((Nz, Nhc), dtype=complex)

# Regul operatotr
v0 = np.ones(Nz)
v1 = np.ones(Nz-1)
D0 = np.diag(v0)
D1 = np.diag(v1, k=-1)+ np.diag(-v1, k=1)

```

```

DD1 = np.matmul(D1.conj().T, D1)
DD0 = np.matmul(D0.conj().T, D0)

fH = 0
if method1 == 'tikh_0':
    for m in range(fH, Max_harm):
        L = TT[:, :, m]
        b = PR[:, m]
        LL = np.matmul(L.conj().T, L)
        temp1 = LL + tol_tikh * DD0
        temp2 = L.conj().T
        xx1 = np.linalg.solve(temp1,temp2)
        xx = np.matmul(xx1, b)
        x_PH[:, m] = xx

elif method1 == 'tikh_0':
    for m in range(fH, Max_harm):
        L = TT[:, :, m]
        b = PR[:, m]
        LL = np.matmul(L.conj().T, L)
        temp1 = LL + tol_tikh * DD1
        temp2 = L.conj().T
        xx1 = np.linalg.solve(temp1,temp2)
        xx = np.matmul(xx1, b)
        x_PH[:, m] = xx

else:
    print('method unavailable.')
    exit()

x_Ph = (np.fft.ifft(x_PH)).real
np.savetxt("image.csv", x_Ph, delimiter=",")
print('image matrix is generated: image.csv')

if rawimg:      # raw image plot
    imgplot = plt.imshow(x_Ph,aspect='auto',extent=[hc[0],hc[-1],z[0],z[-
1]])
    plt.xlabel('Magnetic Field, G')
    plt.ylabel('Position, cm')
    plt.title('VHF Rapid-scan of ' + sample + fn)
    plt.show()
    exit()

#### cut image
inx = np.abs(hc) < h_max
jnx = ((z > zlim[0]) * (z < zlim[1]))
h = hc[inx]
zj = z[jnx]

steph = abs(hc[1]-hc[0])
p1 = np.where(abs(hc + h_max) < steph)[0][0]
q1 = np.where(abs(hc - h_max) < steph)[0][0]
stepz = abs(z[1]-z[0])
p2 = np.where(abs(z - zlim[0]) < stepz)[0][0]
q2 = np.where(abs(z - zlim[1]) < stepz)[0][0]
I = x_Ph[p2:q2, p1:q1]  #z * h matrix
h = h+CF

plt.subplot(211)
imgplot = plt.imshow(I,aspect='auto',extent=[h[0],h[-1],zj[0],zj[-1]])
plt.xlabel('Magnetic Field, G')
plt.ylabel('Position, cm')
plt.title('VHF Rapid-scan of ' + sample + fn)

```

```

# plt.show()
# exit()

##### spectral slice(s)
if specs1:
    z1 = -0.2731    #pick spatial position you want to cut the spectral
slice
    z2 = 0.02101
    p1 = np.where(abs(zj - z1) < stepz)[0][0]
    p2 = np.where(abs(zj - z2) < stepz)[0][0]
    s11 = I[p1, :]
    s12 = I[p2, :]

    if usebackcor:      # use 'backcor' background correction
        AB = s12
        if backcorpar:  # I known what parameters to use!
            BG = backcor(h, s12, 4, 0.01, 'sh')
            AB = AB-BG

        else:          # try different parameters
            np.savetxt("temp/xdata.csv", h, delimiter=",")
            np.savetxt("temp/ydata.csv", AB, delimiter=",")
            window = Tk()
            window.title("backcor")
            window.geometry("300x250+900+200")
            start = mclass(window)
            window.mainloop()

            reader = csv.reader(open('temp/ybackcor.csv', "r"),
delimiter=",")
            x = list(reader)
            AB1 = np.array(x).astype("float")
            AB = AB1[:,0]
            s12=AB

    plt.subplot(212)
    # plt.plot(h, s11, h, s12, linewidth=1) #plot 2 slices
    plt.plot(h, s12, linewidth=1)
    plt.title('Spectral Slice ')
    plt.show()

    m = np.where(abs(h - 87) < steph)[0][0]
    n = np.where(abs(h - 95) < steph)[0][0]
    peak = s12[m:n]
    ##### Calculate linewidth
    if uselw:
        swpeak = len(peak) * abs((h[-1] - h[0])) / len(s12)
        pphh = LW(peak, swpeak)
        print('linewidth,mG: ', pphh)

    ##### Calculate SNR
    if useSNR:
        p = np.where(abs(h - 63) < steph)[0][0]
        q = np.where(abs(h - 70) < steph)[0][0]
        noise1 = np.std(s12[p:q]) # p:q or q:p if h reverses
        p = np.where(abs(h - 113) < steph)[0][0]
        q = np.where(abs(h - 120) < steph)[0][0]
        noise2 = np.std(s12[p:q]) # p:q or q:p if h reverses
        noise = (noise1 + noise2) / 2
        peak_amp = max(peak) # signal
        SNR = peak_amp / noise
        print('S/N: ', SNR)

```

```

##### spatial slice
if spatsl:
    field = 91.74 # pick field on plot by cursor
    p = np.where(abs(h - field) < steph)[0][0]
    spatial = I[:, p]

    plt.subplot(212)
    plt.plot(zj, spatial, linewidth=1)
    plt.title('Spatial Slice ')
    plt.show()

```

Script 3: Function Package

```

##### Rapid-scan EPR function code #####
# Yilin Shi, May 2019, shiyilin890@gmail.com
# choose 0: False, function skipped; 1: True, function performed
# Reference [1,2,3]

import os
import numpy as np
import scipy as sp
import matplotlib.pyplot as plt
import csv
from tkinter import *
import math
import cmath
import struct
import numpy.matlib

def fftM (t,a):
    if len(t) > 1:
        dt = t[1] - t[0]
    else:
        dt = t
    L = len(a)
    Wmax = 1/dt
    T = dt*L
    dw = 1/T
    Left = -Wmax / 2
    Right = Wmax / 2 -dw
    w = np.arange(Left, Right, dw)
    aa = np.fft.fft(a)
    A = np.fft.fftshift(aa)
    if len(w) < len(A):
        temp = w[1] - w[0]
        temp = w[-1] + temp
        w = np.append(w, temp)
    return w, A

# Interleaving data to one periodic cycle
def InterleavingCycles(tb,t,ts,rs,sf,Nfc,Ns,Wm,method):
    P = 1 / sf #period
    inx = t > (t[-1] - P + tb)
    inc = t < Nfc * P
    K = np.arange(-Ns/2, Ns/2)
    rs_i = rs[inc] #rs with Bfc full cycles
    M = len(rs_i)

```

```

t_i = t[inc]      # time vector

if method == 'slow':
    RS_i = np.zeros(Ns)
    for k in range(len(K)):
        tmp = cmath.exp(-1j*K[k]*Wm*t_i)
        RS_i[k] = rs_i * tmp
    aaa = np.fft.fftshift(RS_i)
    rs_x = np.fft.fft(aaa) * tb / ts[1] / Nfc / Ns
    print('method 1')
elif method == 'fast':
    rs_i2 = np.append(rs_i, rs_i)
    v, RS = fftM(t_i, rs_i2)
    RS_i = np.interp(K/P, v, RS)      #Xquery,x,y,

    cnt = len(RS_i)
    if RS_i[-1] == 0:
        check = RS_i[0]
        for i in range(round(cnt/2)):
            if RS_i[i] == check:
                RS_i[i] = 0
    else:
        check = RS_i[-1]
        for i in range(cnt-1, round(cnt/2), -1):
            if RS_i[i] == check:
                RS_i[i] = 0

    aaa = np.fft.fftshift(RS_i)
    rs_x = np.fft.ifft(aaa)/M*Ns/2
    print("method2")
else:
    print("Select appropriate case")
return rs_x, RS_i, v, RS, rs_i, t_i, inc

def H_amplit(xi, yi, Fm):
    #Fm- scan frequency; Nh-number of harmonics
    t = 2 * math.pi * Fm * xi
    c1 = np.cos(t)
    s1 = np.sin(t)
    s2 = np.sin(2 * t)
    c2 = np.cos(2 * t)
    o = c1 * 0 + 1

    f = yi
    fs = (f + np.flipud(f)) / 2
    fa = (f - np.flipud(f)) / 2

    v1 = s1
    v2 = c2
    v3 = o

    a = np.matmul(v1, fs.conj().T)
    b = np.matmul(v2, fs.conj().T)
    c = np.matmul(v3, fs.conj().T)
    f = np.stack((a, b, c))

    a = np.array([np.matmul(v1, v1.conj().T), np.matmul(v1, v2.conj().T),
np.matmul(v1, v3.conj().T)])
    b = np.array([np.matmul(v2, v1.conj().T), np.matmul(v2, v2.conj().T),
np.matmul(v2, v3.conj().T)])
    c = np.array([np.matmul(v3, v1.conj().T), np.matmul(v3, v2.conj().T),
np.matmul(v3, v3.conj().T)])

```

```

T = np.stack((a, b, c))
xs = np.matmul(np.linalg.inv(T), f)

v1 = s2
v2 = c1
a = np.matmul(v1, fa.conj().T)
b = np.matmul(v2, fa.conj().T)
f = np.stack((a, b))

a = np.array([np.matmul(v1, v1.conj().T), np.matmul(v1, v2.conj().T)])
b = np.array([np.matmul(v2, v1.conj().T), np.matmul(v2, v2.conj().T)])
T = np.stack((a, b))
xa = np.matmul(np.linalg.inv(T), f)

          # sinx  sin2x  cosx  cos2x  const
r = np.array([xs[0], xa[0], xa[1], xs[1], xs[2]])
return r

#re-write sinDecoBG
def sinDecoBG (sw, sf, tb, t, rs, ph, fp, method):
    gamma = 1.7608e7
    g2f = gamma/(2*math.pi)      # = 2.8024e6
    Vmax = g2f*sw                # Max possible RS signal frequency
    Ns = 2*math.ceil(Vmax/sf)
    P = 1/sf
    ts = np.arange(Ns)*(P/Ns)
    Fmax = 1/(2*tb)              # Max frequency to be sampled without aliasing
    ratio = Vmax/Fmax            # sampling ratio must be <1
    Wm = 2*math.pi*sf

    pts = rs.shape[0]

    # Error & Warning check
    Nc = round(1/(tb*sf))        # Points per period
    Nfc = math.floor(pts/Nc)     # Number of full cycles
    if Nfc == 0:
        print('ERROR: less than a full cycle')
    if ratio > 1:
        print('Warning: Sampling rate may not be sufficient')

    rs_i, RS_i, v, RS, rs_ii, t_i, inc=InterleavingCycles(tb, t, ts, rs, sf,
Nfc, Ns, Wm, method)

    # Phase correction
    rs_ii = rs_i*cmath.exp(1j*(ph+0)/180*math.pi)

    # Position of 1st point correction
    shift = round(fp*Nc)        # Circular shift to find 1st point
    shift = shift % (len(rs_ii))
    shift1 = len(rs_ii)-shift
    aa = rs_ii[shift1::]
    bb = rs_ii[:shift1:]
    rs_iii = np.append(aa,bb)

    # Driving function
    rs = rs_iii
    t = ts
    tb = ts[1]    # new time base

    WF = -np.cos(2*math.pi*sf*t)
    W = gamma*sw/2*WF          # waverform
    dr = np.exp(-1j*np.cumsum(W)*tb) # driving function for 1 cycle

```



```

# Separation Up from Down
v, RS = fftM(t, rs)

k = int(Ns/2)
ind = v>0
temp = np.fft.ifftshift(RS*ind)
a = np.fft.ifft(temp)          # up scan
jnd = v < 0
temp = np.fft.ifftshift(RS*jnd)
b = np.fft.ifft(temp)          # down scan
aa = a[0:k]
bb = b[k:Ns]
bga = a[k:Ns]
bgb = b[0:k]

t1 = t[0:k]
t2 = t[k:Ns]

## BG removal
# 1st half
x = 2*math.pi*sf*t1;
c1 = np.cos(x);
c2 = np.cos(2*x);
s1 = np.sin(x);
s2 = np.sin(2*x);

# real and imaginary
r = H_amplit(t2, bga.real, sf)
#   sinx  sin2x  cosx  cos2x  const
# r=[xs(1) xa(1) xa(2) xs(2) xs(3)];
bg = r[0]*s1+r[1]*s2+r[2]*c1+r[3]*c2+r[4]

r = H_amplit(t2, bga.imag, sf)
tmp = r[0]*s1+r[1]*s2+r[2]*c1+r[3]*c2+r[4]
bg = bg+1j*tmp
aaa = aa-bg

# 2nd half
x = 2*math.pi*sf*t2;
c1 = np.cos(x);
c2 = np.cos(2*x);
s1 = np.sin(x);
s2 = np.sin(2*x);

# real and imaginary
r = H_amplit(t1, bgb.real, sf)
#   sinx  sin2x  cosx  cos2x  const
# r=[xs(1) xa(1) xa(2) xs(2) xs(3)];
bg = r[0]*s1+r[1]*s2+r[2]*c1+r[3]*c2+r[4]

r = H_amplit(t1, bgb.imag, sf)
tmp = r[0]*s1+r[1]*s2+r[2]*c1+r[3]*c2+r[4]
bg = bg+1j*tmp
bbb = bb-bg

#####
## Deco for A
drA = dr[0:k]
aaaa = aaa*drA
v, A = fftM(t, aaaa)
v, D = fftM(t, drA)

```

```

A = A/D

## Deco for B
drB = dr[k:Ns]
bbbb = bbb*drB
v, B = fftM(t,bbbb)
v, D = fftM(t,drB)
B = B/D

h = v*2*math.pi/gamma
ind = np.abs(h)<sw/2
A = A[ind]
B = B[ind]
h = h[ind]

A = (np.flipud(A)).imag
B = (np.flipud(B)).imag
return h,A, B

def backcor(n, y, ord, s, fct):
    #Background estimation by minimizing a non-quadratic cost function;
    reference[1]
    # Rescaling
    N = len(n)
    i = np.argsort(n)
    n.sort()
    y = y[i]
    maxy = np.amax(y)
    dely = (maxy - np.amin(y)) / 2
    n = 2 * (n[:] - n[N - 1]) / (n[N - 1] - n[0]) + 1
    y = (y[:] - maxy) / dely + 1

    # Vandermonde matrix
    p = np.arange(ord + 1)
    T1 = np.matlib.repmat(n, ord + 1, 1)
    T2 = np.matlib.repmat(p, N, 1)
    TT = np.power(T1.T, T2)
    T3 = np.linalg.pinv(np.matmul(TT.T, TT))
    Tinv = np.matmul(T3, TT.T)

    # Initialisation (least-squares estimation)
    a = np.matmul(Tinv, y)
    z = np.matmul(TT, a)

    # Other variables
    alpha = 0.99 * 1 / 2 # Scale parameter alpha
    it = 0 # Iteration number

    # LEGEND
    while True:
        it = it + 1 # Iteration number
        zp = z # Previous estimation
        res = y - z # Residual

        # Estimate d
        if (fct == 'sh'):
            d = (res * (2 * alpha - 1)) * (abs(res) < s) + (-alpha * 2 * s -
res) * (res <= -s) + (
                alpha * 2 * s - res) * (res >= s)
        elif (fct == 'ah'):
            d = (res * (2 * alpha - 1)) * (res < s) + (alpha * 2 * s - res) *
(res >= s)

```

```

        elif (fct == 'stq'):
            d = (res * (2 * alpha - 1)) * (abs(res) < s) - res * (abs(res) >=
s)
        elif (fct == 'atq'):
            d = (res * (2 * alpha - 1)) * (res < s) - res * (res >= s)

        # Estimate z
        a = np.matmul(Tinv, y + d)
        z = np.matmul(TT, a)

        z1 = sum(np.power(z - zp, 2)) / sum(np.power(zp, 2))
        if z1 < 1e-9:
            break

        # Rescaling
        j = np.argsort(i)
        z = (z[j] - 1) * dely + maxy
        a[0] = a[0] - 1
        a = a * dely # + maxy
        return z

def xForInterp(sweep,N):
    x = np.arange(N) / (N - 1)
    sw2 = sweep / 2
    x = -sw2 + x * sweep
    return x

def mygaussian(h,FWHM):
    Hpp = FWHM/1.1774 #sqrt(2*log(2))
    A = 0.7979/Hpp #sqrt(2/pi)
    x = 2 * np.power(h / Hpp, 2)
    y = A * np.exp(-x)
    return y

def zeroline(spectrum, extent):
    L = len(spectrum)
    edge = round(extent * L)
    if edge == 0:
        edge=1

    Sleft = sum(spectrum[0:edge]) / edge
    Sright = sum(spectrum[L - edge:L+1]) / edge
    s = len(spectrum)

    LL = np.arange(1,L+1)
    tmp = Sleft + (Sright - Sleft) / L * LL
    if len(tmp) != s:
        tmp = tmp.T
    res = spectrum - tmp
    return res

def LW(spectrum, sweep):
    sp = zeroline(spectrum, 0.05)
    N = len(sp)
    n = N - 1
    x = np.arange(n+1)
    xn = (x - n / 2) / n

    M = 2000
    n = M - 1
    x = np.arange(n + 1)
    xm = (x - n / 2) / n

```

```

if M > N:
    sp = np.interp(xm, xn, sp)    #don't need zero baseline

    mx = max(sp)
    inx = sp > (mx / 2)
    N = len(sp)
    linewidth = round(1000 * sum(inx) / N * sweep)
    return linewidth

class mclass:    #for backcor function
    def __init__(self,window):
        self.window = window

        self.l1 = Label(window, text="Background Correction",
font=("Helvetica", 14))
        self.l2 = Label(window, text="Order")
        self.l3 = Label(window, text="Threshold")
        self.l4 = Label(window, text="Function")
        self.l5 = Label(window, text="")

        self.l1.grid(row=1, column=1, sticky=W, columnsspan=5)
        self.l2.grid(row=2, column=1, sticky=E)
        self.l3.grid(row=3, column=1, sticky=E)
        self.l4.grid(row=4, column=1, sticky=E)
        self.l5.grid(row=5, column=1, sticky=E)

        self.e2 = Entry(window)
        self.e2.insert(0, 0.01)
        self.e2.grid(row=3, column=2, sticky=W)

        self.v1 = StringVar(window)
        self.v1.set("6")
        self.w1 = OptionMenu(window, self.v1, '0', '1', '2', '3', '4', '5',
'6', '7', '8', '9', '10')
        self.w1.grid(row=2, column=2, sticky=W)

        self.v3 = StringVar(window)
        self.v3.set("ah")
        self.w = OptionMenu(window, self.v3, "sh", "ah", "stq", "atq")
        self.w.grid(row=4, column=2, sticky=W)

        self.b1 = Button(window, text=' Select and Plot ',
command=self.plotbg)
        self.b1.grid(row=6, column=1, sticky=E)
        # self.b2 = Button(window, text=' OK ', command=window.destroy)
#possible close button
        # self.b2.grid(row=6, column=2, sticky=E)
        self.l6 = Label(window, text="When done, close window \nand background
plot to proceed. ")
        self.l6.grid(row=7, column=1, sticky=W, columnsspan=2)

    def plotbg(self):
        plt.clf()
        ord = int(self.v1.get())
        s = float(self.e2.get())
        fct = self.v3.get()
        reader = csv.reader(open('temp/xdata.csv', "r"), delimiter=",")
        x = list(reader)
        h1 = np.array(x).astype("float")
        h = h1[:, 0]

```

```

reader = csv.reader(open('temp/ydata.csv', "r"), delimiter=",")
x = list(reader)
AB1 = np.array(x).astype("float")
AB = AB1[:,0]

BG = backcor(h, AB, ord, s, fct)
np.savetxt("temp/ybackcor.csv", AB-BG, delimiter=",")

plt.plot(h, AB, h,BG)
plt.gca().legend(('Original', 'Background'))
plt.title('Background Plot ')
# plt.clf()
plt.show()
plt.close()      #must have this so this plot will close

class adjust:    #for first point and phase adjustment
    def __init__(self,window):
        self.window = window

        self.l1 = Label(window, text="Spectrum Parameters Adjustment",
font=("Helvetica", 12))
        self.l2 = Label(window, text="Phase      ")
        self.l3 = Label(window, text="First Point      ")
        self.l4 = Label(window, text="(value exists in (-1, 1)      ")
        self.l5 = Label(window, text=" ")

        self.l1.grid(row=1, column=1, sticky=W, columnspan=5)
        self.l2.grid(row=2, column=1, sticky=E)
        self.l3.grid(row=3, column=1, sticky=E)
        self.l4.grid(row=4, column=1, sticky=E)
        self.l5.grid(row=5, column=1, sticky=E)

        f = open('temp/parvary.txt', "r")
        temp = f.read().splitlines()
        ph = float(temp[0])
        fp = float(temp[1])
        f.close

        self.e1 = Entry(window)
        self.e1.insert(0, ph)
        self.e1.grid(row=2, column=2, sticky=W)
        self.e2 = Entry(window)
        self.e2.insert(0, fp)
        self.e2.grid(row=3, column=2, sticky=W)

        self.b1 = Button(window, text='  Select and Plot  ',
command=self.plotbg)
        self.b1.grid(row=6, column=1, sticky=E)
        self.l6 = Label(window, text="When done, close window \nand plot to
proceed. ")
        self.l6.grid(row=7, column=1, sticky=W, columnspan=2)

    def plotbg(self):
        plt.clf()
        ph = float(self.e1.get())
        fp = float(self.e2.get())
        reader = csv.reader(open('temp/rsr.csv', "r"), delimiter=",")
        x = list(reader)
        y = np.array(x).astype("float")
        rsr = y[:, 0]
        reader = csv.reader(open('temp/rsi.csv', "r"), delimiter=",")

```

```

x = list(reader)
y = np.array(x).astype("float")
rsi = y[:,0]
rs = rsr + lj * rsi
reader = csv.reader(open('temp/t.csv', "r"), delimiter=",")
x = list(reader)
y = np.array(x).astype("float")
t = y[:,0]

f = open('temp/parfix.txt', "r")
temp = f.read().splitlines()
sw = float(temp[0])
sf = float(temp[1])
tb = float(temp[2])
method = temp[3]
f.close()

if os.path.isfile('temp/parvary.txt'):
    os.remove('temp/parvary.txt')
with open('temp/parvary.txt', 'a') as f:
    f.write(str(ph) + '\n')
    f.write(str(fp) + '\n')

h, A, B = sinDecoBG(sw, sf, tb, t, rs, ph, fp, method)

plt.plot(h, A, h, B)
plt.title('Up and down scan ')
# plt.clf()
plt.show()
plt.close()    #must have this so this plot will close

#reference
# [1] Deconvolution and image reconstruction from Dr. Mark Tseitlin's MATLAB
code
# Mark Tseitlin, Joshua R. Biller, Hanan Elajaili, Valery Khramtsov,
# Ilirian Dhimitruka, Gareth R. Eaton, and Sandra S. Eaton
# New spectral-spatial imaging algorithm for full EPR spectra of multiline
nitroxides
# and pH sensitive trityl radicals
# J Magn Reson. 2014 Aug; 245: 150-155.

# [2] Background correction code 'backcor':
# V. Mazet, C. Carteret, D. Brie, J. Idier, B. Humbert. Chemom. Intell. Lab.
Syst. 76 (2), 2005.
# V. Mazet, D. Brie, J. Idier. Proceedings of EUSIPCO, pp. 305-308, 2004.
# V. Mazet. PhD Thesis, University Henri Poincaré@ Nancy 1, 2005.
# 22-June-2004, Revised 19-June-2006, Revised 30-April-2010,
# Revised 12-November-2012 (thanks E.H.M. Ferreira!)
# Comments and questions to: vincent.mazet@unistra.fr.

# [3] Read Bruker data DTA and DSC in Python:
# https://github.com/mortenalbring/BES3Tconvert/blob/master/conv.py

```

Appendix D: Drawings of Hardware

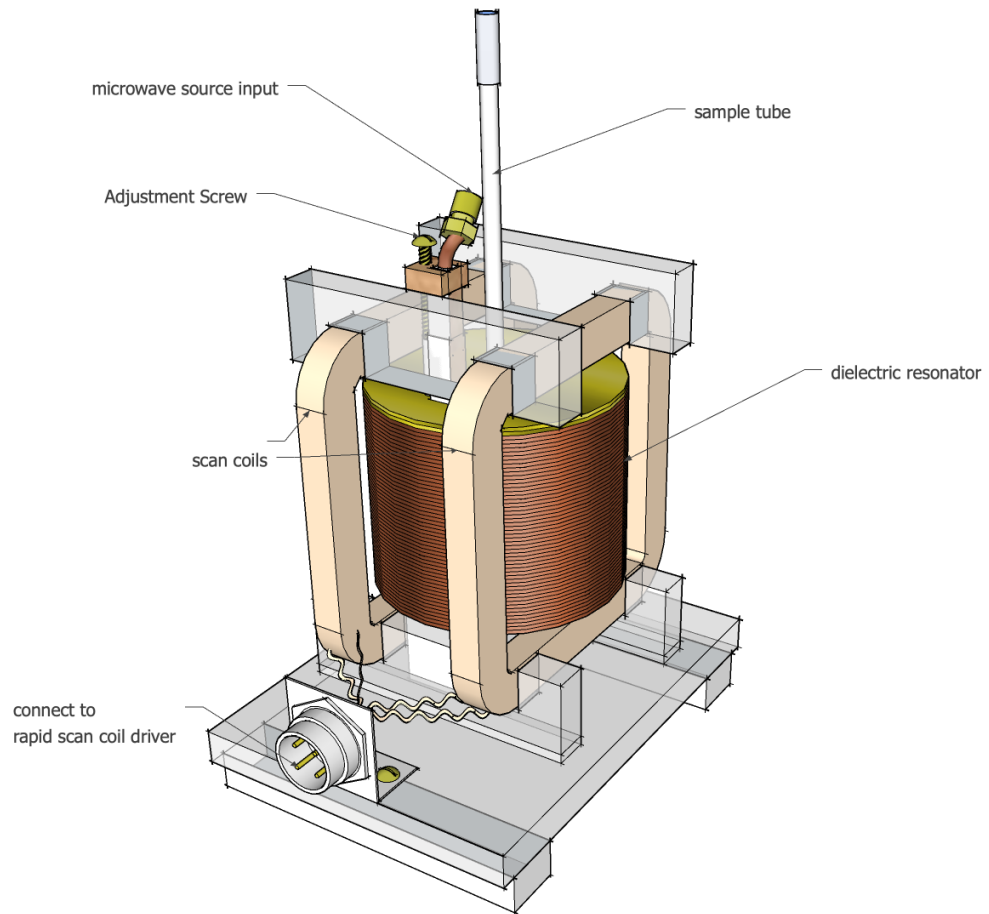


Figure D1 Drawing of L-band dielectric resonator assembly with wire-wound shield and rapid scan coils

Published in [157].

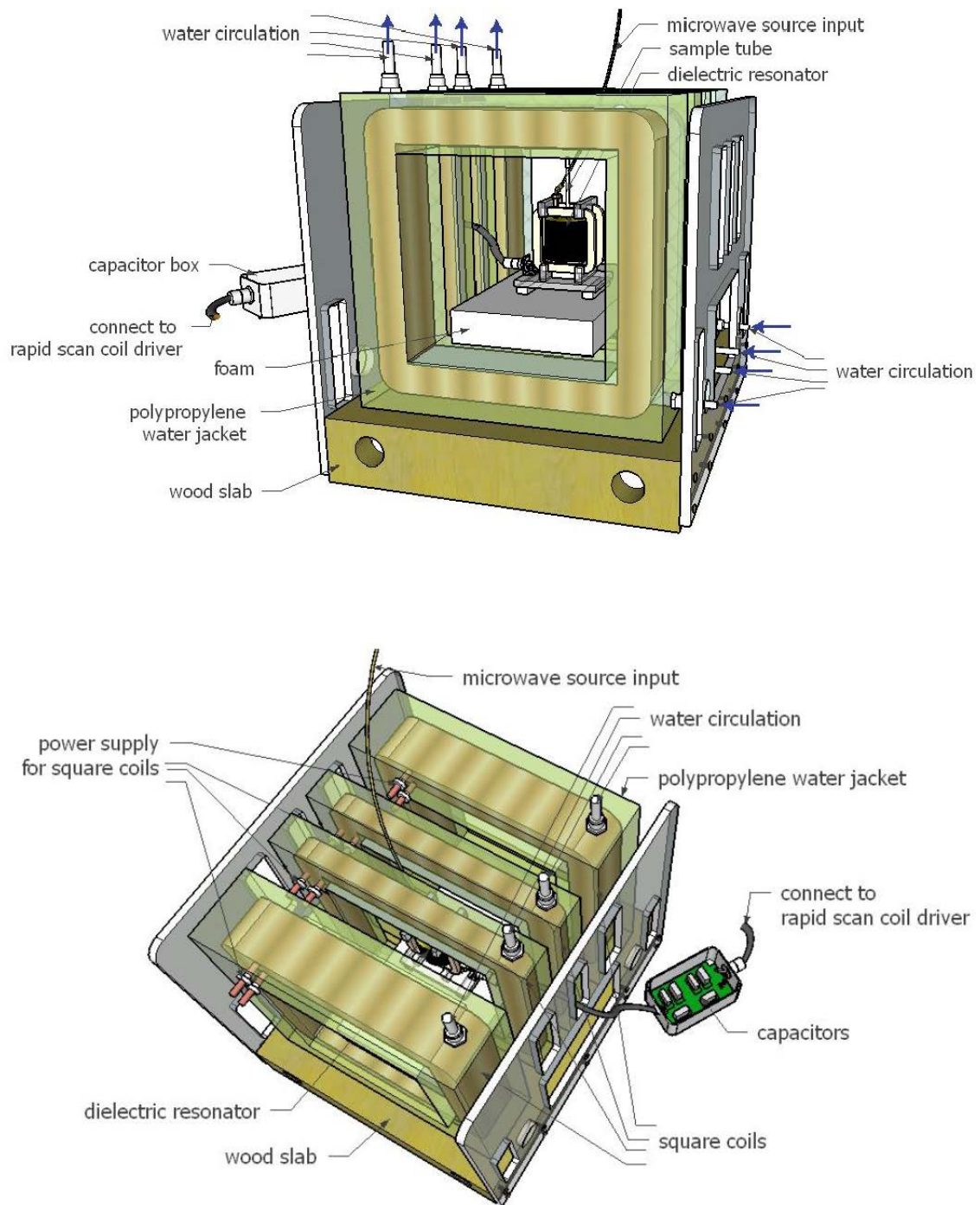


Figure D2 Drawings of the magnet, dielectric resonator, and capacitor box of the L-band rapid-scan system

Published in the supplementary information in [157]. The resonator is shown in more detail in Figure D1.

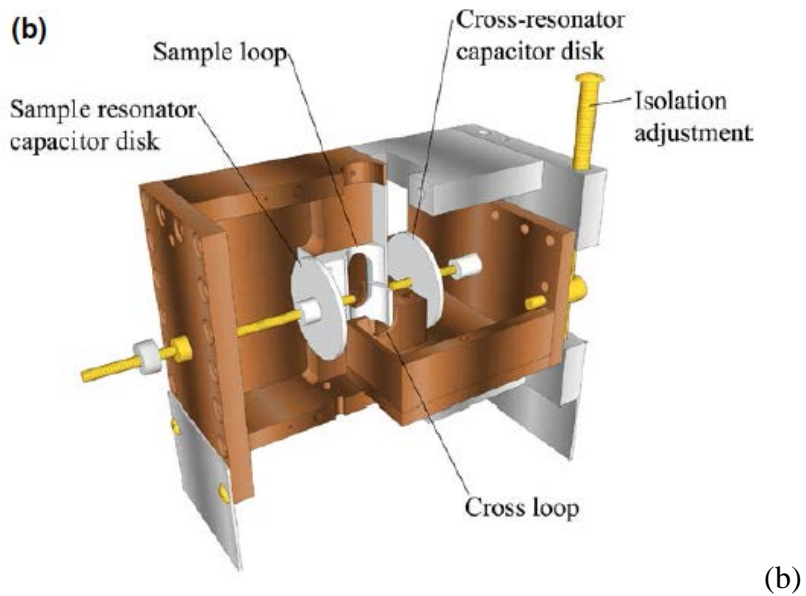
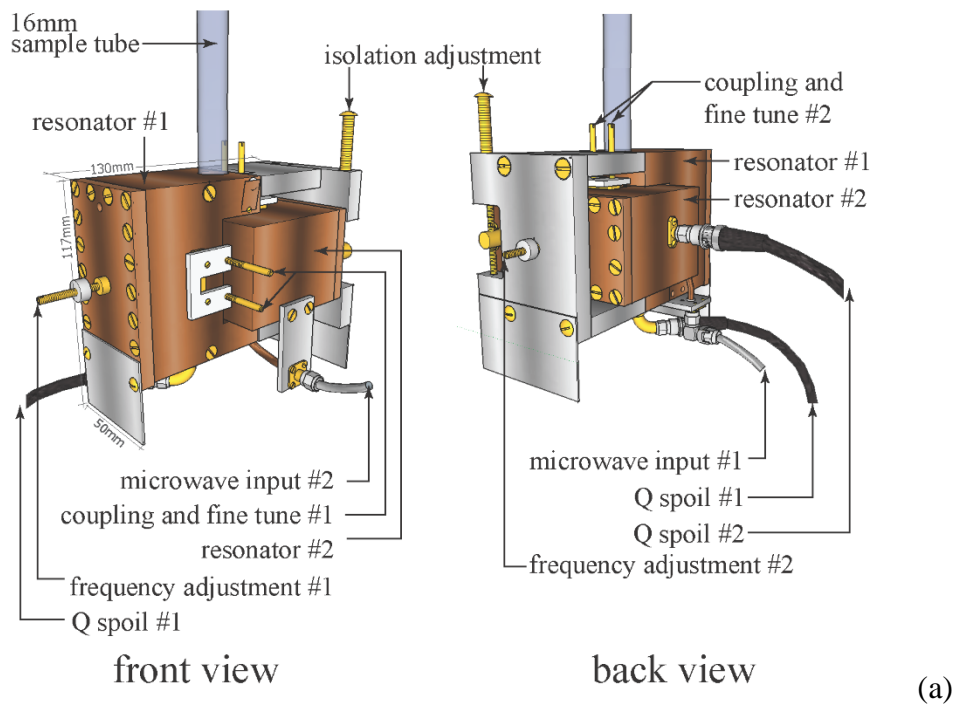
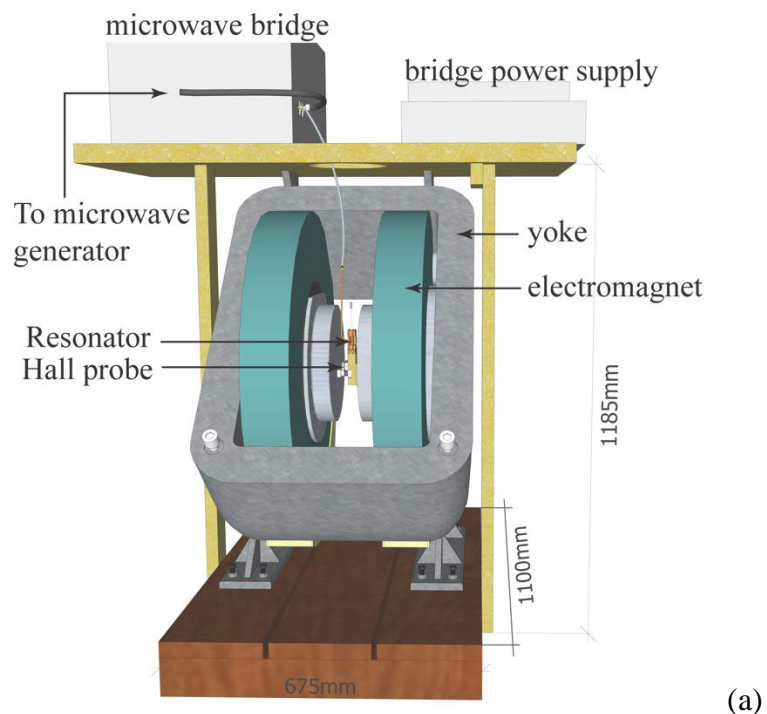
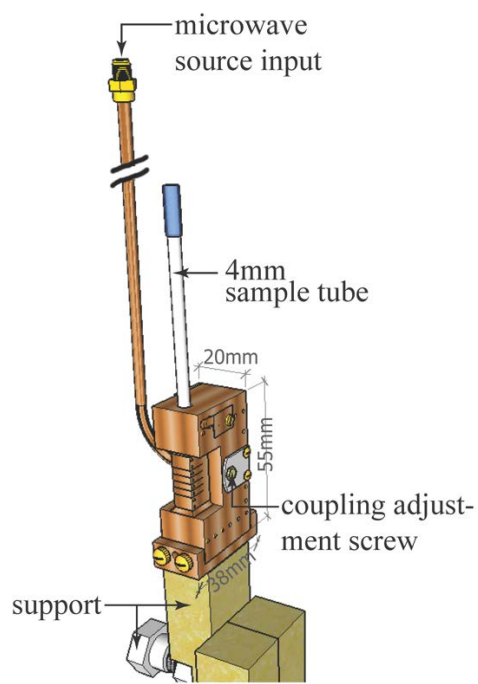


Figure D3 16mm variable frequency pulse cross-loop resonator for UHF
 (a) Front and back perspective drawings of resonator with sample tube. (b) Isometric view showing the capacitor disks used to vary the resonant frequency. Published in [180].

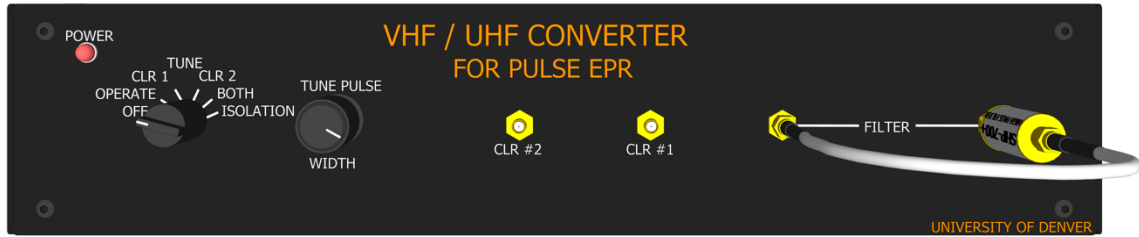


(a)



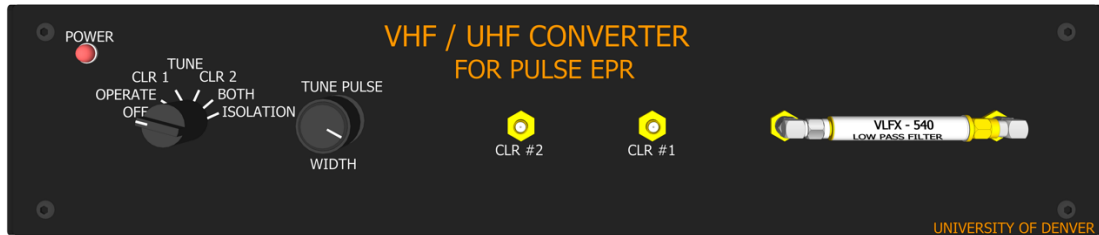
(b)

Figure D4 L-band (a) reflection resonator and (b) pulse spectrometer Unpublished.



5cm

(a)



5cm

(b)



5cm

(c)

Figure D5 The UHF accessory box

(a) Front panel controls with the high-pass or (b) low-pass filter mounted; (c) rear panel connectors. Published in [180].

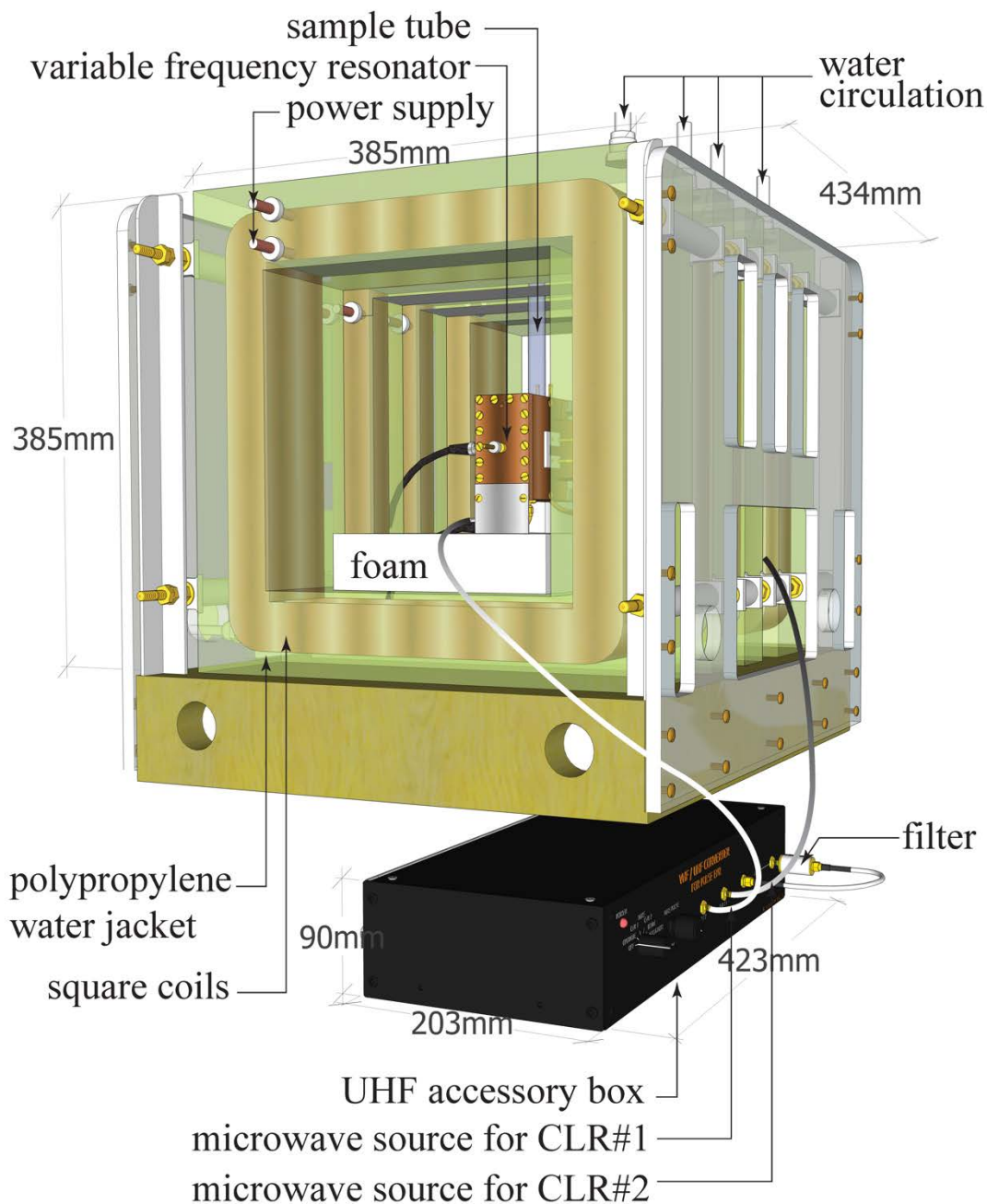
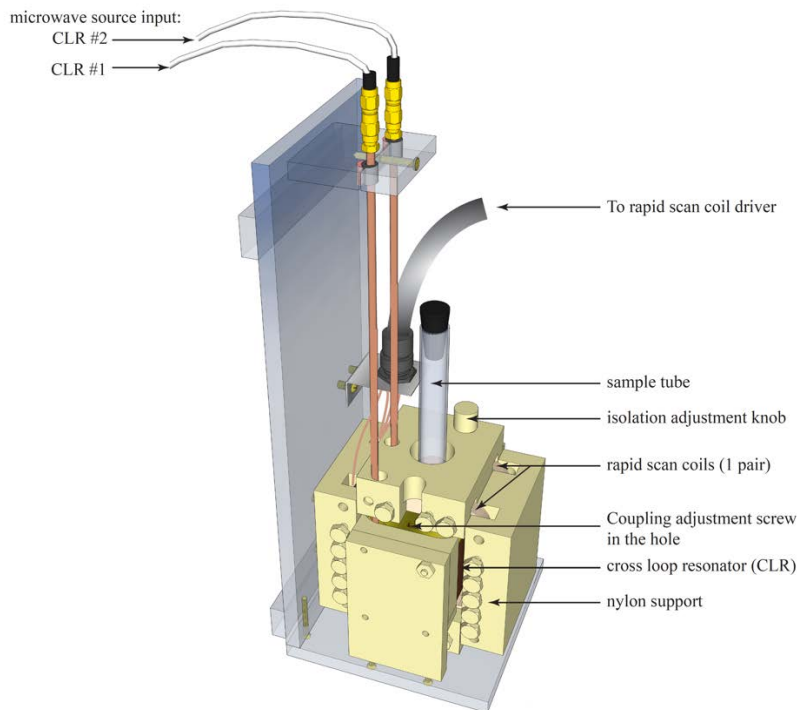
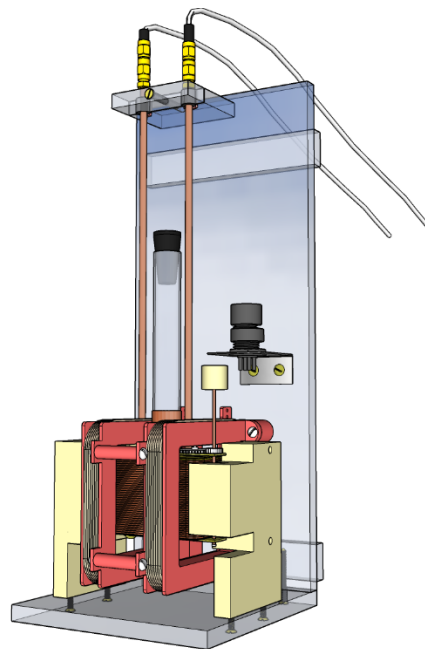


Figure D6 Ultra high frequency (UHF) pulse EPR system

The magnet is the same as shown in Figure D2; pulse resonator (Figure D3) and UHF accessory box (Figure D5) are used. Presented at 58th Rocky Mountain Conference on Magnetic Resonance 2016, poster session.

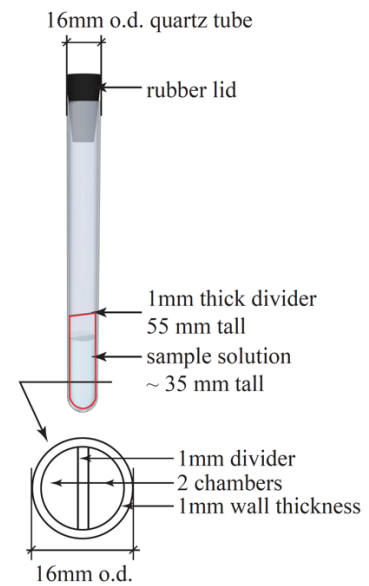


(a) 250 MHz Cross-loop resonator (2016~2017) with Nylon shielding installed



(b)

(b) 250 MHz cross-loop resonator after 2018 with Nylon shielding removed; a gear was installed to keep the tuning rod away from the scan coils, to avoid spark that happened once. (c) Test tube as the phantom. Unpublished.



(c)

Figure D7 16mm cross-loop resonator (CLR) and sample tube for imaging



(A) Front side

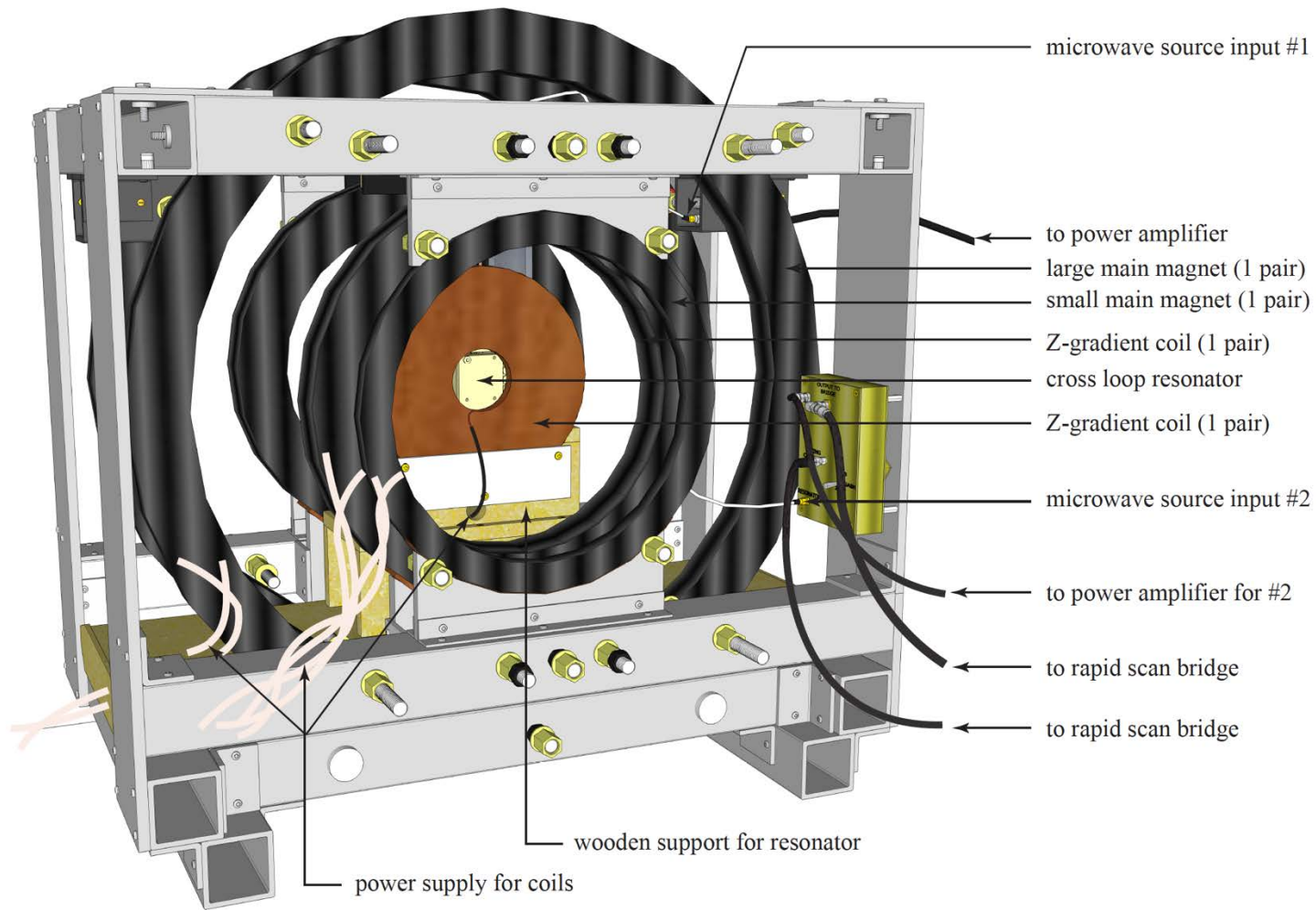


(B) Back side

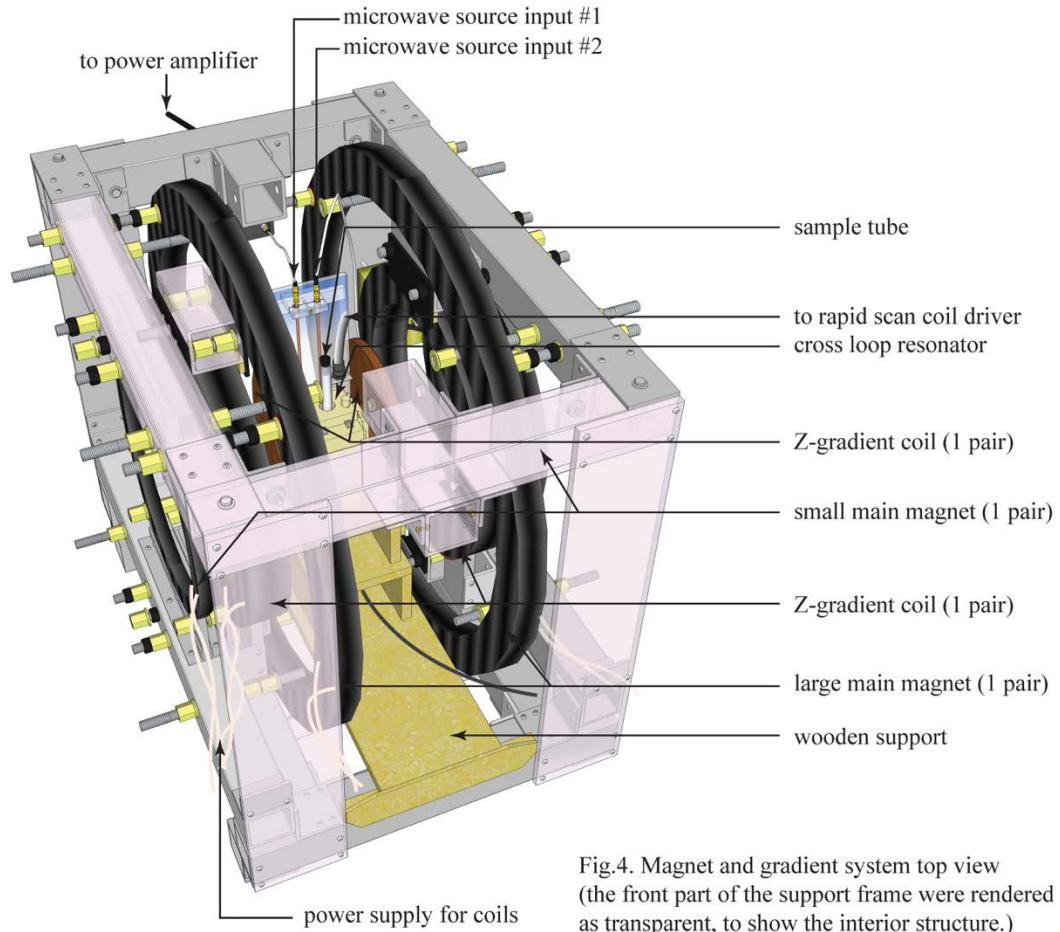
Figure D8 Rapid-scan coil driver

Unpublished.

270

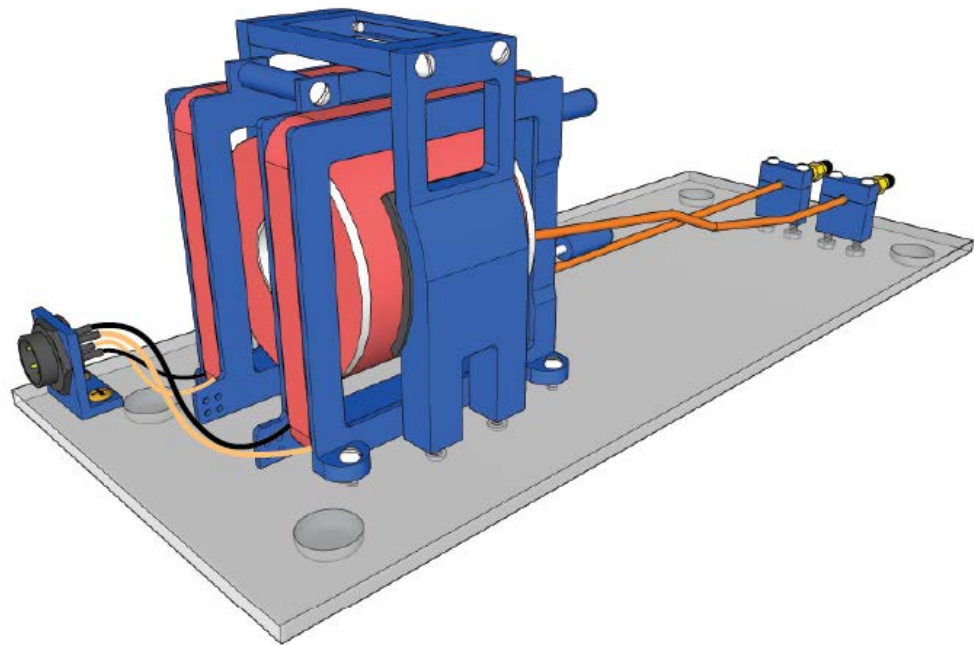


(A) Front view

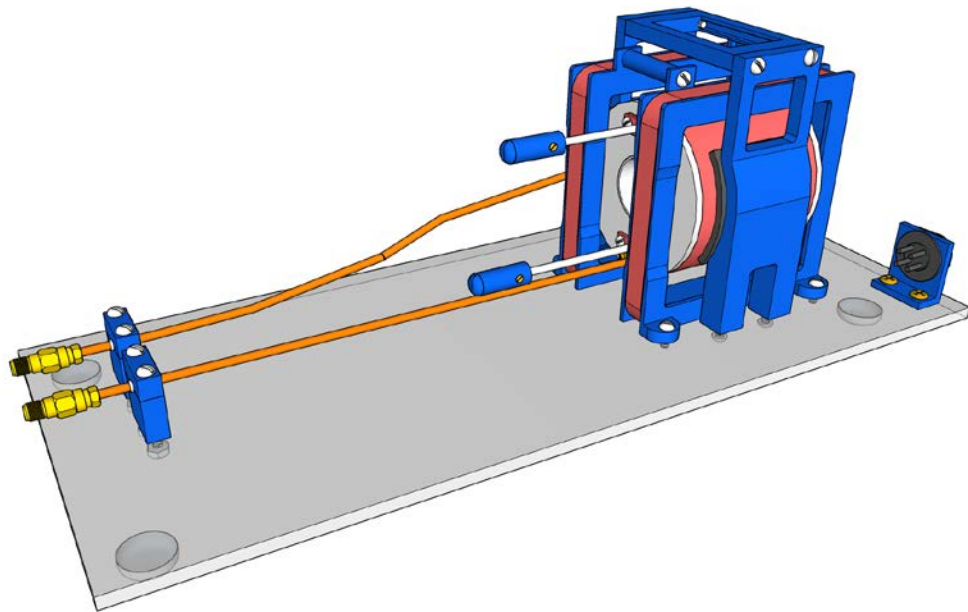


(B) Top view

Figure D9 VHF imaging system with 16mm resonator in place
 This VHF imaging system has been used in [11] [168] [128].



(A) Back view

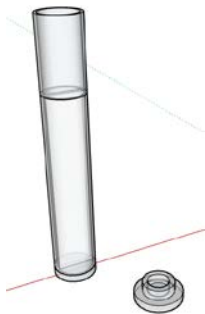

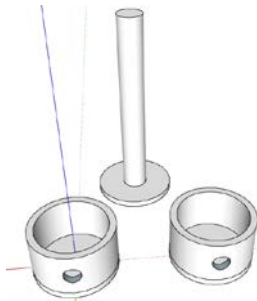

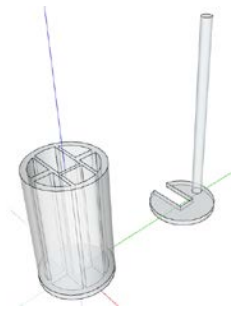



(B) Front view

Figure D10 25mm VHF rapid-scan imaging cross-loop resonator
This resonator was used in [128]. Unpublished.

Appendix E: 3D Printed Sample Holders for Imaging

Table E1 Examples of 3D prints

#	Computer model in Sketchup	3D Prints	Materials	Note
1			ABS (colored, or transparent), PLA (colored)	For 16 mm CLR resonator (Figure D7) on VHF EPRI spectrometer.
2			Transparent ABS	1. For 25 mm CLR on 700 MHz EPRI spectrometer [124]. 2. Disassembled into three parts to print so it won't collapse due to concave space.
3			HIPS, Colored PLA	For 25 mm CLR (Figure D10) on VHF EPRI spectrometer; see Figure 7.13 for cross section.

Appendix F: Equations and Experimental Parameters

1. Experimental parameters for the VHF EPR Imaging system

RS coil constant of 16 mm CLR: 21.75 G/A

RS coil constant of 25 mm CLR: 18.45 G/A

Coil inductance of 25 mm CLR: 1.73 mH

Gradient coil constant: 0.5 G/A

Main magnetic coil constant: 4.74 G/A

2. Calculation of rapid-scan frequency:

$$f = \frac{2\pi}{\sqrt{LC}}$$

L is inductance (*mH*), C is capacitor (μF).

For parallel capacitors:

$$C = \frac{C_0}{2}$$

3. Conversion between magnetic field (G) and RF frequency (MHz):

$$\text{Magnetic field (G)} = \text{RF frequency (MHz)} / 2.8$$

4. Calculate resonator efficiency:

Saturation factor

$$s = \frac{1}{1 + \gamma^2 B_1^2 T_1 T_2}$$

When $s = 1/2$,

$$B1 = \frac{1}{\gamma \sqrt{T_1 * T_2}}$$

$$resonator\ efficiency = \frac{B_1(G)}{\sqrt{P(W)}}$$

5. Calculation of resonator bandwidth: see chapter 4, section 4.3.1

6. Conversion between attenuation (dB) and power (W):

L-band and VHF:

$$power = \frac{0.0326}{10^{attenuation/10}}$$

X-band:

$$power = \frac{0.2106}{10^{attenuation/10}}$$

Appendix G: List of Publications

1. Imaging Disulfide Dinitroxides at 250 MHz to Monitor Thiol Redox Status, H. Elajaili, J. R. Biller, G. M. Rosen, J. P. Y. Kao, M. Tseytlin, L. A. Buchanan, G. A. Rinard, R. W. Quine, J. McPeak, Y. Shi, S. S. Eaton, and G. R. Eaton, *J. Magn. Reson.* **260**, 77 – 82 (2015).
2. Rapid scan electron paramagnetic resonance at 1.0 GHz of defect centers in γ -irradiated organic solids, Y. Shi, G. A. Rinard, R. W. Quine, S. S. Eaton, G. R. Eaton, *Radiation Measurements* **85**, 57 – 63 (2016).
3. UHF EPR spectrometer operating at frequencies between 400 MHz and 1 GHz, R. W. Quine, G. A. Rinard, Y. Shi, L. Buchanan, J. R. Biller, S. S. Eaton, and G. R. Eaton, *Conc. Magn. Reson, Magn. Reson. Engineer* **46B**, 123 – 133 (2016).
4. Triarylmethyl Radical: EPR Signal to Noise at Frequencies between 250 MHz and 1.5 GHz and Dependence of Relaxation on Radical and Salt Concentration and on Frequency, Y. Shi, R. W. Quine, G. A. Rinard, L. Buchanan, S. S. Eaton, G. R. Eaton, B. Epel, S. W. Seagle, and H. J. Halpern, *Z. Physik. Chem.* **231**, 923 – 937 (2017).
5. Triarylmethyl Radical OX063d24 Oximetry: Electron Spin Relaxation at 250 MHz and RF Frequency Dependence of Relaxation and Signal-to-Noise, Y. Shi, R. W. Quine, G. A. Rinard, L. Buchanan, S. S. Eaton, G. R. Eaton, B. Epel, S. W. Seagle, and H. J. Halpern, *Adv. Exp. Med. Biol.* **977**, 327 - 334 (2017).
6. Rapid Scan EPR Imaging, S. S. Eaton, Y. Shi, L. Woodcock, L. A. Buchanan, J. McPeak, R. W. Quine, G. A. Rinard, B. Epel, H. J. Halpern, and G. R. Eaton, *J. Magn. Reson.* **280**, 140 – 148 (2017).

7. 250 MHz Rapid Scan Cross Loop Resonator, L. A. Buchanan, L. B. Woodcock, G. A. Rinard, R. W. Quine, Y. Shi, S. S. Eaton, and G. R. Eaton, *Appl. Magn. Reson.*, **50**, 333 - 345 (2019).